AFRL-IF-RS-TR-2005-307
Final Technical Report
August 2005

BIO-FLUID TRANSPORT MODELS THROUGH NANO AND MICRO-FLUIDIC COMPONENTS

Ohio State University Research Foundation

Sponsored by
Defense Advanced Research Projects Agency
DARPA Order No. K900

AIR FORCE RESEARCH LABORATORY
INFORMATION DIRECTORATE
ROME RESEARCH SITE
ROME, NEW YORK

STINFO FINAL REPORT

This report has been reviewed by the Air Force Research Laboratory, Information Directorate, Public Affairs Office (IFOIPA) and is releasable to the National Technical Information Service (NTIS). At NTIS it will be releasable to the general public, including foreign nations.

AFRL-IF-RS-TR-2005-307 has been reviewed and is approved for publication

APPROVED: /s/

DUANE GILMOUR
Project Engineer

FOR THE DIRECTOR: /s/

JAMES A. COLLINS, Acting Chief
Advanced Computing Division
Information Directorate

REPORT DOCUMENTATION PAGE

Form Approved
OMB No. 074-0188

1. AGENCY USE ONLY (Leave blank)	2. REPORT DATE	3. REPORT TYPE AND DATES COVERED
	AUGUST 2005	Final Jun 00 – Jan 04

4. TITLE AND SUBTITLE
BIO-FLUID TRANSPORT MODELS THROUGH NANO AND MICRO-FLUIDIC COMPONENTS

5. FUNDING NUMBERS
C - F30602-00-2-0613
PE - 61101E
PR - E117
TA - 00
WU - 62

6. AUTHOR(S)
A. T. Conlisk,
Derek Hansford,
Minami Yoda

7. PERFORMING ORGANIZATION NAME(S) AND ADDRESS(ES)
Ohio State University Research Foundation
1960 Kenny Road
Columbus Ohio 43210-1063

8. PERFORMING ORGANIZATION REPORT NUMBER
N/A

9. SPONSORING / MONITORING AGENCY NAME(S) AND ADDRESS(ES)
Defense Advanced Research Projects Agency
3701 North Fairfax Drive
Arlington Virginia 22203-1714

AFRL/IFTC
26 Electronic Parkway
Rome New York 13441-4514

10. SPONSORING / MONITORING AGENCY REPORT NUMBER
AFRL-IF-RS-TR-2005-307

11. SUPPLEMENTARY NOTES
AFRL Project Engineer: Duane Gilmour/IFTC/(315) 330-3550/ Duane.Gilmour@rl.af.mil

12a. DISTRIBUTION / AVAILABILITY STATEMENT
APPROVED FOR PUBLIC RELEASE; DISTRIBUTION UNLIMITED.

12b. DISTRIBUTION CODE

13. ABSTRACT *(Maximum 200 Words)*
This project was a combined fabrication, experimental, and modeling effort to predict transport properties of micro and nanochannels. In this work, the governing equations for electrokinetic flow are solved for not only monovalent binary electrolytes, but also multi-component electrolytic systems containing multivalent ion species. For channel-reservoir systems, the wall concentrations of different ion species are obtained using electrochemical equilibrium consideration. For channel materials with known surface charge density, the results are truly predictive, i.e. there are no assumable constants in the model. The results agree very well with the experimental data from four separate sources at over thirty-five operating conditions. This implies that the model is effective for channel height varying from less than ten nanometers to several micrometers. The experimental effort demonstrated that the novel nano-particle image velocimetry (nPIV) technique could measure velocity fields within 250 nm of the wall in steady electroosmotic flow with good accuracy. The nPIV data were in excellent agreement with the model predictions for monovalent electrolyte solutions, and were further validated by independent experimental measurements. This effort culminated in what we believe to be the first experimental probe inside the electric double layer in electroosmotic flow of an aqueous electrolyte solution.

14. SUBJECT TERMS
Micro And Nanofluidics, Electroosmotic Flow, Nano Particle Image Velocimetry

15. NUMBER OF PAGES
225

16. PRICE CODE

17. SECURITY CLASSIFICATION OF REPORT	18. SECURITY CLASSIFICATION OF THIS PAGE	19. SECURITY CLASSIFICATION OF ABSTRACT	20. LIMITATION OF ABSTRACT
UNCLASSIFIED	UNCLASSIFIED	UNCLASSIFIED	UL

Table of Contents

List of Figures

List of Tables

EXECUTIVE SUMMARY

This four-year project was a combined fabrication, experimental, and modeling effort to predict transport properties of micro and nanochannels. In this work, the governing equations for electrokinetic flow are solved for not only monovalent binary electrolytes, but also multi-component electrolytic systems containing multivalent ion species. For channel-reservoir systems, the wall concentrations of different ion species are obtained using electrochemical equilibrium consideration. For channel materials with known surface charge density, the results are truly predictive, *i.e.* there are no assumable constants in the model. The results agree very well with the experimental data from four separate sources at over thirty-five operating conditions. This implies that the model is effective for channel height varying from less than ten nanometers to several micrometers. In the latter portion of the project we computed the solutions for transient and pulsed electroosmotic flow (EOF) for sensing applications.

We also used CFD-ACE+ (www.cfdrc.com) simulations for micro and nanochannels for comparisons with experimental data. The three systems studied were the iMEDD nanochannel membrane, Oak Ridge National Laboratory (ORNL) micro/nanochannels, and natural and synthetic ion channels. Upon good comparisons with the experimental data, the CFD-ACE+ simulations could then be used in the design and optimization of the devices containing the micro- and nanochannels.

During this research it was discovered that the Navier-Stokes equation solved by the CFD-ACE+ solver was appropriate only for microchannels. The presence of the electric double layer (EDL) on the walls of the channel is handled as a boundary condition. This body force was constant both along and across the channel, much like the pressure gradient term generating flat velocity and concentration profiles which must be viewed as averages. After discussions with CFD-ACE+ developers, a new version of the CFD-ACE+ solver was generated to incorporate the correct body force term appropriate for nanochannels. This new beta version of the software was then implemented and used for all future simulations.

The experimental effort, which comprised the latter half of the project, demonstrated that the novel nano-particle image velocimetry (nPIV) technique could measure velocity fields within 250 nm of the wall in steady electroosmotic flow with good accuracy. The nPIV data were in excellent agreement with the model predictions for monovalent electrolyte solutions, and were further validated by independent experimental measurements from ORNL using neutral molecular tracers. This effort culminated in what we believe to be the first experimental probe inside the electric double layer in electroosmotic flow of an aqueous electrolyte solution.

Additional attachments corresponding to publications of major research results are included in this final report.

1. INTRODUCTION

1.1 Report Overview

This report gives a synopsis of the modeling, fabrication and experimental portions of this effort over the entire four-year project duration. The research objectives and major accomplishments are summarized in Section 1.3. The modeling work over the entire project period is summarized in Sections 1.4 and 1.5. This project was reconfigured approximately eighteen months after initiation and the fabrication component led by Ohio State University (OSU) and the Cleveland clinic was discontinued. The results from this fabrication effort are summarized in Section 2. As part of the project reconfiguration, an experimental effort led by Dr. Minami Yoda at the Georgia Institute of Technology (GT) was started about halfway through the project period. This experimental effort is summarized in Section 1.6. Section 3 on Conclusions and Recommendations for Future Work concludes this report. Additional publications are attached to provide further details on the modeling and experimental aspects of the project.

1.2 Background

Micro- and nano-fabrication began with the creation and shrinking of computer chips. In the past decade, this technology has moved into many other industries to fabricate microelectromechanical systems (MEMS). MEMS are defined as devices that combine electrical and mechanical components and are of the size less than 1 mm but larger than 1 micron. The fabrication techniques have recently expanded into the nanometer regime to create nanodevices.

Within the chemistry and biochemistry industries, MEMS technology is used to create a lab-on-a-chip; a device that incorporates all of the steps of chemical/biochemical analysis to solve a given measurement problem. Currently chemistry/biochemistry analysis labs consist of equipment as large as a microwave oven for each of the steps (collection, separation, and detection). A lab-on-a-chip device integrates sample collection, separation, biological and chemical detection units with fluid pumping, flow control elements, and electronics all into a single device, as seen in Figure 1. Many lab-on-a-chip devices are

made up of replicated channel and reservoir structures. During production, these designs are easily repeated on a single substrate generating a large number of parallel devices. This process allows for the manufacture of inexpensive disposable devices, which have many applications in research and clinical diagnostics.

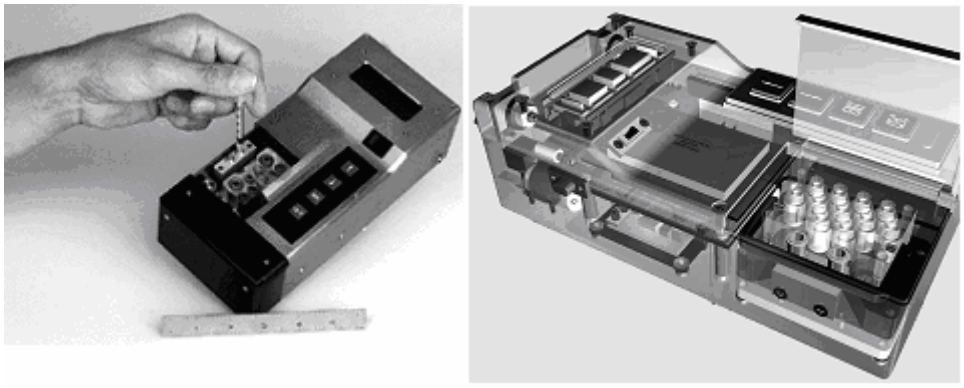

Figure 1 Sandia National Laboratory's fully integrated chemical analysis system that can fit in the palm of a hand. It has the ability to determine constituents of gas and liquid samples within one minute. It is made up of a compact power source, lasers and photodiodes, microprocessor, and micro-sized injection and separation channels. Left: final product, Right: cut-away image of the device showing many of the components (http://www.sandia.gov/media/NewsRel/NR2000/labchip.htm, 2/12/03).

Utilizing lab-on-a-chip devices in a chemical/biochemical analysis lab clearly reduces equipment costs, but can also reduce the cost of other resources. The advantages of a lab-on-a-chip device are comparable to the advantages seen in the computer industry. For example, when reducing the size of a computer chip, the distance electrons need to travel is much shorter, reducing the processing time. This same principle applies to microfluidic devices; reducing the size of the channel reduces the distance molecules need to travel, therefore reducing the processing time. These devices also require much less reagents. For a standard analysis experiment, microliters or even larger volumes of reagents are used for each experiment; however, with lab-on-a-chip devices only nanoliter or picoliter volumes are required for each experiment. These small volumes not only reduce the cost for the reagents, they also produce significantly less waste saving on money for waste disposal.

Lab-on-a-chip devices also require little input from the technician because the sophisticated chemistry/biochemistry procedures are incorporated at production, therefore allowing novices to perform the complex procedures. A combination of all of the advantages listed above makes the use of lab-on-a-chip devices appealing to the medical community. This

type of technology is applied to the genetic and drug screening industry in order to expedite the Human Genome Project and drug development programs. It can also be applied to medical diagnostics, to decrease biofluid testing time, and possibly bring the diagnostic device to the patient's bedside.

Many of the procedures using lab-on-a-chip technology utilize electrokinetic transport principles. Many separation techniques (electrophoresis, isoelectric focusing, etc.) require an electric field in order to perform the separation. Electroosmotic flow (EOF) is used more often for pumping the fluid through the device due to the challenges that arise when working with pressure-driven pumping. The flow rate of the fluid due to electroosmotic pumping when the electric double layers are thin (Q_e) and pressure pumping (Q_p) are defined by:

$$Q_e \approx UhW$$

$$Q_p \approx \frac{Wh^3}{\mu L}\Delta p$$

where U is the electroosmotic velocity scale, h is the channel height, W is the channel width, L is the channel length, μ is the fluid viscosity, and Δp is the pressure drop [1]. These equations show that the volume flow rate for electroosmotic pumping is proportional to h, *vs.* h^3 for pressure pumping. Driving the flow by a pressure gradient is therefore not feasible for nano-sized channels. Figure 2 further illustrates this point by determining the pressure drop and applied potential required to obtain a flow rate of $Q = 1\times10^{-6}$ L/min. For a channel height of 10 nm, a pressure drop of 3 atm. is required, an unrealistic value for most nanochannel systems.

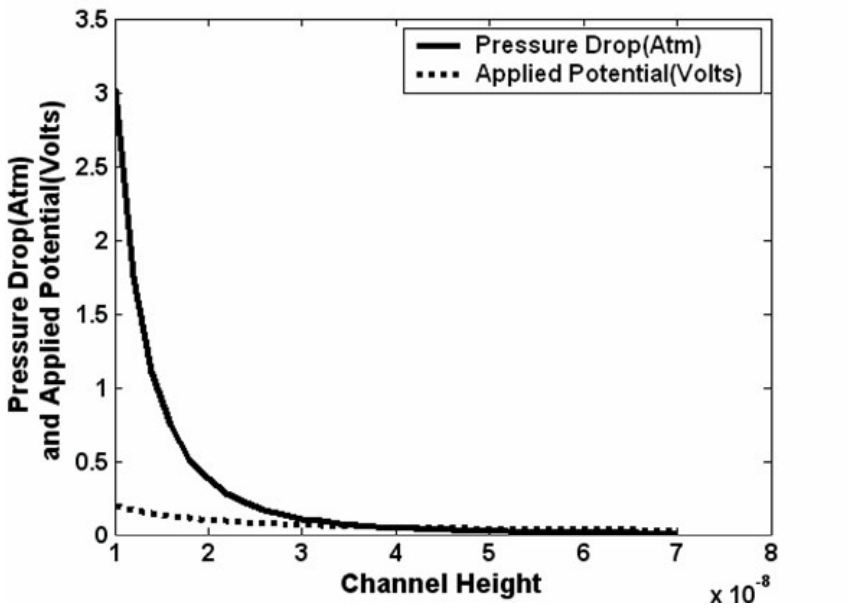

Figure 2 Pressure drop and applied voltage as a function of channel height to achieve a flow rate $Q = 10^{-6}$ L/min for a rectangular channel of width 44 μm [1].

1.3 Objectives and Major Research Accomplishments

The major objective of this work was to develop a scale-dependent theory validated by carefully performed experiments for ionic and biomolecular transport through nanoscale channels. This work investigated the design of micro-devices having nanoscale features for applications to rapid molecular analysis and manipulation, DNA analysis and transport, drug delivery and sensing.

During the period of work a number of research accomplishments have been realized and major advances have occurred. This project has generated over thirty publications, archival publications, conference papers, theses and presentations. Many of these publications are submitted as supplementary material for this report.

Our major accomplishments include:

- Development of an analytical/numerical model for electroosmotic flow in micro and nanochannels which compares well with four distinct sets of experimental data at over thirty-five operating conditions [1-3, 5, 7, 8, 25, 26, 27, 28, 30, 35].
- Completed fabrication of a series of nanochannels in silicon and methacrylates.

- Development of a computational model for electroosmotic flow in nanochannels using a company-updated version of CFD-ACE+ designed specifically for the project [9].
- Development of nano-particle image velocimetry (nPIV) experimental techniques that allow the first ever probe of the diffuse electric double layer (EDL) [6, 16, 18, 24, 33; in preparation].
- Development of multilayer nPIV which enables velocity measurements within 80 nm of the wall and shear stress measurements within 300 nm of the wall [32].
- Development of a model for transport in an ion channel (supporting documentation only) [9, 10, 20].
- Development of a model for transient electroosmotic flow for application to biomolecular sensing (supporting documentation only) [20, 35].
- Development of a model for biomolecular transport in nanochannels based on the concept of hindered diffusion (supporting documentation only) [10, 19, 20].
- Comparison of a continuum theory with molecular dynamics simulations showing excluded volume effects for channel heights under 10 nm (supporting documentation only) [25].

The numbers in these bullets refer to the list of papers and theses published under this contract.

1.4 Continuum Models

A continuum model for electrokinetic flow was developed for not only monovalent binary electrolytes, but also multi-component electrolytic system containing multivalent ion species. For channel-reservoir systems, the wall concentrations of different ion species were obtained using electrochemical equilibrium consideration. For channel materials with known surface charge density, the results are truly predictive, *i.e.*, there are no assumable constants in the model. This implies that the model is effective for channel heights varying from less than ten nanometers to several micrometers. Several parameters for the governing equations are explored, which indicates that the EOF in small channels can be mimicked by the EOF of less concentrated solution in larger channels. The 2D governing

equations which are appropriate to study synthetic ion channels or rectangular nanochannels are also solved in this work. For the ion-channel case, we have produced results for both long and short channels relative to the channel height. For the rectangular-nanochannel case, we have shown results for both symmetric and asymmetric channels. Because of the good agreement between the model and the experimental results, this work shows no evidence that the no-slip condition is invalid, or the surface roughness has to be considered. Overall the modeling component of this work was able to predict results in excellent agreement with four distinct sets of experimental data at over 35 operating conditions for both EOF and biomolecular transport.

Results on EOF through 20 nm nanochannels (produced by the fabrication effort during the first eighteen months of the project were compared to theoretical predictions. The EOF followed the analytical theory developed by our group; the results from this theory have also been validated by experimental flow data for a variety of liquid parameters through nanochannel membranes from iMEDD, Inc.

We also used CFD-ACE+ for some of the computations. During this research it was discovered that the Navier-Stokes equation solved by the CFD-ACE+ solver contained an incorrect electroosmotic body force and assumed electroneutrality within the channel. This is appropriate for a microchannel but not a nanochannel. The presence of the EDL on the walls of the channel is handled as a boundary condition. This body force was constant both along and across the channel, much like the pressure gradient term generating flat velocity and concentration profiles which must be viewed as averages. After discussions with CFD-ACE+ developers, a new version of the CFD-ACE+ solver was generated to incorporate the correct body force term. This new beta version of the software was then implemented and used for all future simulations.

The new CFD-ACE+ code specifically designed for this project was used to compare to the analytical results in Conlisk *et al.* [1]. The system for these simulations is a single nanochannel with a 3.5 μm length, 3 μm width, a varying height, a voltage drop of 6 volts, and a 0.154 M NaCl solution. As with the iMEDD simulations, the new CFD-ACE+ software could not handle the 3.5 μm long channel, so a 70 nm channel with a 0.084 V

voltage drop and a 0.154 M NaCl solution was used for the simulations. With this voltage drop, the results for a 4 nm channel height are similar to the analytical results. The results for a 24 nm channel height are close but not as accurate as the 4 nm channel. While the 70 nm channel results are close, it was unclear if the flow field was independent of length. Again, it is critical that a 3.5 μm long channel be used for the comparison so the correct voltage drop can be used.

1.5 Modeling of Nanofluidic Systems

iMEDD, Inc. (Columbus, OH) manufactures a nanopore membrane to be used for various biomedical applications. The membrane is made up of approximately 370,000 nanochannels in parallel. A scanning electron microscope (SEM) image of a section of the membrane is shown in Figure 3. The dimensions of a single channel are shown in Figure 4, with varying channel height, a length of 3 μm, a width of 44 μm, and the fluid flowing left to right (through the 44 μm long surface).

There are many applications for such a nanopore membrane including biofluidic separation and filtration, electroosmotic pumping, integrated microfluidic vents, controlled released drug delivery, size based protection of biosensors, disease treatment/prevention, and many more. Many of these applications utilize the nanopore membrane as a fluid pumping system. The basic set-up of a nanopump using the iMEDD nanopore membrane is shown in Figure 5. Here, the nanopore membrane is flanked by two reservoirs, which contain electrodes that generate the electrokinetic flow through the membrane.

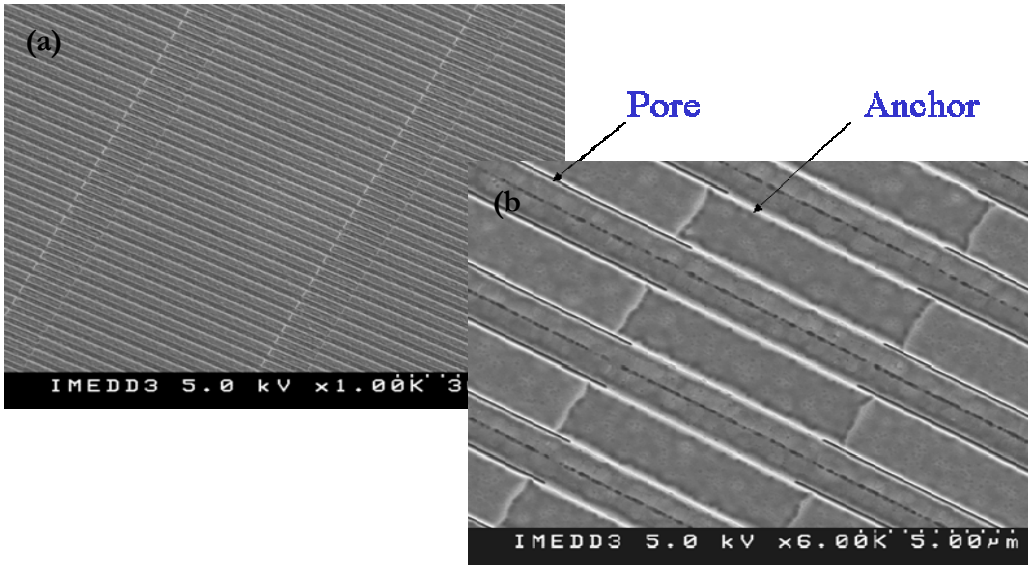

Figure 3 SEM images of iMEDD nanochannels (Each channel is approximately 44 µm long) (a) top view of parallel, 50 nanometer channels (b) 6× higher magnification of the same channels (images provided by Tony Boiarski, iMEDD Inc.).

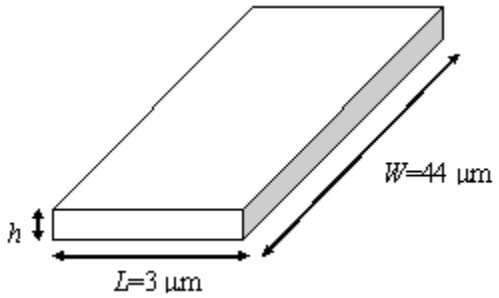

Figure 4 Geometry of a single iMEDD nanochannel. The value of the height (*h*) varies but is on the nanometer scale. The fluid flows from left to right.

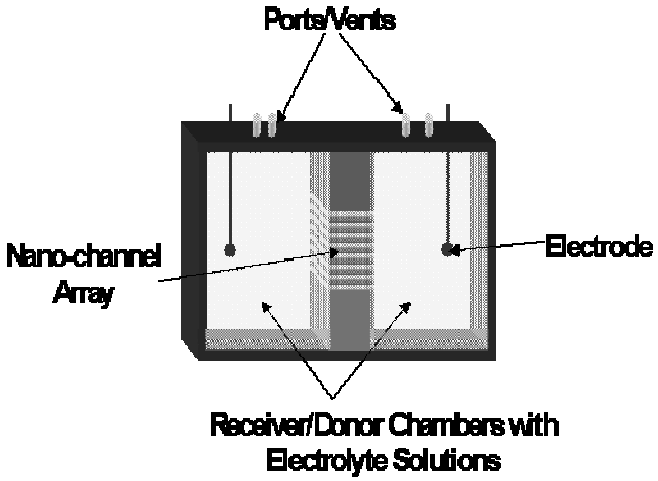

Figure 5 Picture of a nanopump system designed by iMEDD, Inc.

iMEDD has performed flow experiments on the nanopore membrane in order to optimize the system design. As mentioned earlier, it is also important to simulate the flow through the system using analytical and computational methods. One of the goals of this research is to accurately model the flow through the nanopore membrane using CFD-ACE+ and compare these results to the iMEDD experimental data and the analytical model results.

In addition to the iMEDD nanopump system, this research also uses CFD-ACE+ to model the fluid flow through a single nanochannel fabricated by Oak Ridge National Laboratory (ORNL). This geometry was much easier to model than the iMEDD nanopump system since there is only a single channel.

1.6 Experimental Effort

The major objective of the experimental effort by Dr. Yoda's group at the Georgia Institute of Technology (GT) was to develop novel nonintrusive diagnostic techniques for interfacial transport in the electric double layer. The GT effort only covers the period from January 2002 through December 2004, or after project re-configuration. Over this two-year period, the GT group achieved the following milestones:

- Extended the capabilities of nano-particle image velocimetry (nPIV), a technique using evanescent-wave illumination of colloidal particle tracers, to obtain velocities over the

first **250 nm** next to the wall using **100 nm** diameter fluorescently dyed polystyrene spheres;

- Used nPIV to validate the predictions of the model developed by Dr. Conlisk at OSU. Nano-PIV was used to measure velocities within 250 nm of the wall in steady, fully-developed EOF through rectangular microchannels of depth h = 5–25 μm fabricated in fused silica by Dr. Ramsey's group at ORNL. The electroosmotic mobilities obtained from their nPIV data for sodium tetraborate ($Na_2B_4O_7$) buffer at molar concentrations C = 0.02–36 mM are in excellent agreement with those predicted by the OSU group using an asymptotic perturbation analysis [6].
- Found that the nPIV data at the two lowest concentrations, namely C = 0.02 and 0.037 mM to be **within** the diffuse electric double layer (EDL) based upon comparisons with the OSU predictions. These results are believed to be the first experimental observations within the EDL for an aqueous electrolyte solution, nearly a century after the original work by Gouy and Chapman developing the theory of the diffuse EDL.[1,2]
- Demonstrated with these results (which will be submitted to *Physics Review Letters*) that the Debye length λ actually underestimates the extent of the charge and velocity non-uniformity within the EDL by as much as an order of magnitude. For C = 0.02 and 0.037 mM cases, λ = 50 and 68 nm, respectively. Yet the extent of the EDL, defined following boundary-layer theory as the distance from the wall where the velocity recovers to 99% of the bulk value, δ_{99}, is actually 310 nm and 220 nm for C = 0.02 and 0.037 mM, respectively.
- Evaluated the accuracy and robustness of various μPIV and PIV processing techniques, including window shift, cross-correlation averaging (also known as single-pixel correlation), and zero / gray padding. The results were used to improve the accuracy of the GT group's nPIV processing software. Towards this end, Dr Yoda's group developed software to generate "artificial images" typical of nPIV with numerical models predicting the dynamics of nPIV tracers including flow convection and hindered Brownian diffusion (using the Langevin Equation); unlike most such

[1] L.-G. Gouy, *J. Phys.* **9**, 457 (1910)

software, these artificial images include image noise statistically similar to that in the experimental images.

- Demonstrated, using artificial images, the feasibility of **multilayer nPIV**, where we exploit the exponential decay of tracer image intensity with distance normal to the wall *z* (due to the exponential decay of evanescent-wave intensity) to divide a single nPIV image into three sub-images based on tracer image intensity (Figure 6). Processing these sub-images then gives the velocity components parallel to the wall in different "layers" within the region illuminated by the evanescent wave. The GT group's initial results demonstrate that this technique can be used to further improve the spatial resolution of nPIV normal to the wall to **80 nm**, and suggest that multilayer nPIV can also be used to obtain **wall shear stress** measurements within **300 nm** of the wall (Figure 7), or well within the viscous sublayer for even very high Reynolds number ($Re = O(10^9)$) turbulent boundary layers.

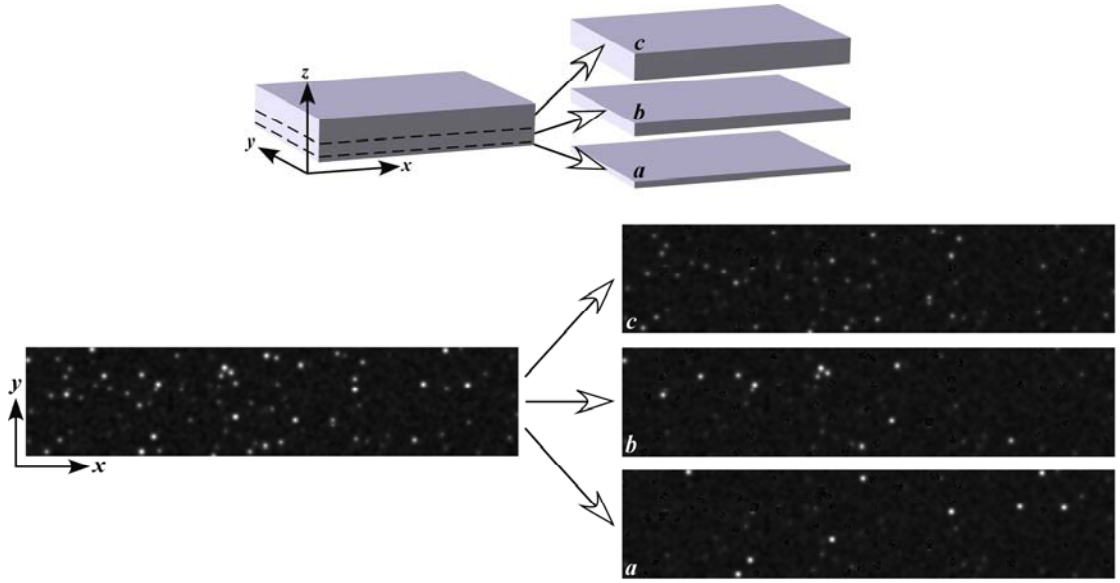

Figure 6 Illustration of "multilayer nPIV" [top], and an artificial image [bottom left] and the three sub-images extracted from this image for multilayer nPIV analysis [bottom right].

[2] D. L. Chapman, *Phil. Mag.* **25**, 475 (1913)

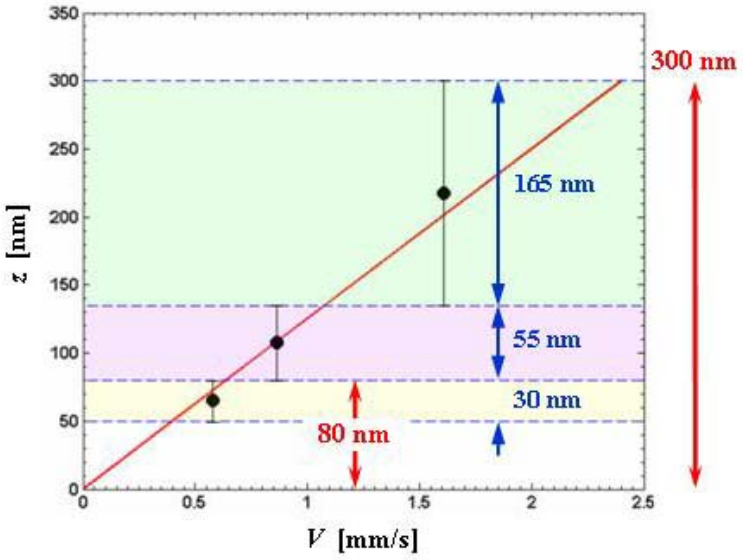

Figure 7 Velocity profile in plane Couette flow obtained for three layers (yellow, pink and green) within the region illuminated by the evanescent wave. The results from multilayer nPIV (●)are in good agreement with the expected velocity profile (—); the first layer (yellow) represents velocity data over the first 80 nm next to the wall (the particle center cannot get any closer to the wall than its own radius, or 50 nm).

2 FABRICATION AND EXPERIMENTAL METHODS

2.1 Summary of Achievements

We successfully fabricated our desired nanochannel geometry with 20 nm channels for the volumetric flow rate testing. To successfully fabricate the nanochannels in silicon, several processing parameters had to be optimized, including surface roughness of the polysilicon (for lithography and sealing considerations), crystallinity of the polysilicon (for channel roughness considerations), and stress levels in the polysilicon (for mechanical stability considerations). We successfully demonstrated the fabrication of nanochannels within poly(dimethylsiloxane) (PDMS) using microstamping and embedding techniques. Several different sacrificial layers were examined for the most desirable fabrication conditions. Our experimental fluid flow testing station was completed and calibrated, and full characterization of gas and liquid flow through 2 μm channels was demonstrated. It was demonstrated that the system is sensitive enough to detect changes in viscosity of a mixture of water and glycerin, attributed to several experimental conditions. The surface modification protocol for silicon was fully developed and characterizations (ellipsometry,

contact angle, and X-ray photoelectron spectroscopy (XPS) of the deposited films indicate that we have successfully deposited a uniform monolayer of silanes across the surface of a 4 inch silicon wafer.

In addition, we successfully completed the fabrication of a series of nanochannels in silicon, fabricated nanochannels in methacrylates and continued the work on characterization of nanochannels fabricated in PDMS, successfully characterized the flow of saline solution through silicon nanochannels under pressure-driven and electroosmotic conditions, and successfully demonstrated the control of surface properties through the vapor phase deposition of silane monolayers with different functional groups on silicon surfaces and silicon nanochannel chips.

The fabrication of nanochannels in silicon fulfilled the second milestone laid out in the original proposal: that of a series of nanochannels with different heights for the investigation of scaling effects on the transport of a homogeneous saline fluid. In addition, the fluid flow characterization station was fully calibrated and was used for the measurement of pressure-driven flow and electroosmotic flow through 20 nm channels. These results were compared to the theories of their respective flow behaviors. The electroosmotic flow followed the analytical theory developed by our group, which has also matched experimental data of fluid flow with various liquid parameters through nanochannel membranes (from iMEDD, Inc.).

2.2 Fabricating Nanochannels from Silicon

2.2.1 Chemical Mechanical Polishing Rate

The standard low-pressure chemical vapor deposition (LPCVD) process used to deposit polysilicon is performed at 615°C. The resulting films exhibit a (110) texture and consists of columnar, hemispherically-capped, non-equiaxed grains. For a 3 μm-thick polysilicon layer, typical surface roughness (R_a) is ~140Å. Chemical mechanical polishing can be used to reduce the roughness to <50Å. Consequently, a systematic experiment was conducted to characterize the rate of the chemical mechanical polishing of polysilicon as a function of

polishing time. In addition, the selectivity of chemical mechanical polishing of polysilicon to SiO_2 was determined.

Experimental Methods

Starting substrates were 100 mm-diameter, 500 μm-thick, single side polished, <100>-oriented Si wafers with 2000Å-thick thermal SiO_2 layers. A 2 μm-thick polysilicon layer was then deposited on 10 starting substrates by LPCVD at 615°C, while 4 starting substrates were set aside. Chemical mechanical polishing was performed using a Struers Pedemax-2 machine with a Rodel Suba 500 polishing pad and Cabot SC1 alkaline slurry (20:1 dilution in deionized H_2O). Prior to polishing the substrates for the experiment, the polishing pad was seasoned for 20 min by polishing polysilicon deposited on a dummy wafer. The 10 substrates with 2 μm-thick polysilicon films were subsequently polished for 10 minutes (2 wafers), 15 minutes (4 wafers), and 20 min (4 wafers). Afterwards, the starting substrates with 2000Å-thick oxide films were polished for 10 and 15 min. The thickness of polysilicon and oxide films was then determined by an ellipsometry (Rudolf Research AutoEL) to provide the polishing rate. In addition, surface roughness measurements were performed using a stylus profilometer (DEKTAK).

Results

Tables I and II summarize the results for the polishing rates as a function of polishing time for polysilicon and oxide, respectively. The polishing rate was ~1000Å/min for polysilicon and <150Å/min for SiO_2 films. The surface roughness was <50Å for all substrates after polishing.

Table I Chemical mechanical polishing rate of polysilicon.

Wafer #	Polishing Time (min)	Polishing Rate (Å/min)
1	10	1135
2	10	1177
3	15	1094
4	15	992
5	15	1198
6	15	1299
7	20	1012

8	20	831
9	20	1149
10	20	1091

Table II Chemical mechanical polishing rate of SiO_2.

Wafer #	Polishing Time (min)	Polishing Rate (Å/min)
1	10	64
2	10	50
3	15	65
4	15	119

2.2.2 Annealing of Polysilicon

The standard LPCVD process for polysilicon, which is performed at 615°C, leads to films with a residual compressive stress. Annealing can be performed to reduce the stress to levels that do not degrade micro/nanochannel quality. Consequently, a systematic experiment was conducted to characterize the residual stress in polysilicon as a function of film thickness and annealing time.

Experimental Methods

Starting substrates were 100 mm-diameter, 500 μm-thick, single side polished, <100>-oriented Si wafers with 1000Å-thick thermal SiO_2 layers. Polysilicon was then deposited by LPCVD at 615°C on the starting substrates. A 2 μm-thick polysilicon layer was deposited on 10 starting substrates, while a 5 μm-thick polysilicon layer was deposited on another 10 starting substrates. The annealing process was performed at 1100°C for 1 hr in nitrogen ambient on 5 substrates with 2 μm-thick polysilicon films and 5 substrates with 5 μm-thick polysilicon films. Afterwards, the residual stresses in both as-deposited and annealed polysilicon films were determined by the substrate curvature technique. First, substrate curvatures were measured using an optical tool (FSM 3800). Next, the polysilicon layer on the substrate backsides was removed using SF_6 plasma. Finally, substrate curvatures were measured again and the differences in curvatures were related to the residual stresses in the polysilicon films using Stoney's equation. In addition, surface roughness measurements were performed using a stylus profilometer (DEKTAK).

Results

Tables III and IV present the compressive residual stresses in as-deposited and annealed polysilicon films, respectively. The as-deposited polysilicon films exhibit significantly higher residual stresses than the annealed films. The thicker polysilicon films generally exhibit lower residual stresses than the thinner films, irrespective of whether the films were annealed or not.

Table III Compressive residual stress in as-deposited polysilicon.

Wafer #	Film Thickness (μm)	Residual Stress (MPa)
1	2	282
2	2	278
3	2	278
4	2	288
5	2	285
6	5	64
7	5	231
8	5	34
9	5	178
10	5	198

Table IV Compressive residual stress in annealed polysilicon.

Wafer #	Film Thickness (μm)	Residual Stress (MPa)
1	2	41
2	2	43
3	2	39
4	2	41
5	2	37
6	5	20
7	5	18
8	5	17
9	5	20
10	5	19

2.2.3 Fine Grain Polysilicon

The standard LPCVD process for polysilicon, which is at 615°C, leads to films with rough surfaces and residual compressive stress. Chemical mechanical polishing and annealing of the polysilicon can reduce surface roughness and compressive stress, respectively. However, the chemical mechanical polishing process requires the simultaneous optimization of multiple process parameters, which can lead to significant

development time and resources. Furthermore, the annealed polysilicon films still exhibit a finite compressive stress (albeit much lower compared to the as-deposited films), which can still lead to buckling of sufficiently large features. In contrast, deposition of polysilicon at 570-610°C can lead to tensile films comprised of fine, ellipsoidal grains that lead to smooth surfaces. Consequently, a systematic experiment was conducted to verify the smoothness and characterize the residual stress in the fine grain polysilicon as a function of film thickness and annealing time.

Experimental Methods

Starting substrates were 100 mm-diameter, 500 μm-thick, single side polished <100>-oriented Si wafers with 1000Å-thick thermal SiO_2 layers. Polysilicon was then deposited by LPCVD at 580°C on the starting substrates. A 2 μm-thick polysilicon layer was deposited on 10 starting substrates, while a 5 μm-thick polysilicon layer was deposited on another 10 starting substrates. The annealing process was performed at 1000°C for 1 hour in nitrogen ambient on 5 substrates with 2 μm-thick polysilicon films and 5 substrates with 5 μm-thick polysilicon films. Afterwards, the residual stresses in both as-deposited and annealed polysilicon films were determined by the substrate curvature technique. First, substrate curvatures were measured using an optical tool (FSM 3800). Next, the polysilicon layer on the substrate backsides was removed using SF_6 plasma. Finally, substrate curvatures were measured again and the differences in curvatures were related to the residual stresses in the polysilicon films using Stoney's equation. In addition, surface roughness measurements were performed using a stylus profilometer (DEKTAK).

Results

Tables V and VI present the tensile residual stresses in as-deposited and annealed polysilicon films. The as-deposited polysilicon exhibits relatively high tensile stress, which sometimes lead to catastrophic film cracking on some of the substrates with 5 μm-thick polysilicon films. The annealed polysilicon exhibits significantly lower residual stress, which is always nominally tensile. The thicker polysilicon films generally exhibit

lower residual stresses than the thinner films. The surface roughness was <40Å for all substrates.

Table V Tensile residual stress in as-deposited fine grain polysilicon.

Wafer #	Film Thickness (μm)	Residual Stress (MPa)
1	2	672
2	2	260
3	2	413
4	2	282
5	2	409
6	5	285
7	5	*Cracked*
8	5	*Cracked*
9	5	*Cracked*
10	5	*Cracked*

Table VI Tensile residual stress in annealed fine grain polysilicon.

Wafer #	Film Thickness (μm)	Residual Stress (MPa)
1	2	24
2	2	27
3	2	22
4	2	24
5	2	26
6	5	50
7	5	46
8	5	48
9	5	47
10	5	*Broken during handling*

2.3 Experimental Testing of Nanochannels

2.3.1 Micro/Nano Channel Flow Fabrication and Testing

Nanochannel chips with 10, 20, 30, 50 and 100 nm channels were fabricated up to the point of release. Flow testing issues relating to chip sealing methodologies in the flow test jig were addressed. The successful resolution of issues relating to the jig allowed for reproducible testing of nano-channel chips under pressure and electroosmotic flow conditions.

Nanochannel Fabrication

Fabrication of 10, 20, 30, 50 and 100 nm channel flow chips was completed using the fine grain polysilicon process described previously. Figure 8 shows an SEM of a 20 nm channel created using this process. The channels show relatively parallel walls and have a small step height difference between poly1 and poly 2. This height differential is a potential source for flow shunting during characterization experiments, but is compensated for in the jig design by using an acrylic plate, which deforms slightly to fill the step heights. This issue will be addressed by making poly 2 thicker and increasing the polishing time during the planarization step.

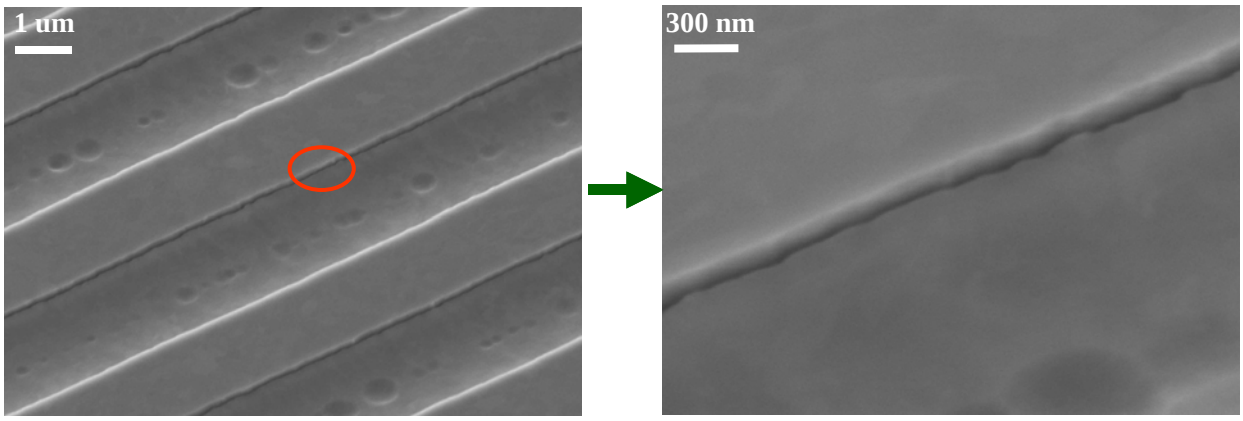

Figure 8 SEM photographs of 20 nm channels fabricated using the fine grain polysilicon process.

Jig Design

The final jig design is shown in Figure 9. After a number of adjustments and minor modifications, the test jig proved to provide reliable sealing of the test chip and delivery of pressure and voltage for fluid flow characterization. A number of micro-channel chips were tested using the new jig design, and the results agreed with those results obtained using the other test fixtures. However, the most recent data were obtained with much greater ease.

Figure 9 Final jig design

The new test jig incorporated several new features:

- Single thumb screw compression of the chip to provide a uniform sealing force across the entire chip
- Clear acrylic pressure plates that allow visualization of the chip during test
- Acrylic pressure plates to compensate for step height differences
- Ports for platinum electrodes for electroosmotic flow testing
- Steel housing for greater rigidity
- Totally plastic fluid ports and tubing to eliminate parasitic chemical reactions.

Nanochannel chips were tested using the new test jig under pressure and electro-osmotic flow conditions. Pressure flow conditions produced flow rates in agreement with theory and data is shown in **Figure 10.**

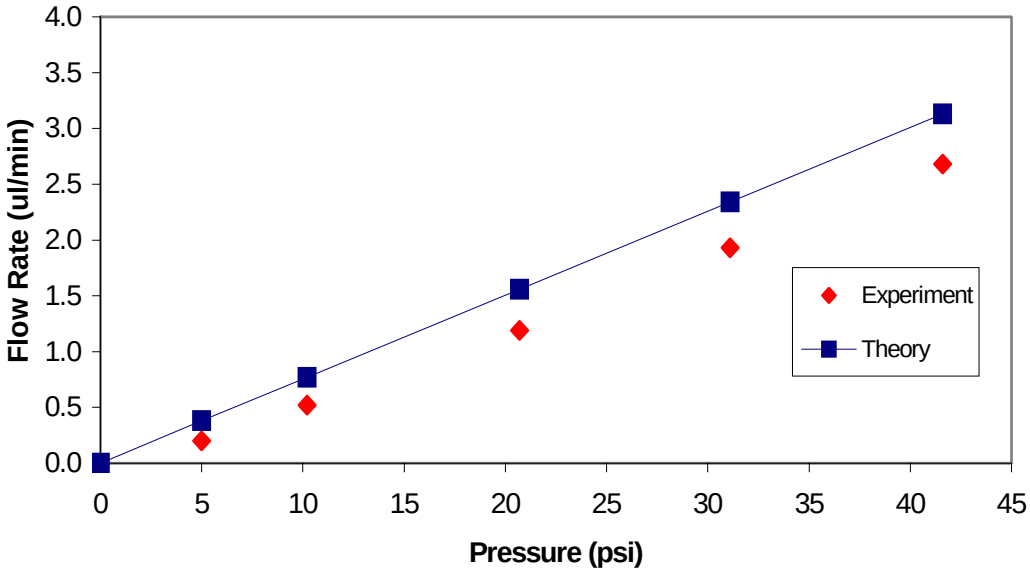

Figure 10 Flow vs. pressure for 640,000 18 nm wide nanochannels.

Testing of the chips under EOF conditions was more challenging. When differential voltage was initially applied across the nano-channel chip, we would observe electro-osmotic flow. However, with continued application of differential voltage we would observe a drop off of flow until flow stopped completely. The chips were inspected and particulate blocking the microchannels was evident. Figure 11 shows a picture of this blockage on a tested chip. Prior to this, pressure flow testing of nanochannels had not resulted in any observed blockages.

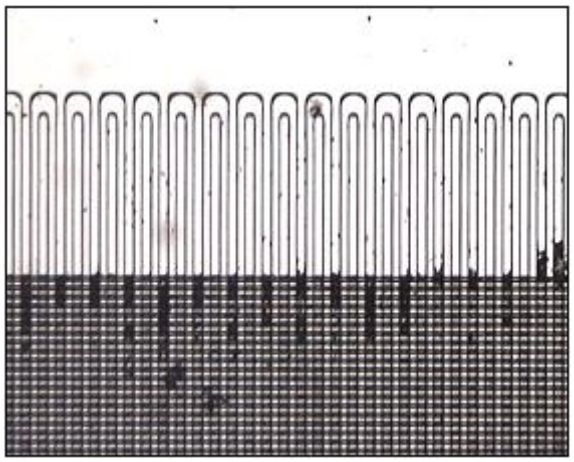

Figure 11 Photograph of nanochannel chip showing blockages at the inlet reservoir.

SEM analysis of particulates in the reservoir region

Figure 12 and an SEM showed evidence of metals such as iron and chromium. At this time, the test jig had stainless steel fluid inlet ports. Though the platinum electrode was Teflon coated in the region of inlet port we hypothesized that and electrochemical reaction had occurred with the stainless steel inlet port, which caused the particulate. The jig was subsequently redesigned to have only plastic fluid ports and the entire fluid system from the main reservoir onward was converted to plastic as well. When tested again, no blockages were observed to occur. EOF data were obtained and are shown in Figure 13.

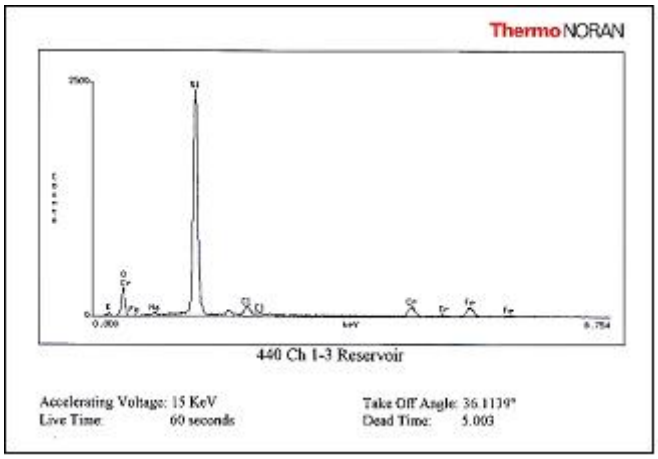

Figure 12 SEM microprobe analysis of debris from the previous Figure showing iron and chromium elements in the debris.

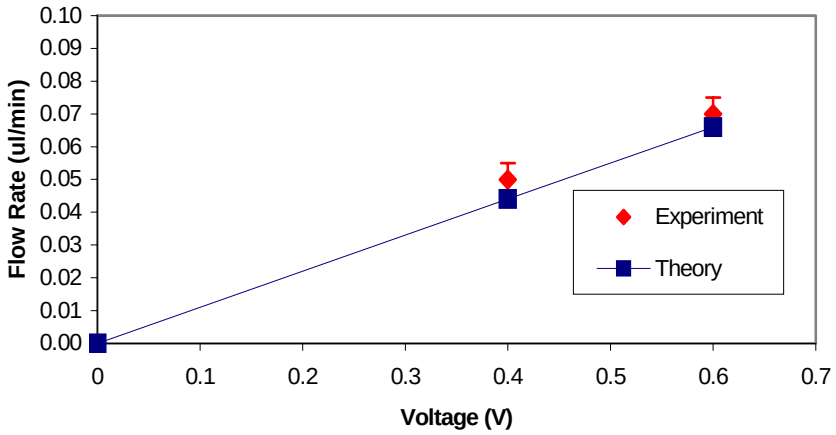

Figure 13 EOF data for the 640,000 18 nm wide nanochannels chip.

2.4 Surface Modification of Silicon Nanochannels

2.4.1 Introduction

The initial investigation of modifying surface properties of silicon surfaces for the prevention of protein adsorption must be completed before the technology can be extrapolated for polymeric surfaces. A vapor phase deposition system was designed and assembled for the deposition of uniform layers of silanes onto any SiO-containing surface up to 4 inches in diameter. The chamber design was also proven successful for the deposition of intact 4 inch silicon wafers. The positive results were characterized by comparing the relative contact angles of water droplets, ellipsometry, and X-ray photoelectron spectroscopy (XPS). The deposition chamber design also proved capable of depositing alternative silanes other than vinyltrimethoxysilane (VTS), trimethylchlorosilane (TCS) and different substrates, a silicon chip etched with nano-channel features.

2.4.2 Vapor Phase Deposition Chamber

The deposition chamber consisted of a sample holder, a glass evaporation reservoir, and a nitrogen gas flow system. Once the efficacy of design was proven, the system was made more robust and user-friendly with the addition of permanent Swagelok® components, variable nitrogen gas flowmeter, and nitrogen-drying gun. The new Swagelok® components (*i.e.*, quick release tube fittings) allow for easier system dismantling for cleaning and created the ability to accommodate a nitrogen-drying gun. The nitrogen-drying gun is used in the preparation of each sample to ensure the substrate is free of moisture and debris. The final additional component included in the system was the integration of a nitrogen flowmeter. This calibrated feature allows precise control over the carrier gas flow.

Experimental Procedures

Once the integrity of design of the vapor phase deposition chamber was proven for 1 in × 1 in sample chips, the same experimental procedures were used to deposit VTS upon intact

4 in silicon wafers. A wafer was first cleaned using a cleaning solution, "piranha," (1:1 solution of 98% sulfuric acid and 30% hydrogen peroxide). The intact wafer was then nitrogen dried and loaded into the deposition chamber where it was exposed to a nitrogen gas carrying VTS vapor for 1 hr at a flowrate of 200 mL/min. Approximately 1–1.5 mL of VTS were used for the deposition. To avoid surface polymerization upon the 4 in wafer, anhydrous calcium sulfate chips were added into the deposition chamber below the substrate.

Ellipsometry Results and Discussion

The film thickness was characterized with a Gaertner Scientific L116S Ellipsometer at an incidence angle of 70^{o} and a wavelength of 6328 Å. A refractive index of 1.46 was assumed for silicon oxide and 1.4 was assumed for the organic thin film. The surface modified sample demonstrated a relatively uniform thickness when compared to that observed on the control sample (Figure 14). The variance in thickness upon the surface of the control is assumed to be the resultant of contaminates. Calibration issues concerning the equipment have been a reoccurring problem and therefore, the exact thickness measurements should be taken as arbitrary units. Collaboration with Gaertner Scientific was established to remedy the calibration issues.

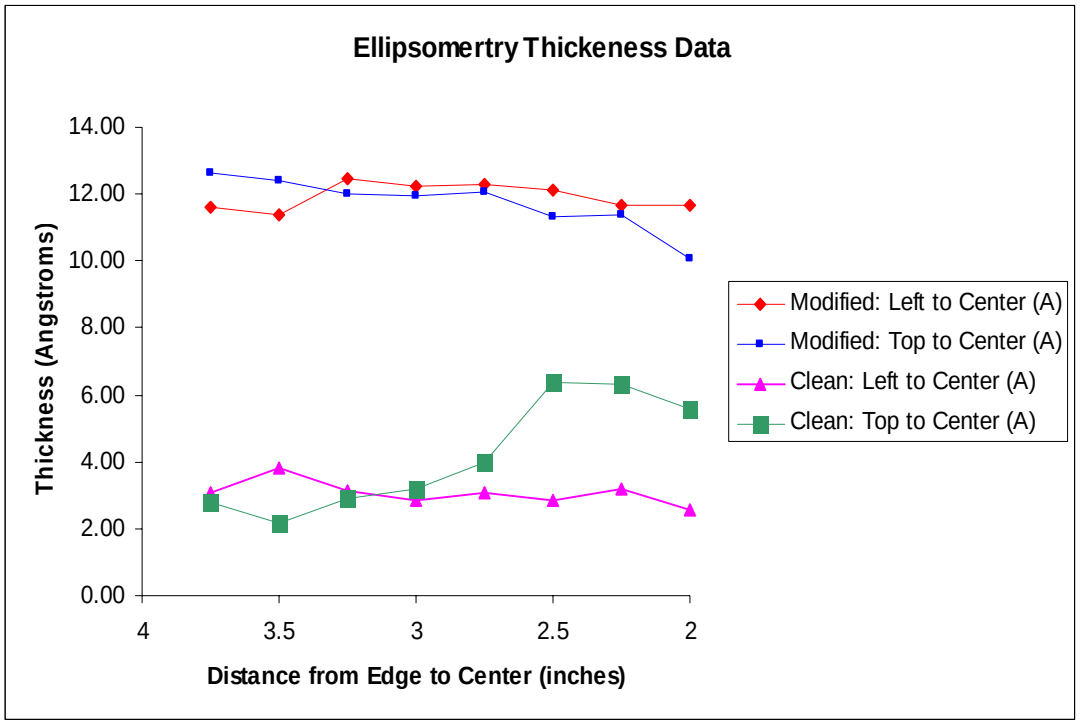

Figure 14 Ellipsometry data for surface modified and control wafers.

XPS Results and Discussion

Characterization of the modified surface was further analyzed using X-ray photoelectron spectroscopy (XPS). The intact 4 in wafer samples were broken into 1 cm ×1 cm chips to accommodate the XPS sample stage. A total of 6 samples were analyzed (4 surface modified samples, 2 control samples). Figure 15 shows an overlay of the spectra created from both the surface modified sample and control sample. The difference in elemental components that XPS can differentiate between a cleaned and modified silicon surface is the presence of carbon. Theoretically, the spectrum from the cleaned silicon surface should not indicate a carbon peak; however, a carbon peak was expressed. This presence of carbon is attributed to debris or contamination. The surface modified sample presented a slightly larger carbon peak that supports the successful modification of the surface. Figure 16 is a blowup of the carbon region. The relative curve area ratio was approximately 1.8457:1, and the relative curve height ratio was approximately 1.7815:1. Since the difference between the two curves was not great, it is assumed that the contamination factor is relatively insignificant.

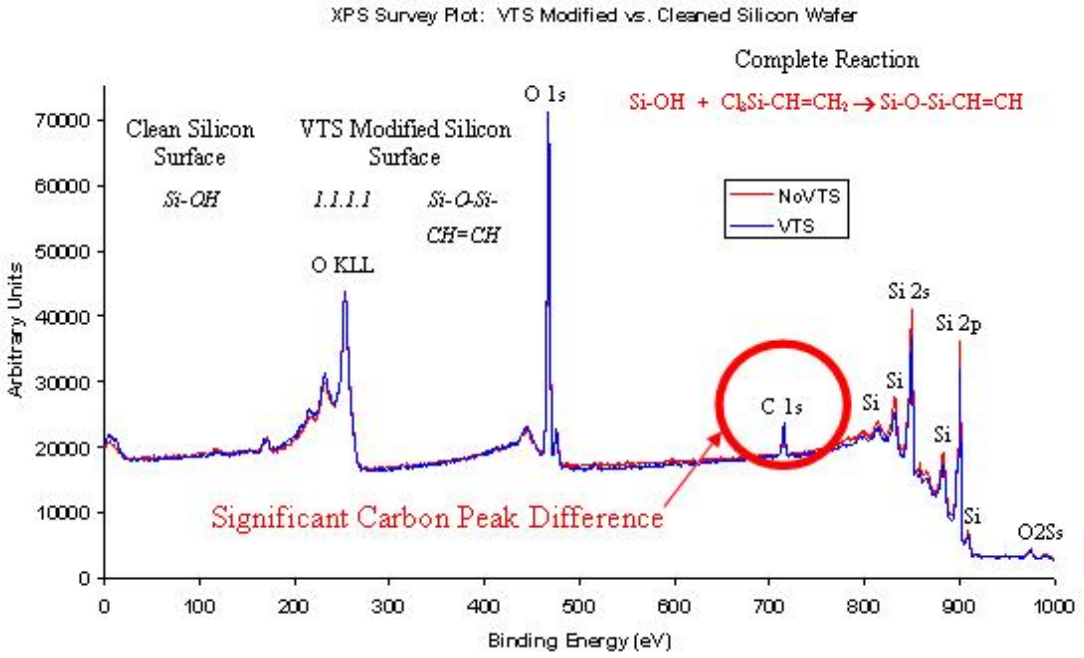

Figure 15 Graphs of ellipsometry data for surface modified and control wafers.

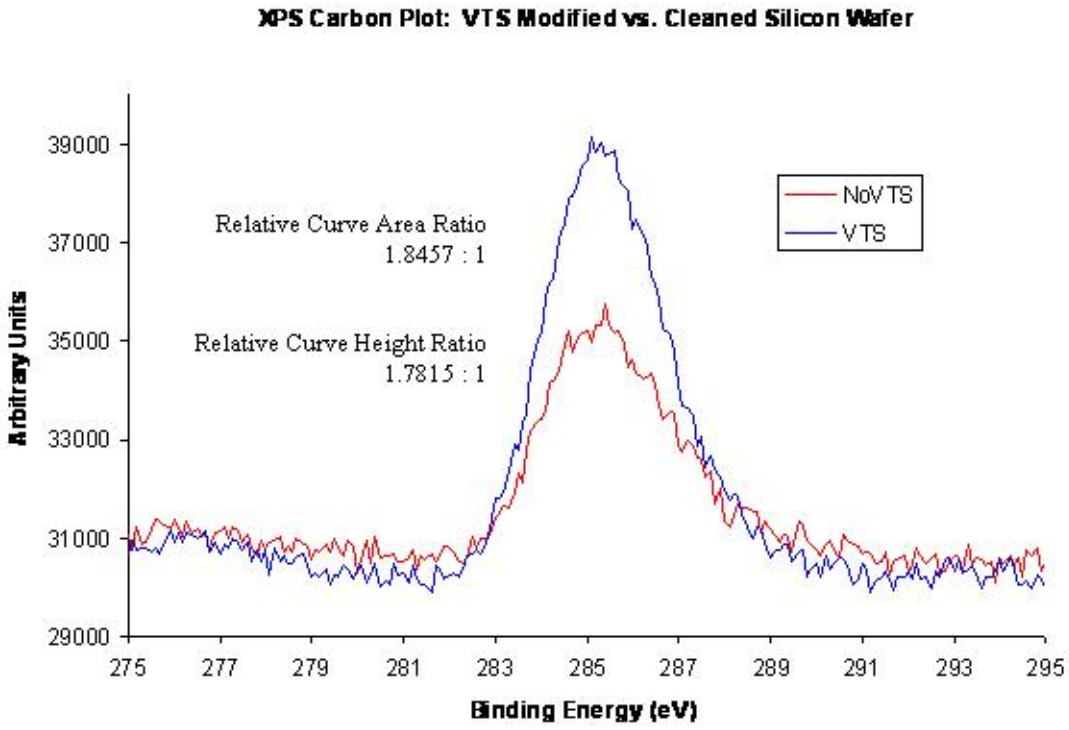

Figure 16 Blowup of XPS Carbon region of both surface modified and control spectra.

Additional Deposition Work

Once the deposition of vinyltrimethoxysilane (VTS) became routine and the monolayer characterized, efforts were concentrated upon depositing other silanes such as trimethylchlorosilanes (TCS). This would result in methylated versus hydroxylated end groups upon the silicon surface. Less volatile than VTS, TCS could be deposited without the use of anhydrous calcium sulfate chips. No excessive polymerization upon the surface was found, and the contact angle of water droplets proved evidence of successful deposition. The results of monolayer deposition is demonstrated in Figure 17, which compares the film thickness of VTS, TCS, and a hydroxylated VTS film with the native oxide present on a Piranha-cleaned silicon wafer.

The most significant new substrate deposited was a chip containing etched nano-channel features. The features of the chip were surface modified by the deposition of VTS with the same deposition protocol as the silicon wafers. No evidence of excess polymerization was found, however, the success of the deposition was not fully tested. The best-case scenario would be that the nano-channels that were surface modified by VTS would demonstrate relatively lower flow rate measurements of saline fluid than non-treated channels, and that nanochannels modified with TCS will provide a substantially lower flow rate based on the fully methylated surfaces. Inconclusive results would require the investigation of alternative characterization methods.

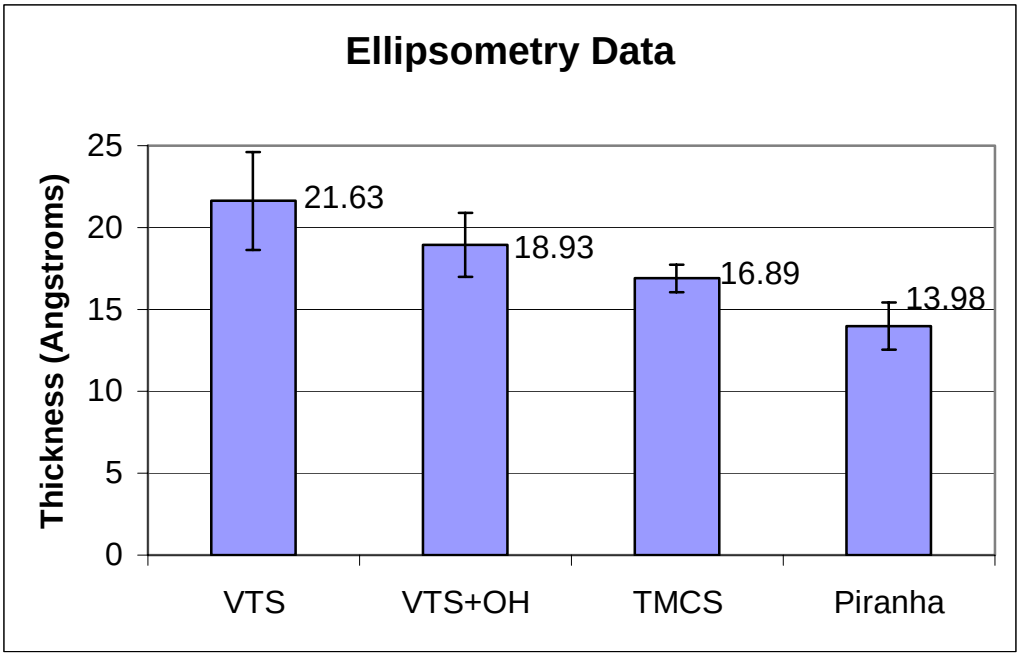

Figure 17 Ellipsometry data with error bars from wafers with various silane monolayers deposited on their surfaces, compared with Piranha-cleaned silicon.

3 CONCLUSIONS / RECOMMENDATIONS FOR FUTURE WORK

3.1 Modeling

This research integrated fabrication, modeling and experimental efforts to develop an understanding of fluid flow and mass transport in nano- to microscale channels. This work is motivated by the need to improve design of various micro-, meso- and nanoscale devices. At present, the resources required to design, fabricate and test successive generations of prototypes preclude effective design optimization at these scales. Accurately modeling these devices is therefore the only possibility for cost-effective design optimization of micro- and nanofluidic devices. Accurate and robust models of how biofluids (*i.e.*, aqueous solutions containing electrolytes and biomolecules) are transported through such devices will enable us to tailor specific channel sizes and geometries for specific applications.

In terms of specific accomplishments over the four-year period, an analytical/numerical model was developed for electroosmotic flow (EOF) in micro and nanochannels which compares well with four independent sets of experimental data spanning more than 35

different operating conditions. To support the modeling, a computational model for electroosmotic flow in nanochannels was also developed using a company-updated version of CFD-ACE+ designed specifically for the project. The EOF model was then extended to modeling transport in an ion channel and in transient EOF with applications to biomolecular sensing. Given the importance of sensing larger biomolecules, we also constructed a model for biomolecular transport in nanochannels that included hindered diffusion effects.

A fundamental question in modeling nanoscale transport is, "When is the continuum approximation valid?" Since all of the modeling work described above treats ions and biomolecules as point charges, the limits of this continuum-based approximation were explored by comparing our results with those from molecular dynamics (MD) simulations. The MD results showed that excluded volume effects are significant for channel heights below 10 nm. These effects will be negligible when all the transported species are relatively small ions (Na^+ has a diameter of about 0.3 nm, for example), since most devices have dimensions exceeding 20 nm. These effects will be important, however, in the transport of larger biomolecules, which can have sizes up to 10 nm; albumin, for example, has a nominal size of around 3.5 nm). We have shown in this work that when such finite-size effects are important, they can be accurately incorporated into the continuum model by simply reducing the channel size by one molecular diameter. This work has therefore successfully used MD simulations (which are time-consuming and require a great deal of *a priori* knowledge about the molecular-scale structure of the channel wall) to extend the accuracy and applicability of far more efficient (and better-developed) continuum modeling approaches. Finally, the good agreement between the model predictions and the experimental results suggest that the no-slip condition still holds, and that surface roughness effects are negligible, at these scales.

In terms of future work, we plan to extend these models to biomolecular transport and transient effects. Biomolecules such as proteins, ribonucleic acids (RNA) and deoxyribonucleic acids (DNA) are macromolecules, whose molecular weight is at least tens of thousand Daltons. Continuum models of these large molecules will obviously require inclusion of finite size effects. They will also require considering different conformations,

e.g. globular molecules such as albumin *vs.* linear molecules such as DNA. Moreover, many sensing applications require rapid molecular analysis and sensing of biomolecules, or transient processes, such as the transient EOF due to the "gating" of a synthetic ion channel.

Other topics of future research include modeling the effects of surface roughness and spatial variation of solution properties. In this work, the channel walls were assumed to be smooth. In reality, however, it is impossible to fabricate channels with truly smooth walls. For the most part, surface roughness is negligible for most microchannels, and the comparisons between experimental data and model predictions at the microscale (of the four experimental datasets, only the iMEDD data involved nanochannels with dimensions of 4-50 nm; the effects of roughness and sinuosity are unclear in these data) suggest that roughness effects had negligible effects on transport. Surface roughness can be significant for nanoscale channels, however, and its effects should be investigated at these scales. We developed an initial model of roughness based on the lubrication approximation for this project, and plan to build upon these initial studies, possibly using the Momentum Resistance and Enhancement features in CFD-ACE+.

The models developed in this four-year effort also assumed constant physical properties for the solution. This assumption should be valid for the most part in isothermal flows, but breaks down if the temperature of the solution varies (in the presence of Joule heating, for example), and may also break down when the channel dimension becomes comparable to the molecular size. For example, in EOF, positive ions tend to accumulate near the channel wall (for Si and glass channels), and the chemical composition of the solution at the wall may be quite different from that within the bulk of the channel. Under such conditions, it is likely that the viscosity and/or density of the solution vary across the channel; such variations could affect velocity and potential profiles within the channel.

3.2 Experiments and Fabrication

During the latter half of the contract, an interfacial velocimetry technique, nano-particle image velocimetry (nPIV), with meso- to nanoscale spatial resolution was developed. Measurements of mobilities obtained using nPIV for EOF of sodium tetraborate buffer at

molar concentrations ranging from 20 μM to 36 mM through 5–25 μm rectangular microchannels were in excellent agreement with the model predictions. The results were found to follow a power-law correlation at concentrations ranging from 0.19–36 mM [16]. Finally, nPIV enabled the first ever probe of the diffuse electric double layer (EDL) at the two lowest concentration values of 20 and 36 μM; the results at these two concentrations clearly demonstrate that the Debye length underestimates the thickness of the EDL by up to an order of magnitude [in preparation].

The accuracy of nPIV was evaluated using simulated, or artificial, images that incorporated the effects of both hindered Brownian diffusion and nonuniform exponentially decaying illumination. Errors due to particle mismatch induced by Brownian diffusion were found to be negligible for the cases studied here [24]. Further studies suggest, however, that hindered Brownian diffusion may, under appropriate conditions, lead to an overestimation of near-wall velocities and hence slip (lengths) in near-wall measurements [33]. An extension of nPIV, multilayer nPIV, has the capability to obtain velocity measurements within 80 nm of the wall and shear stress measurements within 300 nm of the wall [32].

In terms of future work in microfluidics, the potential of multilayer nPIV as both a near-wall velocimetry technique and a wall shear stress sensor with superior spatial resolution will be further evaluated using experimental measurements in Poiseuille flow through microchannels. We also plan to explore using (multilayer) nPIV to investigate (apparent) slip in water flowing through microchannels with hydrophobic walls.

Techniques based upon evanescent-wave illumination also have great potential as novel diagnostics in EOF and electrochemistry. Evanescent wave-based velocimetry techniques such as nPIV present an intriguing possibility for *in situ* measurement of wall zeta-potential ζ_w (we are unaware of any other techniques at present that can monitor this critical surface chemistry parameter *in situ*) will also be investigated. Since fluid velocity and perturbation electric potential are directly proportional to each other (*i.e.*, similar) in EOF driven by a steady electric field, nPIV may be a novel method for monitoring variations in ζ_w over time due, for example, to surface contamination from nonspecific adsorption of biomolecules. Moreover, evanescent-wave illumination of fluorescently labeled protein could also be

used to directly quantify the amount of nonspecific adsorption of such proteins on the microchannel wall.

In terms of experimental studies of EOF, we plan to follow up on our preliminary nPIV results obtained using a square-wave external electric field. Unsteady EOF is of great interest for mixing applications in microfluidics; such experimental data would also be valuable in validating unsteady EOF models.

Over the first eighteen months of the project, a series of nanochannels in silicon and methacrylates were fabricated. In the fabrication area, future work will focus on characterization and flow testing of surface-modified nanochannels.

Appendix A: Publications and Presentations List

2002

[1] A. T. Conlisk, J. McFerran, Z. Zheng, and D. Hansford, "Mass Transfer and Flow in Electrically Charged Micro- and Nano-channels," *Analytical Chemistry* **74**(9), 2139–2150 (2002)

[2] A. T. Conlisk, "On the Debye-Huckel Approximation in Electroosmotic Flow in Micro- and Nano-channels", 3rd AIAA Theoretical Fluid Mechanics Conference, St. Louis, MO (2002)

[3] A. T. Conlisk, "Electroosmotic Flow in Nano-channels", International Conference on Computational Science and Engineering, Reno, NV (2002) [***Invited presentation***]

[4] R. Sadr and M. Yoda, "Nano-PIV Measurements in Microchannel Flows," 55th Annual Meeting of the American Physical Society Division of Fluid Dynamics, Dallas, TX (2002)

2003

[5] Z. Zheng, A. T. Conlisk and D. Hansford, "Effect of Multivalent Ions in Electroosmotic Flow in Nanochannels", *Electrophoresis* **24**, 3006–3017 (2003)

[6] R. Sadr, Z. Zheng, M. Yoda and A. T.Conlisk, "An Experimental and Modeling Study of Electroosmotic Bulk and Near-wall Flows in Two-dimensional Micro- and Nanochannels," ASME paper IMECE2003-42917, ASME International Mechanical Engineering Congress and RD&D Expo, Washington, DC (2003)

[7] S. Bhattacharyya, Zhi Zheng and A. T. Conlisk, "Asymptotic Solutions for Electroosmotic Flow in 2D Charged Micro and Nanochannels", AIAA paper 2003-3582, 33rd AIAA Fluid Dynamics Meeting, Orlando, FL (2003)

[8] Z. Zheng, *Electrokinetic Flow in Micro- and Nano-fluidic Components*. Ph.D. thesis, Biomedical Engineering Center, The Ohio State University (2003)

[9] K. Evers, *Computation of Electroosmotic Flow in Complex Micro- and Nanochannel Geometries*. M.Sc. thesis, Biomedical Engineering Center, The Ohio State University (2003)

[10] J. McFerran, *Biomolecular Transport in Nanochannel Systems*. Honors program thesis, The Ohio State University (2003)

[11] M. Yoda, "Nano-Particle Image Velocimetry (nPIV): A New Technique for Studying Near-wall Nanoscale Transport," Challenges in Micro/Nano-Scale Visualization and Studies Panel, ASME International Mechanical Engineering Congress and RD&D Expo, Washington, DC (2003) [***Invited presentation***]

[12] R. Sadr, Z. Zheng, M. Yoda and A. T. Conlisk, "Electroosmotic Flow in Nano- and Microchannels: Scaling, Modeling and Experiments," Microfluidic/Biosensor Workshop at the University of Pennsylvania, Philadelphia, PA (2003)

[13] R. Sadr, M. Yoda, Z. Zheng and A. T. Conlisk, "Experimental Studies of Electroosmotic Flow in Microchannels," 56th Annual Meeting of the American Physical Society Division of Fluid Dynamics, Meadowlands, NJ (2003)

[14] Zheng, A., Conlisk, A. T., Sadr, R. and Yoda, M., "Models of Electroosmotic Flow in Micro- and Nanochannels," 56th Annual Meeting of the American Physical Society Division of Fluid Dynamics, Meadowlands, NJ (2003)

[15] H. Li, R. Sadr and M. Yoda, "The Accuracy of Nano-Particle Image Velocimetry Data," 56th Annual Meeting of the American Physical Society Division of Fluid Dynamics, Meadowlands, NJ (2003)

2004

[16] R. Sadr, M. Yoda, Z. Zheng and A. T. Conlisk, "An Experimental Study of Electro-osmotic Flow in Rectangular Microchannels," *Journal of Fluid Mechanics* **506**, 357–367 (2004)

[17] Yoda, M., "Applications of Nano-Particle Image Velocimetry (nPIV) for Measuring Near-wall Velocity Fields with Submicron Spatial Resolution," VSJ-SPIE04 International Conference on Advanced Optical Diagnostics in Fluids, Solids and Combustion, Tokyo, Japan (2004) [***Invited keynote lecture***]

[18] M. Yoda and R. Sadr, "Nano-Particle Image Velocimetry (nPIV): A New Technique for Measuring Near-wall Velocity Fields with Submicron Spatial Resolution," AIAA Paper 2004–754, 42nd AIAA Aerospace Sciences Meeting, Reno, NV (2004) [***Invited presentation***]

[19] K. Evers, J. McFerran and A. T. Conlisk, "On the Synthetic Ion Channel Problem", AIAA Paper 2004–0930, 42nd AIAA Aerospace Sciences Meeting, Reno, NV (2004)

[20] Kebbel, *Transient Electroosmotic Flow and Biomolecular Transport in Nanochannels*. Honors program thesis, The Ohio State University (2004)

[21] R. Sadr, M. Yoda, P. Gnanaprakasam and A. T. Conlisk, "Velocity Measurements Inside the Electric Double Layer in Electroosmotic Flow," 57th Annual Meeting of the American Physical Society Division of Fluid Dynamics, Seattle, WA (2004)

[22] M. Yoda and R. Sadr, "Near-wall Velocity Measurements in Poiseuille Flow: Effect of Shear," 57th Annual Meeting of the American Physical Society Division of Fluid Dynamics, Seattle, WA (2004)

[23] H. Li, R. Sadr and M. Yoda, "Extending nano-PIV to three dimensions," 57th Annual Meeting of the American Physical Society Division of Fluid Dynamics, Seattle, WA (2004)

2005

[24] R. Sadr, H. Li and M. Yoda, "Impact of Hindered Brownian Diffusion on the Accuracy of Nano-Particle Image Velocimetry Data," *Experiments in Fluids* **38**, 90–98 (2005)

[25] W. Zhu, S. Singer, A. T. Conlisk and Z. Zheng, "Study of Electroosmotic Flow of a Simple Electrolyte", *Physics Review E* **71**, 041501–1 to 12 (2005)

[26] T. Conlisk, "The Debye-Huckel Approximation: Its Use in Describing Electroosmotic Flow in Micro and Nano-channels", *Electrophoresis* **26**, 1896–1912 (2005)

[27] S. Bhattacharyya, Z. Zheng and A. T. Conlisk, "Numerical Solutions for Electroosmotic Flow in 2D Charged Micro and Nanochannels", To appear in *Journal of Fluid Mechanics* (2005)

[28] T. Conlisk, "Modeling Biomolecular Transport at the Nanoscale", Handbook of *BioMEMS and Biomedical Nanotechnology: Vol. I Biomedical and Biological Nanotechnology* eds. R. Bashir and S. Wereley), Kluwer (2005) [***Invited book chapter***]

[29] M. Yoda, "Nano-Particle Image Velocimetry: A Near-wall Velocimetry Technique with Submicron Spatial Resolution", *Handbook of BioMEMS and Biomedical Nanotechnology: Vol. IV Biomolecular Sensing, Processing and Analysis* (eds. R. Bashir and S. Wereley), Kluwer (2005) [***Invited book chapter***]

[30] T. Conlisk, "Modeling Electroosmotic Flow in Nanochannels", *Handbook of BioMEMS and Biomedical Nanotechnology: Vol. IV Biomolecular Sensing, Processing and Analysis* (eds. R. Bashir and S. Wereley), Kluwer (2005) [***Invited book chapter***]

[31] M. Yoda, "Nano-Particle Image Velocimetry (nPIV) Measurements Inside the Diffuse Electric Double Layer in Electroosmotic Flow," Joint International PIVNET II/ERCOFTAC Workshop on Micro PIV and Applications in Microsystems, Delft, the Netherlands (2005) [***Invited keynote lecture***]

[32] H. Li, R. Sadr and M. Yoda, "Multilayer Nano-Particle Image Velocimetry," submitted to 6th International Symposium on Particle Image Velocimetry, Pasadena, CA (2005)

[33] R. Sadr, H. Li, and M. Yoda, "Bias Due to Hindered Brownian Diffusion in Near-Wall Velocimetry," submitted to 6th International Symposium on Particle Image Velocimetry, Pasadena, CA (2005)

[34] R. Sadr, H. Li and M. Yoda, "Nano-Particle Image Velocity Measurements Within the Electric Double Layer and in Bulk Electroosmotic Flow," Accepted, ASME International Mechanical Engineering Congress and RD&D Expo, Orlando, FL (2005)

[35] P. Gnanaprakasam, A.Kumar and A. T. Conlisk, "Transient Electroosmotic Flow in Nanochannels", AIAA paper 2005-0675, the 43rd AIAA Aerospace Sciences Meeting, Reno, NV (2005)

Appendix B: Personnel

Theses

- Zhi Zheng, *Electrokinetic Flow in Micro- and Nano-fluidic Components*. Ph.D. thesis, Biomedical Engineering Center, The Ohio State University (2003)
- Kelly Evers, *Computation of Electroosmotic Flow in Complex Micro- and Nanochannel Geometries*. M.Sc. thesis, Biomedical Engineering Center, The Ohio State University (2003)
- Jennifer McFerran, *Biomolecular Transport in Nanochannel Systems*. Honors program thesis, The Ohio State University (2003)
- Andrew Kebbel, *Transient Electroosmotic Flow and Biomolecular Transport in Nanochannels*. Honors program thesis, The Ohio State University (2004)

Supporting Personnel

- Somnath Bhattacharyya, Visiting Professor, OSU
- Pradeep Gnanaprakasam, Graduate Research Assistant, Biomedical Engineering, OSU
- Haifeng Li, Graduate Research Assistant, Mechanical Engineering, GT
- Reza Sadr, Research Engineer II, Mechanical Engineering, GT
- Shuvo Roy, Project Staff Biomedical Engineering, OSU
- Aaron Fleischman, Project Staff Biomedical Engineering, OSU

Appendix C: Synergistic Activities

Consulting work for other labs based on this contract

ATP grant application submitted with iMEDD, Inc. (Columbus, OH) based on electroosmotic flow pumps being developed by Prof. Hansford. This project is also part of the consulting agreement between Dr. Hansford and iMEDD. Throughout the project Dr. Conlisk received experimental data from iMEDD for EOF and biomolecular transport.

New discoveries or inventions

Patent applications for electroosmotic pumps for the controlled delivery of drugs and for a potential DNA sequencing device have been filed by Prof. Hansford and iMEDD, Inc. based on work on this project.

Under consideration for publication in J. Fluid Mech.

Appendix D:

Electroosmotic flow in two-dimensional charged micro- and nano-channels

By S. BHATTACHAYYA[1], Z. ZHENG[2] AND A. T. CONLISK[3] †

[1]Permanent address: Department of Mathematics, Indian Institute of Technology, Kharagpur, India

[2]Biomedical Engineering Center, The Ohio State University, Columbus, OH 43210, USA

[3]Department of Mechanical Engineering, The Ohio State University, Columbus, OH 43202, USA

(Received ?? and in revised form ??)

In this work the electroosmotic flow in a rectangular channel such that the channel height is comparable to its width is examined. Almost all of previous work on the electroosmotic flow in a channel has been for the case where the channel width is much greater than the channel height and the flow is essentially one-dimensional and depends only on channel height. We consider a mixture of water or another neutral solvent and a salt compound such as sodium chloride for which the ionic species are entirely dissociated. Results are produced for the case where the channel height is much greater than the electric double layer(EDL)(microchannel) and for the case where the channel height is of the order of the width of the EDL(nanochannel). Both symmetric and asymmetric velocity, potential and mole fraction distributions are considered, unlike previous work on this problem. In the symmetric case where all quantities are symmetric about the centerline, the velocity field and the potential are identical as in the parallel plate, one-dimensional case. In the asymmetric case corresponding to different wall potentials, the velocity and potential can be vastly different and reversed flow can occur. The results indicate that the Debye layer thickness is not a good measure of the actual width of the electric double layer. The binary results are shown to compare well with experiment and asymptotic solutions are also obtained for the case of a three component mixture which may be applied to biomolecular transport.

1. Introduction

In this paper we consider the electroosmotic flow problem in a rectangular channel whose width and height are comparable. We consider an aqueous solution and a salt compound such as sodium chloride. For strong electrolytes, the salt component will be entirely dissociated so that nominally, the mixture has three components: undissociated water, and positive and negative ions making up the salt component.

Almost all of the previous work on this problem has been for parallel plate channels where the height of the channel is much smaller than the width. If the channel walls are charged, there is an induced electric potential due to the surplus of counter ions near the wall. In this case there is no bulk motion of the fluid in the channel. If electrodes are placed upstream and downstream in the desired flow direction, bulk motion of the fluid will occur. The electroosmotic problem for very small channel heights on the order of the

† Corresponding author: conlisk.1@osu.edu

electric double layer has been investigated by a number of authors(Verwey 1948, Qu & Li 2000, Burgeen & Nakache 1964, Levine 1975a, Rice & Whitehead 1965). Much of this work requires the Debye-Huckel Approximation for small potentials to be valid and all of the aforementioned work requires symmetry about the centerline of the parallel plate channel. In addition, all of the previous work described above requires that the ionic species be pairs of ions of equal and opposite valence. Electroosmotic flow in nanaoscale tubes has also been examined experimentally (Bohn *et al.* 1998) and analytically (Levine 1975b).

Conlisk *et al.*(2001) solve the problem for the ionic mole fractions and the velocity and potential for strong electrolyte solutions and consider the case where there is a potential difference in the direction normal to the channel walls corresponding in some cases to oppositely charged walls. They find that under certain conditions reversed flow may occur in the channel which can significantly reduce the flow rate. The validity of the Debye-Huckel Approximation is investigated by Conlisk (Conlisk 2005).

Rectangular channels of the type considered here have been investigated by Yang & Li (1997) and Andreev (1997). In both cases symmetric pairs of ionic species are considered. Yang & Li (1997) solve the fully nonlinear problem using a Green's Function approach and include a pressure-driven component which interacts with the electroosmotic component. They also study the electroviscous effect. Andreev (1997) invoke the Debye-Huckel approximation valid for small potentials and calculate the solution for the velocity by Fourier series methods. They are primarily concerned with channels on the micron scale and all of these papers are for the case of very thin electric double layers. While different $\zeta-$ potentials on different walls are considered, no reversed flow is found to occur. Neither of these papers consider an asymptotic analysis valid for thin double layers, nor the presence of multivalent ions in a mixture of more than two components.

In this paper we examine the behavior of the flow in a rectangular channel of a mixture consisting of two or three possibly multivalent ionic species plus an aqueous solvent; we consider for example, both an $NaCl - H_2O$ mixture and a mixture of three electrolytes having several different valences, under the action of an electric field in the primary direction of motion. However, the methods described here may be applied to mixtures having an arbitrary number of ionic constituents of arbitrary valence. In particular, we calculate the mole fractions of the ions and the potential and velocity and consider the case of both overlapping and thin double layers. In the latter portion of the paper we consider the case of a three component mixture in the asymptotic limit of a thin electric double layer thickness. We need not assume symmetry about the centerline and so we consider both symmetric and asymmetric boundary conditions on the potential. We consider the case of negatively charged walls as is common with silica at a neutral pH and so we expect a surplus of cations near the wall, while in the case of a positively charged wall, we would expect a surplus of anions.

The electroosmotic flow problem is driven by the presence of the electric double layer(EDL) near the surfaces of the channel. The electric double layer is intrinsic to the system since the walls are charged resulting in a non-zero electric potential and hence an electric field. Bulk fluid motion is then created by the insertion of electrodes upstream and downstream. The Debye layer thickness is defined by

$$\lambda = \frac{\sqrt{\epsilon_e RT}}{FI^{1/2}} \tag{1.1}$$

where F is Faraday's constant, ϵ_e is the electrical permittivity of the medium, I is the ionic strength, R is the gas constant, z_i is the valence of species i and T is the temperature. If the electric double layer is thin compared with the channel dimensions the problem for

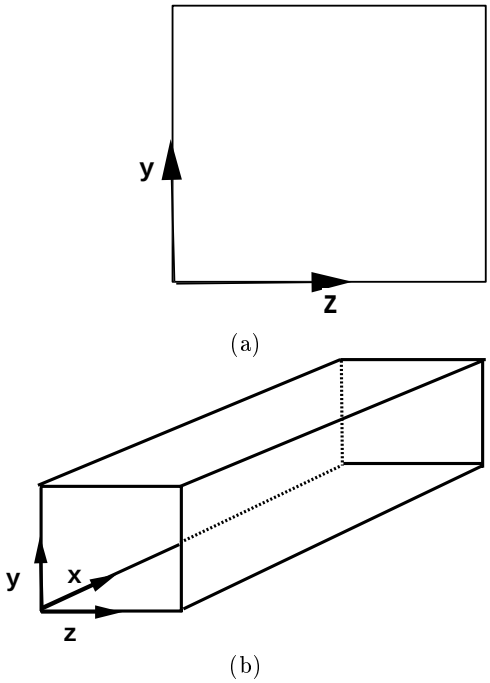

FIGURE 1. Geometry of the channel. u, v, w are the fluid velocities in the x, y, z directions.

the electric potential and the mole fraction of the ions is a singular perturbation problem and the fluid away from the electric double layers is electrically neutral. In this case the actual thickness of the EDL, defined as the position where the velocity reaches 99% of its value in the core is approximately $\delta_{DL} = d\epsilon$ where $\epsilon = \frac{\lambda}{h}$ and d is a number which depends on the ionic strength at the wall. Here δ_{DL} is a dimensionless length scaled on the channel height h, similar to the dimensionless boundary layer thickness in classical fluid mechanics. Typically for a relatively concentrated mixture $d \sim 5$ as for the Blasius boundary layer. We also consider the case where $\epsilon \sim 1$ in which case the channel height is of the order of the EDL thickness and the layers on the walls are overlapping. For extremely dilute mixtures, the EDL thickness can be on the order of $100nm$. We assume that the temperature is constant.

The purpose of the present paper is to present the theory of electroosmotic flow in a two-dimensional channel for the case where the Debye-Huckel approximation is not valid. The geometry is depicted on Figure 1. The plan of the paper is as follows. In the next section the governing equations are derived; the flow field, the electric field and the mass transfer problems are fully coupled. In the following section, we solve the equations both for the case of a double layer that is much thinner than the channel height and $\frac{\lambda}{h} = O(1)$, and calculate the volume flow rate through the channel; as noted above, the width of the channel $W \sim h$. We will also investigate the differences between one-dimensional and two-dimensional flow specifically for those cases that are symmetric about the centerline.

2. Governing equations

Let us now consider the mass transport in a liquid mixture of three components, say water and a salt such as sodium chloride flowing in the channel depicted on Figure 1. The electric field in general can be composed of two components: an externally imposed

electric field, E_0, and a local electric field present near the solid surfaces of the channel corresponding to the presence of an electric double layer. In dimensional form, the molar flux of species A for a dilute mixture is a vector and given by (Bird 1960)

$$\vec{n}_A = -cD_{AB}\nabla X_A + u_A z_A F X_A \vec{E}^* + cX_A \vec{u}^* \tag{2.1}$$

Here D_{AB} is the diffusion coefficient, c is the total concentration, X_A is the mole fraction of species A, which can be either the anion or the cation, u_A is the mobility, z_A is the valence, $\vec{E}^*$ is the total electric field and $\vec{u}^*$ is the mass average velocity of the fluid. The mobility u_A is defined by the Nernst-Planck equation as $u_A = \frac{D_{AB}}{RT}$. In the present paper we assume that the electrolyte concentration is small enough that the only interactions are between the electrolyte and solvent, so that we write $D_{AB} = D_A$.

The coordinates (x, y, z) are nondimensional; for example, $x = \frac{x^*}{L}$ and the scaling lengths in the three directions are (L, h, W). Also (u, v, w) are the dimensionless velocities in each of the coordinate directions (x, y, z); for example $u = u^*/U_0$ where u^* is dimensional. Here $\epsilon_1 = \frac{h}{L}$ and $\epsilon_2 = \frac{h}{W}$. We assume $h, W << L$ so that ϵ_1 is small; here z_A is the valence of species A. $Re = \frac{U_0 h}{\nu}$ is the Reynolds number and $Sc = \frac{\nu}{D_{AB}}$ is the Schmidt number, where ν is the kinematic viscosity and $U_0 = \frac{\epsilon_e E_0 \phi_0}{\mu}$ is the velocity scale (Conlisk *et al.* 2002).

We assume that the dimensional potential is of the form

$$\phi^* = -E_0 x^* + \phi_1^*(y^*, z^*)$$

where it is seen that ϕ_1^* is the perturbation potential from the externally applied field. Note that

$$E_0 = -\frac{\partial \phi^*}{\partial x^*}$$

Nondimensionalizing the equation for the potential as above, dropping the 1 on the perturbation potential and assuming $\phi_{y0} = \phi_{z0} = \phi_0$, $\phi = \frac{\phi^*}{\phi_0}$

$$\epsilon^2 \left(\frac{\partial^2 \phi}{\partial y^2} + \epsilon_1^2 \frac{\partial^2 \phi}{\partial x^2} + \epsilon_2^2 \frac{\partial^2 \phi}{\partial z^2} \right) = -\beta \sum_{i=1}^{N} z_i X_i \tag{2.2}$$

where here ϕ is the dimensionless perturbation potential. Also $\beta = \frac{c}{I}$ where c is the total concentration and I is the ionic strength. Note that equation (2.2) treats the ionic species as point charges. The channel is assumed long compared to its width and breadth i.e., ϵ_1 is small and and $\epsilon_2 = O(1)$. The largest inertial terms in the mass transfer equations are of the order of $ReSc$ and since the Schmidt number is large in liquids, and of the order of 10^3 the calculations here will be valid of all Reynolds numbers of $O(10^{-4})$ and smaller. In this case, the governing equations become, to leading order, and for a binary mixture

$$\frac{\partial v}{\partial y} + A \frac{\partial w}{\partial z} = 0 \tag{2.3}$$

$$\epsilon^2 \left(\frac{\partial^2 u}{\partial y^2} + A^2 \frac{\partial^2 u}{\partial z^2} \right) = \epsilon_1 \epsilon^2 \frac{\partial p}{\partial x} - \beta (z_g g + z_f f) \tag{2.4}$$

$$\epsilon^2 \left(\frac{\partial^2 v}{\partial y^2} + A^2 \frac{\partial^2 v}{\partial z^2} \right) = \epsilon^2 \frac{\partial p}{\partial y} + \Lambda \beta \frac{\partial \phi}{\partial y} (z_g g + z_f f) \tag{2.5}$$

$$\epsilon^2\left(\frac{\partial^2 w}{\partial y^2}+A^2\frac{\partial^2 w}{\partial z^2}\right)=\epsilon^2 A\frac{\partial p}{\partial z}+A\Lambda\beta\frac{\partial\phi}{\partial z}(z_g g+z_f f) \tag{2.6}$$

$$\epsilon^2\left(\frac{\partial^2 \phi}{\partial y^2}+A^2\frac{\partial^2 \phi}{\partial z^2}\right)=-\beta(z_g g+z_f f) \tag{2.7}$$

$$\epsilon^2\left(\frac{\partial^2 g}{\partial y^2}+A^2\frac{\partial^2 g}{\partial z^2}\right)=\beta z_g g(z_g g+z_f f)-\epsilon^2 z_g\left(\frac{\partial\phi}{\partial y}\frac{\partial g}{\partial y}+A^2\frac{\partial\phi}{\partial z}\frac{\partial g}{\partial z}\right) \tag{2.8}$$

$$\epsilon^2\left(\frac{\partial^2 f}{\partial y^2}+A^2\frac{\partial^2 f}{\partial z^2}\right)=-\beta z_f f(z_g g+z_f f)-\epsilon^2 z_f\left(\frac{\partial\phi}{\partial y}\frac{\partial f}{\partial y}+A^2\frac{\partial\phi}{\partial z}\frac{\partial f}{\partial z}\right) \tag{2.9}$$

where we have writtten the cation mole fraction as g and the anion mole fraction as f and $A=\epsilon_2$ is the aspect ratio of the channel. Also $\Lambda=\frac{\phi_0}{E_0 h}$. The parameter $\epsilon=\frac{\lambda}{h}$, where λ is the Debye length. In the present investigation we focus primarily on the flow along the direction of the externally imposed electrical body force, although the possibility of spanwise(w) and vertical(v) velocities is also explored.

To summarize, we have a series of seven equations in seven unknowns to solve for the three dimensional velocity field, the pressure, the potential and the two mole fractions; the boundary conditions are given by

$$\phi=0; f=f^0,\ \ g=g^0\ at\ y=0\ \ and\ \ z=0 \tag{2.10}$$

$$\phi=\phi^1; f=f^1,\ \ g=g^1\ at\ y=1\ \ and\ \ z=1 \tag{2.11}$$

$$u,v,w=0\ \ at\ \ y=0,z=0\ and\ y=1,z=1 \tag{2.12}$$

For this simplified case the dependent variables are functions of eight separate parameters in addition to the three coordinate directions: ϵ, A, β, Λ, g^0, g^1, f^0, and f^1. Consider the symmetric case here where $g^0=g^1$ and $f^0=f^1$. Then there are six independent parameters. We can reduce this number by recognizing that β and ϵ always occur in the ratio $\frac{\epsilon^2}{\beta}$. Further, rescaling the mole fractions on the value g^0, $G=\frac{g}{g^0}$, $F=\frac{f}{g^0}$ then the governing equations are invariant to the rescaling of the mole fractions and the main parameter is now $\delta^2=\frac{\epsilon^2}{\beta g^0}$; the other parameters are channel aspect ratio A and $\gamma=\frac{f^0}{g^0}$. The boundary conditions now become

$$\phi=0; F=\gamma; G=1\ at\ y=0\ \ and\ \ z=0 \tag{2.13}$$

$$\phi=\phi^1; F=\gamma; G=1\ at\ y=1\ \ and\ \ z=1 \tag{2.14}$$

and we have cut the number of parameters in half. In the asymmetric case where the electric potentials at $y=0$ and $y=1$ are not the same, there are three more parameters corresponding to two sets of the ratio of wall mole fractions at $y=1$ to g^0 and the value of the potential at $y=1$.

Note that δ is a function of both geometry and concentration. This is an important observation since it allows comparison of small channels at larger concentrations with larger channels at smaller concentrations. For example, a value of $\delta=0.075$ corresponds both to a cation concentration of $.15mM$ with $\lambda=34nm$ and a channel dimension of $470nm$ and to a cation concentration of $0.15M$ and a channel dimension of $15nm$ with $\lambda=1nm$. Thus because physical limitations prevent the measurement of velocity and concentration profiles under approximately $h=200nm$ (Sadr *et al.* 2004), modeling can be used to relate flows in nanoscale conduits to those in microscale conduits where these profiles can be measured.

For computational purposes we need to derive an equation for the pressure. In the same way as in classical computational fluid dynamics we differentiate the momentum equations and after some algebra, we obtain a Poisson equation for the pressure in the form,

$$\delta^2 \left(\frac{\partial^2 p}{\partial y^2} + \frac{\partial^2 p}{\partial z^2} \right) = \Lambda \left(\frac{\partial^2 g}{\partial y^2} + A^2 \frac{\partial^2 g}{\partial z^2} + \frac{\partial^2 f}{\partial y^2} + A^2 \frac{\partial^2 f}{\partial z^2} \right) \tag{2.15}$$

We now consider the case where $\delta \sim \epsilon << 1$ before considering full numerical solutions.

3. Asymptotic solution for binary electrolytes of arbitrary valence

In the case where $\delta << 1$ we can obtain analytical solutions for the flow within the EDL. This situation is a classical singular perturbation problem. Consider the case of two species of arbitrary valence, with say $X_1 = g$, $X_2 = f$. It is easier to start in the region near the walls. For example, near $y = 0$ we set $Y = \frac{y}{\delta}$. Then using the governing equations for the mole fractions we find that for g

$$\frac{\partial}{\partial Y} \left(\frac{\partial g}{\partial Y} + z_g g \frac{\partial \phi}{\partial Y} \right) = 0 \tag{3.1}$$

This is simply the one dimensional Boltzmann equation which has the well-known solution

$$g = g^0 e^{-z_g \phi} \tag{3.2}$$

where we have assumed that $\phi^0 = 0$. The solution for f follows immediately

$$f = f^0 e^{-z_f \phi} \tag{3.3}$$

To obtain the matching conditions, we find that the outer solution for the electrolyte of positive valence, g_o, must be

$$g_o = \lim_{Y \to \infty} g = g^0 e^{-z_g \phi_o} \tag{3.4}$$

where the subscript "o" denotes "outer". Similarly

$$f_o = \lim_{Y \to \infty} f = f^0 e^{-z_f \phi_o} \tag{3.5}$$

In the core region, it is obvious that for $\epsilon << 1$,

$$f_o = -\frac{z_g}{z_f} g_o \tag{3.6}$$

Thus we have from the limit of the inner solution,

$$z_g g^0 e^{-z_g \phi_o} = z_f f^0 e^{-z_f \phi_o} \tag{3.7}$$

and solving for the outer solution ϕ_o we find that

$$u_o = \phi_o = \frac{1}{z_g - z_f} ln \frac{-z_g g^0}{z_f f^0} \tag{3.8}$$

This is the one-dimensional result for the symmetric case generalized to arbitrary valence(Conlisk *et al.* 2002). The subscript o again denotes the outer solution valid away from the wall. Clearly, $z_g \neq z_f$ in order to avoid a singularity. As in the one-dimensional case(Conlisk *et al.* 2002), the result for the mole fraction is

$$f_o = \sqrt{-\frac{z_g}{z_f} g^0 f^0 e^{-(z_g + z_f)\phi_o}} \tag{3.9}$$

Now consider the $y-$momentum equation. The appropriate balance is obtained by considering the continuity equation where it is apparent that $v \sim \delta$. This means that the left side of equation (2.5) is $O(\delta)$ and the two terms on the right side balance if

$$p = \delta^{-2} p_1 + ...$$

and thus

$$\frac{\partial p_1}{\partial Y} + \Lambda \frac{\partial \phi}{\partial Y}(g - f) = 0 \tag{3.10}$$

Equation (2.5) becomes

$$\frac{\partial^2 p_1}{\partial Y^2} = \Lambda \left(\frac{\partial^2 g}{\partial Y^2} + \frac{\partial^2 f}{\partial Y^2} \right) \tag{3.11}$$

and it can be shown using the equations for f, g that equation (3.11) is the differentiated form of equation (3.10). Integrating and putting $p_1 = 0$ at the surface we obtain

$$p_1 = \Lambda \left(g + f \right) - \Lambda \left(g^0 + f^0 \right) \tag{3.12}$$

and so there is a pressure gradient generated within the EDL. The scaled version of equation (2.6) shows that for uniform wall concentrations the velocity $w = 0$. Clearly in this situation, $v = 0$ from continuity. Note that in the case where the potential is symmetric about the centerline, the equations for the streamwise velocity, u and the potential ϕ are the same and solutions in the inner region can be calculated numerically (Conlisk *et al.* 2002).

Clearly the solution in the boundary layers near $z = 0, 1$ will yield the same solution as in the one dimensional case and is formally equivalent to the solution on $y = 0$ for the same boundary conditions for aspect ratio $A = 1$. For $A \neq 1$ the boundary layer variable near the side walls is $Z = \frac{z}{\delta A}$ and so the effective boundary layer thickness is different from that on the top and bottom walls. Note that in the case where the potential is symmetric about the centerline, the equations for the streamwise velocity, u and the potential ϕ are the same and solutions in the inner region can be calculated numerically (Conlisk *et al.* 2002).

In the case where there is a potential difference across the channel, the potential can at most be a linear function of y and thus

$$\phi_o = \left(\frac{1}{z_g - z_f} ln \frac{-z_g g^1}{z_f f^1} - \frac{1}{z_g - z_f} ln \frac{-z_g g^0}{z_f f^0} \right) y$$

$$+ \frac{1}{z_g - z_f} ln \frac{-z_g g^0}{z_f f^0} \tag{3.13}$$

Similarly the mole fractions can at most be linear and for f we get

$$f_o = \left(-\frac{z_g}{z_f} g^1 f^1 e^{-(z_g + z_f)\phi_o^1} + \frac{z_g}{z_f} g^0 f^0 e^{-(z_g + z_f)\phi_o^0} \right) y$$

$$- \frac{z_g}{z_f} g^0 f^0 e^{-(z_g + z_f)\phi_o^0} \tag{3.14}$$

and the velocity is given by

$$u_o = \phi_o - \phi^1 \tag{3.15}$$

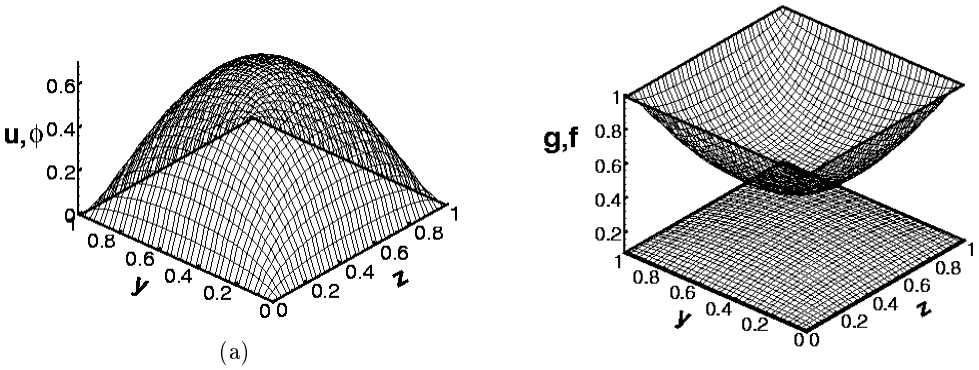

FIGURE 2. The dimensionless velocity and potential along with the mole fraction for $h = 5nm$; here $\delta = 0.23$, $A = 1$. Here the electric field corresponds to 6 volts over a channel of length $L = 3.5\mu m$. The mole fractions are scaled on g^0. (a) Potential and velocity. (b) Rescaled mole fractions for $f^0 = f^1 = 0.000252$ and $g^0 = g^1 = 0.00276$.

4. Numerical methods

To consider overlapped double layers and in anticipation of extending the results to arbitrary numbers of components of arbitrary valence we compute solutions numerically. For both the symmetric and the asymmetric cases, we use second-order central differences to approximate the derivatives in the governing equations. This procedure leads to a system of non-linear algebraic equations and Newton's linearization technique is applied to cope with the non-linearity. In this technique we solve for the dependent variables in a iterative manner. The recurrence relation between the k and $k+1$ iteration at each grid point is given by

$$X_{i,j}^{k+1} = X_{i,j}^{k} + DX_{i,j}^{k} \tag{4.1}$$

with $i = 2, ..., N-1$ and $j = 2, ..., M-1$ and $k > 0$. Here $DX_{i,j}^{k}$ is the error of approximation at the kth iteration and $X_{i,j}$ represents the dependent variables $u_{i,j}$,$\phi_{i,j}$, $f_{i,j}$ and $g_{i,j}$. The system of tridiagonal algebraic equations is solved using line relaxation with an underrelaxation factor. The iteration procedure is repeated till the following convergence criteria is satisfied

$$max| \ X_{i,j}^{k+1} - X_{i,j}^{k} \ | < \Delta$$

for $i = 2, 3, ..., N-1$; $j = 2, 3, ..., M-1$. where $\Delta = 10^{-5}$.

For larger values of channel height, $\Delta = 10^{-5}$ was used. In general, four digit accuracy was achieved in solutions for 81 and 161 points across the channel in all of the variables for all of the runs made. For $h = 20nm$ and above, four digit accuracy was achieved for 161 and 321 points across the channel.

In order to obtain the results out to 100 nm numerically, we use the solution for the channel of height $h - \Delta h$ and the initial guess for the channel of height h. In general for smaller channel heights Δh could be fairly large but as h increases it is difficult to converge for the larger values of Δh. Thus to get to $100nm$ we used a value $\Delta h = 1\, nm$.

5. Numerical results for specified wall concentrations

We have produced results for channel heights up to $100nm = 0.1\mu m$. For channel heights larger than about $20nm$, for about a $0.1M$ mixture, the asymptotic analysis

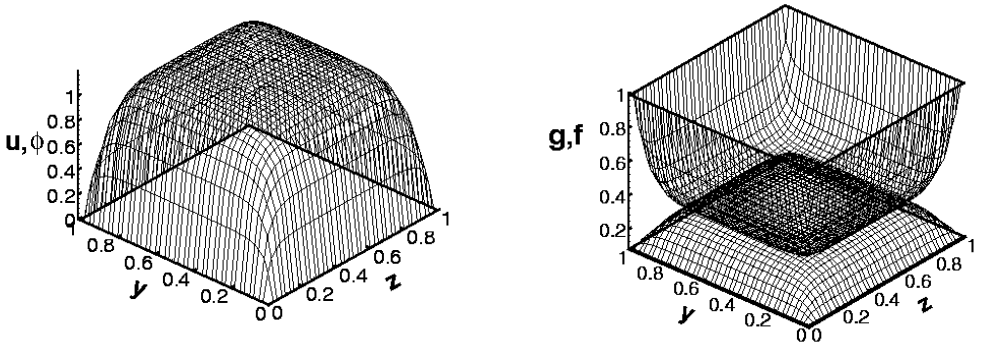

(a) (b)

FIGURE 3. Results for the dimensionless velocity and potential along with mole fractions for the case of an NaCl-water mixture. Here the electric field corresponds to 6 volts over a channel of length $L = 3.5\mu m$; the channel height $h = 25nm$. The mole fractions are scaled on g^0. (a) Velocity and potential. (b) Rescaled mole fractions for $f^0 = f^1 = 0.000252$ and $g^0 = g^1 = 0.00276$.

discussed previously can be used. For small potentials less than about $26mV$ we would expect that the Debye-Huckel approximation holds for which the Poisson-Boltzmann distribution is linearized leading to analytical solutions for the velocity and potential (Yang & Li (1997), Andreev (1997)). Here we present results for relatively large differences in mole fraction. On Figure 2 are results for the velocity and potential and mole fractions for channel height $5nm$. The concentrations shown here correspond to $0.154M$ of the cation and $0.0141M$ for the anion. We use the notation (g, f) for the rescaled mole fractions depicted on the figures.

It should be pointed out that this case is near the limit where the finite size of the ions would be expected to become important. The diameter of a water molecule and common univalent ions is about three angstroms; thus the "liquid" Knudsen number defined as the ratio of a molecular diameter to the channel height is about 0.06. It would be beneficial to compare these continuum results which treat the ions as point charges with MD simulations and this has already been done in one dimension (Zhu *et al.* 2005) where it is shown that wall exclusion effects become important at about $h = 6nm$ or about twenty molecular diameters. However in the one-dimensional case, the continuum solution is easily adjusted to account for the ion exclusion effects. As in the 1D case (Conlisk *et al.* 2002), the core of the channel is not electrically neutral.

Results for $h = 25nm$ and $50nm$ appear on the next two figures. Note that the EDL thickness is extremely thin; by $h = 100nm$, (Figure not shown) the EDL thickness is negligible. The familiar top-hat velocity profile appears as in the one-dimensional result and for these cases where all of the EDLs are thin, the one-dimensional and two dimensional results for the velocity are equivalent. The value of the potential and velocity in the core is about 1.189 for $h = 50nm$ which is very close to the asymptotic value of $\phi_o = \frac{1}{2} ln \frac{g^0}{f^0} = 1.195$ for monovalent species. The boundary layer thickness can be defined as in the classical high Reynolds number flow as the position where the velocity or potential reaches 99% of its bulk value. The boundary layer thickness will depend on the molarity and for $h = 25nm$ for the molarities chosen the boundary layer thickness is $\delta_{25} = 5.8\epsilon$ and for $h = 50nm$, $\delta_{50} = 5.7\epsilon$.

On Figure 5 are results for ionic strength 10 times less than on the previous figures for $h = 25nm$. Here $\delta = \frac{\lambda}{h} = 0.14$. The results look like a channel much larger at a

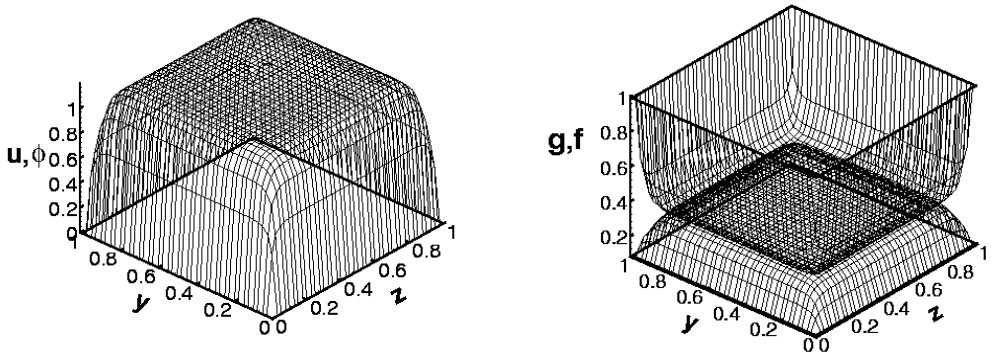

(a) (b)

FIGURE 4. Results for the dimensionless velocity and potential along with mole fractions for the case of an NaCl-water mixture. Here the electric field corresponds to 6 volts over a channel of length $L = 3.5\mu m$; the channel height $h = 50nm$. (a) Velocity and potential. (b) Rescaled mole fractions for $f^0 = f^1 = 0.000252$ and $g^0 = g^1 = .00276$.

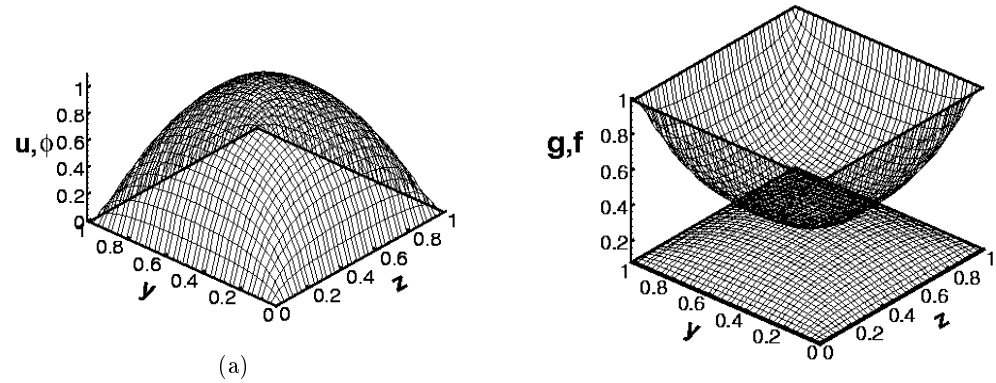

(a) (b)

FIGURE 5. Results for the dimensionless velocity and potential along with mole fractions for a more dilute mixture of an NaCl-water. Here the electric field corresponds to 6 volts over a channel of length $L = 3.5\mu m$; the channel height $h = 25nm$. (a) Velocity and potential. (b) Rescaled mole fractions for $f^0 = f^1 = 0.0000252$ and $g^0 = g^1 = .000276$.

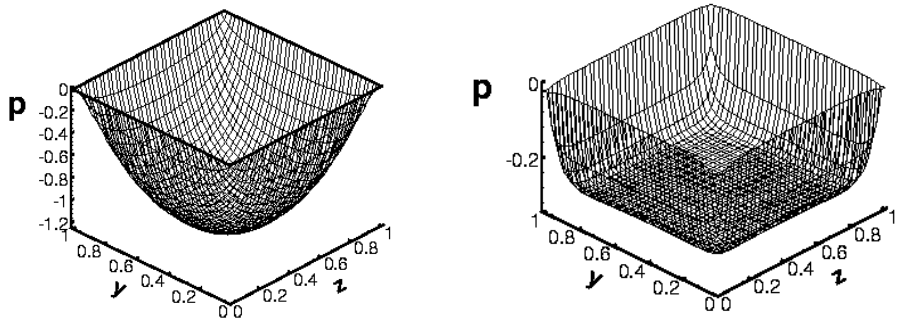

(a) (a)

FIGURE 6. Pressure distribution for the parameters of Figure 2, and 3. (a) $h = 5nm$; (b) $h = 25nm$.

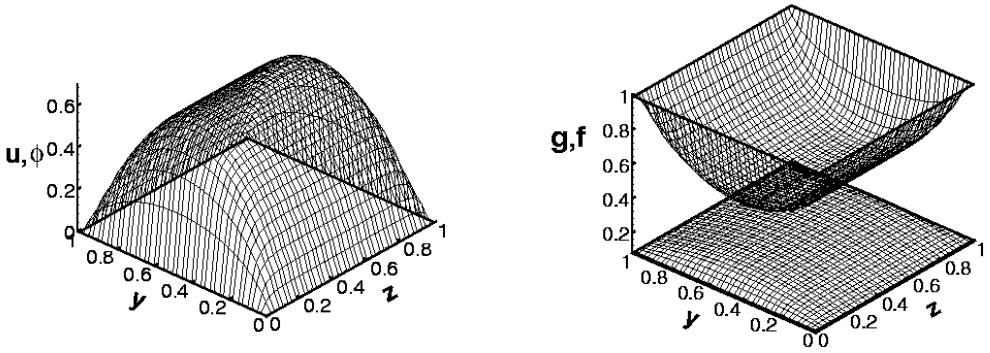

(a) (b)

FIGURE 7. Results for the dimensionless velocity and potential along with mole fractions for channel width $W = 20nm$, $h = 4nm$ so that the aspect ratio $A = 0.2$. Here $\delta \sim \epsilon = 0.2$. The electric field corresponds to 6 volts over a channel of length $L = 3.5\mu m$. (a) Velocity and potential. (b) Mole fractions $f^0 = f^1 = 0.000252$ and $g^0 = g^1 = .00276$.

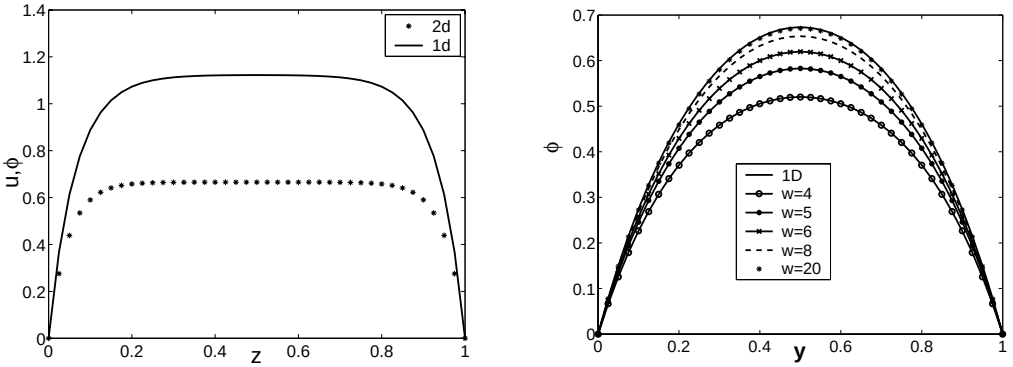

(a) (b)

FIGURE 8. (a) Results for the dimensionless velocity and potential for channel width $W = 20nm$, $h = 4nm$ plotted as a function of spanwise position and compared with the one-dimensional value. The electric field corresponds to 6 volts over a channel of length $L = 3.5\mu m$. Mole fractions $f^0 = f^1 = 0.000252$ and $g^0 = g^1 = .00276$. (b) Plot of the velocity and potential as a function of y for several channel widths.

smaller ionic strength and the EDLs are overlapping for this molarity. A δ value of 0.14 is equivalent to a $1\mu m$ channel at $10\mu M$ concentration.

The pressure for $h = 5,25nm$ is shown on Figure 6. Here the pressure is put equal to zero on the boundary and note that the pressure drops in the core and is symmetric about both axes. Here we note also that the pressure gradients in both directions exist because of the presence of the electric double layers on the side wall and the gradients exist despite the fact that the flow is one-dimensional.

The mole fractions, potential and velocity, are depicted on Figure 7 for unequal height and width. Note that the electric double layers are thin near the walls $z = 0, 1$ but overlapping on $y = 0, 1$. This means that one dimensional models will not be accurate in describing the spanwise behavior of the potential and velocities and mole fractions. This is shown on Figure 8(a). Here we see that the two-dimensional results are roughly half of the amplitude of the one-dimensional results. On Figure 8(b) are results for the velocity and

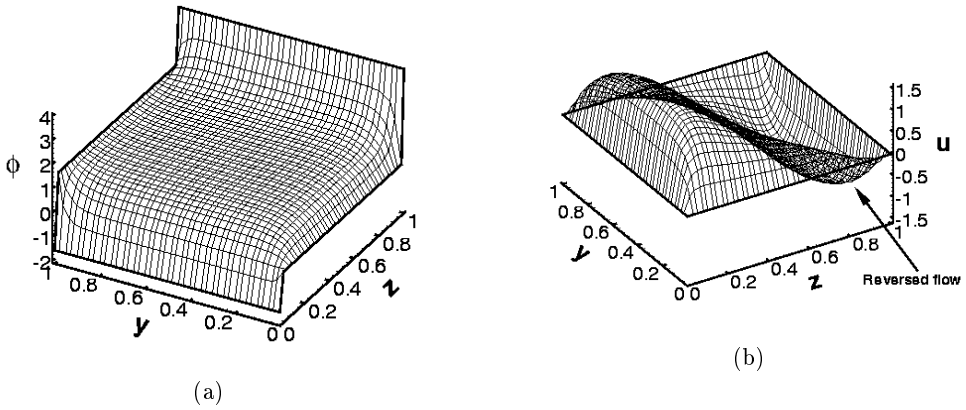

(a) (b)

FIGURE 9. Results for the dimensionless potential (a) and velocity (b) along with mole fractions for an asymmetric case. Here the electric field corresponds to 6 volts over a channel of length $L = 3.5\mu m$; the channel height $h = 20\ nm$ and aspect ratio $A = 1$. Wall molarity of cation species: $g = 0.154M$ at $y = 0$, $g = 0.033M$ at $y = 1$, $g = 0.724M$, at $z = 0$ and $g = 0.003M$ at $z = 1$; in the same order $f = 0.014M, 0.066M, 0.003M, 0.075M$. The potential at the walls also in the same order $\phi = 0, 0.04V, -0.04V, 0.100V$ and the value of $\epsilon = 0.04$.

potential for varying channel width plotted against channel height coordinate y. Note that the one-dimensional result is recovered at a width of about $20nm$. However the spanwise variation does not match with the one-dimensional result even for $W = 20nm$ as shown on Figure 8(a).

Asymmetric results are presented on Figure 9. The boundary conditions are chosen to correspond to equal electrochemical potential at the walls since there can be no net flow through the walls. Note the appearance of reversed flow in Figure 9 which significantly reduces the flow rate. Thus adjusting the wall potential can have a significant effect on the transport of species through the channel.

6. Reservoir-channel systems

6.1. *Equilibrium considerations*

Nanochannel systems are usually connected to upstream and downstream reservoirs in which the electrodes are placed. In experiments, the molarities in the reservoirs are known and the mixture is electrically neutral there; a sketch of a typical device is shown on Figure 10. We calculate the wall mole fractions using the requirement that the electrochemical potential in the reservoirs far upstream be the same as the average value at any channel cross section(Zheng *et al.* 2003). This requirement leads to the Nernst equation (Hunter 1981) which is given by

$$\Delta\Psi = \frac{RT}{z_i F} ln \frac{c_{iR}}{\bar{c}_{iC}} \quad i = 1, ..., N \tag{6.1}$$

where c_{iR} and $\bar{c}_{iC}$ are the average values of the concentration of species i in the reservoir and the fully developed region within the channel respectively.

We assume a negatively charged wall as is customary for a silicon channel in which the negative charge is due to deprotonated silanol groups. Then electroneutrality in the channel requires

$$z_f c_f + \sum_i z_i \bar{c}_{iC} = 0 \tag{6.2}$$

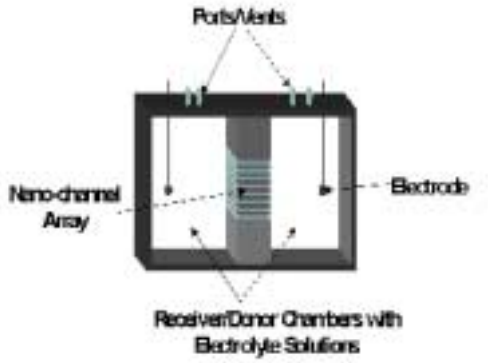

FIGURE 10. Nanopump system demonstrated by iMEDD, Inc. of Columbus, Ohio showing upstream and downstream reservoirs. The molarity(i.e. ionic strength is assumed known in the reservoir.

where z_f and c_f are the valence and the concentration of the fixed charges on the wall. Electroneutrality in the reservoir requires

$$\sum_i z_i c_{iR} = 0 \tag{6.3}$$

where usually in experiments c_{iR} is known for each species. Equations (6.1) and (6.2) are $N+1$ equations in $N+1$ unknowns for the average molar concentrations in the channel and the Nernst Potential $\Delta\Psi$.

If the volume of the reservoir is much larger than the volume of the channels as is the case in practice, then the concentration in the reservoir will be fixed at the value of the concentration prior to the initiation of flow into the reservoir. To obtain each of the average concentrations in the channel, we equate the Nernst potential for each of the species which leads to

$$\bar{c}_{iC} = \left(\frac{\bar{c}_{1C}}{c_{1R}}\right)^{\frac{z_i}{z_1}} c_{iR} \tag{6.4}$$

where species 1 is say the most populous ionic species. Substituting into equation (6.2) we have

$$z_f c_f + z_1 \bar{c}_{1C} + \sum_{i=2}^{N} \frac{z_i c_{iR}}{(c_{1R})^{\frac{z_i}{z_1}}} (\bar{c}_{1C})^{\frac{z_i}{z_1}} = 0 \tag{6.5}$$

This is a single equation for the average concentration of species 1 in the channel $\bar{c}_{1C}$, assuming the surface charge density is known.

To be dimensionally consistent in equation (6.5) the surface charge density should be converted to Moles/liter(M). To do this we assume that the charges are uniformly distributed and the result is

$$c_f = \frac{A\sigma}{1000 V_0 F} \tag{6.6}$$

where A is the surface area and V_0 is the volume. The factor 1000 converts m^3 to liter.

The average concentration in the channel is defined in dimensional form as

$$\bar{c}_i = \frac{1}{h}\int_0^h c_i dy^* \tag{6.7}$$

and in nondimensional form, dividing by the total concentration of the mixture we have

$$\bar{X}_i = \int_0^1 X_i dy \tag{6.8}$$

where X_i is the mole fraction and for example, $\bar{X}_i = \bar{g}$ for the cation and $\bar{X}_i = \bar{f}$ for the anion in a binary electrolyte mixture. Since the governing equations are nonlinear and iteration is required anyway, we iterate on the wall mole fractions as well. The procedure is the following: at the first iteration, the wall mole fraction is assumed to be the average mole fraction as calculated above. After convergence of the governing equations, the average mole fraction is calculated from equation (6.8). Clearly the only way that these two quantities can be equal is if the mole fractions across the channel are constant. This is not the case and so the equations are solved again with the new wall mole fraction defined by the equation, for example for the cation g^0

$$g^0_{m+1} = g^0_m \frac{\bar{g}}{\bar{g}_m}$$

where m denotes the iteration number and $\bar{g}$ is the average value of the mole fraction obtained by the procedure described above and is fixed. The form of this equation is motivated by the fact that a higher value of the average mole fraction will lead to a higher wall mole fraction. The iteration procedure continues until successive iterates of the wall mole fraction differ by less than 10^{-4}.

As is mentioned above, the surface charge density is assumed. To check the calculations are consistent with the assumed surface charge density, we recalulate the surface charge density from the formula

$$\sigma = -\frac{\epsilon_e RT}{\epsilon h F}\int_0^1 (g - f)dy \tag{6.9}$$

If the recalculated charge density is equal to the assumed charge density the solution is found. If not, the surface charge density is changed and the program is run again. It turns out that there is a unique solution where the assumed surface charge density matches the post-convergence calculated value.

The procedure for calculating the wall mole fractions simplifies in the asymptotic case. For the case of a binary electrolyte the three unknowns corresponding to the Nernst Potential and the two wall mole fractions may be obtained by using the outer solutions of the corresponding quantities; this avoids having to integrate the mole fraction across the channel numerically. In this way we solve

$$\Delta\psi = \frac{1}{z_f} ln f^R - ln f_o \tag{6.10}$$

$$\Delta\psi = \frac{1}{z_g} ln g^R - ln g_o \tag{6.11}$$

and the electroneutrality condition. It is clear that this procedure may be extended to an arbitrary number of electrolytes of arbitrary valence.

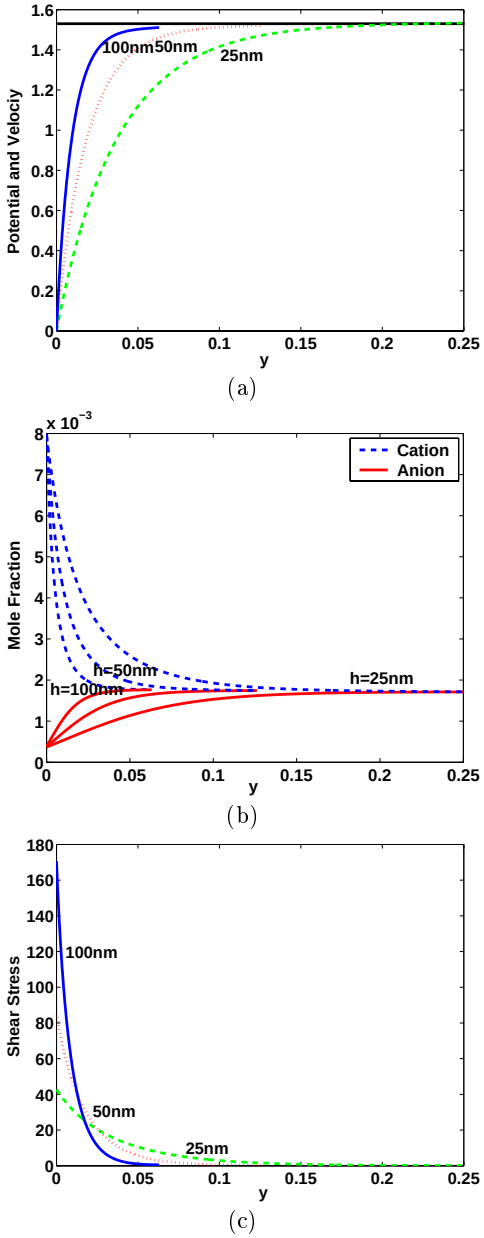

FIGURE 11. Asymptotic results for the dimensionless velocity and potential along with mole fractions(unscaled) and shear stress plotted in the outer variable for the case of an 0.1M 1:1 electrolyte-water solution in the reservoir. Here the electric field corresponds to 0.05 volts over a channel of length $L = 3.5\mu m$; the channel height $h = 25, 50, 100nm$ and the reservoir concentration is $2mM$. (a) Velocity and potential. The solid line is the result given by equation (3.8). (b) Mole fractions. (c) Shear stress.

6.2. *Asymptotic results for calculated wall concentrations for binary electrolytes*

We present numerical results for the inner region near the wall, using the outer solution values as boundary conditions. The wall mole fractions are calculated based on the procedure just described for a given ionic strength in the upstream reservoir.

mM	μ_e	μ_m	ζ_e	ζ_m	$\epsilon = \delta$	B_4O_7(wall)	Na(wall)	$\sigma(C/m^2)$
0.02	5.51×10^{-4}	6.10×10^{-4}	-0.173	-0.197	2.17×10^{-4}	$< 10^{-6}$	0.028	-0.007
0.2	4.60×10^{-4}	5.30×10^{-4}	-0.138	-0.170	9.85×10^{-5}	$< 10^{-6}$	0.133	-0.0154
2	3.52×10^{-4}	3.43×10^{-4}	-0.098	-0.111	9.60×10^{-5}	2.80×10^{-5}	0.141	-0.0154
20	1.71×10^{-4}	1.74×10^{-4}	-0.054	-0.056	8.59×10^{-5}	0.0023	0.1734	-0.0154

TABLE 1. Mobility and $\zeta-$potential for the ORNL data for the $10.4\mu m$ by $26\mu m$ channel. Note that in this regime $\delta = \epsilon << 1$ so that the asymptotic theory applies. The mobilities are in $cm^2V^{-1}sec^{-1}$ and the ζ-potential is in V.

Consider first the case of a binary electrolyte system. Figure 11 shows velocity, potential, mole fractions and shear stress for three different square channels plotted against the outer variable. The height of the three channels are 25nm, 50nm and 100nm. As the channel height increases, note that the thickness of the EDL becomes smaller and the familiar top hat profile characteristic of electroosmotic flow in micro-channels appears.

7. Comparison with experimental data

We have compared the model to two sets of experimental data and the comparisons are very good (Zheng *et al.* 2003). We have also compared the model described here with the work of Professor Yoda's group(Sadr *et al.* 2004). Here we compare the results for calculated wall mole fraction with the experimental data provided to us by Ramsey's group at Oak Ridge National Laboratory(Ramsey 2002) for a rectangular channel. The mixture is a sodium tetraborate, methanol solution with a viscosity of $0.00168Pa * sec$ and a dielectric constant of 59.24 as supplied by Ramsey's group. The mixture is a 1:1 electrolyte and the molarity in the upstream reservoir ranges from $0.02mM$ up to $150mM$; the channel is $10.4\mu m$ by $26\mu m$ as in the Georgia Tech case. The electric double layer is very thin so that asymptotic analysis for calculated wall concentrations is sufficient for the comparison. The experimental data corresponds to the average velocity divided by the electric field and this is called the electroosmotic mobility

$$\mu_{eo} = \frac{\frac{1}{2}U_0 ln\frac{g^0}{f^0}}{E_0}$$

which is the result for the outer velocity is given by equation (3.8). Note that the mobility is independent of the electric field since U_0 is linearly dependent on the electric field. The present model for the case of a thin electric double layer can predict the wall ζ-potential which is measured by the Ramsey group.

The results are depicted on Table 1 for four concentrations in the upstream reservoirs. Note that the wall concentration of the sodium is much greater than that in the reservoir for the more concentrated cases. In the present case, since the EDLs are thin we can define the ζ-potential as the negative of the value of ϕ in the core. On a dimensionless

basis since ϕ denotes the *perturbation* from the wall potential($\phi = 0$ at the walls) we have

$$\psi = \zeta + \phi \tag{7.1}$$

Defining $\psi = 0$ in the core results in

$$\zeta^* = -\phi = -\frac{1}{2} ln \frac{g^0}{f^0} \tag{7.2}$$

In dimensional form, which is the value that appears in Table 1 we have

$$\zeta = -\phi^* = -\frac{1}{2} \frac{RT}{F} ln \frac{g^0}{f^0} \tag{7.3}$$

The values compare well with the experimental data for both mobility and $\zeta-$potential.

8. Asymptotic solution for ternary electrolytes

Consider now the case of a three-electrolyte system. Denote the species by (g, f, r). Then the inner solution is the Poisson-Boltzmann expression as above

$$X_i = X_i^0 e^{-z_i \phi} \tag{8.1}$$

where X_i is any one of (g, f, r). By the same process as for the N=2 case, the outer solutions can be obtained and the results for the symmetric case as

$$g_o = \sqrt{\frac{-z_f g^0 f^0 e^{-(z_g + z_f)\phi_o}}{z_g + z_r \frac{r^0}{g^0} e^{(z_g - z_r)\phi_o}}} \tag{8.2}$$

$$f_o = \sqrt{\frac{-z_g g^0 f^0 e^{-(z_g + z_f)\phi_o}}{z_f + z_r \frac{r^0}{g^0} e^{(z_f - z_r)\phi_o}}} \tag{8.3}$$

$$r_o = -\frac{z_f f + z_g g}{z_r} \tag{8.4}$$

The outer solution for ϕ is given by the solution of the equation

$$e^{(z_g - z_f)\phi_o} = -\frac{z_g g^0}{z_f f^0} - \frac{z_r r^0}{z_f f^0} + e^{(z_g - z_r)\phi_o} \tag{8.5}$$

and $u_o = \phi_o$ in the symmetric case.

We can determine the potential and hence velocity analytically for special cases. If $z_r = z_g$ then

$$\phi_o = \frac{1}{z_g - z_f} ln \left(\frac{-z_g g^0}{z_f f^0} + \frac{-z_r r^0}{z_f f^0} \right) \tag{8.6}$$

If $z_r = 2, z_g = 1, z_f = -1$, then

$$x^3 - \frac{g^0}{f^0} x - 2\frac{r^0}{f^0} = 0 \tag{8.7}$$

where $x = e^{\phi_o}$. These valences are appropriate for a sodium-chloride, calcium mixture.

If $z_r = z_g$, we have

$$\phi_o = \frac{1}{z_g - z_f} \ln \left(\frac{z_g \left(g^0 + r^0 \right)}{-z_f f^0} \right) \tag{8.8}$$

For $z_r = z_f$ or $z_f = z_g$, equation (8.5) can be solved similarly. Next if $z_g + z_f = 2z_r$, the outer solution is given by

$$\phi_o = \frac{1}{z_g - z_r} \ln \left(\frac{-z_r r^0 \pm \sqrt{(z_r r^0)^2 - 4 z_g z_f g^0 f^0}}{2 z_f f^0} \right) \tag{8.9}$$

Similarly, cases such as $z_g + z_r = 2z_f$ or $z_f + z_r = 2z_g$ can also be solved. Finally, if $2z_g + z_r = 3z_f$, we have

$$\phi_o = \frac{1}{z_g - z_f} \ln \left(\frac{t}{6 z_r r^0} - \frac{2 z_f f^0}{t} \right) \tag{8.10}$$

where $t = \left(\left(-108 z_g g^0 + 12\sqrt{3} \sqrt{\frac{4(z_f f^0)^3 + 27 (z_g g^0)^2 z_r r^0}{z_r r^0}} \right) \cdot \left(z_r r^0 \right)^2 \right)^{\frac{1}{3}}$.

For the asymmetric case we find

$$g_o = \left(g_o^1 - g_o^0 \right) y + g_o^0 \tag{8.11}$$

$$f_o = \left(f_o^1 - f_o^0 \right) y + f_o^0 \tag{8.12}$$

where for example f_o^0 is the limit of the outer solution near $y = 1$

$$f_o^0 = \sqrt{\frac{-z_g g^0 f^0 e^{-(z_g + z_f)\phi_o^0}}{z_f + z_r \frac{r^0}{g^0} e^{(z_f - z_r)\phi_o^0}}} \tag{8.13}$$

The potential is given in the same way as for $N = 2$ by,

$$\phi_o = \left(\phi_o^1 - \phi_o^0 \right) y + \phi_o^0 \tag{8.14}$$

The presence of a small amount of a divalent cation in a channel having negatively charged walls has a great effect on the flow (Zheng *et al.* 2003). Figure 12 shows the asymptotic solutions for a 1:1:2 electrolyte mixture for surface charge density σ =-0.0154C/m^2 on the channel wall. Note that the core is still electrically neutral and the the electric double layer thins considerably as before. These results are much different from the binary case and a bivalent anion will have little or no effect on the flow compared to the binary case (Zheng *et al.* 2003).

9. Summary

We have produced analytical and numerical results for the electroosmotic flow in a rectangular channel both in the case of overlapped double layers and in the case of thin double layers. In cross-section, when the EDL is very thin, the the results look similar to the results for a one dimensional or slit pore channel. However, if the EDLs are overlapping in one direction, one-dimensional flow models will not match the two-dimensional results in the dimension normal to the overlapped dimension. The one-dimensional result in the overlapped direction is recovered at about a channel height of $20nm$ for the molarities chosen.

The results show that the Debye layer thickness is not a good measure of the actual width of the electric double layer. This work has shown that for the molarities considered, the actual dimensional width of the EDL is $\delta^* \sim 6\lambda$ similar to the case in high Reynolds number flow.

We have also shown how non-zero wall potentials can produce reversed flow. Thus

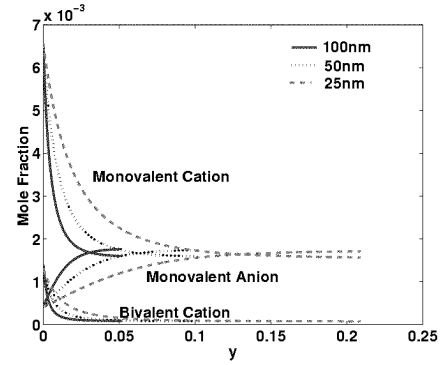

(a)

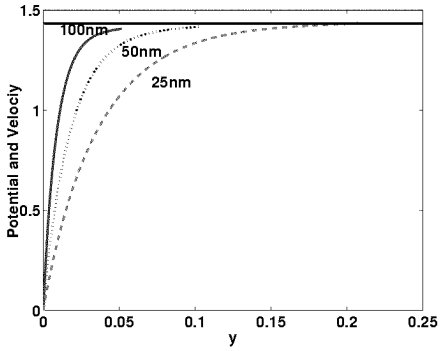

(b)

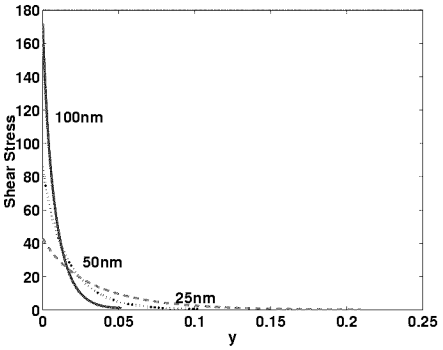

(c)

FIGURE 12. Results for a 1:1:2 electrolyte mixture for channel heights $h = 25, 50$ and 100 nm. The width of the channel is 100 μm, the surface charge density $\sigma = -0.0154 C/m^2$, and the concentration of electrolytes in the reservoir is $0.002M$. (a) Mole fractions near the wall. (b) Potential and velocity; (c) Shear stress.

chemically treating a wall can have significant effects on the character of the flow. Theoretically, the proper adjustment of wall potential and hence surface charge can result in either mixing or separation and these phenomena are currently being explored.

Analytical solutions for the case of thin double layers characterized by $\delta \sim \epsilon << 1$ have been shown to compare well with experimental data for rectangular pores generated by Ramsey's group at Oak Ridge National Laboratory (Ramsey 2002).

We have produced results for channel heights as small as $h = 5nm$. This case is near the limit where the finite size of the ions would be expected to become important. The diameter of a water molecule and common univalent ions is about three angstroms; thus the "liquid" Knudsen number defined as the ratio of a molecular diameter to the channel height is about 0.06. It would be beneficial to compare these continuum results with MD simulations to determine if the two-dimensional case is significantly different from the one-dimensional case where the continuum results can easily be adjusted to match the MD solutions (Zhu *et al.* 2005). It is desireable to have continuum models of nanofluidic devices since nanoscale devices cannot be designed solely by running MD simulations because of the significant computation time required ($\sim$ weeks).

In addition, many interesting problems in the biological arena require the solution for more than two species. This is the case for modeling the transport of a biomolecule in an electrolyte solution. We have presented analytical results for the outer solution for several parameter ranges of the relative valences for the case of three species in the case where $\epsilon << 1$. We have also presented numerical results for the inner solution in the case of three species containing a bivalent cation($z = 2$).

Because of the assumption of fully developed flow, the velocity is one dimensional and no spanwise motion can occur. Future work will focus on the case where the wall potentials are not uniform leading to multi-directional flow and the formation of complicated vortical flow patterns.

Acknowledgements: This work is funded by DARPA under agreement number F30602-00-2-0613. The authors are grateful to the contract monitors Dr. Anantha Krishnan (DARPA), Mr. Clare Thiem and Mr. Duane Gilmour of Air Force Research Lab (IFTC) for their support. Lei Chen performed the numerical computations for this paper produced many of the figures. For this work ATC is grateful. The authors are grateful to the Referees for their helpful comments.

REFERENCES

Andreev, Victor P., Dubrovski, Sergey G., and Stepanov, Yuri V. 1997 *J. Micro. Sep.* **9** pp. 443-450.

Bird, R. B., Stewart, W. E., Lightfoot, E. N. *Transport Phenomena*, John Wiley and Sons.

Burgeen, D. and Nakache, F. R. 1964 Electrokinetic Flow in Ultrafine Capillary Slits *The Journal of Physical Chemistry* **68**, pp. 1084-1091.

Conlisk, A. T., McFerran, Jennifer, Zheng, Z. and Hansford, Derek 2002 Mass Transfer and Flow in Electrically Charged Micro- and Nano-channels *Analytical Chemistry* **74** pp. 2139-2150.

Conlisk, A. T. 2005 The Debye-Huckel Approximation: Its Use in Describing Electroosmotic Flow in Micro- and Nano-channels, to appear *Electrophoresis*, May, 2005.

Hunter, R. J. 1981 Zeta Potential in Colloid Science Academic Press: London

Kemery, P. J., Steehler, J. K. & Bohn, P. W. 1998 *Langmuir* **14**, 2884-2889.

Levine, Samuel, Marriott, John R., and Robinson Kenneth 1975 Theory of Electrokinetic Flow in a Narrow Parallel-plate Channel *Faraday Transactions II* **71**, pp. 1-11

Levine, S., Marriott, J. R., Neale, G., and Epstein,N. 1975 Theory of Electrokinetic Flow in Fine Cylindrical Capillaries at High Zeta Potentials *Journal of Colloid and Interface Science* **52, no. 1** pp. 136-149, 1975.

Qu, W. and Li, D. 2000 A Model for Overlapped EDL Fields. *J. Colloid and Interface Science* **224**, pp. 397-407.

Ramsey, J. M. Private communication.

Rice, C. L. and Whitehead, R. 1965 Electrokinetic Flow in a Narrow Capillary *Journal of Physical Chemistry* **69, no. 11** pp. 4017-4024.

Sadr, R., Yoda, Minami, Zheng , Z. and Conlisk, A. T. 2004 An Experimental Study of Electroosmotic Flow in Rectangular Microchannels *Journal of Fluid Mechanics* **306**, pp. 357-367.

Verwey, E.J.W. and verbeek, J.Th.,G. 1948 Theory of Stability of Lyophobic Colloids *Elsevier: Amsterdam.*

Yang Chun and Li, Dongquing 1997 Electrokinetic Effects on Pressure Driven Liquid Flows in Rectangular Microchannels *Journal of Colloid and Interface Science* **194** pp. 95-107.

Zheng, Z., Hansford, Derek J., Conlisk, A. T. 2003 Effect of Multivalent Ions on Electroosmotic Flow in Micro and Nanochannels *Electrophoresis* **24**, pp. 3006-3017.

Zhu, Wei, Singer, Sherwin J., Zheng, Z., and Conlisk, A. T. 2005 Study of Electroosmotic Flow of a Model Electrolyte, to appear Phys. Rev. E.

42nd AIAA Aerospace Sciences Meeting **Paper No. AIAA–2004–754**
Reno, Nevada
January 6–9, 2004

Appendix E:

NANO-PARTICLE IMAGE VELOCIMETRY (NPIV): A NEW TECHNIQUE FOR MEASURING NEAR-WALL VELOCITY FIELDS WITH SUBMICRON SPATIAL RESOLUTION*

Minami Yoda (minami.yoda@me.gatech.edu)†
Reza Sadr (reza.sadr@me.gatech.edu)
G. Woodruff School of Mechanical Engineering
Georgia Institute of Technology
Atlanta, GA 30332–0405 USA

ABSTRACT

Characterizing flow fields at sub-micron, or "nano," length scales is important in developing both modeling and design capabilities for MEMS and bio-NEMS devices. The new nano-PIV technique was used to measure the two components of the velocity field parallel to the channel wall within 100 nm of the wall in fully developed and steady electroosmotic flow of dilute sodium tetraborate buffer through rectangular microchannels. In all cases, the electric double layer thickness λ was much less than the channel height h. An initial analysis was performed using synthetic images of the errors in nPIV associated with tracer particle mismatch within an image pair due to Brownian diffusion. The experimentally determined mobilities of the particle tracers calculated from averaged nPIV data are compared with analytical predictions of the electroosmotic mobility. The mobility results appear to have a power-law dependence upon buffer concentration.

INTRODUCTION

Characterizing flow fields at sub-micron, or "nano," length scales is crucial in developing both modeling and design capabilities for bio-NEMS. Although spatially and temporally resolved experimental data are required to validate existing analytical and numerical models of electrokinetically driven transport at the micro- and nanoscale, experimental studies at these scales are at present greatly limited by the lack of measurement techniques with appropriate spatial resolution. At present, the most common technique for measuring velocities in microchannels, micro-particle image velocimetry (μPIV) [1], has an out-of-plane spatial resolution of 2–6 μm [1, 2]. Moreover, flows at these spatial scales are dominated by surface, or near-wall, phenomena. Yet μPIV data to date are limited to distance of at least 450 nm from the wall [3]. Micro-PIV is therefore best suited to bulk flow studies in microchannels with dimensions exceeding 10 μm.

Over the last two years, we have therefore developed a new near-wall velocimetry technique, nano-particle image velocimetry (nPIV) [4, 5]. Unlike μPIV, the technique uses evanescent-wave (*vs.* volumetric) illumination generated by total internal reflection at the interface between the wall and the fluid instead of volumetric illumination. The out-of-plane spatial resolution of nano-PIV is therefore determined by the illumination source, much like conventional PIV. Because nPIV is inherently limited to velocity measurements adjacent to the wall and within a distance comparable to the wavelength of the illumination, the technique complements the bulk flow velocimetry capabilities of μPIV.

The technique was used to study fully developed and steady electroosmotic flow (EOF) through rectangular microchannels. In EOF, an electrolyte solution is driven by an external electric field E through a channel with charged walls; this surface charge is due to

† Corresponding author

adsorption of ions from the electrolyte solution onto the channel walls. The charged channel walls in turn attract free ions of the opposite sign from the electrolyte solution to create an electric double layer (EDL), with a thickness characterized by the Debye length λ. The Debye length is typically about 0.1 nm to 10 nm for aqueous solutions at molar concentrations C ranging from 1 M to 0.1 mM, respectively. Outside this thin EDL, which is analogous to the momentum boundary layer, steady and fully-developed EOF has a uniform velocity profile.

Electrokinetic "pumping" is currently the favored technology for driving flows through micro- and nanochannels. In fully-developed EOF, the volumetric flow rate $Q \propto h$ for a given E; where as in Poiseuille flow, $Q \propto h^3$ for a given pressure gradient. EOF can therefore achieve much higher Q for smaller microchannels for a given energy input. EOF is also preferred for biochemical separations at the microscale, since the nearly uniform velocity profiles of EOF give much less Taylor dispersion than Poiseuille flow.

There are numerous analytical and numerical studies of fully developed and steady EOF through channels with slit, rectangular and round cross-section [6–8, for example]. Conlisk [9] recently considered EOF of two ionic species in both parallel-plate and rectangular micro- and nanochannels and obtained numerical results for velocity, potential and species mole fractions. Their asymptotic solution for the uniform (outer) EOF in rectangular microchannels assuming symmetry about the channel centerline gives a bulk flow velocity that is linearly proportional to the electric field:

$$U = \frac{\varepsilon_e RT}{2\mu F} E \ln\left\{\frac{g^0}{f^0}\right\} \qquad (1)$$

Here, ε_e, μ and T are the fluid electrical permittivity, viscosity and temperature, respectively, R and F are the ideal gas and Faraday's constants, respectively, and f^0 and g^0 are the anion and cation wall mole fractions, respectively. In contrast with most previous work, these wall mole fractions were not calculated from the wall zeta-potentials, and were instead calculated iteratively from the electrolyte concentrations in the upstream reservoir based upon electrochemical equilibrium between the reservoir and channel electrolyte concentrations [10].

However, there are far fewer experimental studies of electroosmotic flow in microchannels, and we are aware of only four studies that report velocity profiles. Paul [11] and Herr [12] used scalar imaging velocimetry of a caged fluorescent dye to obtain radial velocity profiles in EOF through 75 and 100 μm fused silica capillaries. Sinton and Li [13] also used excitation of a caged fluorescent dye to obtain velocity profiles in square and circular microchannels ranging from 20–200 μm and presented a technique to eliminate the effects of Joule heating and its marked impact upon fluorophore mobility in their experiments. Finally, Cummings [14] obtained μPIV velocity data in EOF between parallel plates spaced 10 μm apart by periodic arrays of square and circular posts.

EXPERIMENTS

Experiments were carried out on steady, fully-developed EOF through rectangular microchannels. The flow coordinate system is defined so that x is along the flow direction, y is normal to the wall, and z is along the wall normal to x.

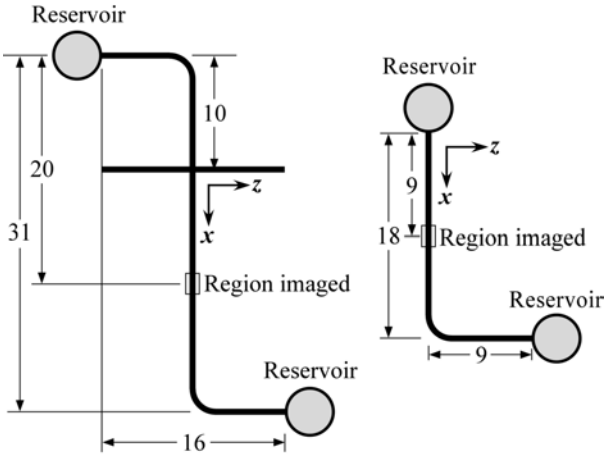

Figure 1: Top view of the cross (Cr) [left] and single channel (SC) [right] microchannel geometries. Dimensions are given in mm.

Two different microchannel geometries were used: a "single channel" with one elbow (Fig. 1 left); and a "cross" with two intersecting channels (Fig. 1 right). The microchannels were provided by Dr. M. Ramsey's group in the Chemical Sciences Division at Oak Ridge National Laboratories. The chemical wet-etch process used to fabricate these microchannels in fused silica gives a nominally trapezoidal open cross-section. A fused silica cover slip is then sealed over the top of this channel to create the "rectangular" microchannels. The height (y-dimension) and width (z-dimension) at the

half-depth of the channel are defined as h and W, respectively. Further details of the microchannel chips are given in Sadr *et al.* [15].

In all cases, the region studied in these experiments was at least 300h downstream of any bends or intersections to ensure fully-developed flow. Steady EOF was created using a constant electric field E = 0–50 V/cm using a DC power supply and platinum electrodes immersed in the upstream and downstream reservoirs.

The working fluid was sodium tetraborate buffer composed of sodium tetraborate decahydrate salt ($Na_2B_4O_7{\cdot}10H_2O$) (Acros Organics ACS reagent grade) dissolved in Nanopure water at molar concentrations C = 0.19–36 mM. Sodium tetraborate was chosen for its buffering properties as a weak base. Fluorescent polystyrene spheres of diameter d = 100 nm (Bangs Laboratories Inc. Estapor XC) were added to the working fluid as tracers at volume fractions $\phi \approx 10^{-3}$. The tracers had a specific gravity of 1.05 and excitation and emission maxima of 480 and 520 nm, respectively. Table 1 summarizes the experimental parameters.

C [mM]	h [μm]	W [μm]	Channel type
0.19	4.9	17.3	Cr
1.9	10.2	26.1	SC
3.6	24.7	51.2	SC
18.4	4.8	17.9	Cr
36	24.7	51.2	SC

Table 1: Summary of experimental parameters.

Nano-PIV measures two components of the flow velocity by determining the displacement over a known time interval of neutrally buoyant fluorescent colloidal particle tracers as they are convected by the flow. The unique aspect of nPIV is its use of evanescent waves as the illumination source. Evanescent waves are generated when light undergoes total internal reflection (TIR) at the interface between the solid channel wall and the fluid with refractive indices n_1 and n_2, respectively, where $n_1 > n_2$. The evanescent wave propagates *parallel* to the wall in the fluid with an intensity I that decays exponentially with distance *normal* to the interface y [16]:

$$I = I_o \exp\{-y / y_p\} \tag{2}$$

where the penetration depth

$$y_p = \frac{\lambda_o}{4\pi}\left[n_1^2 \sin^2\theta - n_2^2\right]^{-1/2} \tag{3}$$

I_o is the light intensity at the interface (i.e., y = 0), λ_o is the light wavelength in vacuum, and θ is the angle of incidence.

The microchannels were mounted horizontally on the stage of an inverted epifluorescent microscope (Leica DMIRE2). The evanescent-wave illumination was generated from a λ_o = 488 nm beam from an argon-ion laser (Coherent Innova 90) with an output power of 0.1 W. The beam was focused at an angle with respect to the normal of about 40° onto the "short" side of a 45°–45°–90° fused silica prism optically coupled along its hypotenuse with glycerin to the upper surface of the microchannel chip (Fig. 2 top). The light, refracted through the prism and the height of the entire chip, undergoes TIR with an angle of incidence $\theta \approx 70°$ at the fused silica-water interface at the top of the 1 mm thick cover slip at the bottom wall of the microchannel. The evanescent waves that are imaged here are from the first or second TIR at the top of the cover slip. As shown in Figure 2 bottom, the region in the channel illuminated by the evanescent wave is above the cover slip to minimize surface roughness effects and in the center of the channel to minimize edge effects.

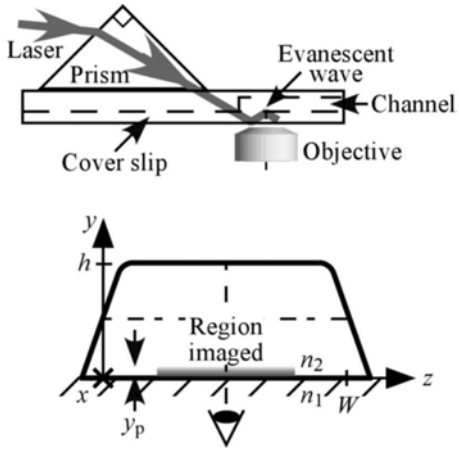

Figure 2: Sketch of nPIV imaging setup [top] and the region imaged with respect to the channel cross-section [bottom].

The penetration depth determines the out-of-plane spatial resolution of the nPIV measurements. Equation (3) gives $y_p \approx 100$ nm based upon the refractive indices of fused silica and water, or n_1 = 1.46 and n_2 = 1.33, respectively.

The fluorescent particle tracers are viewed through a 63 × 0.5 objective (Leica PL Fluotar L). A dichroic beamsplitter cube (Leica I3) separates the red-shifted fluorescence from the evanescent wave illumination so that only the fluorescence from the particles is imaged by the microscope. The images of the particle tracers are recorded typically as 80 row × 653 col images on a Photometrics Cascade 650 CCD camera with on-chip gain at framing rates up to 160 Hz with 1 ms exposure. Figure 3 shows a typical raw image of 100 nm tracer particles in EOF obtained with this setup spanning a region 13 μm (v) × 90 μm (h), with the horizontal along the flow direction. Here, the working fluid is 18.4 mM sodium tetraborate buffer driven by an external electric field E = 48 V/cm. In all cases, 1000 consecutive images spanning more than 6 s are written in real time onto to the HD on a PC.

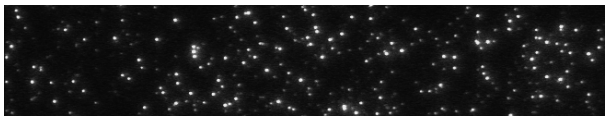

Figure 3: Typical image of tracer particles convected by EOF. The flow direction is from left to right.

With this imaging system, a 100 nm fluorescent particle illuminated by the evanescent wave spans up to 9 pixels due to diffraction effects [1]. The particles that are closer to the wall within the evanescent-wave layer are illuminated with a higher light intensity, since the evanescent wave intensity decreases as distance from the wall increases (*cf.* Equation (2)) and hence have larger images.

The EdPIV software of Wereley *et al.* [17] was used to determine the two components of particle displacement over time, and hence velocity, parallel to the wall. An FFT-based algorithm was used to cross-correlate two interrogation windows extracted from two consecutive images with an exposure of 1 ms and an interimage interval of 6.25 ms. The typical dimensions of the windows were 110 pixels × 80 pixels (x × z), corresponding to a spatial resolution in the object plane of about 18 μm and 13 μm, respectively. . The relatively large interrogation windows used here ensure enough particle images per interrogation window to give cross-correlation peaks with good SNR and improve the accuracy of the cross-correlation [18]. The windows had a 50% overlap, giving typically 18 displacement or velocity vectors for each pair of images. No window shift is used in the nPIV processing; note that the particle displacement is always less than 7 pixels.

An important issue in nPIV processing is particle tracer mismatch between two consecutive images due to Brownian diffusion normal to the wall. Although errors due to Brownian diffusion parallel to the wall can be drastically reduced by averaging results for steady flows, particle "dropout" and "dropin" due to tracer diffusion out of and into the region next to the wall illuminated by the evanescent wave reduces the signal-to-noise-ratio, or SNR, of the cross-correlation peak. The effect of Brownian motion in nPIV is especially pronounced due to the relatively small thickness (*i.e., y*-extent) of the illuminated region.

The rms displacement due to Brownian diffusion in an infinite fluid is estimated by

$$\delta x = \sqrt{2 D_\infty \delta t} \tag{4}$$

where δt is the time interval over which diffusion occurs and D_∞ is the Brownian diffusion coefficient given by the Stokes-Einstein equation [19]:

$$D_\infty = \frac{kT}{3\pi\mu d} \tag{5}$$

Here, d is particle diameter, k is the Boltzmann constant, and T and μ are the fluid absolute temperature and viscosity, respectively. For the d = 100 nm tracer particles used here in water at T = 300K, Equation (5) gives a diffusion coefficient $D_\infty = 5.13 \times 10^{-12}$ m^2/s. For the experimental data, the time interval within the image pair δt = 6.25 ms (corresponding to a framing rate of 160 Hz). The rms displacement, given by Equation (4), is then δx = 250 nm, *vs.* the thickness of the evanescent wave $y_p \approx 100$ nm

BROWNIAN DIFFUSION ANALYSIS

An initial study of the error due to Brownian-induced particle mismatch was carried out using synthetic images generated under the "worst case" assumption of unconfined (*vs.* hindered) Brownian diffusion. When the colloidal particle is near a wall, its Brownian diffusion is reduced relative to its value in the bulk by the additional hydrodynamic drag due to the wall. These wall effects give "confined" Brownian diffusion coefficients for motion normal and parallel to the wall that are functions of distance from the wall and in all cases are less than D_∞ [20].

Synthetic images consisting of a large number (up to 500) of randomly located particles with a given particle

image size distribution and density, velocity field and Brownian displacement were generated using in-house software. Note that the particles are distributed over a region next to the wall spanning $3y_p$ to ensure that the region beyond that illuminated by the evanescent wave has sufficient particle density to accurately simulate the effects of Brownian diffusion into and out of the evanescent-wave region. The particle image intensities are modeled as Gaussian with a peak magnitude evaluated from Equation (2) based upon the position of the particle within the region illuminated by the evanescent wave. After generating the first image, the second image within the pair is generated by calculating the intensity and location of each particle image over a given time interval δt based upon its displacement due to both Brownian motion and the bulk flow. Here, the bulk flow for the synthetic images is assumed to be uniform with a velocity U along the x-direction to match the experimental EOF data. The software also tracks the number of mismatched tracer particles (due to both dropout and dropin) within each image pair. All other parameters of the synthetic images are adjusted accordingly so that the grayscale histograms of the artificial images match those of the actual experimental images. Figure 4 shows a typical synthetic image generated by this software.

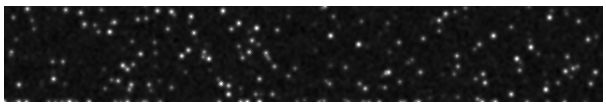

Figure 4: Typical synthetic image of tracer particles.

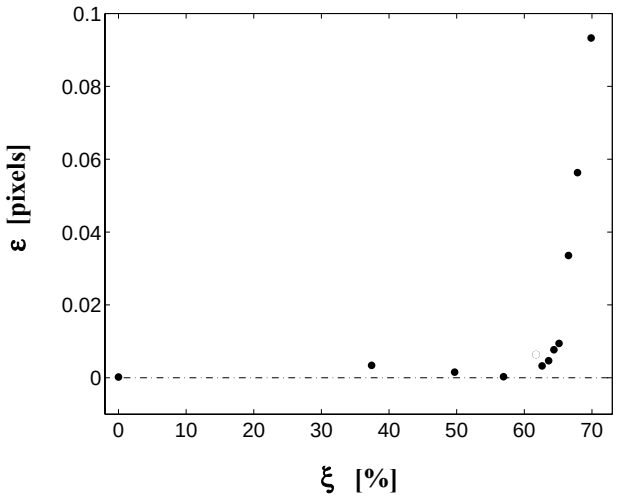

Figure 5: Absolute displacement error ε in pixels as a function of the fraction of mismatched particles ξ in % averaged over 1000 image pairs.

The effects of Brownian-induced particle mismatch were studied by generating datasets consisting of pairs of synthetic images separated by different time intervals δt with constant $D_\infty = 5.13 \times 10^{-12}$ m^2/s and $U = 40$ μm/s; these values correspond to typical values for the experimental data. Brownian-induced mismatch, quantified by the number of mismatched particles, will obviously increase with δt. For each dataset studied here, 1000 synthetic image pairs were created and processed using in-house nPIV software that implements a direct cross-correlation method with a Gaussian peak finding algorithm for sub pixel accuracy. The processing parameters such as window size and overlap were similar to those used for processing the experimental images.

For each image pair, the displacement error between the displacement obtained from the nPIV software and the actual displacement given by $U(\delta t)$ was calculated. Figure 5 shows this error ε averaged over 1000 image pairs as a function of the mismatched particle pairs ξ (given here as the percentage of the total number of particle pairs) in each image pair. Surprisingly, the results demonstrate that the average displacement error remains very small (less than 0.01 pixels, *vs.* displacements up to 3 pixels) for $\xi \leq 60\%$, or a value where a majority of the tracer particles dropin or dropout due to Brownian diffusion.

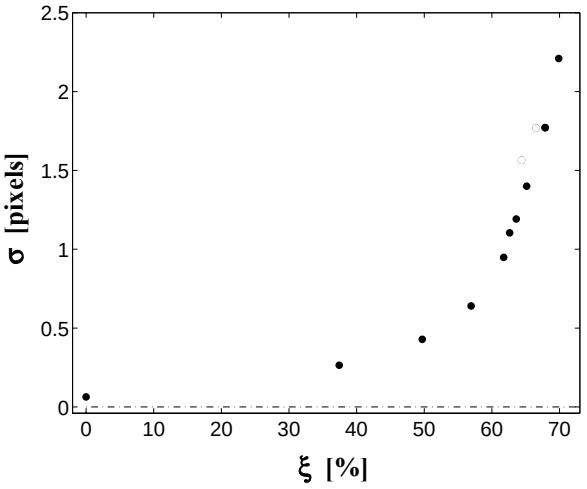

Figure 6: Standard deviation of the estimated mean displacement as a function of particle mismatch for nPIV processing.

Figure 6 shows σ, or the standard deviation in the displacement error calculated over 1000 image pairs, as a function of ξ. As expected, the standard deviation increases as ξ increases due to two factors: first, an

increase in the number of mismatched particle pairs reduces the SNR of the cross-correlation peak and hence introduces errors in estimating particle displacement; second, the Brownian rms displacement also increases with ξ for these synthetic images, increasing the standard deviation. Minimizing the time interval between images within the pair to minimize Brownian-induced particle mismatch will therefore reduce σ, and hence the number of images required to obtain an average displacement (for steady flows) with reasonable accuracy.

The results obtained in this initial study considering the "worst case" of unconfined Brownian diffusion in synthetic images suggest that the error in the actual nPIV data due to Brownian diffusion-induced particle mismatch is very small—less than 0.5%—for uniform steady flow data averaged over a large number of realizations. Given that the average number of particles in each interrogation window is about 30 in both the synthetic and experimental images for these relatively large windows, 60% mismatch suggests that there still remain at least 12 matched particle pairs in each window—or enough particle pairs, based upon macroscale PIV analyses, to obtain a cross-correlation peak with reasonable SNR [21].

EXPERIMENTAL RESULTS

Figure 7 shows typical nPIV velocity vectors (consisting only of the two components parallel to the channel wall) averaged over an entire dataset of 1000 consecutive images or 999 image pairs for the case shown in Figure 3. As expected, the EOF is essentially uniform over the field of view, since the EDL thickness $\lambda < 9$ nm for all the cases studied here [15], and these velocity data are averaged over the 100 nm adjacent to the wall.

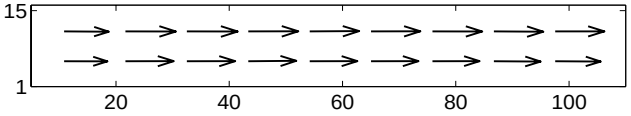

Figure 7: Time-averaged velocity vectors (parallel to the wall) for the case shown in Figure 3. These vectors correspond to an average bulk flow velocity U = 59 μm/s. The x- and z-dimensions are given in μm.

Given that the results are for uniform and steady EOF, the nPIV measurements are presented in terms of the velocity averaged both over time and the entire field of view, or essentially the bulk flow velocity U outside the thin EDL. Figure 8 plots the bulk velocity magnitude as a function of driving electric field E for a buffer molar concentration C = 18.4 mM. This Figure verifies that U varies linearly with E as predicted by Equation (1), with the dashed line giving the best fit to the data obtained from a linear regression analysis.

The error bars on the datapoints, which are the averaged results from several independent experiments, represent 95% confidence intervals [22]. The size of these error bars—typically 10%—and the analysis of the previous Section suggest that the errors due to Brownian diffusion-induced particle mismatch are a minor source of error in these data.

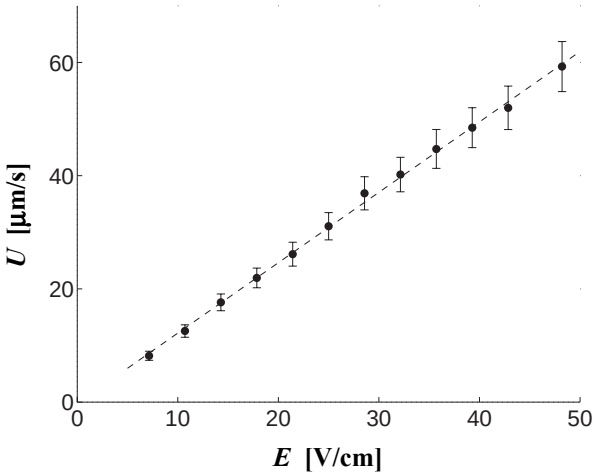

Figure 8: Plot of bulk EOF velocity U as a function of driving electric field E for C = 18.4 mM sodium tetraborate buffer.

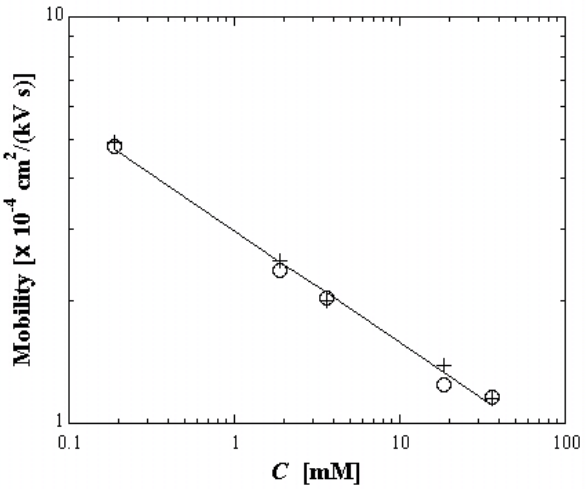

Figure 9: Log-log plot of mobility values calculated from the nPIV data (○) and predicted by Equation (6 (+) as a function of buffer molar concentration C.

The slope of the experimental data then represents the mobility μ_{ex} of these particles due to EOF and electrophoresis. Figure 9 summarizes the experimental results for the mobility for all the cases described in Table 1, and compares the mobility values calculated from the nPIV data with the electroosmotic mobility μ_{eo} predicted by Conlisk [6]:

$$\mu_{eo} = \frac{U}{E} = \frac{\varepsilon_e RT}{2\mu F} \ln\left\{\frac{g^0}{f^0}\right\} \tag{6}$$

The experimental values and model predictions for mobility are in very good agreement—within 4% in all cases except at C = 18.4 mM, where the discrepancy is 9%. The effect of electrophoresis on the particle mobilities obtained from the nPIV data appears therefore to be minimal. The scatter in the model values is likely due to small errors in the iterative scheme used to calculate (f^0, g^0). Moreover, the results from this log-log plot suggest that mobility has a power-law dependence upon buffer molar concentration. A power-law curve-fit to both the model predictions and the experimental values gives (solid line in Figure 9):

$$\mu = \left(2.98\times10^{-4}\ \frac{\text{cm}^2}{\text{V}\cdot\text{s}}\right)\left\{\frac{C}{1\ \text{mM}}\right\}^{-0.28} \tag{7}$$

CONCLUSIONS

The new nano-particle image velocimetry technique was applied to electroosmotic flow driven by electric fields up to 50 V/cm of dilute sodium tetraborate buffer through fused silica rectangular microchannels with a minimum dimension of 5–25 μm. The two components of velocity parallel to the channel wall were measured within about 100 nm of the wall using 100 nm fluorescent tracer particles. The mobility values obtained from the nPIV results are in very good agreement with independent analytical predictions for buffer concentrations varying by more than two orders of magnitude. Moreover, the results suggest that the electroosmotic mobility has a power-law dependence upon concentration.

To our knowledge, these results are the first near-wall measurements with this level of spatial resolution in steady fully-developed EOF in this geometry. Moreover, we are unaware of any other studies suggesting that electroosmotic mobility has a power-law dependence on buffer molar concentration. These results therefore demonstrate the utility and accuracy of the nPIV technique. We plan next to use nPIV to study EOF in these geometries driven by a time-periodic electric field.

An important issue in nPIV applications is tracer particle mismatch in consecutive images due to Brownian diffusion normal to the wall. An initial study of this error was carried out using synthetic images generated under the "worst case" assumption of unconfined (*vs.* hindered) Brownian diffusion. The nPIV results obtained from processing these synthetic images suggest that the error due to these effects is quite small for the large interrogation windows used in these studies of steady uniform EOF. We plan next to extend these analyses to hindered Brownian diffusion and shear flows and to use synthetic images to evaluate various processing algorithms developed for both μPIV and macroscale PIV in order to optimize the accuracy, robustness and in-plane spatial resolution of nPIV.

ACKNOWLEDGEMENTS

This work was funded by DARPA DSO under agreement F30602-00-2-0613. We thank H. Li for his analyses of the synthetic images; A. T. Conlisk and Z. Zheng at the Ohio State University for sharing the results of their analytical model and numerous discussions; and J. P. Alarie, S. Jacobson, and J. M. Ramsey of the Oak Ridge National Laboratories for the microchannel used in these measurements and their advice.

REFERENCES

[1] Santiago, J. G., Wereley, S. T., Meinhart, C. D., Beebe, D. J. and Adrian, R. J., 1998, "A Particle Image Velocimetry System for Microfluidics," Expts. Fluids, 25, pp. 316–319.

[2] Stone, S., Meinhart, C. D. and Wereley, S. T., 2002, "Out of Plane Spatial Resolution of Volume Illumination PIV," Bull. Am. Phys. Soc., 47(10), p. 49.

[3] Tretheway, D. C. and Meinhart, C. D., 2002, "Apparent Fluid Slip at Hydrophobic Microchannel Walls," Phys. Fluids, 14, pp. L9–L12.

[4] Zettner, C. M. and Yoda, M., 2003, "Particle Velocity Field Measurements in a Near-Wall Flow Using Evanescent Wave Illumination," Expts. Fluids, 34, pp. 115–121.

[5] Sadr, R., Zheng, Z., Yoda, M. and Conlisk, A. T., 2003, "An Experimental and Modeling Study of Electroosmotic Bulk and Near-Wall Flows in Two-

Dimensional Micro- and Nanochannels," ASME paper IMECE2003-42917.
[6] Rice, C. L. and Whitehead, R., 1965, "Electrokinetic Flow in a Narrow Capillary," J. Phys. Chem., 69, pp. 4017–4024.
[7] Levine, S., Marriott, J. R. and Robinson, K., 1975, "Theory of Electrokinetic Flow in a Narrow Parallel-Plate Channel," J. Chem. Soc., Faraday Trans. II, 71, 1–11.
[8] Yang, C., Li, D. and Masliyah, J. H., 1998, "Modeling Forced Liquid Convection in Rectangular Microchannels With Electrokinetic Effects," Int. J. Heat Mass Transfer, 41, 4229–4249.
[9] Conlisk, A. T., McFerran, J., Zheng, Z. and Hansford D. J., 2002, "Mass Transfer and Flow in Electrically Charged Micro- and Nano-channels," Anal. Chem., 74, pp. 2139–2150.
[10] Zheng, A., Hansford, D. and Conlisk, A. T., 2003, "Effect of Multivalent Ions on Electroosmotic Flow in Micro- and Nanochannels," Electrophoresis, 24, pp. 3006–3017.
[11] Paul, P. H., Garguilo, M. G. and Rakestraw, R., 1998, "Imaging of Pressure- and Electrokinetically Driven Flows Through Open Capillaries," Anal. Chem., 70, 2459–2467.
[12] Herr, A. E., Molho, J. I., Santiago, J. G. Mungal, M. G., Kenny, T. W. and Garguilo, M. G., 2000, "Electroosmotic Capillary Flow With Nonuniform Zeta Potential," Anal. Chem., 72, 1053–1057.
[13] Sinton, D. and Li, D., 2003, "Electroosmotic Velocity Profiles in Microchannels," Colloids and Surfaces A: Physicochem. Eng. Aspects, 222, 273–283.
[14] Cummings, E. B., 2002, "A Comparison of Theoretical and Experimental Electrokinetic and Dielectrophoretic Flow Fields," AIAA paper 2002–3193.
[15] Sadr, R., Yoda, M., Zheng, Z. and Conlisk, A. T., 2003, "An Experimental and Analytical Study of Electroosmotic Flow in Rectangular Microchannels," Submitted to J. Fluid Mech.
[16] Axelrod, D., Burghardt, T. P. and Thompson, N. L., 1984, "Total Internal Reflection Fluorescence," Ann. Rev. Biophys. Bioeng., 13, 247–268.
[17] Wereley, S. T., Gui, L. and Meinhart, C. D., 2002, "Advanced Algorithms for Microscale Particle Image Velocimetry," AIAA J., 40, 1047–1055.
[18] Raffel, M., Willert, C. and Kompenhans, J., 1998, Particle Image Velocimetry: A Practical Guide, Springer, New York
[19] Einstein A.., 1905, Ann. Phys. (Leipzig), 17, p. 549 [English translation reprinted in *Albert Einstein, Investigations on the Theory of Brownian Movement,* edited by R. Furth (Dover, New York, 1956)].
[20] Bevan, M. A. and Prieve, D. C., 2000, "Hindered Diffusion of Colloidal Particles Very Near to a Wall: Revisited", J. Chem. Phys., 113, pp. 1228–1236.
[21] Keane, R. D. and Adrian, R. J., 1991, "Optimization of Particle Image Velocimeters. II. Multiple Pulsed Systems," Meas. Sci. Technol., 3, pp. 963–974.
[22] Kline, S. J., 1985, "The Purpose of Uncertainty Analysis," ASME J. of Fluids Eng., 107, pp. 153–260.

42nd AIAA Aerospace Sciences Meeting
Reno, Nevada
AIAA 2004-0930
January 5-8, 2004

Appendix F:

On the Synthetic Ion Channel Problem *

Kelly Evers
Jennifer McFerran
A. T. Conlisk †
Department of Mechanical Engineering
The Ohio State University
Columbus, Ohio 43210-1107

ABSTRACT

Natural ion channels are ion-selective nanoscale conduits in the body which allow nutrients in and waste products out. In this paper we consider synthetic ion channels consisting of rectangular silicon channels for which the walls are negatively charged. Variations in the streamwise flow direction are considered by averaging the flow properties across the channel and the influence of the electric double layers (EDLs) on the channel walls(i.e. fixed charges) is identified; this feature of the problem is neglected in the work of Barcilon *et al.*[1] Asymptotic methods are employed to obtain full analytical solutions for the potential and the concentrations. Results are also obtained numerically for a two component and three component ionic solution. The results for the two-component system are compared to the results published by Barcilon *et al.*[1] and the comparison is very good. We can consider ionic species of arbitrary valence. The three-component problem is employed to model biomolecular transport of albumin and glucose and numerical results are compared with experimental data.

INTRODUCTION

Nanopumps used to transport fluids through nanochannels are essentially ion channels. This device in which the channel walls are usually made of silicon is termed a synthetic ion channel. The governing equations and boundary conditions are the same as for the natural ion problem.[2] There are a large number of references on this problem, and the references cited here are chosen because they have significantly influenced the development of this work. A nanopump fabricated by iMEDD, Inc. of Columbus, Ohio(Sketch supplied by A. Boiarski) is depicted on Figure 1. The channels are of dimension $W \sim 44\mu m$, $L \sim 3.5\mu m$ and channel heights $h \sim 4 - 50nm$. Thus the channels are nano-constrained in one dimension.

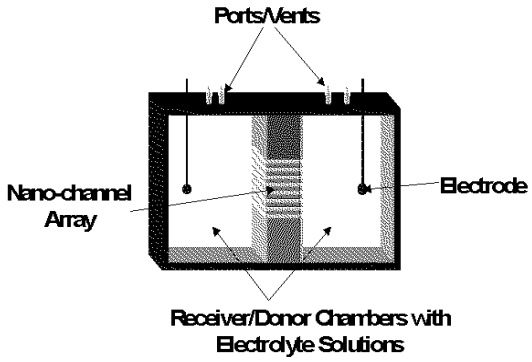

Figure 1: iMEDD, Inc of Columbus electroosmotic pump.

Natural ion channels play a crucial role in the transport of biofluids into and out of cells. The basic units of all living organisms are cells. In order to keep the cells func-

* Supported by DARPA.

† Corresponding author E.Mail: conlisk.1@osu.edu.

tioning properly a continuous flux of ions in and out of the cell and the cell components is required. The cell is surrounded by a plasma membrane which provides selective transfer of ions. The membrane is made up of a double layer of lipid molecules (lipid bilayer) in which proteins are embedded. The lipid molecules are made up of a charged polar end (spheres in Figure 2), oriented towards the surface of the membranes, which are attached to two nonpolar fatty acid chains (lines attached to the spheres in Figure 2). The polarity of the membrane makes it challenging for molecules to move in and out of cells and its components. Ions (Ca^{2+}, Cl^{-}, K^{+}, Na^{+}, H^{+}, Mg^{2+}, HCO_3^{-}, PO_4^{2-}) selectively move through the membrane via ion channels made of proteins. These protein channels are made up of a polypeptide chain with two polar regions connected by a nonpolar region which associates with the nonpolar region of the phospholipids membrane. Natural ion channels are roughly circular, although the cross-sectional area varies in the primary flow direction.[3]

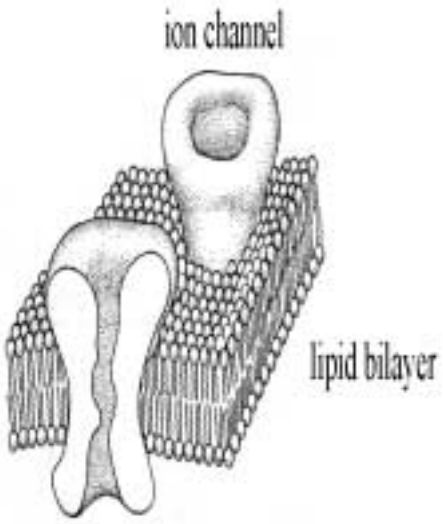

Figure 2: Image of ion channels within the lipid bilayer. (http://hebb.mit.edu/courses/8.515/lecture1/sld013.htm, 3/11/03)

Synthetic ion channels are of interest because they can be used as pumps to deliver a drug, for example, to a target site. The iMEDD, Inc. nanochannel membrane is essentially an array of synthetic ion channels. In this paper we present an asymptotic analysis of the problem supplemented by numerical solutions of the one-dimensional Poisson-Nernst-Planck equations for a two component ionic solution as well as a three component ionic solution; the program is valid for ions of arbitrary valence. The two-component results are compared to the results obtained by Barcilon *et al.*[1] The three-component system is then used to determine the effect that additional ions have on the flow through an ion channel. The three-component system is also used to model biomolecular transport of albumin and glucose, and numerical results are compared with experimental data.

There are hundreds of papers on ion channels and most of them assume that the transport is governed by one-dimensional equations, with the single dimension in the direction of the flow of ionic species.[4] The three dimensional problem has been considered by Cardenas *et al.*[5] A relatitively complicated mathematical derivation of the one-dimensional governing equations from the full three-dimensional equations is given by Gillespie.[3] Essentially, Gillespie[3] shows that the one-dimensional form of the equations arises from an averaging process along given curves on which the concentration and potential are constant. The purpose of this paper is to show that the same equations arise by a simple integration across the channel. In the process we show that the fixed charge on the side wall may be modeled analytically using the Debye-Huckel approximation. The fixed charges on the side walls are neglected in the work of Barcilon *et al.*[1] We will also compare our computational results with experimental data describing biomolecular transport in a synthetic nanochannel membrane.

BACKGROUND

Natural ion channels are one class of membrane transport proteins and are narrow, water-filled tunnels, permeable to the few ions and molecules small enough to fit through the tunnels (approximately 10 Å in diameter).[6] Ion channels present in excitable membranes are a common pore protein channel. Ion channels are responsible for electrical signaling in nerves and muscles.[7] The ions responsible for the majority of nervous signaling are Ca^{2+}, Cl^{-}, K^{+}, and Na^{+}. The channels are responsive to different stimuli: a membrane potential change, a neurotransmitter or other chemical stimulus, a mechanical deformation, and more. The channel's response to these stimuli, called gating, corresponds to an opening or closing of the pore. The open pore has a selective permeability to ions, only allowing certain ions to flow through its electrochemical activity gradients. The ions flow at a very high rate, greater than 10^6 ions per second, with a single ion taking on the order of one microsecond to traverse the channel.

According to Levitt,[4] five major methods of modeling ion channels have appeared in the literature: molecular dynamics, three-dimensional Brownian dynam-

ics, three-dimensional Poisson-Nernst-Planck (PNP), one-dimensional Brownian dyanamics, and the one-dimensional Poisson-Nernst-Planck approach. It has been suggested often in the literature that if the channel properties are known to an atomic level then the most direct method is molecular dynamic simulations, because they take into consideration the atomic structure of the water molecules and channel proteins. The weakness of this method is the computation time; a simulation of an acetylcholine channel took approximately one year for a single ion crossing (in 1998!). This long computation time is due to the fact that molecular simulation can only describe nanoseconds of real time, which is not long enough for modeling ion movement through the entire channel which takes place on the microsecond scale. Molecular dynamic simulations can be simplified by using advanced computational techniques. These techniques include alchemical free energy perturbation and umbrella sampling.

In three-dimensional Brownian dynamics, the protein structure is held fixed and the water molecules within the channel are treated as a continuum. The advantage of this method is that the ion-ion interactions are still taken into consideration. According to Levitt,[4] the best method of modeling ion channels is a combination of molecular dynamics and Brownian dynamics. The three-dimensional Poisson-Nernst-Planck approach simplifies the Brownian dynamic approach by averaging the electric field on an ion over all the possible positions of the other ions. This average electric field is calculated using Poisson's equation. The Poisson equation is coupled with the Nernst-Planck equation, which models ions undergoing Brownian motion in the electric field. This approach is much faster than Brownian dynamics because it replaces a sequence of time step calculations with a global numerical solution. The disadvantage of this method is that the ion-ion interactions are reduced to a ion-mean field interaction.

The Brownian dynamic and Poisson-Nernst-Planck approaches can be further simplified by averaging the concentration over the cross section. However, Levitt[4] notes that it is difficult to quantify this approximation and its range of validity is not known. One of the objectives of this paper is to quantify this aproximation. It has been observed that in most circumstances this assumption does not generate much error, because it often cancels out the error introduced by uncertainties in atomic channel structure.

The continuum electrostatic Poisson-Boltzmann (PB) theory treats the polar solvent as a structureless dielectric medium and illustrates the fundamental principles of ion permeation. The standard PB theory can be expanded to incorporate the transmembrane voltage.[8]

Many models have been developed for ion channel flow.

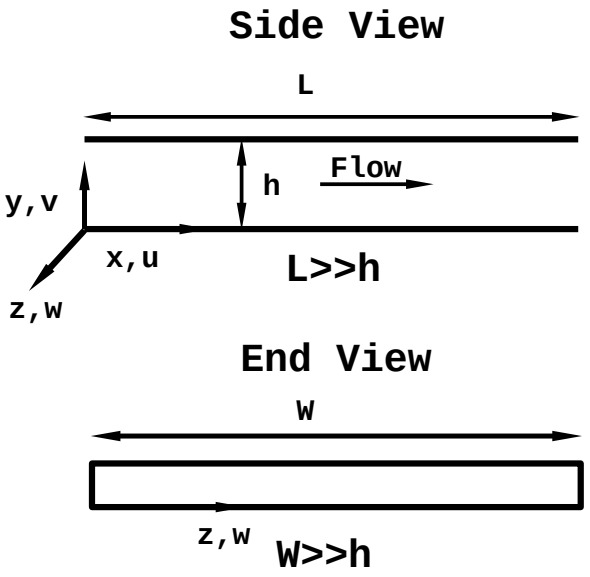

Figure 3: Geometry of the channel. Here it is only required that $h << W$ where W is the width of the channel; the length L in the primary flow direction can be of the order of the channel height or much smaller as depicted in the figure. u, v, w are the fluid velocities in the x, y, z directions.

However, most of these models are based on molecular dynamics. The use of Poisson-Nernst-Planck equations to model ion channels began in the early 1990s with Chen *et al.*[2] This model has been used to model Ca^{2+} channels[9,10] as well as Gramicidin channels.[11] In addition to simply modeling the flow within the channel, these models usually incorporate the flow within the baths on each end of the channel.[3,12] Non-ideal effects which occur at higher electrolyte concentration levels have recently been examined by Gillespie *et al.*[13]

GOVERNING EQUATIONS

PNP Equations

For simplicity we consider a channel which is rectangular in cross-section as depicted in Figure 3. The potential through a very wide ion channel (Figure 1) is controlled by the two-dimensional Poisson equation,

$$\epsilon^2 \left\{ \frac{\partial^2 \phi}{\partial y^2} + \left(\frac{h}{L}\right)^2 \frac{\partial^2 \phi}{\partial x^2} \right\} = -\sum z_i x_i \qquad (1)$$

where z_i are the valences and x_i are concentrations. Consider the case of two electrolyte species: p and n, and $\epsilon = \frac{\lambda}{h}$.

Here λ is the electric double layer thickness. We assume that x is the flow direction and we note that if $h >> L$ then the one dimensional ion channel equations emerge as an approximate system of equations without averaging. On the other hand if $h \sim L$ or $h << L$ then averaging is necessary to formally obtain the one-dimensional equations.

We consider only the two-dimensional equations; however, it is clear how to extend the analysis to three-dimensions. Integrating equation (1) across the channel,

$$\epsilon^2 \left\{ \left.\frac{\partial \phi}{\partial y}\right|_1 - \left.\frac{\partial \phi}{\partial y}\right|_0 + \left(\frac{h}{L}\right)^2 \frac{\partial^2 \bar{\phi}}{\partial x^2} \right\} = -\left(z_p \bar{p} + z_n \bar{n}\right). \tag{2}$$

A bar over a variable stands for the average of that variable along y,

$$\bar{s} = \int_0^1 s dy \tag{3}$$

where s is any function. Equation (2) may be simplified to

$$\epsilon_1^2 \frac{\partial^2 \bar{\phi}}{\partial x^2} = -\left(z_p \bar{p} + z_n \bar{n}\right) - 2\epsilon^2 \sigma_0 \tag{4}$$

where $\epsilon_1 = \frac{\lambda}{L}$ where λ is the electric double layer thickness. Also σ_0 is the surface charge density at $y = 0$

$$\sigma = \sigma_0 = \frac{\partial \phi}{\partial y}(0) = \sigma_1$$

if the flow is symmetric about the centerline of the channel. For simplicity we have taken $\sigma > 0$ and the actual surface charge density is $-\sigma$. Here σ is dimensionless and

$$\sigma = \frac{\sigma^*}{\frac{\epsilon_e RT}{F\lambda}}$$

σ^* is the dimensional surface charge density in C/m^2. Here F is Faraday's constant, ϵ_e is the permittivity, R is the universal gas constant and T is temperature.

The ion concentrations within the channel are controlled by the Nernst-Planck equation,

$$\frac{\partial}{\partial y}\left(\frac{\partial p}{\partial y} + z_p p \frac{\partial \phi}{\partial y}\right) + \left(\frac{\lambda}{L}\right)^2 \frac{\partial}{\partial x}\left(\frac{\partial p}{\partial x} + z_p p \frac{\partial \phi}{\partial x}\right) = 0 \tag{5}$$

where z_p is the valence of the positive ion. This same equation can be applied to the negative ion species (n). Integrating equation (5) over y,

$$\left(\frac{\partial p}{\partial y} + z_p p \frac{\partial \phi}{\partial y}\right)\Big|_0^1 + \epsilon_1^2 \left(\frac{\partial}{\partial x}\frac{\partial \bar{p}}{\partial x} + z_p \frac{\partial}{\partial x}\int_0^1 p \frac{\partial \phi}{\partial x} dy\right) = 0. \tag{6}$$

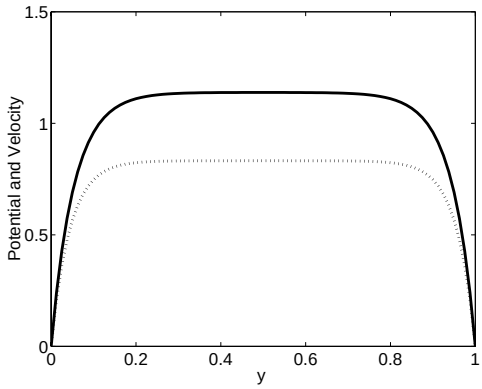

Figure 4: Results for the dimensionless velocity and potential magnitudes for the symmetric case of a two-component electrolyte aqueous mixture. Here the electric field corresponds to 0.06 volts over a channel of length $L = 3.5\mu m$; the channel height $h = 24\ nm$. The dash line is the Debye-Huckel approximation. Here the wall mole fractions of the anion and cation respectively are $n^0 = n^1 = 0.00025$ and $p^0 = n^1 = 0.00276$.

The first term vanishes because there is no flux of p at the walls $y = 0, 1$. The second term may be approximated by

$$\int_0^1 p \frac{\partial \phi}{\partial x} dy = \bar{p} \frac{\partial \bar{\phi}}{\partial x} \tag{7}$$

if the variables are not functions of y. On the scale of the channel height, both p and ϕ are functions of y; however for small h/L, on the scale of the channel length, the channel height approaches zero, and from Taylor series considerations, both p and ϕ can be considered constant. Thus,

$$\frac{\partial}{\partial x}\left(\frac{\partial \bar{p}}{\partial x} + z_p \bar{p} \frac{\partial \bar{\phi}}{\partial x}\right) = 0. \tag{8}$$

For $\sigma_0 = 0$, these are the equations used by Barcilon *et al.*[1]

To calculate the surface charge density, we can assume that the Debye-Huckel approximation, valid for potential below $26mV$, holds. To demonstrate this, Figure 4 shows results for the full solution[14–16] compared with the Debye-Huckel approximation. Note that while the Debye-Huckel approximation does not hold in the core of the channel, the slope at the wall is the same for each case. The same is true at smaller channel heights(Figure 5).

It is easily shown that the dimensionless surface charge density is[14]

$$\sigma_0 = -\frac{1}{\epsilon^2} \frac{\sum_{i=1}^N z_i X_i^0}{\sum_{i=1}^N z_i^2 X_i^0} tanh(\frac{1}{\epsilon}) \tag{9}$$

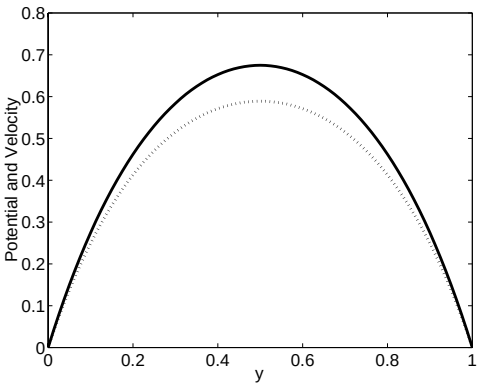

Figure 5: Results for the dimensionless velocity and potential for the symmetric case of a two-component electrolyte aqueous mixture. Here the electric field corresponds to 0.06 volts over a channel of length $L = 3.5\mu m$; the channel height $h = 4\ nm$. The solid lines are the numerical solution and the dash lines are the Debye-Huckel Approximation. Here the wall mole fractions of the anion and cation respectively are $n^0 = n^1 = 0.00025$ and $p^0 = p^1 = 0.00276$.

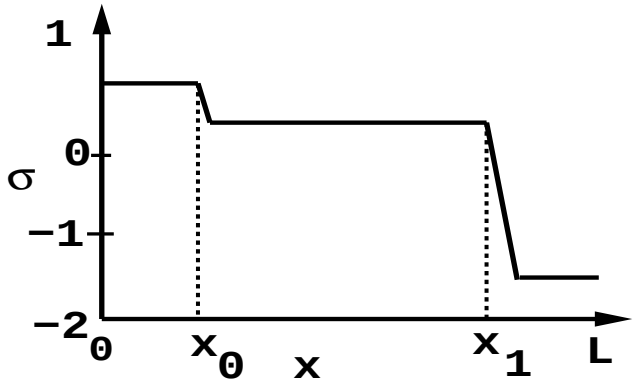

Figure 6: Sketch of the fixed charge on the side wall as depicted in Chen *et al.*[17] The units of the charge are in Molar.

where the X_i are the concentrations scaled by ionic strength and N is the number of species. Thus the correction term is O(1). As seen in equation (4) the presence of the fixed charge term leads to a parabolic correction. In practice, however as noted by Chen *et al.*[17] the surface charge distribution is not constant but varies along the channel. It turns out that for many channels, the surface charge density is piecewise constant as shown on Figure 6.[17] The scale shown is from Chen[17] for a synthetic protein channel called the LS channel. From this distribution it is seen that the correction term results in boundary layers near the entrance and exit of the channel. For the purposes of this paper we consider only the case where the fixed charge distribution is constant, effectively for $x_0 \leq x \leq x_1$.

For a three component solution (n, p, and n_2) ,

$$\epsilon_1^2 \phi'' - n - n_2 + p = -2\epsilon^2 \sigma_0, \tag{10}$$

where $\phi'' = \frac{d^2\phi}{dx^2}$, n, n_2, and p are the concentration of the negative ion, the second type of negative ion, and the positive ion scaled on ionic strength with the valences already incorporated($z_p = 1, z_n = -1, z_{n2} = -1$). Note that it does not matter which ionic strength is used for the scaling. Here we use the ionic strength at the downstream boundary $x = 1$. For simplicity, the average bars are removed from equation (10) and all of the following equations, but the variables are all still averages over y. A single prime denotes a first derivtive with respect to x, while a double prime denotes a second derivative with respect to x. Applying the same scaling factor and simplification to equation (8) and the other ions yields

$$n' - n\phi' = J_n \tag{11}$$

$$p' + p\phi' = -J_p \tag{12}$$

$$n_2' - n_2\phi' = J_{n_2}. \tag{13}$$

where J_i is the flux of ion i and is constant.

For ion channels, the concentrations of the ions at the inlet and outlet are determined by the concentrations within the baths on either side of the membrane. Therefore, the boundary conditions for the system are

$$p = p_L, \quad n = n_L, \quad n_2 = n_{2L}, \quad \phi = V, \quad x = 0 \tag{14}$$

$$p = p_R, \quad n = n_R, \quad n_2 = n_{2R}, \quad \phi = 0, \quad x = 1, \tag{15}$$

where the subscripts L and R refer to the left ($x = 0$) and right ($x = 1$) boundaries. It is useful to point out that averaging the continuity equation leads to the result that the average velocity is constant in x to maintain constant mixture flow rate.

Before comparing our numerical solutions with those of Barcilon,[1] we calculate the solution for the case of a three component solution.

ASYMPTOTIC ANALYSIS FOR A THREE COMPONENT SOLUTION

Here we obtain complete, explicit expressions for the ion channel model for a three-component ionic mixture. To our knowledge, this analysis has not been done. We will then use these solutions to model biomolecular transport. The full solution will be made up of an interior solution (far from the inlet and outlet), a left boundary layer solution, and a right boundary solution. The interior solution is denoted by a subscipt i, the left boundary layer solution is denoted by a subscript 0, and the right boundary layer is denoted by a subscript 1. The full solution is

$$S = S_0 + S_i + S_1 - common\ \ part \tag{16}$$

for any variable S, where 'common part' stands for the parts of the full solution that the separate parts have in common.

Here we present the case for an additional species of valence z_{n2} and concentration n_2 including the effect of the wall charge correction; for glucose or albumin the valence will be negative. For the interior solution (far from the inlet and outlet) we can set $\epsilon = 0$ and we have

$$p_i - n_{2i} - n_i = \sigma_c \tag{17}$$

where the subscript i represents the interior variable and $\sigma_c = -2\epsilon^2\sigma_0$. Note that if the wall charge is neglected the core of the channel is electrically neutral. Adding equations corresponding to (11) through (13) for the three-component mixture for the interior solution and using equation (17),

$$(n_i + p_i + n_{2i})' = J_n - J_p + J_{n2} - \sigma_c\phi_i' = J_1 - \sigma_c\phi_i' \tag{18}$$

Integrating equation (18) yields

$$n_i + p_i + n_{2i} = J_1(x + A) - \sigma_c\phi_i \tag{19}$$

Subtracting equations (11) through (13) for three components the interior solution and using equation (17),

$$(n_i + p_i + n_{2i})\phi_i' = -J_{n2} - J_p - J_n = J_2 \tag{20}$$

Substituting from equation (19)

$$(J_1(x + A) - \sigma_c\phi_i)\phi_i' = -J_{n2} - J_p - J_n = J_2 \tag{21}$$

If we neglect the wall correction, we can solve equation (20) for ϕ_i

$$\phi_i = \frac{J_2}{J_1}\ln(x + A) + B \tag{22}$$

This is the interior solution for the ion channel of the form presented by Barcilon[1] for a two-component mixture. The four unknowns (J_1, J_2, A, B) will be determined from the boundary layer solutions.

For the left boundary layer solutions (near x=0), a stretched variable is introduced, $\zeta = \frac{x}{\epsilon_1}$. The solutions are obtained by holding ζ fixed and letting ϵ_1 approach zero,

$$\phi_0'' - n_0 - n_{20} + p_0 = \sigma_c \tag{23}$$

$$n_0' - n_0\phi_0' = 0 \tag{24}$$

$$n_{20}' - n_{20}\phi_0' = 0 \tag{25}$$

$$p_0' + p_0\phi_0' = 0 \tag{26}$$

where the left boundary layer variable is indicated with a subscript 0 and is a function of ζ. Integrating the Nernst-Planck equations (equations (24) through (26)) over the boundary layer and applying the left boundary condition,

$$n_0 = n_L e^{\phi_0 - V} \tag{27}$$

$$n_{20} = n_{2L} e^{\phi_0 - V} \tag{28}$$

$$p_0 = p_L e^{-\phi_0 + V} \tag{29}$$

To match with the interior, the limit of left boundary layer equations as $\zeta \to \infty$ are matched to the limit of the interior equations as $x \to 0$, In the case where the correction is negligible this leads to

$$J_1 A = 2\sqrt{p_L n_{2L} + p_L n_L} \tag{30}$$

$$\frac{J_2}{J_1}\ln A + B = \frac{1}{2}\ln\frac{p_L}{n_L}\left\{\frac{n_L}{\left(1 + \frac{n_{2L}}{n_L}\right)(n_{2L} + n_L)}\right\}^{1/2} + V \tag{31}$$

There are now two equations and four unknowns. In order to complete the solution, the boundary layer solution at $x = 1$ needs to be calculated. The same procedure used for the left boundary is applied to the right boundary, yielding two more equations for the four unknowns,

$$J_1(A + 1) = 2\sqrt{p_R n_{2R} + p_R n_R} \tag{32}$$

$$\frac{J_2}{J_1}\ln(1 + A) + B = \frac{1}{2}\ln\frac{p_R}{n_R}\left\{\frac{n_R}{\left(1 + \frac{n_{2R}}{n_R}\right)(n_{2R} + n_R)}\right\}^{1/2} \tag{33}$$

The four unknowns can now be solved using equations (30) through (33). In particular the solution hinges critically on the value of the constant A. Solving we obtain

$$A = -\frac{\sqrt{p_L n_{2L} + p_L n_L}}{\sqrt{p_L n_{2L} + p_L n_L} - \sqrt{p_R n_{2R} + p_R n_R}} \tag{34}$$

In order for the solution to be physically acceptable $A > 0$ (see equation 22). This means that

$$\sqrt{p_L n_{2L} + p_L n_L} < \sqrt{p_R n_{2R} + p_R n_R}$$

and so it makes sense to scale the concentrations on the ionic strength at $x = 1$.

The equations for a two component system can be derived by setting n_2=0 in the above equations,

$$J_1 A = 2\sqrt{p_L n_L} \tag{35}$$

$$\frac{J_2}{J_1} \ln A + B = \frac{1}{2} \ln \frac{p_L}{n_L} + V \tag{36}$$

$$J_1 (1 + A) = 2\sqrt{p_R n_R} \tag{37}$$

$$\frac{J_2}{J_1} \ln (1 + A) + B = \frac{1}{2} \ln \frac{p_R}{n_R} \tag{38}$$

The solutions for A and J_1 are found by dividing equation (35) into (37),

$$\frac{1 + A}{A} = \sqrt{\frac{p_R n_R}{p_L n_L}} \tag{39}$$

and

$$A = \frac{\sqrt{p_L n_L}}{\sqrt{p_R n_R} - \sqrt{p_L n_L}} \tag{40}$$

$$J_1 = 2 \left(\sqrt{p_R n_R} - \sqrt{p_L n_L}\right) \tag{41}$$

The solutions for B and J_2 can now be solved by plugging A and J_1 into equations (36) and (38).

If the correction is not negligible, then equation (21) for the potential ϕ is more difficult to solve. However, progress can still be made. From the boundary layer solutions it is evident that

$$p_0 n_0 = p_L n_L \tag{42}$$

$$p_0 n_{20} = p_L n_{2L} \tag{43}$$

and using equation (17) in the limit $x \to 0$ where for example $n_i(0) = n_0(\infty)$ we find that

$$n_0(\infty) = n_i(0) = \frac{-\sigma_c(0) \pm \sqrt{\sigma_c(0)^2 + 4 p_L n_L \left(1 + \frac{n_{2L}}{n_L}\right)}}{2\left(1 + \frac{n_{2L}}{n_L}\right)} \tag{44}$$

where we must take the + sign since $n_0(\infty) > 0$. Similarly

$$p_0(\infty) = p_i(0) = \frac{\sigma_c(0) \pm \sqrt{\sigma_c(0)^2 + 4(p_L n_L + p_L n_{2L})}}{2} \tag{45}$$

and

$$n_{20}(\infty) = n_i(0) = p_0(\infty) - n_0(\infty) - \sigma_c(0) \tag{46}$$

Similar calculations may be made on the right boundary.

We can solve for p by adding equations (17) and (19) and the result is

$$p_i = \frac{1}{2} \left(J_1(x + A) + \sigma_c(1 - \phi_i)\right) \tag{47}$$

so that p_i is nearly linear in x; in the absence of the wall correction p_i is linear and this is seen in the numerical solutions.

For variable fixed charge as shown on Figure 6 there will be boundary layers at $x = 0$ and $x = 1$; equations (44) and (45) will have both left and right side limits around the boundary layers at the inlet and the outlet of the channel. In principle the interior solutions already calculated will be valid away from these boundary layers.

RESULTS

Two Component Solution

The two-component program asymptotic analysis can easily be obtained from the above solutions by setting the third-component quantities equal to zero. We will compare to results published by Barcilon *et al.*,[1] who models ion channels for a two component system using the one-dimensional Poisson-Nernst-Planck equations. We will be using concentrations ten times less than Barcilon since the equations are independent of scale. This will improve the accuracy of the results.

In all of the numerical results, 301 points are used which gives four figure accuracy with 601 points. Note that the numerical solutions do not require thin double layers, although the solutions presented here are for thin double layers in order to compare with the results of Barcilon *et al.*[1] Figures 7 and 8 compare the Barcilon *et al.*[1] results with the results obtained by the current model. Figure 7 shows the results of Barcilon *et al.*[1] Figure 8 shows our numerical results (indicated by 'num') and the Barcilon interior solution results (indicated by 'asym'). The comparison is good. These results presented here only model the ion flow through the ion channel and do not take into consideration the effects of the bath. The effects of the bath have been discussed by Chen *et al.*[2] and Gilliespie,[3] to name two references.

Three Component Solution

We first present results for constant surface charge density on the side walls. Figure 9(a) shows the result for an additional species of valence -1; in these results we assume the correction is zero. The dash dot line in the potential

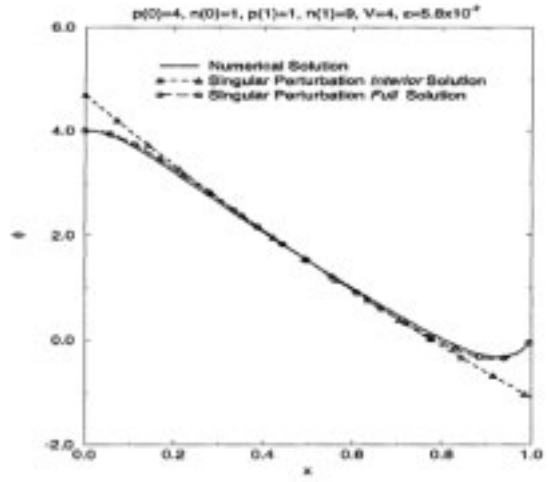

(a)

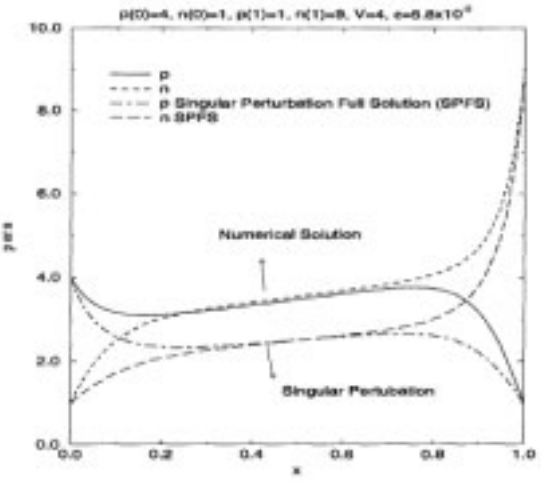

(b)

Figure 7: Barcilon *et al.*[1] potential and concentration results for the boundary conditions pL=4, nL=1, pR=1, nR=9, V=4, ϵ=5.8x10^{-2}. (a) Dimensionless potential. (b) Dimensionless concentrations.

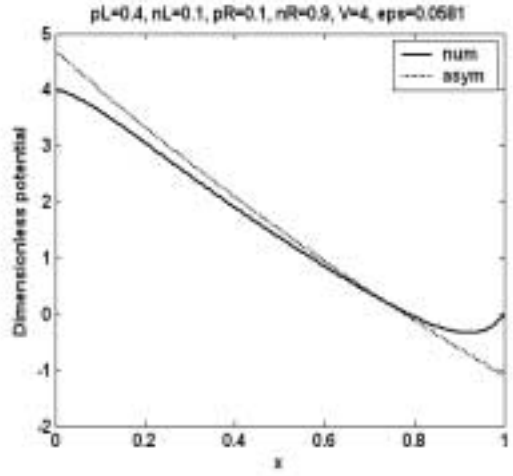

(a)

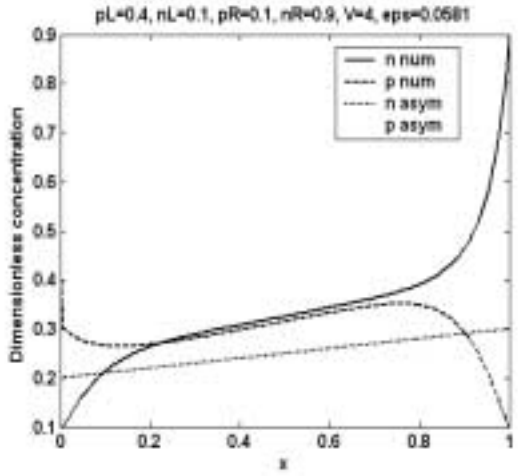

(b)

Figure 8: Dimensionless potential and concentration results for the boundary conditions pL=0.4, nL=0.1, pR=0.1, nR=0.9, V=4, ϵ=5.8x10^{-2}, Number of points = 301. (a) Dimensionless potential. (b) Dimensionless concentrations. The straight line is the interior asymptotic solution.

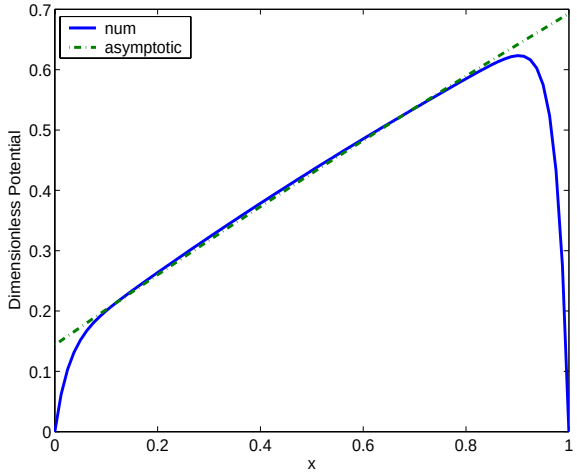

(a)

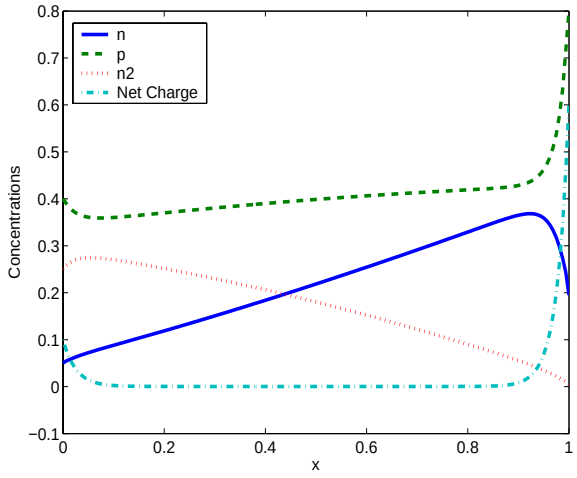

(b)

Figure 9: Concentration and potential results for the three component solution for constant surface charge density for the length of the channel $L = 20$ nm. Boundary conditions: $p_L = 0.4, n_L = 0.05, n_{2L} = 0.25, p_R = 0.8, n_R = 0.195, n_{2R} = 0.005, V = 0$. (a) Potential (b) Concentrations.

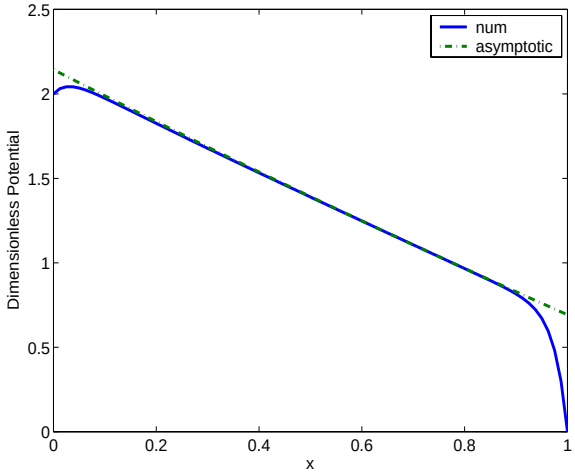

(a)

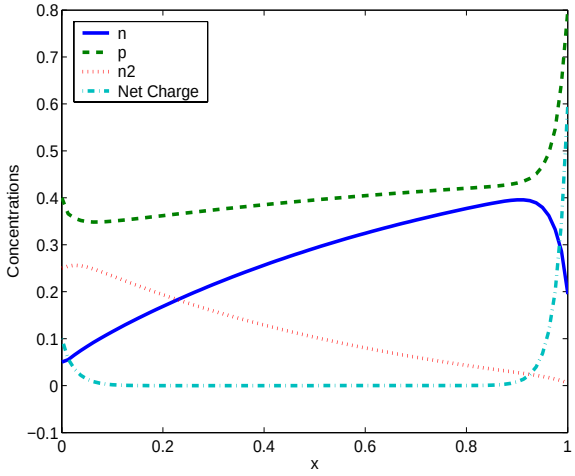

(b)

Figure 10: Concentration and potential results for the parameters of Figure 9, except $V = 2$. (a) Potential (b) Concentrations.

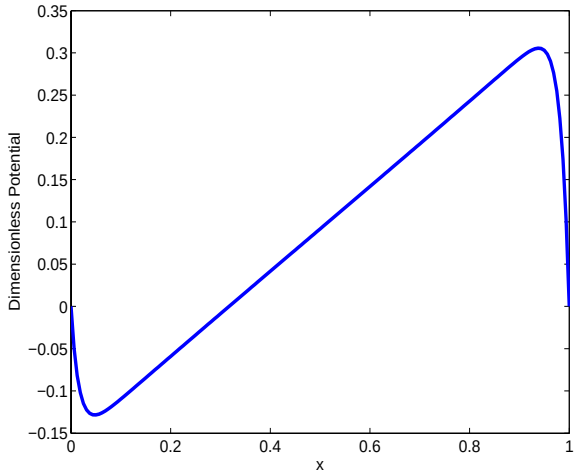

(a)

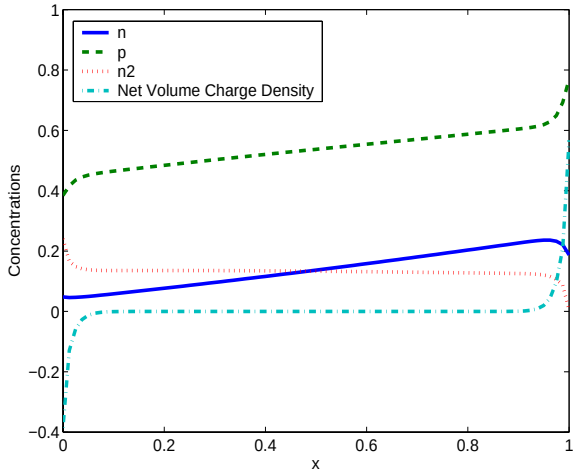

(b)

Figure 11: Concentration and potential results for the paremeters of Figure 9 except the valence $z_{n2} = -3$. (a) Potential (b) Concentrations.

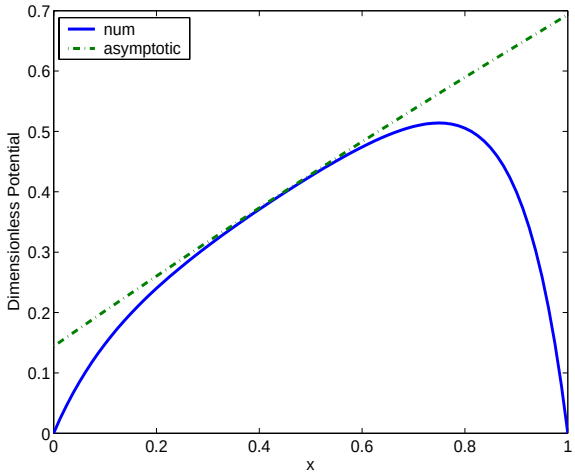

(a)

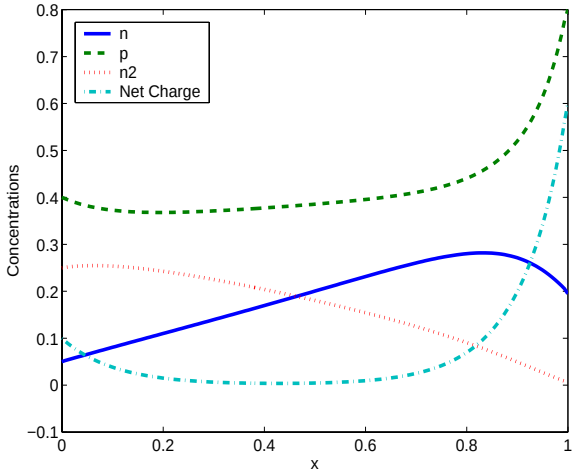

(b)

Figure 12: Concentration and potential results for the paremeters of Figure 9 except the length of the channel $L = 5nm$. (a) Potential (b) Concentrations.

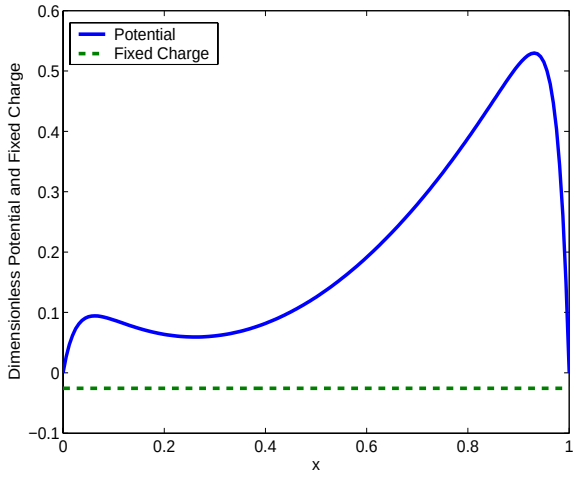

(a)

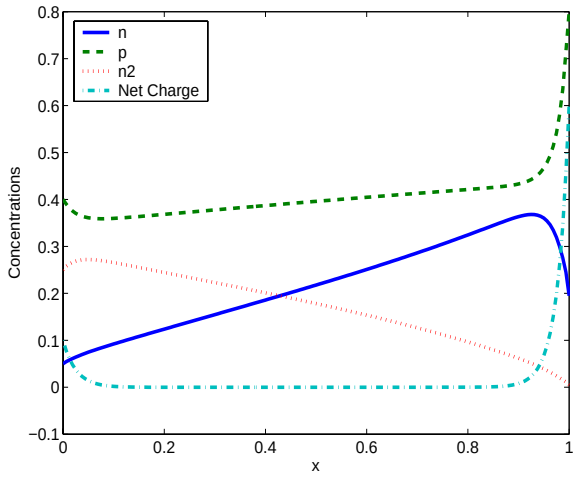

(b)

Figure 13: Concentration and potential results for the paremeters of Figure 9 including the effect of permanent or fixed charge. Here the wall concentrations scaled by ionic strength at $x = 0$, $p^0 = 2.0$, $n^0 = 1.9$. The length $L = 20nm$. (a) Potential (b) Concentrations.

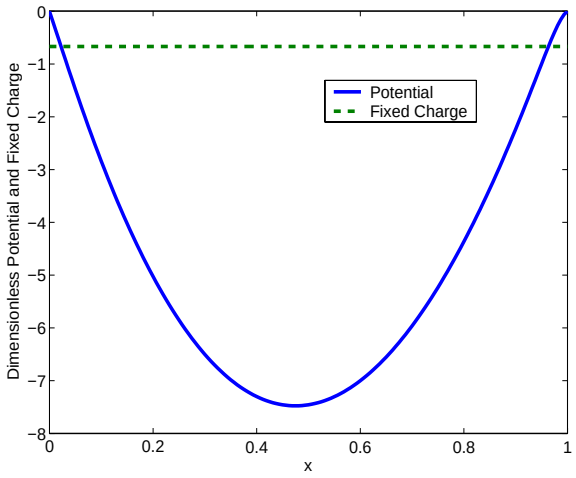

(a)

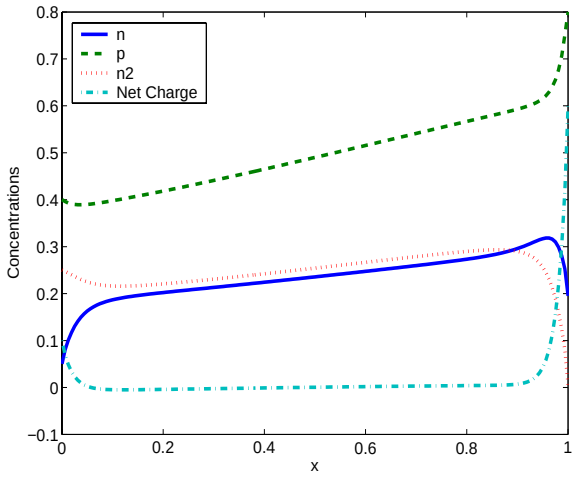

(b)

Figure 14: Concentration and potential results for the paremeters of Figure 9. including the effect of permanent or fixed charge. Here the wall concentrations scaled by ionic strength at $x = 0$, $p^0 = 2.0$, $n^0 = 0.4$. The length $L = 20nm$. (a) Potential (b) Concentrations.

curve is the asymptotic result in the interior. The channel length is $L = 20nm$ and the EDL thickness is based on the ionic strength at $x = 0$. Note that the core of the channel is electrically neutral as noted by the net volume charge density curve.

Figure 10 shows results for the same parameters as on Figure 9 except now there is a potential drop of $V = 2$ across the channel. On Figure 11 are results for the parameters of Figure 9 except that the valence of the third species is $z_{n2} = -3$. On Figure 12 are results for the parameters of Figure 9 except the length of the channel is $L = 5nm$. Note now that the core of the channel is not electrically neutral.

It is useful to note that if the upstream and downstream concentrations are chosen to satisfy electroneutrality at $x = 0, 1$ there are no boundary layers and all of the quantities are linear with x.

We now look at the case where the surface charge density correction is not zero. On Figure 13 are results for the case of Figure 9 with the correction added in. Here we note that the sidewall mole fractions are not that different yet there is a large difference in the potential profile.

On the other hand, when there is significant difference in the mole fractions there is both a significant difference in the potential and the mole fractions as noted in Figure 14. These results show that the potential is extremely sensitive to the fixed charge distribution.[9]

BIOMOLECULAR TRANSPORT

We have used the synthetic ion channel model to predict the flow rate of bovine serum albumin(BSA) through an iMEDD nano pore membrane. The device is shown on Figure 1. The concept of hindered transport to large, complex macromolecules such as DNA has been discussed by Davidson and Deen.[18] Hindered diffusion is the term applied to the mass transfer process in which the diffusion coefficient depends on the ratio of the species size to the smallest dimension of the device and is much less(up to several orders of magnitude) than the diffusion coefficient when the ratio of the molecule size to the channel dimension approaches zero. Experimental research has also been conducted on the transport of DNA through microdevices similar to the one considered in this work.[19,20]

The hindered diffusion models are of the form

$$D_H = C(a, y_p) D_A$$

where $C < 1$ and a is the molecular size, and y_p is the distance from the wall. In this work we assume that $y_p = h/2$. The model which gives the best results is given by Levitt.[21,22] He uses the relationship between drag coefficients and pore radius for electrolytic particles diffusing through a membrane. This analysis is meant to apply to the pores found in cell and artificial membranes such as the ones considered in this work. This is the only model of three tested[23] that is based on analysis of these types of systems and the only one of the three that compares well with the iMEDD, Inc. data. This model assumes a spherical particle diffusing in a cylindrical pore. The constant C for the hindered diffusion coefficient is given by

$$C = \frac{D_H}{D_{AB}} = \frac{1 - 2.1054\frac{a}{y_p} + 2.0805\left(\frac{a}{y_p}\right)^3}{T\left(\frac{a}{y_p}\right)} + \frac{-1.7068\left(\frac{a}{y_p}\right)^5 + 0.72603\left(\frac{a}{y_p}\right)^6}{T\left(\frac{a}{y_p}\right)} \quad (48)$$

where

$$T\left(\frac{a}{y_p}\right) = 1 - 0.75857\left(\frac{a}{y_p}\right)^5$$

We apply the Levitt model for a cylindrical pore to the rectangular channels in the iMEDD experiments. The experimental data to which our results are compared is from a series of experiments using Costar Transwell 6-well plates. Each well consists of a small donor region separated by a nanochannel membrane from a large receiver region as depicted on Figure 1. The volume of the donor region is 0.22 mL, while the volume of the receiver region is 11 mL. The nanoscale pores in the membranes are assumed to be of uniform length L and width W, but have different values for channel height h. Specifically, all of the nanopores have L = 5 μm and W = 45 μm. The values of h are 7, 13, 20 and 27 nanometers.

The iMEDD membranes have around 10^6 pores/cm^2. For the purpose of the numerical model the entire membrane is treated as a single channel with a length of 5 μm and an effective cross-sectional area A_{eff} given by[24]

$$A_{eff} = \frac{A_m P}{10^4}$$

where A_m is the physical area of the membrane (in this case, 2 mm^2) and P is the membrane porosity. The porosity is given by

$$P = \frac{42.5h}{10^4}$$

where h is the channel height. Table 1 lists the porosity and effective area for the four different pore sizes used.

The Costar Transwell experiment was conducted for nanopore membranes having h = 7, 13, 20 and 27 for both glucose and albumin. Each experiment was conducted as follows. The Costar plates were placed on an orbital plate

h, nm	P, %	Aeff, cm^2
7	0.30	6.0E-05
13	0.55	1.1E-04
20	0.85	1.7E-04
27	1.15	2.3E-04

Table 1: Porosity values for the iMEDD membranes.

shaker in an area of subdued lighting, and 11 mL of the buffer solution which is Phosphate Buffered Saline(PBS with 0.02% sodium azide) was loaded into the receiver region. Then, 0.22 mL of the glucose or albumin solution with buffer was added to the donor region. A concentration of 300 mg/mL was used for glucose. A concentration of 80 mg/mL was used for albumin in the 7 nm channels, and 5 mg/mL was used for albumin in the 13, 20 and 27 nanometer channels. The higher concentration in the 7 nm case was needed to improve the experimental running time. The amount of the macromolecular species in the donor was then measured periodically. To measure glucose, 5 μL samples were taken from the receiver and analyzed. To measure albumin, 20 μL samples were taken from the receiver and the same volume of fresh buffer was returned.

The components in the working solutions are listed in Table 2. The solution in the receiver region is initially standard PBS solution plus 2% sodium azide (NaN_3). PBS is not a 2-species solution, but for the purpose of the numerical model it is taken as such. This is a reasonable approximation because most of the ions in PBS are monovalent, and the divalent ions are present in very small amounts. In order to approximate the buffer solution as a binary monovalent ionic solution, the total moles of both positive and negative charge per liter was calculated. The buffer, as can be expected, is electrically neutral and can be approximated as a solution with 0.189 moles/L of a monovalent positive ion and an equal concentration of a monovalent negative ion. To calculate the concentration of the biomolecule, a net surface charge must be assumed. For the purposes of this work the net charge for albumin corresponds to an effective valence[25] of $z_{n2} = -19$ and for glucose we take $z_{n2} = -1$.

The flux equation used to predict the mass flux of each species is

$$N_A = -\frac{\partial X_A}{\partial x} - z_A X_A \frac{\partial \phi}{\partial x} \tag{49}$$

where X_A is the mole fraction. In the iMEDD experiments, there is no overall potential drop and so the second term in equation (49) is zero. To compare with the data which is in dimensional form, the nondimensional flux is dimensionalized by dividing by the scaling factor $\frac{L}{A_{eff} D_{ABI}}$. The concentration profiles of each species along the channel are determined both analytically and numerically, with both methods giving identical results. From the previous results it is evident that the concentration profiles in the core are linear and the analytical solutions for the concentration profiles of species p, n and n_2 in the interior of the channel, as previously noted are described by

Species	Donor	Receiver
Glucose		
n	0.01	0.189
p	1.68	0.190
n_2	1.67	0.001
80 mg/mL Albumin		
n	0.1660	0.189
p	0.1890	0.189
n_2	1.21E-03	0
5 mg/mL Albumin		
n	0.1876	0.189
p	0.1890	0.189
n_2	7.58E-05	0

Table 2: Molarity of the three-component solution in the upstream reservoir to model the iMEDD experiments.

$$X_n(x) = (n_i(1) - n_i(0))\, x + n_i(0) \tag{50}$$

$$X_p(x) = (p_i(1) - p_i(0))\, x + p_i(0) \tag{51}$$

$$X_{n2}(x) = (n_{2i}(1) - n_{2i}(0))\, x + n_{2i}(0) \tag{52}$$

The flux of species N_2 is just the derivative of the concentration:

$$N_{n2} = n_{2i}(1) - n_{2i}(0)$$

It has been suggested(Boiarksi, Private Communication, 2002) that the present experimental data describes single-file diffusion for which many physical phenomena are missed by the PNP system described here.[7,12] However the average current-time behavior and the current-voltage relationship of many channels are predicted well by the PNP system.[12] This situation seems to be the case here; while not explicitly considering the possible single-file nature of the ionic transport the PNP system is able to predict the transport of biomolecules through the synthetic ion channels considered here. The results of the comparison are shown on Figures 15 and 16. These results do not include the correction for wall EDL. Despite the simplicity of the model the results are very good. It turns out that the glucose experiment is actually within the transient regime so that the model significantly over predicts the experimental values except at $h = 27nm$. Thus we averaged the experimental data over time and those results are the circles on

the figure. This brings the model into much better agreement with the data when the assumed size of the glucose is $a = 1.49nm$.

The albumin data comparisons are also very good considering the simplicity of the model.

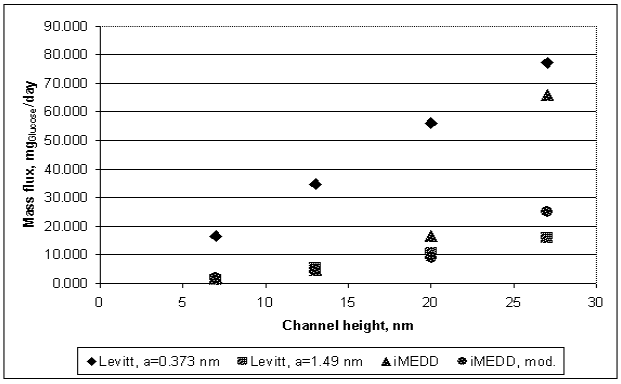

Figure 15: Results for the mass flow of glucose through the iMEDD membrane.

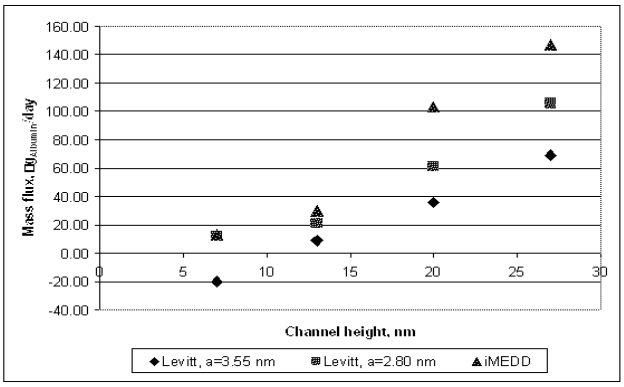

Figure 16: Results for the mass flow of albumin through the iMEDD membrane.

SUMMARY

In this paper, we have derived the one-dimensional Poisson-Nernst-Planck ion channel equations as an average of the two-dimensional equations integrated across the channel. For small ratio of the EDL thickness to the channel length, we have derived an analytical solution for the concentrations and potential for a three component ionic solution. We have compared the analytical solutions with numerical solutions of the PNP system and the comparisons are very good.

The two-component results are compared with the results published by Barcilon *et al.*[1] and the synthetic ion channel model fits well with the Barcilon data. We have presented asymptotic results for the case of a three component mixture and numerical results for constant fixed charge in the channel. In the course of the solution, we have shown how the fixed charge on the wall can be calculated using the Debye-Huckel approximation of the fully-developed electroosmotic flow equations. An analytical solution for the fixed charge is obtained in terms of the wall concentrations. It is noted that the potential is very sensitive to the value of the fixed charge.

We have employed the ion channel model to biomolecular transport of glucose and albumin through nanochannels of size ranging from $7nm$ to $27nm$. The length scale associated with these two molecules as they pass through the channel is difficult to determine, but the results indicate that good agreement with experimental data is achieved with minor adjustment of these values. In fact, the agreement is surprisingly good despite the simplicity of the model.

Acknowledgements: This work is supported by DARPA, Defense Sciences Office. The authors are grateful to the contract monitors Dr. Anantha Krishnan(DARPA), Mr Clare Thiem and Duane Gilmour of the Air Force Research Lab(IFTC) for their support. ATC is grateful for discussions with Dr. Dirk Gillespie And Dr. Bob Eisenberg. Drew Kebbel prepared some of the figures.

References

[1] Barcilon, Victor, Chen, D. P., Eisenberg, R. S., and Jerome, J. W., 1997, "Qualitative Properties of Steady-State Poisson-Nernst-Planck Systems: Perturbation and Simulation Study," *SIAM J. Appl. Math.*, v. 57, No. 3, pp. 631-648.

[2] Chen, D. P., W. Nonner, and R. S. Eisenberg, 1995, "PNP theory fits current-voltage (IV) relations of a neuronal anion channel in 13 solutions," *Biophys. J.*, v. 68, A370.

[3] Gillespie, Dirk, 1999 "A Singular Perturbation analysis of the Poisson-Nernst-Planck System: Applications to Ionic Channels", PhD Thesis, Rush Medical School, Chicago.

[4] Levitt, D.G., 1999 "Modeling of Ion Channels," *J. Gen. Physiol.*, v. 113, p. 789-794.

[5] Cardenas, Alfredo E., Coalson, Rob D., and Kurnikova, Maria G.,2000, "Three-Dimensional Poisson-Nernst-

Planck Theory Studies: Influence of Membrane Electrostatics on Gramicidin A Channel Conductance", *Biophysical Journal*, v. 79, no. 1, pp. 80-93.

[6] Alberts, Bruce *et al. Essential Cell Biology*, Garland Publishing, New York, 1998.

[7] Eisenberg, Bob, 1998 "Ion Channels in Biological Membranes-Electrostatic Ananysis of a Natural Nanotube", *Contemporary Physics*, v. 39, no. 6, pp. 447-466.

[8] Roux, Benoit, 2002 "Theoretical and Computational Models of Ion Channels," *Current Opinion in Structural Biology*, v. 12, pp. 182-189.

[9] Nonner, Wolfgang and Eisenberg, Bob, 1998, "Ion Permeation and Glutamate Residues Linked by Poisson-Nernst-Planck Theory in L-Type Calcium Channels", *Biophysical Journal*, v. 75, pp. 1287-1305.

[10] Nonner, Wolfgang, Gillespie, Dirk, Henderson, Douglas, and Eisenberg, Bob, 2001 "Ion Accumulation in a Biological Calcium Channel: Effects of Solvent and Confining Pressure," *J. Phys. Chem. B*, v. 105, pp. 6427-6436.

[11] Hollerback, Uwe, Chen, Duan P., and Eisenberg, Robert, 2001 "Two- and Three-Dimensional Poisson-Nernst-Planck Simulations of Current Flow Through Gramicidin A," *Journal of Scientific Computing*, v. 16, No. 4, pp. 373-409.

[12] Schuss, Z., Nadler, B., and Eisenberg, R. S., 2001 "Derivation of Poisson and Nernst-Planck equation in a bath and channel from a molecular model," *Physical Review E*, v. 64, pp. 036116-1-036116-14.

[13] Gillespie, Dirk, Nonner, Wolfgang and Eisenberg, Robert S., 2002 "Coupling Poisson-Nernst-Planck and Density Functional Theory to Calculate Ion Flux", *J. Condensed Matter*, v. 14, pp. 12129-12145.

[14] Conlisk, A. T. 2002 "On the Debye-Huckel Approximation in Electroosmotic Flow in Micro and Nanochannels", AIAA paper 2003-2869, AIAA 3^{rd} Theoretical Fluid Mechanics Meeting, St. Louis, June 2002.

[15] Conlisk, A. T., McFerran, J., Zheng, Z., Hansford, D., 2002 "Mass Transfer and Flow in Electrically Charged Micro- and Nanochannels," *Analytical Chemistry*, v. 74, n. 9), pp. 2139-2150.

[16] Zheng, Zhi, Hansford, Derek J., Conlisk, A. T., 2003 "Effect of Multivalent Ions on Electroosmotic Flow in Micro and Nanochannels", *Electrophoresis*, v. 24, no. 17 pp. 3006-3017, August.

[17] Chen, Duan P., Lear, James and Eisenberg, Robert, 1997 "Permeation through an Open Channel: Poisson-Nernst-Planck Theory of a Synthetic Ion Channel", *Biophysical J.*, v. 72, pp. 97-116.

[18] Davidson, M. G., Deen, W. M., 1988 "Hydrodynamic Theory for the Hindered Transport of Flexible Macromolecules in Porous Membranes," *Journal of Membrane Science*, v. 35, p. 167-192.

[19] Schmalzing, D., et. al., 1998 "DNA Sequencing on Microfabricated Electrophoretic Devices," *Analytical Chemistry*, v. 70, n. 11, p. 2303-2310.

[20] Shrewsbury, P. J., Muller, S.J., Liepmann, D., 2001 "Effect of Flow on Complex Biological Macromolecules in Microfluidic Devices," *Biomedical Microdevices*, v. 3, n. 3, p. 225-238.

[21] Levitt, D. G., 1975 "General Continuum Analysis of Transport through Pores, I. Proof of Onsager's Reciprocity Postulate for Uniform Pore," *Biophysical Journal*, v. 15, p. 533-551.

[22] Levitt, D. G., 1975 "General Continuum Analysis of Transport Through Pores, II. Nonuniform Pores," *Biophysical Journal*, v. 15, p. 553-563.

[23] McFerran, Jennifer, 2003 "Biomolecular Transport in Nanochannel Systems"', MSc. Thesis, The Ohio State University.

[24] Walczak, Rob and Boiarski, Anthony, Private Communication, 2002.

[25] Peters, T. Jr. *All About Albumin: Biochemistry, Genetics and Medical Applications*, 3^{rd} Ed., Academic Press, San Diego, 1996.

Appendix G:

The Debye-Huckel Approximation: Its Use in Describing Electroosmotic Flow in Micro- and Nano-channels

A. T. Conlisk
Department of Mechanical Engineering
The Ohio State University
Columbus, Ohio 43210-1107
conlisk.1@osu.edu

Abstract

In this work we consider the electroosmotic flow in a rectangular channel. We consider a mixture of water or other neutral solvent and a salt compound such as sodium chloride and other buffers for which the ionic species are entirely dissociated. Results are produced for the case where the channel height is much greater than the width of the electric double layer(EDL)(microchannel) and for the case where the channel height is of the order or slightly greater than the width of the EDL(nanochannel). At small cation, anion concentration differences the Debye-Huckel approximation is appropriate; at larger concentration differences, the Gouy-Chapman picture of the electric double emerges naturally. In the symmetric case , the velocity field and the potential are identical. We specifically focus in this paper on the limits of the Debye-Huckel approximation for a simplified version of a phosphate buffered saline(PBS) mixture. The fluid is assumed to behave as a continuum and the volume flow rate is observed to vary linearly with channel height for electrically driven flow in contrast to pressure driven flow which varies as height cubed. This means that very large pressure drops are required to drive flows in small channels. However, useful volume flow rates may be obtained at a very low driving voltage. In the course of the solution, we establish the relationship between the wall mole fractions of the electrolytes and the ζ potential. Multivalent electrolyte mixtures are also considered.

1 Introduction

In this paper, we consider the flow, the electric field and mass transfer problems in a channel in which the mass transfer is due to diffusion and to the presence of an imposed electric field. The primary purpose of the paper is to compare numerical solutions of the full nonlinear system of equations governing electroosmotic flow in channels with linearized solutions under the Debye-Huckel approximation valid for small potentials. While the case of monovalent ionic species is of considerable importance, we also present Debye-Huckel solutions for multivalent ionic constituents.

There are a number of textbooks on the subject of flow driven by the presence of an electric field[1–7] among many others. In this paper we consider electroosmosis, which is defined as the motion of a fluid past a solid surface due to an externally applied electric field. In addition, it is shown that an electric field is generated in a direction transverse to the primary flow direction; in turn a pressure gradient in the direction normal to the primary flow direction is set up.

The behavior of the flow in a rectangular channel of a mixture consisting of two monovalent ions plus an aqueous solvent is of interest here; we consider an $NaCl - H_2O$ mixture under the action of an electric field in the primary direction of motion. In particular, we calculate the mole fractions of the ions and the potential and velocity assuming the Debye-Huckel approximation holds; in this case, analytical solutions for the potential(and hence velocity) may be obtained. The Reynolds number is small and thus convection is neglected. The present theory can be applied to any combination of ionic constituents of arbitrary valences; all of the previous work requires that the ionic species be pairs of ions of equal and opposite valence.

In dissociated electrolyte mixtures, an electric double layer(EDL) will be present near the surfaces of the channel. The nominal thickness of the EDL is given by

$$\lambda = \frac{\sqrt{\epsilon_e RT}}{FI^{1/2}} \tag{1}$$

where F is Faraday's constant, ϵ_e is the electrical permittivity of the medium, c_i the concentrations of the electrolyte constituents, R is the gas constant, z_i is the valence of species i and T is the temperature. Here the ionic strength $I = \sum_i z_i^2 c_i$ and is based on the wall concentrations.

Typically, the width of the electric double layer is on the order of $1 \quad nm$ for a moderately dilute mixture; for extremely dilute mixtures, width of the electric double layer may reach several hundred nanometers. Thus if the channel height h is not too small, then $\frac{\lambda}{h} << 1$. In this case the problem for the electric potential and the mole fraction of the ions is a singular perturbation problem and the fluid away from the electric double layers is electrically neutral. We also consider the case where $\frac{\lambda}{h} = O(1)$ in which case the channel height is of the order of the EDL thickness. In this case, electroneutrality need not be preserved anywhere in the channel. This fact is true both for the Debye-Huckel approximation and for the full Poisson-Boltzmann representation. We assume that the temperature is constant and that the ionic components of the mixture are dilute.

In this paper, we examine in detail the validity of the Debye-Huckel approximation for both thin double layers and overlapping double layers. We show how the classical electroosmotic flow profile emerges as the double layers thin. The Debye-Huckel approximation breaks down as the magnitude of the electric potential becomes greater than about $26mV$; this increase in potential results in an increase in the difference in mole fraction of the cations and anions at the wall increases. In addition, asymmetric potential distributions with respect to the channel centerline will be considered; none of the previous work except Conlisk *et al*[8] presents detailed numerical solutions for this case.

Compared to the amount of work done on flow in micro-channels, there has been relatively little work done on flow in channels whose smallest dimension is on the order of the width of the electric double layer. The electroosmotic problem for channel heights on the order of the electric double layer has been investigated.[9] There the solution for the potential is based on a Boltzmann distribution for the number concentration of the ions; the potential is calculated based on a symmetry condition at the centerline. Qu and Li[10] have recently produced solutions which do not require the Boltzmann distribution, but they also assume symmetry at the centerline; the results show significant differences from the results of Verwey and Overbeek.[9] The results of Qu and Li[10] are valid for small potentials since the Debye-Huckel approximation is invoked.

The first work on the electroosmotic flow problem discussed here appears to have been done by Burgeen and Nakache[11] who considered channel heights of the order of the electric double layer thickness. They produced results for the velocity field and potential for two equally charged ions of valence z; a Boltzmann distribution is assumed for the number of ions in solution. The convective

terms in the velocity momentum equation are assumed to be negligible and the solution for the velocity and potential is assumed to be symmetric about the centerline of the channel.

Levine et al.[12] solved the same problem as Burgeen and Nakache[11] and produced results for both thin and overlapping double layers for a single pair of monovalent ions. Again symmetry of the flow with respect to the direction normal to the channel walls is assumed.

Rice and Whitehead[13] seem to be the first to calculate the electrokinetic flow in a circular tube; they assume a weak electrolyte and so assume the Debye-Huckel approximation holds. Levine et al.[14] also consider flow in a tube under the Debye-Huckel approximation; an analytical solution is found in this case. Stronger electrolyte solutions valid for higher potentials are also considered using a simplified ad hoc model for the charge density.

Conlisk *et al*[8] solve the problem for the ionic mole fractions and the velocity and potential for strong electrolyte solutions and consider the case where there is a potential difference in the direction normal to the channel walls corresponding in some cases to oppositely charged walls. They find that under certain conditions reversed flow may occur in the channel and this situation can significantly reduce the flow rate.

All of the work discussed so far assumes a pair of monovalent ions. However, many bio-fluids contain a number of other ionic species. An example of one of these fluids is the common Phosphate Buffered Saline(PBS) solution. This solution contains five ionic species, with some being divalent. Zheng *et al*[15] have solved the entire system of equations numerically; they show that the presence of divalent ions has a significant effect on the flow rate through the channel.

Applications of electrokinetic flow are numerous. In these small channels rapid bio-molecular analysis is possible and so these channels can act as sensors.[16] Small drug delivery devices may employ electrokinetic flow to control the rate of flow of drug to the patient. These devices may also be used as bio-molecular separators[17–19] because different ionic species travel at different speeds in these channels. Natural nanochannels exist in cells for the purpose of providing nutrients and discarding waste. In general, these devices act as electroosmotic pumps.[20–26] For the most part in the aforementioned papers the channels are of dimension on the microscale.

Nanochannel systems are not easy to fabricate. An example is depicted on Figure 1(a). These nanochannels are fabricated by a sacrificial layer lithography method which can produce channels with different surface properties.[27] On Figure 1(b) is a sketch of a nanopump whose operation has been documented by iMEDD, Inc. of Columbus, Ohio(Dr. Tony Boiarski, private communication.).

On Figure 1(a), note that fluid enters from a bath on one side and is forced through several microchannels(Figure 1(a)). The fluid is then forced to turn into a number of much smaller channels which may have their smallest dimension on the nanometer scale. On the other hand, in the iMEDD device, fluid is forced directly into the nanochannels.

There is a clear advantage to electroosmotic pumping versus pressure pumping in very small channels. When the EDL's are thin the flow rate is given to leading order by

$$Q_e \sim U_0 h W \tag{2}$$

where U_0 is independent of h(as we will see) and W is the width. Thus the flow rate is proportional to h and not h^3 as for pressure-driven flow for which the volume flow rate in a parallel plate channel is

$$Q_p = \frac{W h^3}{12 \mu L} \Delta p \tag{3}$$

where Δp is the pressure drop. This means that driving the flow by a pressure gradient is not feasible as depicted on Figure 2; note that at a channel height of $10nm$ three atmospheres of pressure drop are required to drive a flow of $Q = 10^{-6}L/min$. This is a large pressure drop in a liquid and clearly, a relatively awkward pump would be required to provide this pressure drop. Clearly this would not be consistent with the idea of a very small portable implant.

As will be seen in the results the solutions for all of the quantities of interest under the Debye-Huckel approximation differ from the full non-linear case primarily in amplitude for monovalent ionic species. The general character of the DH solutions is similar to the fully non-linear results for this case. In particular, since we calculate the perturbation from the $\zeta-$potential, the slope of the potential for both the non-linear case and under the DH approximation are very close in the immediate vicinity of the wall so the surface charge density is not much different from the Debye-Huckel case.

On the other hand for $+n_1/-n_2$ multivalent ionic species, for which $n_1 \neq n_2$, the velocity and potential profiles are more parabolic-like, increasing the shear stress in the core of the channel. The Debye-Huckel results indicate that the velocity and potential are constants in the core of the channel.

The plan of the paper is as follows. In the next section various aspects of the problem are outlined and then the governing equations are derived; the flow field, the electric field and the mass transfer problems are coupled. We then present results for several different channel heights and for various wall mole fraction distributions. In the course of the solution a unique relationship between the wall mole fractions and the ζ potential is established and multivalent ionic species are also considered.

2 Governing Equations

2.1 Mass Transfer Driven by an Electric Field

Consider the mass transport in a liquid mixture of three components flowing in the channel depicted on Figure 3. We have in mind the mixture consisting of water and a salt such as sodium chloride. We consider the case where the salt is dissociated so that mixture consists of positively and negatively charged ions, say Na^+ and Cl^-. The driving forces for mass transfer are assumed to be ordinary Fick diffusion and migration due to the presence of an electric field. The electric field, in general can be composed of two components: an externally imposed electric field and a local electric field present near the solid surfaces of the channel corresponding to the presence of an electric double layer. We consider both the case of a very thin EDL and an EDL comparable to the channel height(Figure 4). The molar flux of species A for a dilute mixture is a vector and given by

$$\vec{N}_A = -cD_{AB}\nabla X_A - cu_A z_A F X_A \nabla\phi^* + cX_A\vec{u}^* \tag{4}$$

Here D_{AB} is the diffusion coefficient, c the total concentration, X_A is the mole fraction of species A. Here u_A is the mobility, z_A is the valence, F is Faraday's constant, ϕ^* is the electric potential and $\vec{u}^*$ is the mass average velocity of the fluid. The mobility u_A is defined by the Nernst-Planck equation as

$$u_A = \frac{D_{AB}}{RT}$$

where R is the gas constant, T is the temperature,[4]

Note that the molar flux can be written incorporating the electrochemical potential. In terms of the mole fraction the electrochemical potential is defined by

$$\mu_e = RTlnX_A + z_A F\phi^* + const \tag{5}$$

Substituting for the mobility in the flux equation we find that

$$\vec{N}_A = -\frac{cX_A D_A}{RT}\nabla\mu_e + cX_A\vec{u}^* \tag{6}$$

where we have written $D_{AB} \sim D_A$, that is, we assume that the charged species concentrations are so dilute that they do not interact and hence the diffusion coefficient is that between the charged species and the solvent.

The mass transport equation at steady state is given by

$$\nabla \bullet \vec{N}_A = 0 \tag{7}$$

In non-dimensional form the equation becomes

$$\frac{\partial^2 X_A}{\partial y^2} + \epsilon_1^2\frac{\partial^2 X_A}{\partial x^2} + \epsilon_2^2\frac{\partial^2 X_A}{\partial z^2} =$$

$$ReSc\left(\epsilon_1 u\frac{\partial X_A}{\partial x} + v\frac{\partial X_A}{\partial y} + \epsilon_2 w\frac{\partial X_A}{\partial z}\right)$$

$$+\left(\alpha_x\epsilon_1\frac{\partial X_A E_x}{\partial x} + \alpha_y\frac{\partial X_A E_y}{\partial y} + \alpha_z\epsilon_2\frac{\partial X_A E_z}{\partial z}\right) \tag{8}$$

Here we note that α_i are scale factors for the potential field; for the configuration of interest,

$$\alpha_x = \frac{hE_0 z_A F}{RT}$$

$$\alpha_y = \frac{\phi_{y0} z_A F}{RT}$$

$$\alpha_z = \frac{\phi_{z0} z_A F}{RT}$$

The externally imposed electric field is constant in the x direction, whereas variations in the potential in y and z directions are permitted. The coordinates have been non-dimensionalized on the appropriate length in the three directions (L, h, W) as depicted on Figure 3. Also (u, v, w) are the velocities in each of the coordinate directions (x, y, z). Here $\epsilon_1 = \frac{h}{L}$ and $\epsilon_2 = \frac{h}{W}$. We assume $h << W, L$ so that both ϵ_1 and ϵ_2 are small. $Re = \frac{U_0 h}{\nu}$ is the Reynolds number and $Sc = \frac{\nu}{D_{AB}}$ is the Schmidt number, where ν is the kinematic viscosity. The valence $z_A = 1$ for the positive ion and $z_B = -1$ for the negative ion, although generalization to arbitrary valence is obvious. The determination of the velocity scale U_0 will be discussed below.

The mass transfer equation is subject to boundary conditions at a solid surface. Consider the wall at $y = 0$. Then if A refers to either of the ion distributions, it follows that we can specify the ion concentration or the flux at the surface. Specifically the boundary condition is applied at the edge of the Stern layer. For the case of specified mole fraction,

$$X_A = X^0 \;\; y = 0$$

and

$$X_A = X^1 \;\; y = 1$$

It will be shown later that the wall mole fractions are directly related to the ζ potential.

The mass transfer equation must be supplemented by an equation for the electric field. This is the Poisson equation given by

$$\nabla \bullet (\epsilon_e \vec{E^*}) = -\nabla \bullet \epsilon_e \nabla \phi^* = \rho_e \tag{9}$$

where ρ_e is the volume charge density and ϵ_e is the dielectric constant and the * denotes a dimensional quantity. The charge density is defined by

$$\rho_e = F \sum_i z_i c_i = Fc \sum_i z_i X_i \tag{10}$$

where c_i is the molar concentration of species i and c is the total molar concentration and is assumed constant. For example, for a pair of monovalent ions

$$\rho_e = Fc(X_+ - X_-) \tag{11}$$

Nondimensionalizing the equation as above, and working with the potential and assuming $\phi_{y0} = \phi_{z0} = \phi_0$, $\phi = \frac{\phi^*}{\phi_0}$

$$\frac{\partial^2 \phi}{\partial y^2} + \epsilon_1^2 \frac{\partial^2 \phi}{\partial x^2} + \epsilon_2^2 \frac{\partial^2 \phi}{\partial z^2} = -\frac{Fch^2}{\epsilon_e \phi_0}(X_+ - X_-) \tag{12}$$

Since differences in potential only are important we can specify the potential boundary conditions as

$$\phi = 0 \;\; y = 0$$

and

$$\phi = \phi^1 \;\; y = 1$$

2.2 Fully-Developed Flow

We assume that the channel is long and narrow($h << W, L$), so that the variation of the variables in the y-direction will be dominant. We thus assume fully developed flow and in addition to the equations for the mole fractions, the potential, the streamwise component of the fluid momentum equation must be considered. For sufficiently small Reynolds number (for the channel sizes considered in this work $Re \sim 10^{-4}$ or smaller) the convective terms in the momentum equation are negligible and neglecting the pressure gradient in the streamwise momentum equation the governing equations for binary electrolytes become to leading order[3]

$$\frac{\partial}{\partial y}\left(\frac{\partial X_+}{\partial y} + z_+ X_+ \frac{\partial \phi}{\partial y}\right) = 0 \tag{13}$$

$$\frac{\partial}{\partial y}\left(\frac{\partial X_-}{\partial y} + z_- X_- \frac{\partial \phi}{\partial y}\right) = 0 \tag{14}$$

$$\frac{\partial^2 \phi}{\partial y^2} = -\frac{Fch^2}{\epsilon_e \phi_0}(z_+ X_+ + z_- X_-) \tag{15}$$

and

$$\frac{\partial^2 u}{\partial y^2} = -\frac{FcE_0h^2}{\mu U_0}(z_+X_+ + z_-X_-) \tag{16}$$

where E_0 is the value of the (constant) electric field in the primary flow direction. Equations (13-16) are four equations in four unknowns for the mole fractions of the ions, the potential and the fluid velocity.

We now assume that the potential scale is defined by taking

$$\phi_{y0} = \phi_0 = \frac{RT}{F} = 0.026V$$

and the Debye-Huckel approximation is valid if the dimensionless potential

$$\phi = \frac{\phi^*}{\phi_0} << 1$$

or $\phi^* << 0.026V$.

We can rewrite the governing equations in terms of the nominal Debye length and we have

$$\epsilon^2 \frac{\partial^2 \phi}{\partial y^2} = -\beta(z_+X_+ + z_-X_-) \tag{17}$$

where

$$\beta = \frac{c}{I}$$

where c is the total concentration of the mixture, I is the ionic strength and $\epsilon = \frac{\lambda}{h}$. The parameter β arises from the use of the mole fraction in the volume charge density. Similarly for the velocity equation,

$$\epsilon^2 \frac{\partial^2 u}{\partial y^2} = -\frac{\epsilon_e E_0 RT}{F\mu U_0}\beta(z_+X_+ + z_-X_-) \tag{18}$$

Equation (18) sets the velocity scale as

$$U_0 = \frac{\epsilon_e E_0 \phi_0}{\mu}$$

which is recognized as the electroosmotic velocity scale. Note that the equations for the velocity and potential are the same and if the boundary conditions are the same, the velocity and the potential are said to be similar. Also, from the governing equations that there is a pressure gradient in the $y-$direction which is proportional to the potential gradient in the $y-$ direction, but since variations in x are at most mild, it does not affect the flow.

To simplify the notation we write $g = X_+$ and $f = X_-$ and for clarity and completeness we repeat the boundary conditions for the simplified problem as

$$\phi = 0 \, at \, y = 0 \tag{19}$$

$$\phi = \phi^1 \, at \, y = 1 \tag{20}$$

$$f = f^0 \, at \, y = 0 \tag{21}$$

$$f = f^1 \, at \, y = 1 \tag{22}$$

$$g = g^0 \, at \, y = 0 \tag{23}$$

$$g = g^1 \, at \, y = 1 \tag{24}$$

$$u = 0 \;\; at \;\; y = 0, \; and \, y = 1 \tag{25}$$

3 Numerical Methods

Standard second-order central differences are employed to approximate the derivatives in the governing equations and solve each set of difference equations by the Thomas Algorithm. The equations are nonlinear and coupled so that the solution procedure requires iteration. The program is very short and requires less than 20 iterations to converge for smaller values of the channel height h. The iteration procedure is said to converge if $\left|\frac{g_{new}-g_{old}}{g_{new}}\right| < \delta$ at all grid points, where $\delta = 10^{-4}$. In general, four digit accuracy was achieved in solutions for 81 and 161 points across the channel in all of the variables for all of the runs made. For $h = 24nm$, four digit accuracy was achieved for 161 and 321 points across the channel. Because central difference formulas are used, the accuracy increases quadratically as the grid spacing is decreased.

We assume the solvent is water at a temperature $T = 300^0K$. The pressure gradient along the channel vanishes and the magnitude of the externally imposed potential is 0.06 volts applied over a length of $3.5\mu m$. The dielectric constant of the medium has been taken to be that of water, 78.54. We present results for both monovalent and multivalent ionic species; the baseline mixture wall mole fractions correspond to a concentration of the cation (say Na) equal to .154 M, and the anion(say Cl .141 M)and water 55.6 M for which $\beta \sim 190$. However multivalent ionic species are also considered. These concentrations give a nominal Debye Length at $y = 0$ of about one nanometer. Results are also produced for other concentrations as noted but the differences do not appreciably change the EDL thickness.

4 Results: The Symmetric Case

4.1 The Debye-Huckel Approximation

First consider a pair of monovalent ionic species with flow symmetry about the centerline of the channel. Since equations (13) and (14) are independent of ϵ we can integrate to obtain

$$f = f^0 e^{\phi - \phi(0)} \tag{26}$$

$$g = g^0 e^{-\phi + \phi(0)} \tag{27}$$

Note now that the reference mole fraction is that at the wall $y = 0$. The governing equation for the potential or the velocity is

$$\epsilon^2 \frac{\partial^2 \phi}{\partial y^2} = -\beta(X_+ - X_-) \tag{28}$$

and substituting for the mole fractions we have

$$\epsilon^2 \frac{\partial^2 \phi}{\partial y^2} = -\beta(g^0 e^{-\phi + \phi(0)} - f^0 e^{\phi - \phi(0)}) \tag{29}$$

Expanding for small ϕ we have($\phi(0) = \phi^0 = 0$),

$$g \sim g^0(1 - \phi) \tag{30}$$

$$f \sim f^0(1 + \phi) \tag{31}$$

and so we have

$$\epsilon^2 \frac{\partial^2 \phi}{\partial y^2} = -\beta(g^0 - f^0 - (f^0 + g^0)\phi) \tag{32}$$

Equations (30) and (31) form the Debye-Huckel Approximation and allows analytical solutions for the potential, velocity and mole fractions to be obtained.

4.2 Thin EDL: $\epsilon << 1$

We consider the symmetric case where $\phi^1 = 0$. Consider now the case of $\epsilon << 1$ and we define the boundary layer variable $\hat{y} = \frac{y}{\epsilon}$. Then the solution to the equation is given by

$$\phi = Ae^{-\hat{y}} + \frac{g^0 - f^0}{g^0 + f^0} \tag{33}$$

Applying the boundary condition at $\hat{y} = 0$ we have

$$\phi = \frac{g^0 - f^0}{g^0 + f^0}(1 - e^{-\hat{y}}) \tag{34}$$

Note that the solution depends both on the difference of the mole fractions and on the total mole fraction of the ionic components of the mixture. Clearly at $\hat{y} = \infty$ we have

$$\phi_\infty = u_\infty = \frac{g^0 - f^0}{g^0 + f^0} \tag{35}$$

The uniformly valid solution is given by

$$u = \phi = \frac{g^0 - f^0}{g^0 + f^0}(1 - e^{-\hat{y}} - e^{-\hat{y}_1}) \tag{36}$$

where

$$\hat{y}_1 = \frac{1 - y}{\epsilon}$$

Clearly we can extend the analysis to the case of N dilute species of arbitrary valence; in this case algebra shows that the first term on the right side of equation (32) becomes

$$-\beta \sum_{i=1}^{N} z_i X_i^0$$

and the second term in the same equation is given by

$$\beta \sum_{i=1}^{N} z_i^2 X_i^0$$

and the result for the velocity is

$$u = \phi = \frac{\sum_{i=1}^{N} z_i X_i^0}{\sum_{i=1}^{N} z_i^2 X_i^0}(1 - e^{-\hat{y}} - e^{-\hat{y}_1}) \tag{37}$$

Clearly this is a powerful result in the sense that we can describe the solution for the electroosmotic velocity for an infinite number of electrolyte mixtures.

Results for the velocity and potential for $h = 24nm$ for a small difference in the wall mole fractions are shown on Figure 5(a) and the mole fractions are shown on Figure 5(b). Note the classical plug flow profile as seen in textbooks. Also the core is electrically neutral as it should be and the potential is small. The solid lines are the numerical solution and the dashed lines are the Debye-Huckel Approximation. Note that at the Debye-Huckel approximation is valid since there is little difference in the two solutions. Here the mole fraction distributions are symmetrical about a mean value and this corresponds to the Debye-Huckel picture of the EDL.[28]

In the present case the velocity and the potential are equivalent; the width of the electric double layer can be defined as that location where the velocity and potential reach 99% of their free stream value. In the DH case the width is given by $\delta = 4.61\epsilon$ where δ is non-dimensional and scaled on the channel height. Thus the dimensional width of the electric double layer is given by $\delta^* = 4.61\lambda$. The numerical result in this case is $\delta^* = 4.62\lambda$. Note that the Debye length is not a good measure of the asymptotic width of the EDL and that the constant 4.6 is similar to the result obtained from the Blasius boundary layer in fluid mechanics for which the boundary layer thickness is given by $\delta = 5Re^{-1/2}$ for large Reynolds number.

On Figure 6 are results for the mole fraction of the anion ten times less than on Figure 5. Here we see that the potential is not small and the Debye-Huckel approximation no longer holds. It should also be noted that the Debye-Huckel approximation breaks down in the core where the potential is highest. Deep within the EDL itself the velocity and the potential agree with the DH value; note also that the same is true for the cation mole fraction but not the anion mole fraction. The mole fraction distribution in Figure 6 corresponds to the Gouy-Chapman picture of the EDL.[29] Note that the boundary layer thickness is larger for the numerical case and $\delta^* = 5.99\lambda$.

Because the EDL's are so thin, to leading order the dimensional volume flowrate is given by velocity in the core which is constant times the area; the correction for the presence of the two double layers may be calculated directly from the solution for the velocity and to second order,

$$Q = U_0 A(\frac{g^0 - f^0}{g^0 + f^0} - 2\epsilon)$$

where $U_0 = \frac{\epsilon_e E_0 \phi_0}{\mu}$, the electroosmotic velocity. In all of the results presented in this paper, we assume that the width of the channel is $W = 3.0 \times 10^{-6} m$. The flow rate for Figure 5 is $Q = 6.32 \times 10^{-14} L/min$ and for Figure 6 $Q = 1.57 \times 10^{-12} L/min$.

It is useful to calculate the surface charge density. When the core is electrically neutral each surface charge density is obtained by integrating across the electrical double layer to insure overall electroneutrality; we have in dimensional form

$$\sigma_0 = \epsilon_e \int_0^\infty \frac{\partial^2 \phi^*}{\partial y^{*2}} dy^* \tag{38}$$

where σ_0 is the charge density on the wall at $y = 0$. Nondimensionalizing the potential and the length, we find that

$$\sigma_0 = \frac{\epsilon_e RT}{\epsilon hF} \int_0^\infty \frac{\partial^2 \phi}{\partial \hat{y}^2} d\hat{y} = \frac{\epsilon_e RT}{\epsilon hF} \frac{\partial \phi}{\partial \hat{y}} |_0^\infty \tag{39}$$

In the general nonlinear case, the derivatives may be calculated numerically. Substituting for the dimensionless DH potential and performing the integration we find that

$$\sigma_0 = -\frac{\epsilon_e RT}{\epsilon hF}\frac{g^0 - f^0}{f^0 + g^0} \tag{40}$$

Note that for $g^0 > f^0$ the wall is negatively charged as is common for silica surfaces above $pH = 4$.[7]

The boundary conditions at the surface of the channel for the potential have been taken as $\phi = 0$; thus we have been working with the potential relative to that at the walls of the channel. Let $\psi = \zeta + \phi$ where ζ is the dimensionless potential at the wall, the $\zeta-$potential. Then we define $\psi = 0$ in the core of the channel as is common[6] so that

$$\zeta = -\frac{g^0 - f^0}{g^0 + f^0} \tag{41}$$

and is a unique relationship between the wall mole fractions and the $\zeta-$potential. Referring to the surface charge density given above we find that

$$\sigma_0 = \frac{\epsilon_e \zeta^*}{\lambda} \tag{42}$$

which is Grahamme's equation.[7] Here ζ^* is the dimensional zeta potential. For the case of wall mole fractions depicted on Figure 5, $\zeta^* = -1.2mV$.

To begin to understand the limitations of the Debye-Huckel Theory it is useful to compare the $\zeta-$ potential calculated using the DH approximation and the fully nonlinear result which is[8]

$$\zeta = -\frac{1}{2} ln \frac{g^0}{f^0} \tag{43}$$

On Table 1 are values of the $\zeta-$potential for the sodium wall concentration $g_w^0 = .154nM$ where $n = 1, 2, 4, 6, 8$ with the concentration of the chloride f_c^0 held fixed. The middle column is the Debye-Huckel result from equation (41) and the right hand column is the full nonlinear result from equation (43). Note that at the highest concentration used, there is about a 20% difference in the two values.

4.3 Overlapping EDLs: $\epsilon \sim 1$

In this case the EDLs extend throughout the channel. We now must include the positive exponential term in the solution and we can write the potential as

$$\phi = Acosh(\gamma y) + Bsinh(\gamma y) + \frac{g^0 - f^0}{g^0 + f^0} \tag{44}$$

where here $\gamma = \frac{1}{\epsilon}$. The condition $\phi(0) = 0$ leads to

$$A = -\frac{g^0 - f^0}{g^0 + f^0}$$

and in the symmetric case we apply the condition

$$\frac{\partial \phi}{\partial y} = 0 \ at \ \ y = 1/2$$

The solution must then be symmetric and the results which satisfies the equation and boundary conditions is

$$\phi = \frac{g^0 - f^0}{g^0 + f^0} \left(1 - \frac{cosh\gamma(y - 1/2)}{cosh\gamma/2} \right) \tag{45}$$

The flow rate in this case is

$$Q = U_0 A \frac{g^0 - f^0}{g^0 + f^0} \left(1 - \frac{2}{\gamma} tanh(\frac{1}{2}\gamma) \right) \tag{46}$$

The results are shown on Figures 7 and 8 for $h = 4nm$; Figure 7 corresponds to the baseline mole fractions while

Here we note that at the larger mole fraction difference, the Debye-Huckel approximation is not valid. However, consistent with the previous results for $h = 24nm$ the DH approximation breaks down in the core for velocity and potential. On the other hand, at this channel height the Debye-Huckel approximation works well for the anions but not for the cations. The primary effect of overlapping electric double layers is to remove the electrical neutrality in the core of the channel. The flow rate for Figure 7 is $Q = 6.9 \times 10^{-15} L/min$ and for Figure 8 is $Q = 1.2 \times 10^{-13} L/min$.

As with the case of thin EDLs we can calculate the surface charge density except we now integrate across the whole channel and the result is

$$\sigma_0 = -2 \frac{\epsilon_e RT}{\epsilon h F} \frac{g^0 - f^0}{f^0 + g^0} tanh \frac{1}{2}\gamma \tag{47}$$

This gives the total surface charge density and for the symmetric case each wall will have a charge density of 1/2 the value given here. The $\zeta-$potential is then given by the same formula as in the $\epsilon << 1$ case and solution agrees with the result of Qu and Li.[10]

It is useful to plot the flow rate and surface charge density as a function of concentration for the parameters of Table 1 for $h = 4nm$. On Figure 9 there are two curves corresponding to the full numerical result and the DH approximation value. Note the difference in flow rate emerges at about a cation concentration of 2 M. Surprisingly, there is not much difference in the surface charge density even at the highest concentration. This is because the slope of the potential under the DH approximation at the wall is only slightly different from the slope for the full nonlinear solution. For the smallest ionic strength considered $\epsilon = 0.2$ and it turns out that the asymptotic formulas discussed in the previous section are accurate even for this small value of channel height.

5 Results: The Asymmetric Case

5.1 Thin EDL: $\epsilon << 1$

A detailed consideration of the case where the mole fraction and the velocity and potential are not symmetric about the centerline has been given by Conlisk et al.[8] We term these solutions asymmetric. The major results of that analysis are that the outer solution is

$$u_o = \phi_o - \phi^1$$

and in the inner region near the walls

$$u_i = \phi$$

near $y = 0$ and

$$u_i = \phi_i - \phi^1$$

near $y = 1$. We can always consider the potential at $y = 0$ to be $\phi^0 = 0$ and the uniformly valid solution for the velocity is given by

$$u_{uv} = u_i^0 - \phi^1 y + u_i^1 \tag{48}$$

where u_i^0 is the inner solution near $y = 0$ for example. Note that near $y = 0$, $u_{uv} = \phi_i^0$, and $u_{uv} = \phi_i^1 - \phi^1$ near $y = 1$ where ϕ_i^0 is the inner solution for the potential near $y = 0$.

Under the Debye-Huckel Approximation the solution for the potential is similar to the symmetric case and

$$\phi = \frac{g^0 - f^0}{g^0 + f^0}(1 - e^{-\hat{y}} - e^{-\hat{y_1}}) + \phi^1 e^{-\hat{y}_1} \tag{49}$$

and the velocity is thus

$$u = \frac{g^0 - f^0}{g^0 + f^0}(1 - e^{-\hat{y}} - e^{-\hat{y_1}}) + \phi^1 e^{-\hat{y}_1} - \phi^1 y \tag{50}$$

The flow rate is calculated in the same way as for the symmetric case and to second order,

$$Q = U_0 A(\frac{g^0 - f^0}{g^0 + f^0} - 2\epsilon) - \phi^1(\frac{1}{2} - \epsilon) \tag{51}$$

and the charge density on the wall at $y = 1$ is

$$\sigma_1 = -\frac{\epsilon_e RT}{\epsilon h F}\left(\frac{g^0 - f^0}{f^0 + g^0} - \phi^1\right) \tag{52}$$

Note that for $\phi^1 > 0$ the flow rate is reduced and the charge is increased. As with the symmetric case

$$\zeta = -\frac{g^0 - f^0}{g^0 + f^0} \tag{53}$$

is a unique relationship between the wall mole fractions and the $\zeta-$potential. Refering to the surface charge density given above we find that

$$\sigma_0 = \frac{\epsilon_e \zeta^*}{\lambda}(1 + \phi^{1*}) \tag{54}$$

where ζ^* again is the dimensional zeta potential.

On Figure 10 is a case where the DH approximation does not hold. The$'*'$ curve is the computed velocity and note that it is smaller than the potential. Near $y = 0$ the velocity and the potential are very close as shown by the asymptotic analysis. Also near $y = 1$, the velocity and potential differ by a constant. Because the velocity is smaller than the potential, there is a decrease in flow rate in the case compared to the symmetric case and $Q = 1.45 \times 10^{-12} L/min$. Note that the dimensional potential at $y = 1$ is about $18mV$.

5.2 Overlapping EDLs: $\epsilon \sim 1$

In this case the EDLs extend throughout the channel. We now must include the positive exponential and we can write the solution for ψ as

$$\phi = Acosh(\gamma y) + Bsinh(\gamma y) + \frac{g^0 - f^0}{g^0 + f^0} \tag{55}$$

where here $\gamma = \frac{1}{\epsilon}$. The solution for the potential is

$$\phi = -\frac{g^0 - f^0}{g^0 + f^0} cosh\gamma y + Bsinh\gamma + \frac{g^0 - f^0}{g^0 + f^0} \tag{56}$$

where B is a constant and

$$B = \frac{\phi^1 + \frac{g^0 - f^0}{g^0 + f^0}(cosh\gamma - 1)}{sinh\gamma}$$

The velocity $u = \phi - \phi^1 y$. The flow rate in this case is

$$Q = U_0 A \left(\frac{g^0 - f^0}{g^0 + f^0} \left(1 - \frac{1}{\gamma} sinh(\gamma) \right) + \frac{B}{\gamma} cosh\gamma - \frac{\phi^1}{2} \right) \tag{57}$$

The total surface charge density is

$$\sigma_0 = \frac{\epsilon_e RT}{\epsilon h F} \left(-\frac{g^0 - f^0}{f^0 + g^0} sinh\gamma + B\gamma \left(cosh\gamma - 1 \right) \right) \tag{58}$$

The $\zeta-$potential is the same as in the symmetric case.

On Figure 11 are results for which the DH approximation holds for channel height $h = 4nm$. Note that the mole fractions are slightly different but the difference is small since the scale on the y-axis is small. The flow rate for this plot is $Q = 2.3 \times 10^{-14}$.

The results for a positively charged wall at $y = 1$ are shown on Figure 12. Here again the difference in the mole fractions at the walls is large enough so that the DH approximation does not hold even though the potential and velocity are close to the DH value. The flow rate is $Q = 7.7 \times 10^{-15} L/min.$

6 Results: Mulitvalent Ionic Species

In the previous sections we have developed the solutions for the mole fractions, potential and velocity for a electrolyte containing two monovalent electrolytes. In the course of the analysis we have established a unique relationship between the wall mole fractions or concentrations, and their bulk values and between the surface charge density and the wall mole fractions. In the Debye-Huckel approximation Grahame's equation emerges naturally.

The focus of this section is to evaluate the validity of the DH approximation for more complicated electrolyte mixtures. We consider here the effect of multivalent ions in an electrolyte mixture of two and three constituents. The solution for the symmetric case is given in equation (37). The full nonlinear problem has been investigated by Zheng *et al*[15] who considered a number of mixtures including PBS. They showed that for a negatively charged wall, a small amount of a counterion o

valence $+2$ significantly reduces the flowrate. Only a trace amount of multivalent cation is necessary to reduce the flow rate by 100%. The addition of a small amount of either a monovalent cation or ion has a negligible effect on the results when compared with the effect of the divalent counterion. No results for the Debye-Huckel limit were obtained.

For $\epsilon << 1$, analytical solutions may be obtained for the full non-linear problem for the velocity, potential and mole fractions for a binary mixture of species of arbitrary valence. These solutions may be obtained by extending the analysis in Conlisk *et al*[8] and the result

$$u_o = \phi_o = \frac{1}{z_g - z_f} ln \left(\frac{-z_g g^0}{z_f f^0} \right) \tag{59}$$

$$f_o = \sqrt{-\frac{z_g}{z_f} g^0 f^0 e^{-(z_g + z_f)\phi_o}} \tag{60}$$

$$g_o = -\frac{z_f}{z_g} f_o \tag{61}$$

The subscript 'o' denotes the "outer" solution in the asymptotic sense.[8]

For the case of a thin electric double layer, the $\zeta-$ potential may be calculated for an arbitrary number of species as

$$\zeta^* = -\phi_0 \frac{\sum_{i=1}^{N} z_i X_i^0}{\sum_{i=1}^{N} z_i^2 X_i^0} \tag{62}$$

The surface charge density may also be calculated in the same way.

We have computed results for a fixed channel height of $h = 20nm$ for both +n/-n electrolytes and for $+n_1/-n_2$ electrolytes. The +2/-2 results are shown on Figure 13; these results should be compared with Figure 6. Here we see again that the shape of both of the curves are similar and only the amplitude is different. The ζ potential is a bit lower than the $+1/-1$ on Figure 6 but the difference between the numerical result and the DH approximation is about the same. It should be noted that Zheng *et al*[15] has shown that the divalent cation should have a greater affinity for the wall than a monovalent cation and thus these results should be viewed as conservative in predicting differences between the DH approximation and the numerical result.

The +2/-1 result results are shown on Figure 14. Here we see that the nonlinear results depict overlapped double layers whereas the DH approximation predicts thin double layers. Consequently, the shear stress in the core of the increases and this is the primary result of Zheng.[15] The ζ potential is a bit lower than the $+1/-1$ case but the difference between the numerical and DH results is much greater.

On Figure 15 are results for the case of a +3/-1 mixture. These results are similar to that for the case of a +2/-1 mixture; again the difference in potential/velocity amplitude between the DH approximation and the numerical results has increased with the DH approximation predicting $\zeta^* \sim -8mV$ and the numerical result predicting about $\zeta^* \sim -22mV$. Again this result should be viewed as conservative. The trend of descreasing ζ potential as the ionic strength increases is consistent with the results of Zheng[30] who compared his results with several sets of experimental data.[31]

7 Summary

In this work we have analyzed the use of the Debye-Huckel Approximation in micro and nanochannels. The advantage of the DH approximation is that it leads to analytical solutions for the bulk fluid

velocity and for the electric potential. We have compared the numerical solutions for the full nonlinear problem with the corresponding solutions using the Debye-Huckel Approximation. We have examined channels of height on the nanometer scale up through channels which have heights on the micron scale.[8] Moreover, the Gouy-Chapman picture of the EDL emerges naturally at higher potentials and hence greater cation - anion concentration differences which implies higher surface charge densities. We have established a region of validity of the Debye-Huckel approximation which is seen to depend on whether the magnitude of the potential is less than 26 mV. Analytical solutions for the surface charge density, the $\zeta-$potential and the volume flowrate have been derived based on the values of the wall mole fractions. The width of the EDL scales on the Debye length and for the results presented here, where applicable the width of the electric double layer is $\delta \sim 5\lambda$.

We have also considered the case where a potential difference exists across the channel which can correspond to the case where the walls of the channel are oppositely charged. The asymmetric solutions of the type described in this paper has appeared in the open literature only once[8], although early experimental work on asymmetry potentials has been discussed by Hunter[3]. In addition, we have been able to relate the ζ-potential to the mole fractions at the walls of the channel and so we have shown that specifying $\zeta-$potential at the wall is equivalent to specifying the mole fractions.

We have also shown how the present results valid for a pair of monovalent ions can be generalized to the case of an arbitrary number of multivalent species. In this case, the DH approximation fails sooner than for monovalent electrolyte solutions. Both asymmetric and symmetric electrolyte solutions have been considered.

It is observed that for ionic strength $I \sim 0.1M$ and slightly above, beyond a value of the channel height of about $20 - 25\,nm$ the bulk velocity is constant for a pair of monovalent ions and corresponds to the classical electroosmotic profile for the given values of wall mole fraction. Of course, the precise channel height where the electroosmotic profile emerges depends on mole fraction. In the case of multivalent ionic species, for $+n_1/-n_2$ multivalent ionic species, for which $n_1 \neq n_2$, the velocity and potential profiles are more parabolic-like, increasing the shear stress in the core of the channel.

It is useful to speculate on the limits of continuum theory. Our continuum results compare well with the experimental taken by iMEDD, Inc. for rectangular channels down under ten nanometers in height. Work by Zhu *et al*[32] shows that Molecular Dynamics simulations exclude ions from the first wall layer and so disagrees with the classical Poisson-Boltzmann theory presented here for an effective channel height of about six nanometers or about twenty water diameters. Thus classical continuum approaches should be valid for the design of synthetic nanoscale devices for transport, separation, rapid molecular analysis and manipulation since these devices have channels on the order of ten nanometers at the minimum.

Acknowledgements: This work is part of a larger effort is funded by DARPA under agreement number F30602-00-2-0613. The author is grateful to the contract monitors Dr. Anantha Krishnan (DARPA), Mr. Clare Thiem and Mr. Duane Gilmour of Air Force Research Lab (IFTC) for their support. Srinivasa Nimmala and Pradeep Gnanaprakasam aided in the preparation of some of the plots.

References

[1] R. A. Robinson and R. H. Stokes. *Electrolyte Solutions*, Academic Press: New York, 1959.

[2] J. S. Newman, *Electrochemical Systems*, Prentiss-Hall : Englewood Cliffs, NJ, 138-240, 1973.

[3] R. J. Hunter, *Zeta Potential in Colloid Science*, Academic Press: London, 59-124, 1981.

[4] R. F. Probstein, *Physicochemical Hydrodynamics*, Butterworths: Boston, 161-200, 1989.

[5] Paul Delahay, *Double Layer and Electrode Kinetics*, Wiley Interscience, New York, 1965.

[6] John O'M. Bockris and Amulya K. N. Reddy, *Modern Electrochemistry, Volume 1 Ionics*, Second Edition. Plenum Press, New York and London, 1998.

[7] Jacob Israelachvili, *Intermolecular and Surface Forces*, 2nd Edition, Academic Press, London, 1991.

[8] A. T. Conlisk, Jennifer McFerran, Zhi Zheng, and Derek Hansford, *Analytical Chemistry*, 2002, *74*, 2139-2150.

[9] E.J.W. Verwey and J.Th. G. Overbeek, *Theory of Stability of Lyophobic Colloids*, Elsevier: Amsterdam, 1948.

[10] W. Qu and D. Li, *J. Colloid and Interface Science*, 2000, *224*, 397-407.

[11] D. Burgeen and F. R. Nakache, *The Journal of Physical Chemistry*, 1964, *68*, 1084-1091.

[12] S. Levine, John R. Marriott, and Kenneth Robinson, *Faraday Transactions II*, 1975, *71*, 1-11.

[13] C. L. Rice and R. Whitehead, *Journal of Physical Chemistry*, 1965, *69*, no. 11, 4017-4024.

[14] S. Levine, J. R. Marriott, G. Neale, and N. Epstein, N., *Journal of Colloid and Interface Science*, 1975, *52*, no. 1, 136-149.

[15] Zheng, Z., Hansford, Derek J, Conlisk, A. T., *Electrophoresis*, 2003, 24, 3006-3017.

[16] Guenat, O. T., Ghiglione, D., Morf, W. E., and de Rooij, *Sensors and Actuators B*, 2001, *72*, 273-282.

[17] Dasgupta, Purnendu K., Kar, Satyajit, *Analytica Chimica Acta*, 1999, *394*, 1-12.

[18] Kar, Satyajit, Dasgupta, Purnendu K., *Microchemical Journal*, 1999, *62*, 128-137.

[19] Kirby, Brian J., Shepodd, Timothy J., Haesselbrink, Ernest F., *Journal of Chromatography A*, 2002, *979*, 147-154.

[20] Bull, J. L., Hunt A. J., Hasselbrink, E. F., Guo, L. J., Kurabayashi, K., Meyhofer, E., Proceedings of the Second Joint EMBS/BMES Conference, Houston, 2002.

[21] Lazar, Iulia M., Karger, Barry L., *Anal. Chem.* , 2002, *74*, 6259-6268.

[22] Morf, W. E., Guenat, O. T., de Rooij, N. F., *Sensors and Actuators B*, 2001, *72* , 266-272.

[23] Min, Jung Yim, Hasselbrink, E. F., Kim, Sung Jin, *Sensors and Actuators B*, 2004, *98*, 368-377.

[24] Paul, P. H., Garguilo, M. G., Rakestraw, D. J., *Anal. Chem.* , 1998, *70*, 2459-2467.

[25] Herr, A. E., Mohlo, J.I., Santiago, J. G., Mungal, M. G., Kenny, T. W., 2000, *Ann. Chem.*, *72*, 1053-1057.

[26] Santiago, J. G., 2001, *Analytical Chemistry*, *73*, 2353-2365.

[27] Hansford, Derek, Desai, T. Ferrari, M., *Biochip Technology*, eds. J. Cheng, L. J. Kricka, Harwood Academic Publishers, 341, 2001.

[28] Debye, P. and Huckel, E., *Z. Phys.* , 1923, *24*, 185.

[29] Gouy, G. *J. Physics A*, 1910, *9*, 457.

[30] Zheng, Z. "Electrokinetic Flow in Micro- and Nano-fluidic Components", PhD. Thesis, The Ohio State University, 2003.

[31] Ramsey, J. M. Private Communication 2003.

[32] Zhu, Wei, Singer, Sherwin, Zheng, Z., and Conlisk, A. T., accepted *Phys. Rev. E.*

List of Figure Captions

Figure 1. (a) A micro/nanochannel system fabricated by Hansford.[27] (b) Nanochannels fabricated by iMEDD, Inc. of Columbus, Ohio.

Figure 2. Pressure drop and applied voltage as a function of channel height to achieve a flowrate of $Q = 10^{-6} L/min$ in the system of Figure 1.

Figure 3. Geometry of the channel. Here it is only required that $h << W, L$ where W is the width of the channel and L its length in the primary flow direction. u, v, w are the fluid velocities in the x, y, z directions.

Figure 4. Sketch of the channel showing the negatively charged surface attracting positive ions. (a) The case where the electric double layer is thin; the core is electrically neutral. (b) Finite electrical double layer width; here the core is not electrically neutral.

Figure 5. Results for the dimensionless velocity and potential along with mole fractions for the symmetric case of an NaCl-water mixture. Here the electric field corresponds to 0.06 volts over a channel of length $L = 3.5\mu m$; the channel height $h = 24\ nm$. The solid lines are the numerical solution and the dasheded lines are the Debye-Huckel Approximation. (a) Velocity and potential. (b) Mole fractions for $f^0 = f^1 = 0.00252$ and $g^0 = g^1 = 0.00276$.

Figure 6. Results for the dimensionless velocity and potential along with mole fractions for the symmetric case of an NaCl-water mixture. Here the electric field corresponds to 0.06 volts over a channel of length $L = 3.5\mu m$; the channel height $h = 24\ nm$. The solid lines are the numerical solution and the dashed lines are the Debye-Huckel Approximation. (a) Velocity and potential. (b) Mole fractions for $f^0 = f^1 = 0.00025$ and $g^0 = g^1 = 0.00276$.

Figure 7. Results for the dimensionless velocity and potential along with mole fractions for the symmetric case of an NaCl-water mixture. Here the electric field corresponds to 0.06 volts over a channel of length $L = 3.5\mu m$; the channel height $h = 4\ nm$. The solid lines are the numerical solution and the dashed lines are the Debye-Huckel Approximation. (a) Velocity and potential. (b) Mole fractions for $f^0 = f^1 = 0.00252$ and $g^0 = g^1 = 0.00276$.

Figure 7. Results for the dimensionless velocity and potential along with mole fractions for the symmetric case of an NaCl-water mixture. Here the electric field corresponds to 0.06 volts over a channel of length $L = 3.5\mu m$; the channel height $h = 4\ nm$. The solid lines are the numerical solution and the dashed lines are the Debye-Huckel Approximation. (a) Velocity and potential. (b) Mole fractions for $f^0 = f^1 = 0.00025$ and $g^0 = g^1 = 0.00276$.

Figure 8. Results for the dimensionless velocity and potential along with mole fractions for the symmetric case of an NaCl-water mixture. Here the electric field corresponds to 0.06 volts over a channel of length $L = 3.5\mu m$; the channel height $h = 4\ nm$. The solid lines are the numerical solution and the dashed lines are the Debye-Huckel Approximation. (a) Velocity and potential. (b) Mole fractions for $f^0 = f^1 = 0.00025$ and $g^0 = g^1 = 0.00276$.

Figure 9 Results for the volume flow rate and surface charge density for the parameters of Table 1; here $h = 24nm$ and $f_c^0 = 0.154M$ and is held fixed. The width of the channel is $W = 3.5\mu m$. (a) Flow rate, (b) surface charge density.

Figure 10 Results for the dimensionless velocity and potential along with mole fractions for the asymmetric case of an NaCl-water mixture. Here the electric field corresponds to 0.06 volts over a channel of length $L = 3.5\mu m$; the channel height $h = 24\ nm$. The solid lines are the numerical solution and the dash lines are the Debye-Huckel Approximation. The '*' curve is the velocity calculated numerically. (a) Velocity and potential. (b) Mole fractions for $f^0 = 0.00025$,

$f^1 = 0.00031$ and $g^0 = 0.00276$, $g^1 = .00220$.

Figure 11. Results for the dimensionless velocity and potential along with mole fractions for the asymmetric case of an NaCl-water mixture. Here the electric field corresponds to 0.06 volts over a channel of length $L = 3.5\mu m$; the channel height $h = 4\ nm$. The solid lines are the numerical solution and the dashed lines are the Debye-Huckel Approximation. (a) Velocity and potential. The lower line is the velocity. (b) Mole fractions for $f^0 = 0.00252$, $f^1 = 0.00315$ and $g^0 = 0.00413$, $g^1 = .00330$.

Figure 12. Results for the dimensionless velocity and potential along with mole fractions for the asymmetric case of an NaCl-water mixture. Here the electric field corresponds to 0.06 volts over a channel of length $L = 3.5\mu m$; the channel height $h = 4\ nm$. The solid lines are the numerical solution and the dashed lines are the Debye-Huckel Approximation. The $*$ is the numerical evaluation of the velocity. (a) Velocity and potential. (b) Mole fractions for $f^0 = 0.0025$, $f^1 = 0.00503$ and $g^0 = 0.00550$, $g^1 = 0.00275$.

Figure 13 Results for the dimensionless velocity and potential along with mole fractions for the case of a $+2/-2$ electrolytes for $h = 24nm$. The same parameters are used as in the previous figures. (a) Velocity and potential. (b) Mole fractions for $f^0 = f^1 = 0.00025$ and $g^0 = g^1 = 0.00276$. The straight lines are the asymptotic results for potential and velocity (a) and cation mole fraction (b).

Figure 14 Results for the dimensionless velocity and potential along with mole fractions for the case of a $+2/-1$ electrolytes for $h = 24nm$. The same parameters are used as in the previous figures. (a) Velocity and potential. (b) Mole fractions for $f^0 = f^1 = 0.00025$ and $g^0 = g^1 = 0.00276$. The straight lines are the asymptotic results for potential and velocity (a) and cation mole fraction (b).

Figure 15 Results for the dimensionless velocity and potential along with mole fractions for the case of a $+3/-1$ electrolytes for $h = 24nm$. The same parameters are used as in the previous figures. (a) Velocity and potential. (b) Mole fractions for $f^0 = f^1 = 0.00025$ and $g^0 = g^1 = 0.00276$. The straight lines are the asymptotic results for potential and velocity (a) and cation mole fraction (b).

g_c^0	-ζ(DH)	-ζ(NL)
0.154	0.0441	0.0441
0.308	0.3719	0.3907
0.616	0.6275	0.7372
0.924	0.7352	0.9399
1.232	0.7946	1.0840

Table 1: Dimensionless ζ potential for wall molar concentrations of sodium $g_c^0 = .154nM$ where $n = 1, 2, 4, 6, 8$. A dimensionless $\zeta = 1$ corresponds to 25mV. The left hand column is the Debye Huckel approximation and the right hand column is the full nonlinear solution.

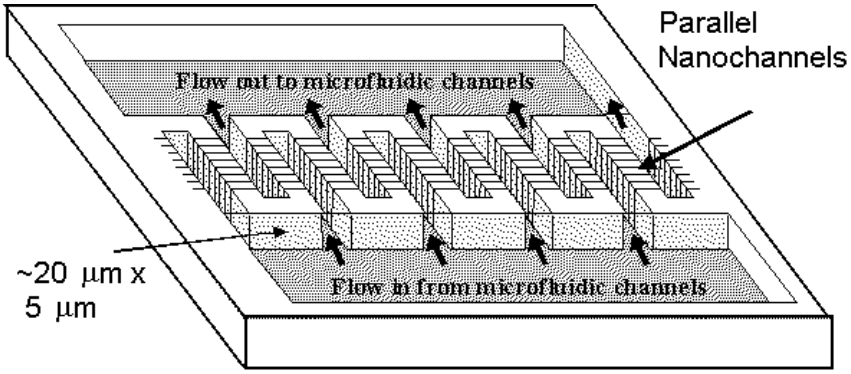

(a)

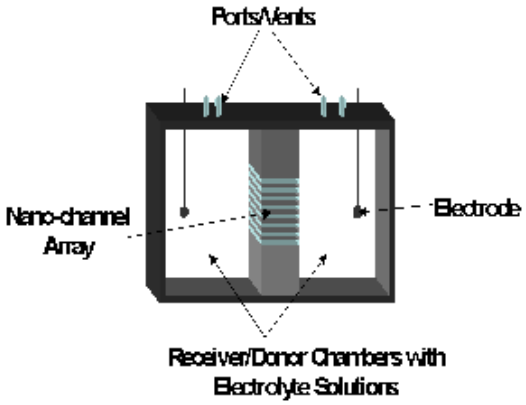

(b)

Figure 1: Conlisk, Electrophoresis, Special Issue on CEC and EKC

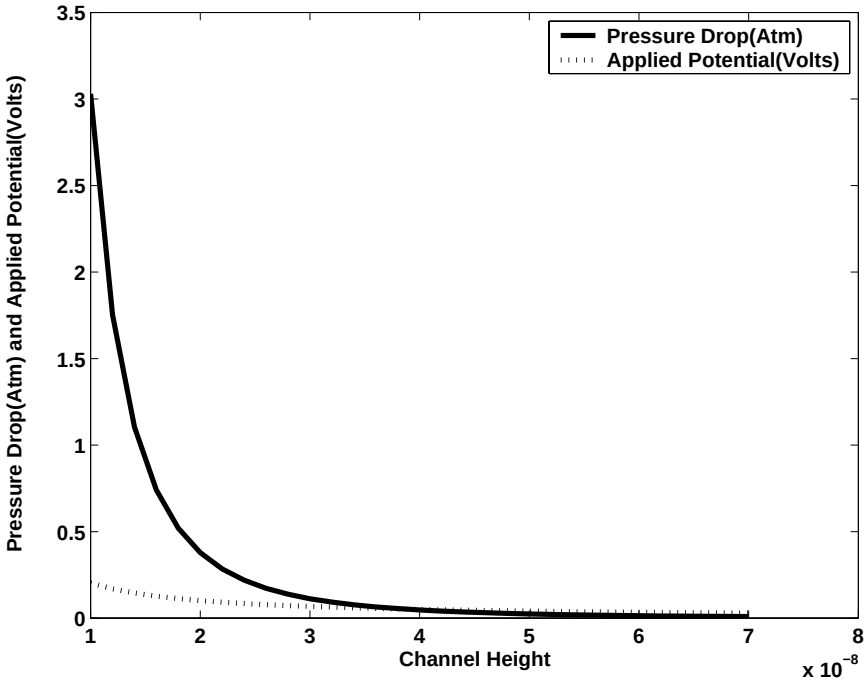

Figure 2: Conlisk, Electrophoresis, Special Issue on CEC and EKC

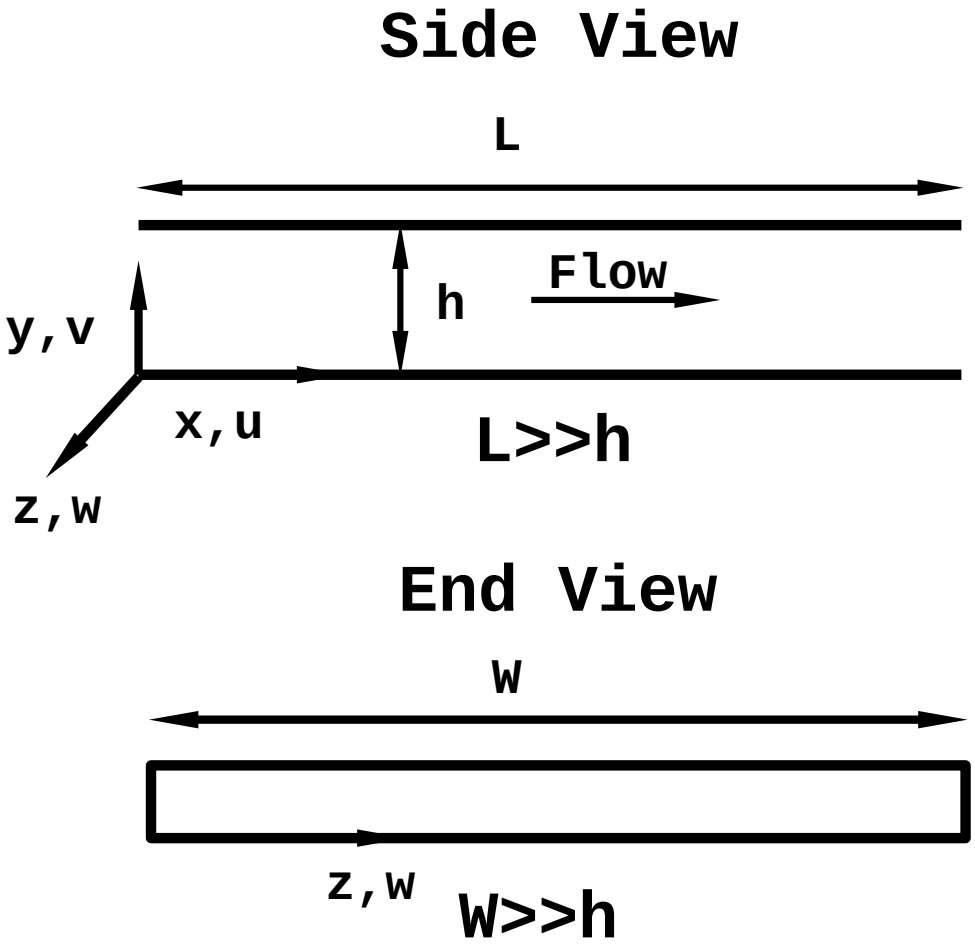

Figure 3: Conlisk, Electrophoresis, Special Issue on CEC and EKC

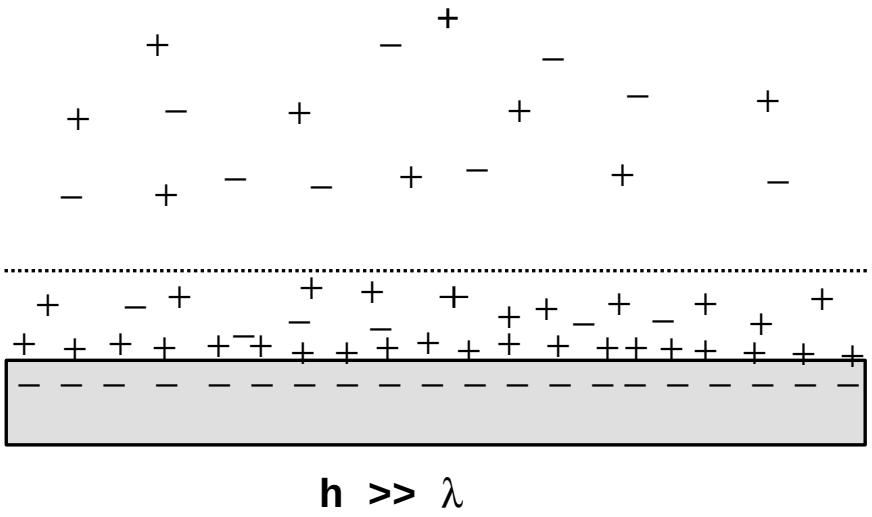

h >> λ

(a)

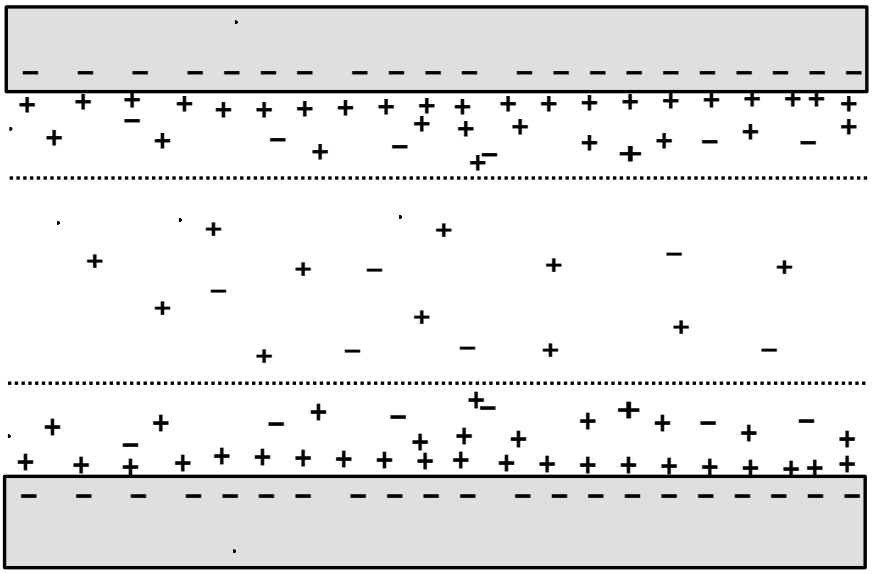

h ~ λ

(b)

Figure 4: Conlisk, Electrophoresis, Special Issue on CEC and EKC

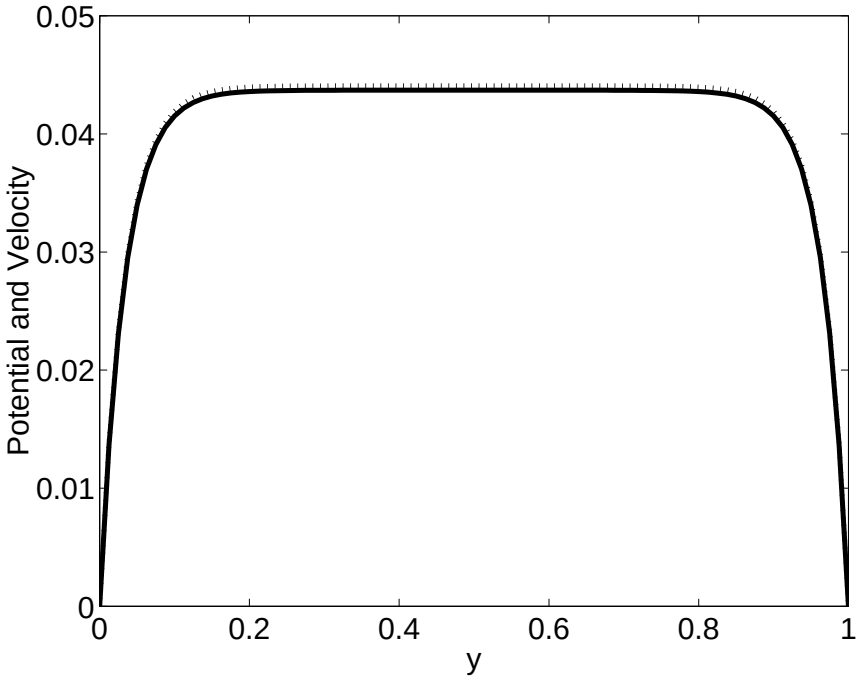

(a)

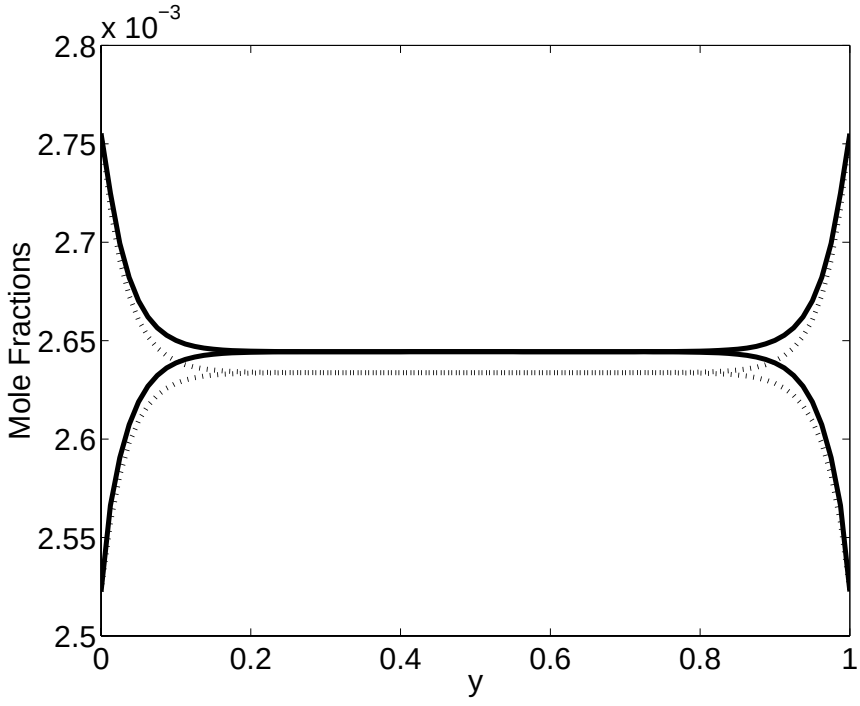

(b)

Figure 5: Conlisk, Electrophoresis, Special Issue on CEC and EKC

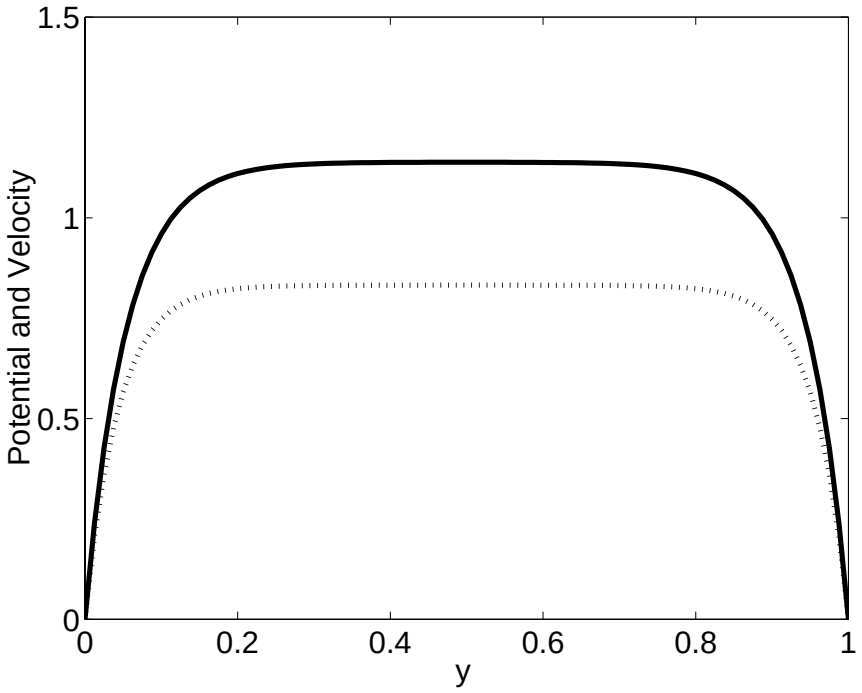

(a)

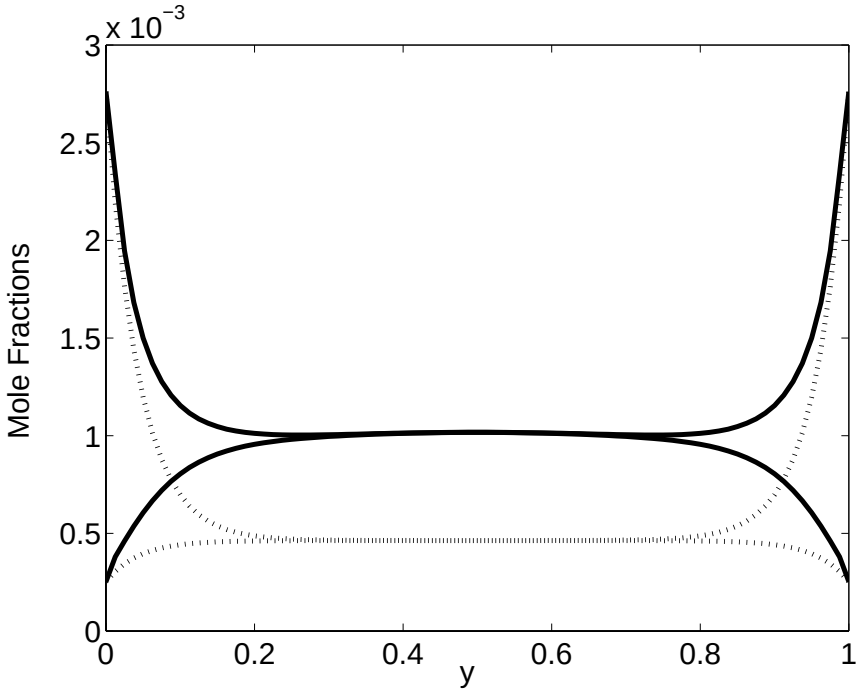

(b)

Figure 6: Conlisk, Electrophoresis, Special Issue on CEC and EKC

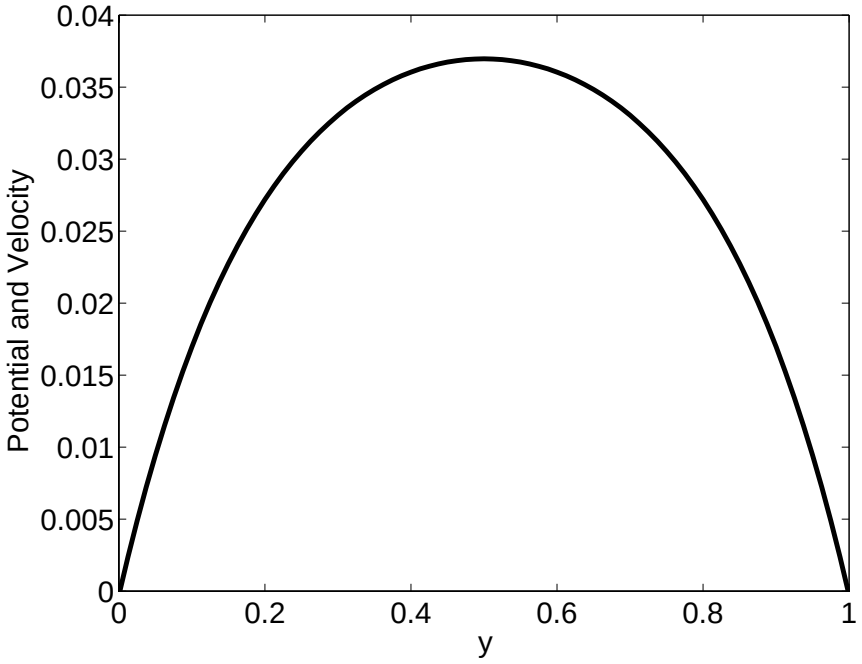

(a)

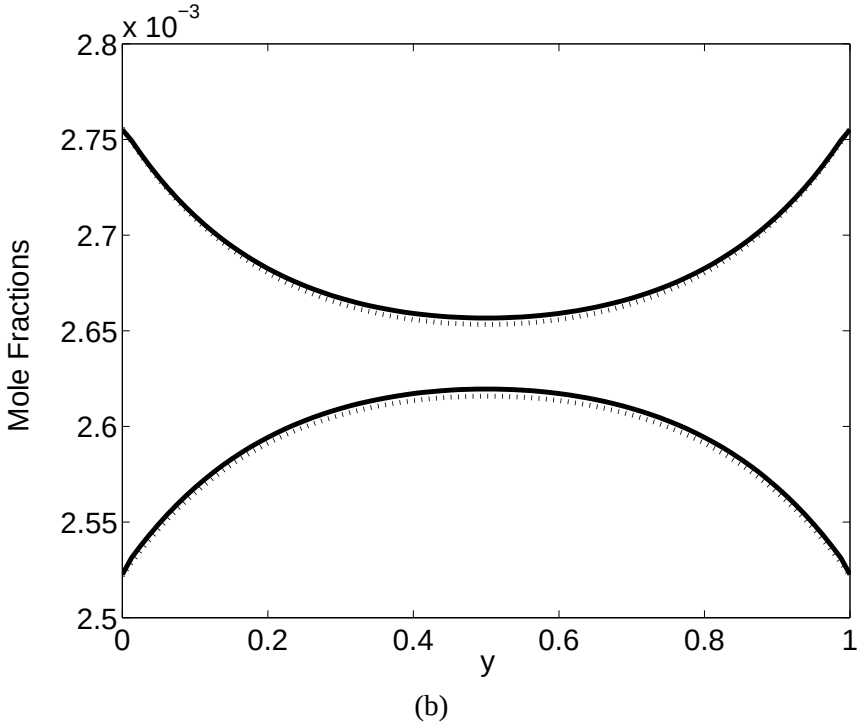

(b)

Figure 7: Conlisk, Electrophoresis, Special Issue on CEC and EKC

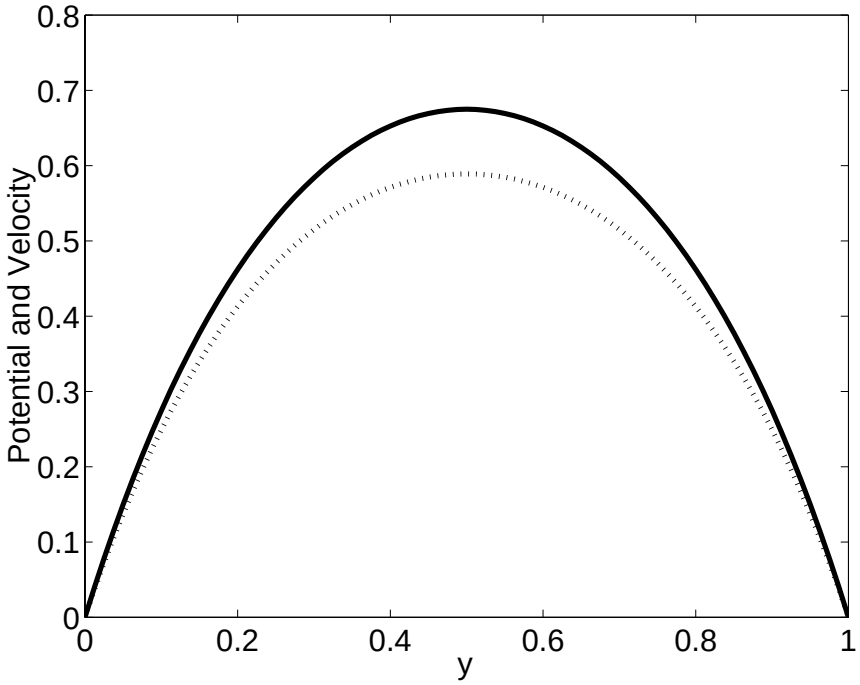

(a)

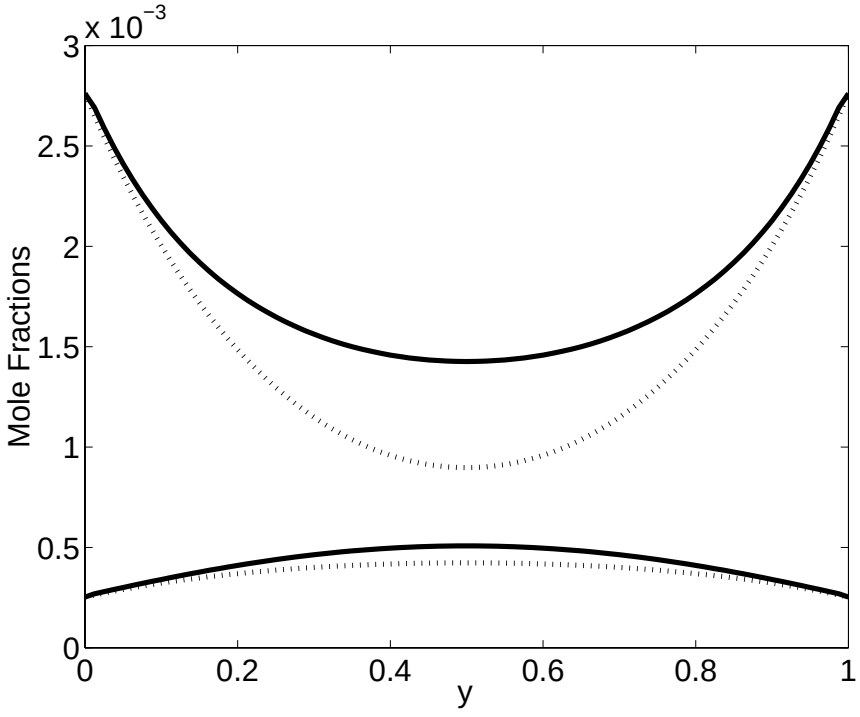

(b)

Figure 8: Conlisk, Electrophoresis, Special Issue on CEC and EKC

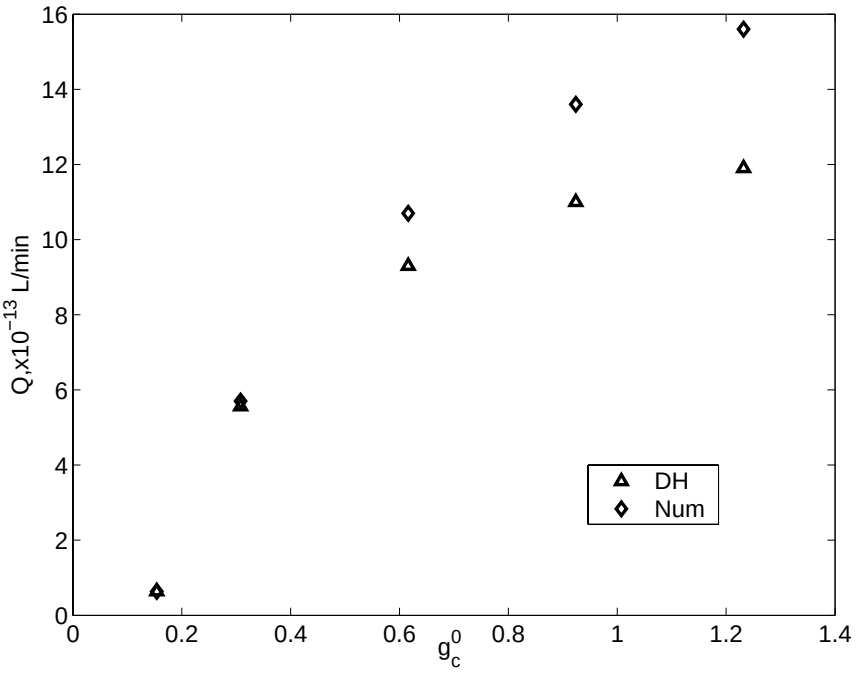

(a)

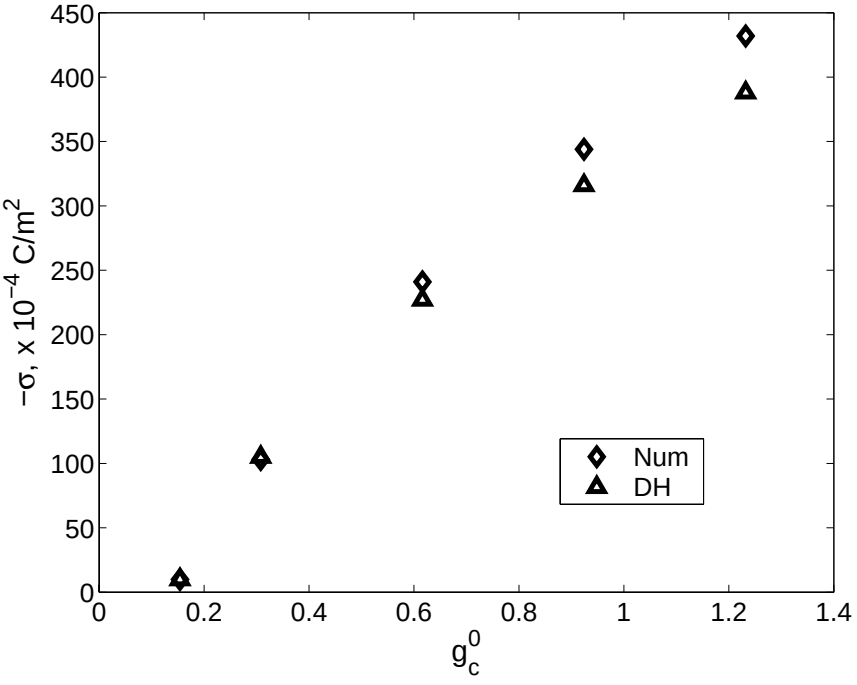

(b)

Figure 9: Conlisk, Electrophoresis, Special Issue on CEC and EKC

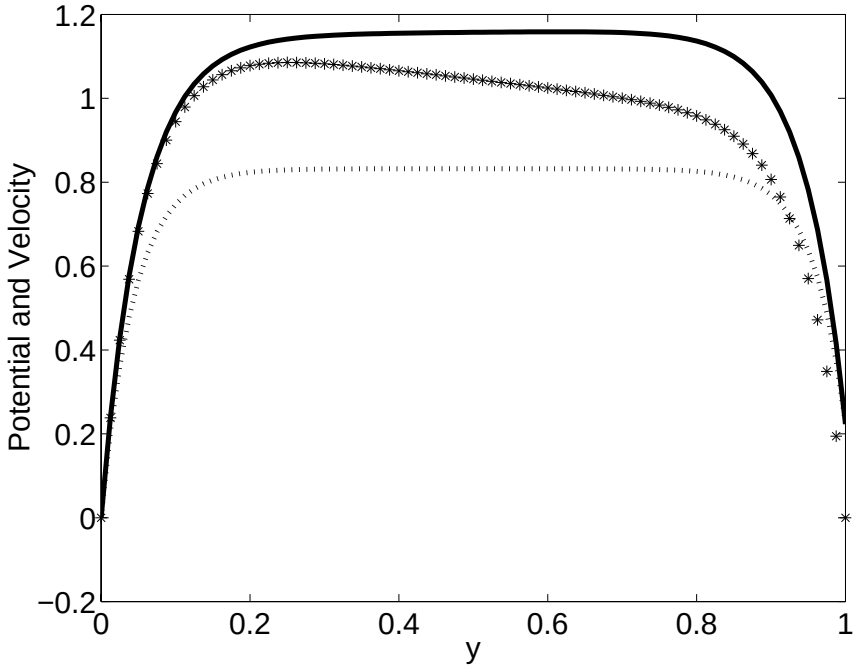

(a)

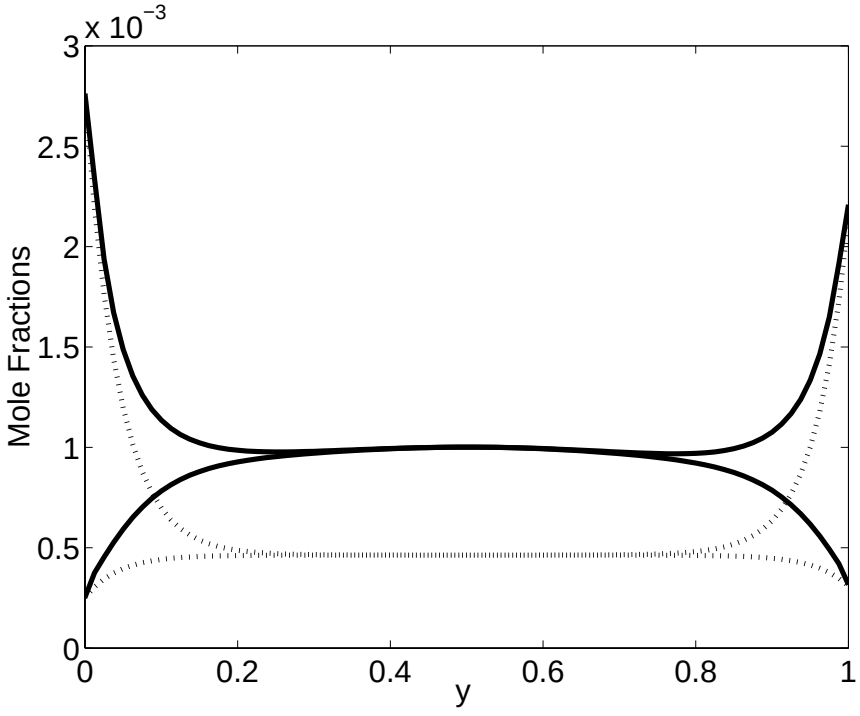

(b)

Figure 10: Conlisk, Physics of Fluid

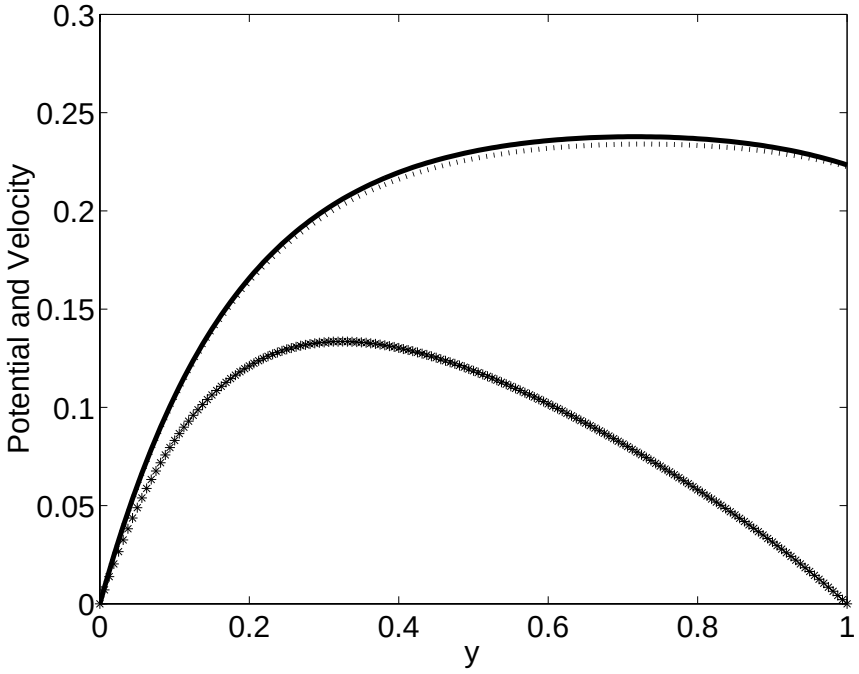

(a)

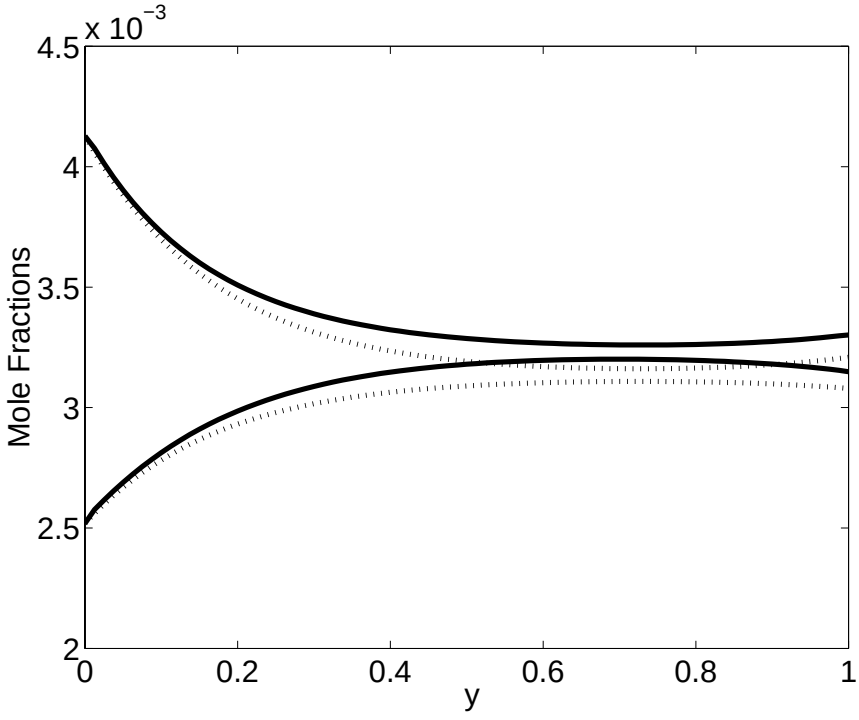

(b)

Figure 11: Conlisk, Electrophoresis, Special Issue on CEC and EKC

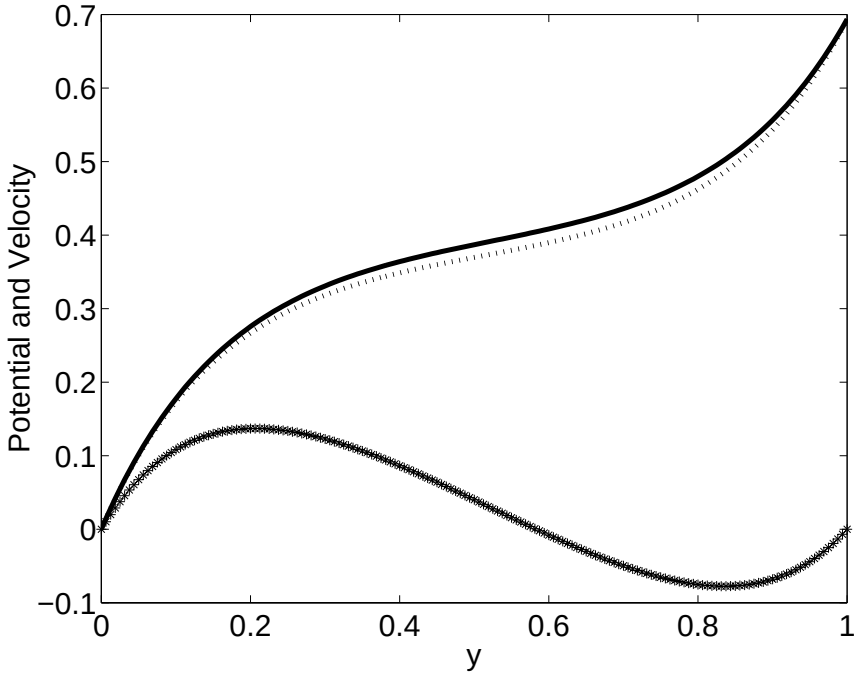

(a)

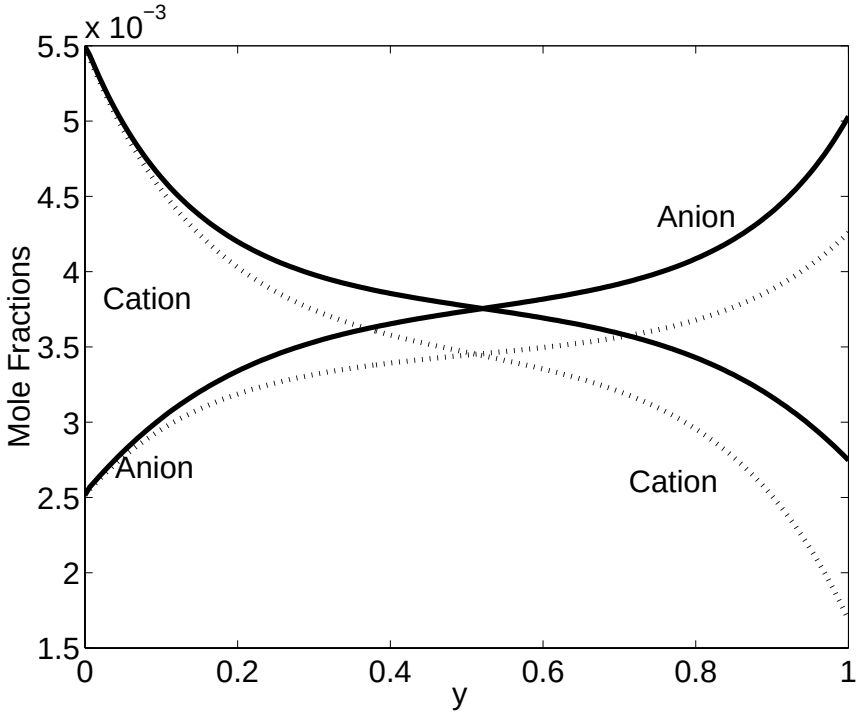

(b)

Figure 12: Conlisk, Electrophoresis, Special Issue on CEC and EKC

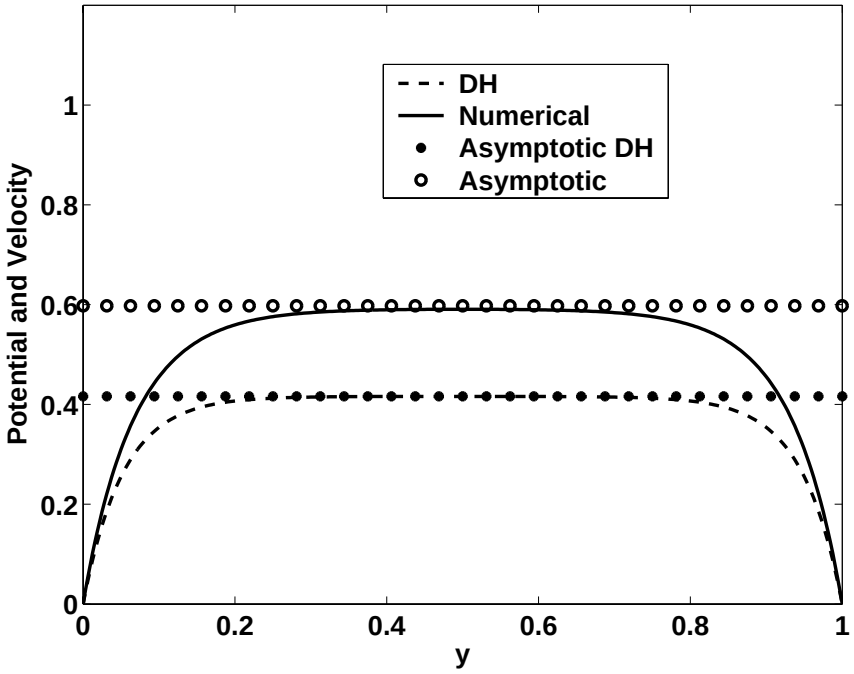

(a)

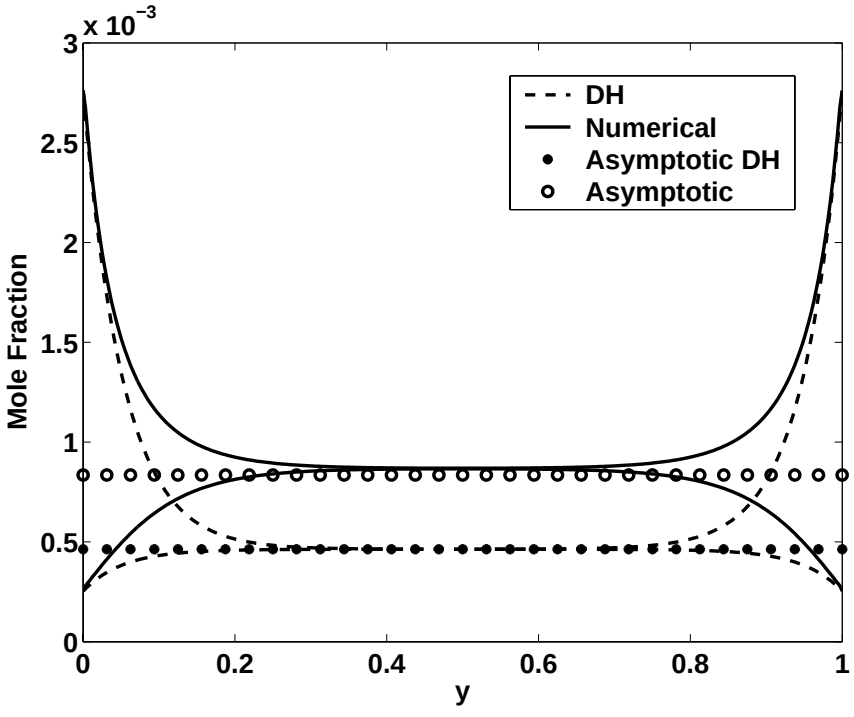

(b)

Figure 13: Conlisk, Electrophoresis, Special Issue on CEC and EKC

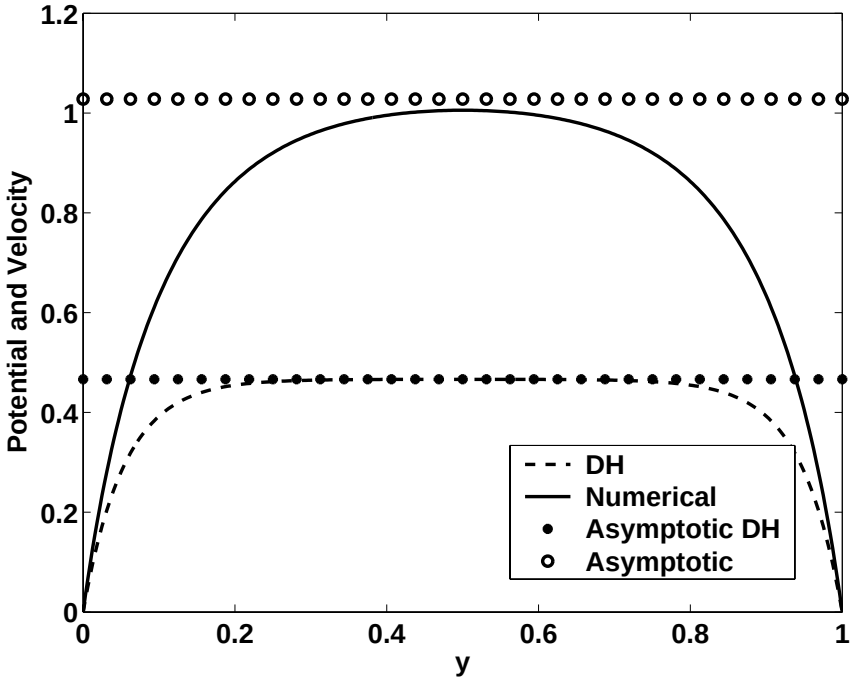

(a)

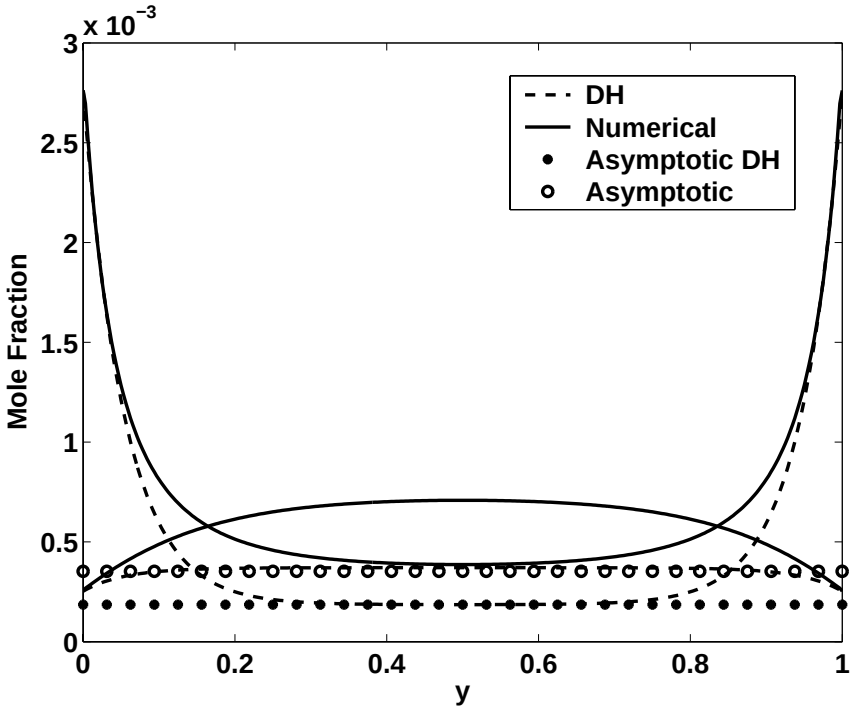

(b)

Figure 14: Conlisk, Electrophoresis, Special Issue on CEC and EK

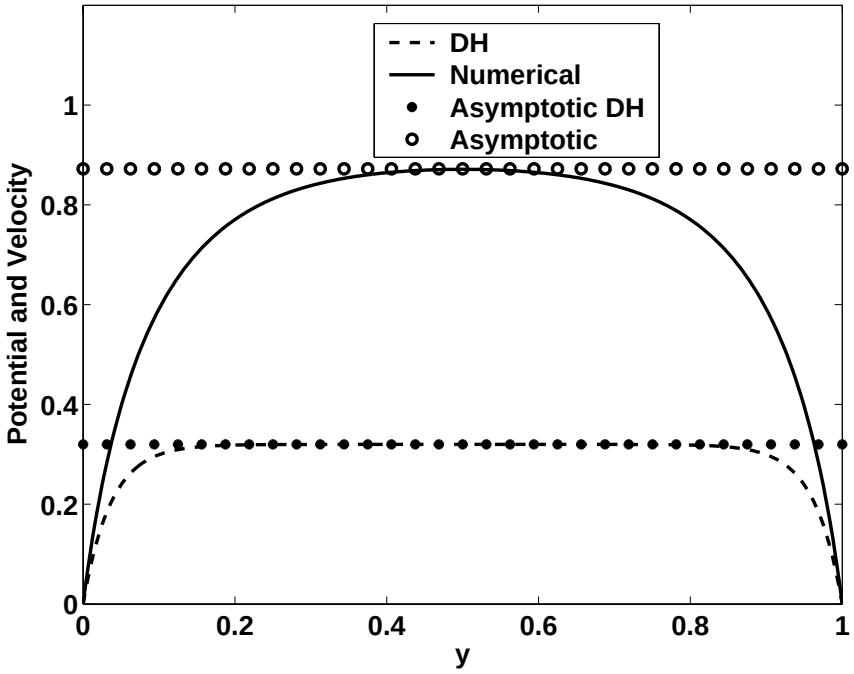

(a)

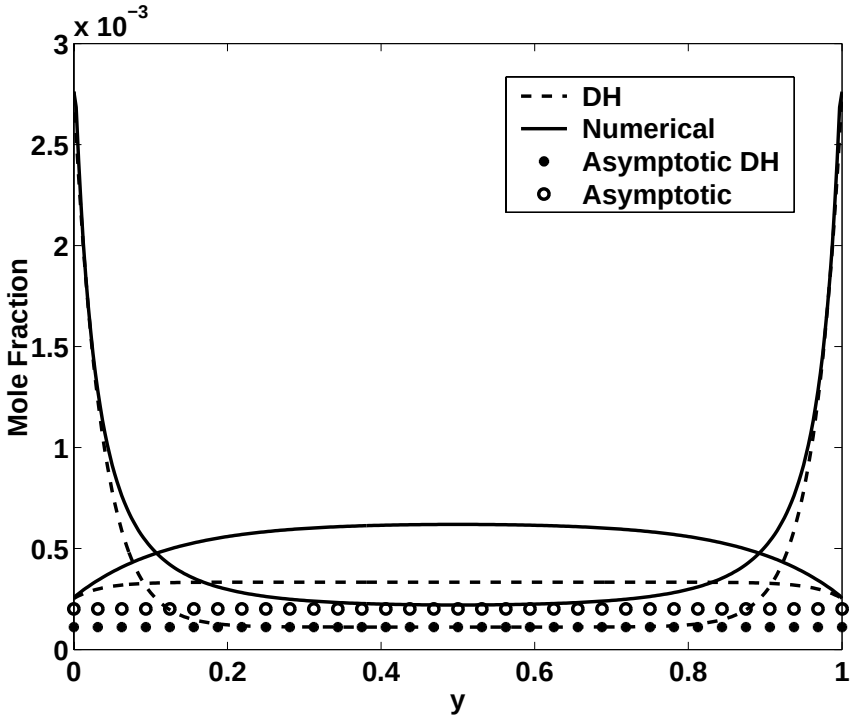

(b)

Figure 15: Conlisk, Electrophoresis, Special Issue on CEC and EKC

Appendix H:

Modeling Biomolecular Transport at the Nanoscale[1]

A. T. Conlisk
Department of Mechanical Engineering
The Ohio State University
Columbus, Ohio 43210-1107
conlisk.1@osu.edu

ABSTRACT

Biomolecular transport devices are now being used for drug development and delivery, single molecule manipulation, detection and transport and rapid molecular analysis. Many of these processes are illustrated by natural ion channels which are ion-selective nanoscale conduits in the body which allow nutrients in and waste products out. In this chapter we review the state of the art of modeling and computation of biomolecular transport in what we term synthetic ion nanochannels consisting of rectangular silicon channels for which the walls are negatively charged; we also consider the case where the walls are not charged. We consider computational techniques ranging from continuum models utilizing the Poisson-Nernst-Planck system to molecular dynamic simulations that allow tracking of individual molecules. Biomolecular transport can be modeled by incorporating hindered diffusion concepts and the methods are employed to predict the transport of albumin and glucose in silicon nanochannels. Brownian Dynamics and Molecular Dynamics methods represent techniques that must be used when continuum methods break down and these methods are also reviewed. It should be noted that the exact boundary between between continuum methods and molecular simulation methods is not always clear.

1 Introduction

Transport of ionic and biomolecular species has become an important problem with applications to rapid molecular analysis, drug development and delivery, separation and mixing and other problems. These synthetic devices operate in a manner similar to natural ion channels, although the parameter ranges of operation may be different. Natural ion channels play a crucial role in the transport of biofluids into and out of cells.[1–3]

The basic units of all living organisms are cells. In order to keep the cells functioning properly a continuous flux of ions in and out of the cell and the cell components is required. The cell is surrounded by a plasma membrane which provides selective transfer of ions. The cell membrane is made up of a double layer of lipid molecules (lipid bilayer) in which proteins are embedded. The lipid molecules are made up of a charged polar end (spheres in Figure 1), oriented towards the surface of the membranes, which are attached to two nonpolar fatty acid chains (lines attached to the spheres in Figure 1). The polarity of the membrane makes it challenging for molecules to move

in and out of cells and its components. Ions (Ca^{2+}, Cl^{-}, K^{+}, Na^{+}, H^{+}, Mg^{2+}, HCO_3^{-}, PO_4^{2-}) selectively move through the membrane via ion channels made of proteins. These protein channels are made up of a polypeptide chain with two polar regions connected by a nonpolar region which associates with the nonpolar region of the phospholipids membrane. The channel walls are charged and and the ions are transported by a transmembrane voltage drop. Natural ion channels are roughly circular, although the cross-sectional area varies in the primary flow direction[2]; synthetic channels are usually rectangular in cross-section and often much bigger than natural ion channels whose diameter is on the order of 1 nm or so.

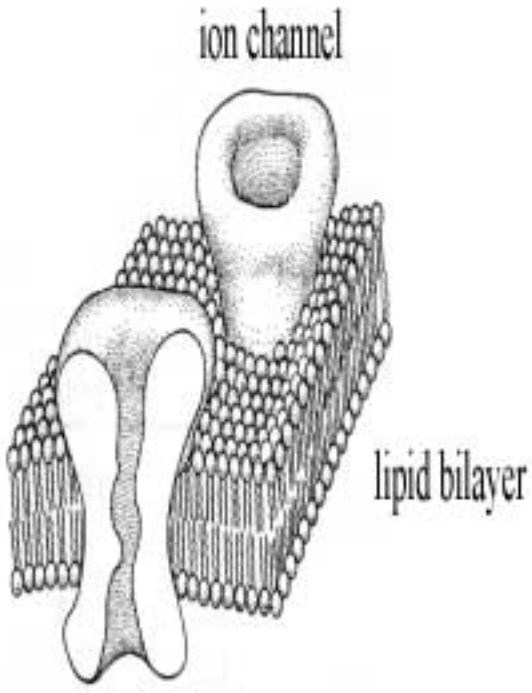

Figure 1: Image of ion channels within the lipid bilayer. From ($http$: $//hebb.mit.edu/courses/8.515/lecture1/sld013.htm$, 3/11/03)

Nanopumps which we term *synthetic ion channels* and used to transport fluids through nanochannels are essentially ion channels; these pumps may have walls that are charged or uncharged and may or may not have a voltage drop across them. A nanopump fabricated by iMEDD, Inc. of Columbus, Ohio(Sketch supplied by A. Boiarski) is depicted on Figure 2. The channels are of dimension $W \sim 44\mu m$, $L \sim 3.5\mu m$ and channel heights $h \sim 4 - 50nm$. Thus the channels are nano-constrained in one dimension and are somewhat bigger than natural ion channels.

Synthetic ion channels are of interest because they can be used as pumps to deliver a drug, for example, to a target site. The iMEDD, Inc. nanochannel membrane is essentially an array of synthetic ion channels. In this chapter we discuss the basic principles of biomolecular transport in nanoscale channels with the particular application to drug delivery and biomolecular sensing. The simplest way of modeling biomolecular transport is to treat the biomolecule similar to an ionic

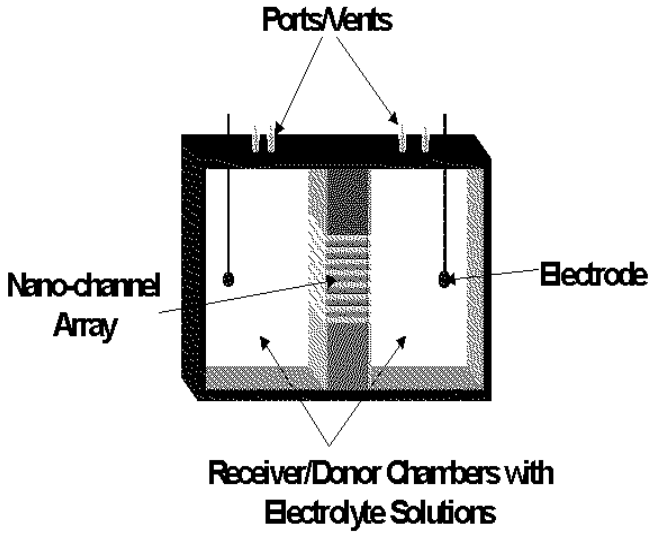

Figure 2: iMEDD, Inc of Columbus electroosmotic pump.

species, its transport characterized by a diffusion coefficient and imbedded in a buffer solution such as Phosphate Buffered Saline(PBS). The strength of this approach is that continuum methods mey be used; however a major weakness is that conformation and shape changes cannot be incorporated.

In very small channels, where the ratio of the of the biomolecular length scale to smallest channel dimension is of O(1), the diffusion coefficient is much smaller than what is measured in the bulk. Consequently, accurate rates of transport depend on the ability to determine these "hindered diffusion" coefficients and two models are discussed.

The characterization of the transport of a biomolecule as another species in a fluid mixture ignores the possibility of deformation of the molecule as it is transported into a channel or tube; this deformation is critical in some cases determining the selectivity properties of a given device. Thus continuum models which treat the biomoleule specifically have been developed and these methods will also be discussed. Brownian Dynamics methods treat the solvent as a continuum and an explicit model of the biomolecule is developed. Finally, the use of molecular techniques such as Molecular Dynamics(MD) simulations in which both the solvent and solute are treated as individual molecules will also be presented.

Biomolecules are usually charged and the electrostatic interactions with the walls is complex. While many proteins are globular, they can deform significantly and the nature and precise determination of the shape of a protein is difficult to quantify. Thus modeling efforts often use only the overall charge and size of the molecule. Experimental studies have shown that once the ratio of the biomolecular length scale to smallest channel dimension is of a certain size, the molecule may even block the channel resulting in a sudden drop of current.[4] The author is aware of no model that can predict this phenomenon from first principles.

There are perhaps thousands of papers on natural ion channels and most of them assume that the transport is governed by one-dimensional equations, with the single dimension in the direction of the flow of ionic species.[5] The three dimensional problem has been considered by Cardenas *et al.*[6] A mathematical derivation of the one-dimensional governing equations from the full three-

dimensional equations is given by Gillespie.[2] Essentially, Gillespie[2] shows that the one-dimensional form of the equations arises from an averaging process along given curves on which the concentration and potential are constant. These same equations describing biomolecular transport can be obtained by simply integrating over the cross section of the channel.

Given the breadth of this review, it is impossible to cite all of the relevant references; nevertheless, it is hoped that the references cited here can be used as a starting point for an in-depth study of transport at the nanoscale.

In this chapter we discuss the properties of natural and synthetic ion channels and review the computational methods used to evaluate transport through these channels. The focus of this review is on the three main classes of methods corresponding to the Poisson-Nernst-Planck system, on Brownian Dynamics methods and on Molecular Dynamics methods. After an initial discussion of the nature of natural ion channels, we discuss rectangular synthetic ion channels having one nano-constrained dimension. These channels are appropriate for use in single molecule detection and analysis, and drug delivery.

Based on the continuum methods of analysis we then apply the results to the transport of albumin and glucose and compare the theoretical results with the experimental data from iMEDD. The comparisons are surprisingly good considering that the only physical parameter of the protein accounted for in the model is the globular size.

2 Background

It is useful to begin the discussion with a review of the modeling procedures employed for natural ion channels since the theory of such models has been significantly improved in recent years. Natural ion channels are one class of membrane transport proteins and are narrow, water-filled tunnels, permeable to the few ions and molecules small enough to fit through the tunnels (approximately 10 Å in diameter).[7] Ion channels present in excitable membranes are a common pore protein channel. Ion channels are responsible for electrical signaling in nerves and muscles.[8] The ions responsible for the majority of nervous signaling are Ca^{2+}, Cl^{-}, K^{+}, and Na^{+}. The channels are responsive to different stimuli: a membrane potential change, a neurotransmitter or other chemical stimulus, a mechanical deformation, and more. The channel's response to these stimuli, called gating, corresponds to an opening or closing of the pore. The open pore has a selective permeability to ions, only allowing certain ions to flow through its electrochemical activity gradients. The ions flow at a very high rate, greater than 10^6 ions per second, with a single ion taking on the order of one microsecond to traverse the channel.

According to Levitt,[5] five major methods of modeling natural ion channels have appeared in the literature: molecular dynamics, three-dimensional Brownian dynamics, three-dimensional Poisson-Nernst-Planck (PNP), one-dimensional Brownian dyanamics, and the one-dimensional Poisson-Nernst-Planck approach. It has been suggested often in the literature that if the channel properties are known to an atomic level then the most direct method is molecular dynamic simulations, because they take into consideration the atomic structure of the water molecules and channel proteins. The weakness of this method is the computation time; a simulation of an acetylcholine channel took approximately one year for a single ion crossing (in 1998!). This long computation time is due to the fact that molecular simulation can only describe nanoseconds of real time, which is not long enough for modeling ion movement through the entire channel which takes place on the microsecond scale.

Molecular dynamic simulations can be simplified by using advanced computational techniques. These techniques include alchemical free energy perturbation and umbrella sampling.

In three-dimensional Brownian dynamics, the protein structure is held fixed and the water molecules within the channel are treated as a continuum. The solutes are treated discretely and the ion-ion interactions are accounted for. According to Levitt,[5] the best method of modeling natural ion channels is a combination of molecular dynamics and Brownian dynamics. The three-dimensional Poisson-Nernst-Planck approach simplifies the Brownian dynamic approach by averaging the electric field on an ion over all the possible positions of the other ions. This average electric field is calculated using Poisson's equation. The Poisson equation is coupled with the Nernst-Planck equation, which models ions undergoing Brownian motion in the electric field. This approach is much faster than Brownian dynamics because it replaces a sequence of time step calculations with a global numerical solution. The disadvantage of this method is that the ion-ion interactions are reduced to a ion-mean field interaction. Recall that natural ion channels are around 1 nm in diameter and molecular effects can become important at $\sim 5nm$.

The three-dimensional Brownian Dynamics and Poisson-Nernst-Planck approaches can be further simplified by averaging the concentration over the cross section. By comparison with experimental data we will be able to quantify this aproximation. It has been observed that in most circumstances this assumption does not generate much error, because it often cancels out the error introduced by uncertainties in atomic channel structure and this is the basis for the use of the Poisson-Nernst-Planck system to model flow in ion channels.[2, 3, 9, 10]

Many models have been developed for ion channel flow. However, most of these models are based on molecular dynamics.[11] An extensive reading list is given at the end of the paper by Roux.[11] The use of Poisson-Nernst-Planck equations, a continuum theory, to model ion channels began in the early 1990s with Chen *et al*.[10] This model has been used to model Ca^{2+} channels[12, 13] as well as Gramicidin channels.[14] In addition to simply modeling the flow within the channel, these models usually incorporate the flow within the baths on each end of the channel.[2, 15] Non-ideal effects which occur at higher electrolyte concentration levels have recently been examined by Gillespie *et al*.[16]

3 Governing Equations for Synthetic Ion Channels in the Continuum Regime: The Poisson-Nernst-Planck System

The equations governing transport of a given species in an electrolyte buffer solution are given by the Navier-Stokes equations along with an electrical potential equation, and equations for the concentration of each of the species.[17] The flux of a given species in an electrolyte solution is due in general to Fickian diffusion, electrical migration and to bulk fluid motion. Thus most biomolecular transport studies begin with the expression for the dimensional flux of species A in the form

$$\vec{n}_A^* = -cD_A \nabla X_A + u_A z_A F X_A \vec{E}^* + cX_A \vec{u}^* \tag{1}$$

Here D_A is the diffusion coefficient, c the total concentration, X_A is the mole fraction of species A, which can be either an anion or a cation, $u_A = \frac{D_A}{RT}$ is the mobility, where R is the gas constant, T is the temperature, u_A is the mobility, z_A is the valence, F is Faraday's constant, $\vec{E}^*$ is the total electric field and $\vec{u}^*$ is the mass average velocity of the fluid. In almost all cases of practical interest, the mixture is dilute in the electrolytes and so the diffusion coefficient can be approximated by its

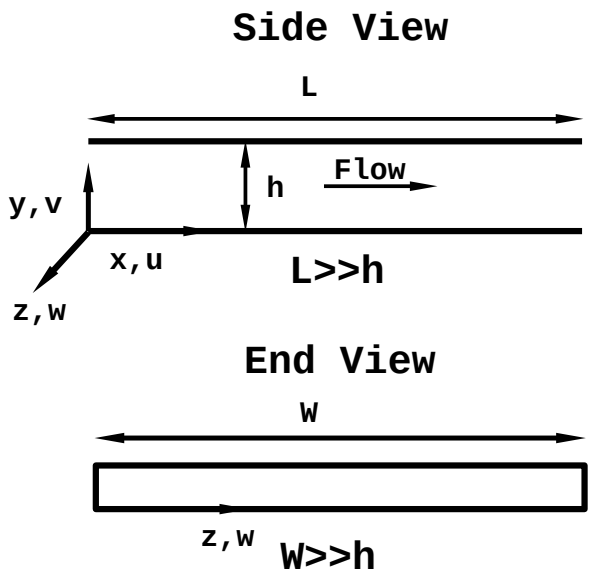

Figure 3: Geometry of the channel. Here it is only required that $h << W$ where W is the width of the channel; the length L in the primary flow direction can be of the order of the channel height or much smaller as depicted in the figure. u, v, w are the fluid velocities in the x, y, z directions.

value for the solvent. The mole fraction distribution is governed by taking $\nabla\cdot$ of the flux equation (1) and the result is

$$\frac{\partial}{\partial y}\left(\frac{\partial D_A X_A}{\partial y}\right) + \epsilon_1^2 \frac{\partial}{\partial x}\left(\frac{\partial D_A X_A}{\partial x}\right) + \epsilon_2^2 \frac{\partial}{\partial z}\left(\frac{\partial D_A X_A}{\partial z}\right) =$$

$$z_A\left(\epsilon_1 \frac{\partial X_A E_x}{\partial x} + \frac{\partial X_A E_y}{\partial y} + \epsilon_2 \frac{\partial X_A E_z}{\partial z}\right) \tag{2}$$

Here we have assumed that the mole fractions are small and so the mixture is dilute; in this case the diffusion coefficient of an ionic species can be approximated by its value with respect to the solvent, water. Also we have not assumed that the diffusion coefficient is a constant; D_A is a scaled dimensionless diffusion coefficient, the scaling factor corresponding to say its value in the bulk. We will disucuss the possible form of a variable diffusion coefficient later.

The dimensionless equations governing bulk fluid motion for a mixture containing two electrolytes in the absence of the nonlinear convective terms which at nanoscale will be small are given by

$$0 = -\epsilon_1 \epsilon^2 \frac{\partial p}{\partial x} + \beta(X_+ - X_-) + \epsilon^2 \nabla^2 u \tag{3}$$

$$0 = -\epsilon^2 \frac{\partial p}{\partial y} + \Lambda \beta \epsilon^2 \frac{\partial \phi}{\partial y}(X_+ - X_-) + \epsilon^2 \nabla^2 v \tag{4}$$

$$0 = -\epsilon_2 \epsilon^2 \frac{\partial p}{\partial z} + \epsilon_2 \epsilon^2 \Lambda \frac{\partial \phi}{\partial z}(X_+ - X_-) + \epsilon^2 \nabla^2 w \tag{5}$$

where the convective terms have been neglected since the Reynolds $Re = \frac{\rho U_0 h}{\mu}$ is small. Conservation of mass requires

$$\epsilon_1 \frac{\partial u}{\partial x} + \frac{\partial v}{\partial y} + \epsilon_2 \frac{\partial w}{\partial z} = 0 \tag{6}$$

Finally, the electrical potential is governed by

$$\epsilon^2 \left(\frac{\partial^2 \phi}{\partial y^2} + \epsilon_1^2 \frac{\partial^2 \phi}{\partial x^2} + \epsilon_2^2 \frac{\partial^2 \phi}{\partial z^2} \right) = -\beta (X_+ - X_-) \tag{7}$$

where

$$\beta = 1 + \frac{c_3}{I}$$

where c_3 is the concentration of the solvent, $\epsilon = \frac{\lambda}{h}$, $\epsilon_1 = \frac{h}{L}$, $\epsilon_2 = \frac{h}{W}$ and I is the ionic strength. Here we have assumed that the mole fractions are small and so the mixture is dilute; in this case the diffusion coefficient of an ionic species can be approximated by its value with respect to the solvent, water and this diffusion coefficient is denoted by D_A. The coordinates (x,y,z) are nondimensional; for example, $x = \frac{x^*}{L}$ and the scaling lengths in the three directions are (L, h, W) as depicted on Figure 3. Also (u, v, w) are the dimensionless velocities in each of the coordinate directions (x, y, z); for example $u = u^*/U_0$ where u^* is dimensional. The dimensionless pressure and potential are defined by[17]

$$p = \frac{p^* h}{\mu U_0}, \;\; \phi = \frac{\phi^*}{\phi_0}$$

and the velocity scale $U_0 = \frac{\epsilon_e E_0 \phi_0}{\mu}$ and $\phi_0 = \frac{RT}{F}$. The scaling of the pressure is typical for low reynolds number problems.

In the general case this is a set of N+5 governing equations in the N+5 unknowns, velocity, potential and pressure, plus the N species mole fractions or concentrations. All of these equations are subject to boundary conditions. Generally Dirichlet or Neumann boundary conditions for the mole fractions and the potential and the velocity field is usually assumed to vanish at non-porous surfaces.

Often, the geometry of channels in applications allow approximate forms of the equations to be used in modeling. For example, in the case of electroosmotic pumps, rapid molecular analyzers and drug delivery systems, fabrication techniques do not permit nanoscale dimensions(under $50nm$) in more than one dimension. Thus the three dimensionality of the general problem can be reduced to one or two dimensions. How to do this is considered next.

4 The One-Dimensional Poisson-Nernst-Planck Equations

Most synthetic ion channels considered for use in these applications are rectangular in cross-section as depicted in Figure 3. For very wide channels $\epsilon_2 << 1$ and the side walls have only a local effect. In this case, the potential through a very wide ion channel is controlled by the two-dimensional Poisson equation,

$$\epsilon^2 \left\{ \frac{\partial^2 \phi}{\partial y^2} + \left(\frac{h}{L} \right)^2 \frac{\partial^2 \phi}{\partial x^2} \right\} = -\sum_{i=1}^{N} z_i X_i \tag{8}$$

where z_i are the valences and X_i are concentrations. case of two electrolyte species. We assume that x is the flow direction and we note that if $h >> L$ then the one dimensional ion channel equations

emerge as an approximate system of equations without averaging. On the other hand if $h \sim L$ or $h << L$ then averaging is necessary to formally obtain the one-dimensional equations.

Integrating equation (8) across the channel,

$$\epsilon^2 \left\{ \left.\frac{\partial \phi}{\partial y}\right|_1 - \left.\frac{\partial \phi}{\partial y}\right|_0 + \left(\frac{h}{L}\right)^2 \frac{\partial^2 \bar{\phi}}{\partial x^2} \right\} = -\sum_{i=1}^{N} z_i \bar{X}_i \tag{9}$$

A bar over a variable stands for the average of that variable across the channel in y,

$$\bar{s} = \int_0^1 s dy \tag{10}$$

where s is any function. Equation (9) may be simplified to

$$\epsilon_1^2 \frac{\partial^2 \bar{\phi}}{\partial x^2} = -\sum_{i=1}^{N} z_i \bar{X}_i - 2\epsilon^2 \sigma_0 \tag{11}$$

where we redefine $\epsilon_1 = \frac{\lambda}{L}$ where λ is the electric double layer thickness. Also σ_0 is the surface charge density at $y = 0$

$$\sigma = \sigma_0 = -\frac{\partial \phi}{\partial y}(0) = \sigma_1$$

if the flow is symmetric about the centerline of the channel. Here σ is the dimensionless surface charge density and

$$\sigma = \frac{\sigma^*}{\frac{\epsilon_e RT}{F\lambda}}$$

σ^* is the dimensional surface charge density in C/m^2.

The ion concentrations within the channel are controlled by the Nernst-Planck equation, and for species A

$$\frac{\partial}{\partial y}\left(\frac{\partial X_A}{\partial y} + z_A X_A \frac{\partial \phi}{\partial y}\right) + \epsilon_1^2 \frac{\partial}{\partial x}\left(\frac{\partial X_A}{\partial x} + z_A X_A \frac{\partial \phi}{\partial x}\right) = 0 \tag{12}$$

where z_A is the valence of species A. Integrating equation (12) over y,

$$\left(\frac{\partial X_A}{\partial y} + z_A X_A \frac{\partial \phi}{\partial y}\right)\Big|_0^1 + \epsilon_1^2 \left(\frac{\partial^2 \bar{X}_A}{\partial x^2} + z_A \frac{\partial}{\partial x} \int_0^1 X_A \frac{\partial \phi}{\partial x} dy\right) = 0. \tag{13}$$

The first set of terms vanishes because there is no flux of species A at the walls $y = 0, 1$. The third term may be approximated by

$$\int_0^1 X_A \frac{\partial \phi}{\partial x} dy = \bar{X}_A \frac{\partial \bar{\phi}}{\partial x} \tag{14}$$

if the variables are not functions of y. This will be the case in most of the channel if $\frac{\lambda}{h} << 1$; that is the electric double layer is thin and it is readily shown that the core velocity is constant.[17] On the scale of the channel height, both X_A and ϕ are functions of y; however for small h/L, on the scale

of the channel length, the channel height approaches zero, and from Taylor series considerations, both X_A and ϕ can be considered constant. Thus,

$$\frac{\partial}{\partial x}\left(\frac{\partial \bar{X}_A}{\partial x} + z_A \bar{X}_A \frac{\partial \bar{\phi}}{\partial x}\right) = 0. \tag{15}$$

For $\sigma_0 = 0$, these are the equations used by Barcilon *et al*.[9] Equation (15) is the Nernst-Planck equation for the species A and thus the sytem of equations corresponding to equations (14) and (15) is called the Poisson-Nernst -Planck system.

In the case when the walls of the channel are not charged, there is no electric double layer and the integrated equations will be exact since the potential and mole fraction distributions will be independent of y. In this case the ions and biomolecules move under the action of diffusion and electrical migration and if there is no voltage drop across the channel the process is called *electrophoresis*.

For these channels, the concentrations of the ions at the inlet and outlet are determined by the concentrations within the baths on either side of the membrane. We will consider a mixture of two ionic species plus a third species corresponding to the biomolecule. Therefore, the boundary conditions for the system are(dropping the bars for convenience)

$$X_A = X_{AL}, \quad X_B = X_{BL}, \quad X_C = X_{CL}, \quad \phi = V, \quad x = 0 \tag{16}$$

$$X_A = X_{AR}, \quad X_B = X_{BR}, \quad X_C = X_{CR}, \quad \phi = 0, \quad x = 1, \tag{17}$$

where the subscripts L and R refer to the left ($x = 0$) and right ($x = 1$) boundaries. It is useful to point out that averaging the continuity equation leads to the result that the average velocity is constant in x to maintain constant mixture flow rate.

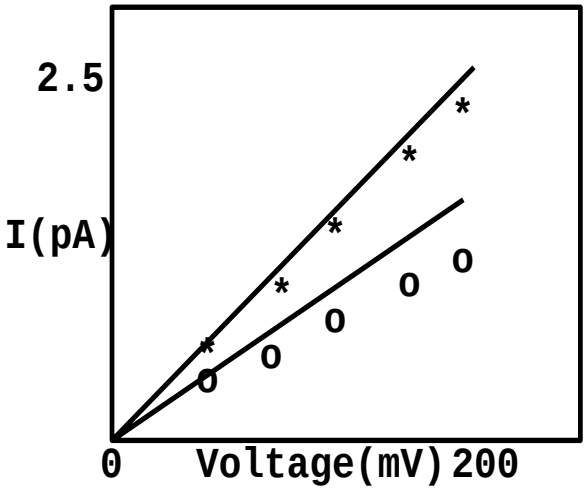

Figure 4: Sketch of typical current-Voltage curves and the comparison with experimental data as computed with three-dimensional PNP model for a Gamaicidin channel. Numbers denote approximate renge and differents lines denote different concentrations in the baths upstream.

The three-dimensional PNP equations have been solved by Hollerbach et al[14] and a qualitative sketch of their results and comparison with experimental data is shown on Figure 4. Note that the

current is linear with voltage and the comparison with the data is extremely good. Some fitting of the diffusion coefficients of sodium and chloride ions was peformed although the authors note that the results are not a strong function of these parameters.

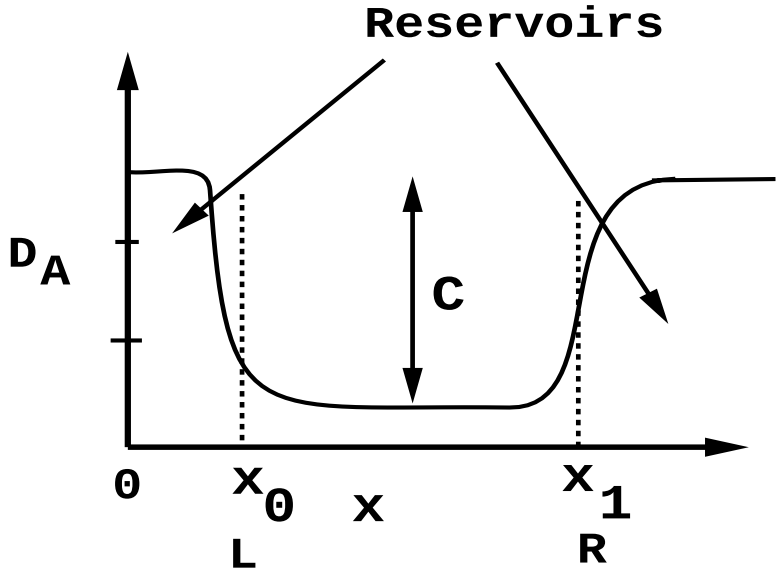

Figure 5: Sketch of the expected variation of the diffusion coefficient in as a function of distance from the upstream bath through the channel and into the downstream bath.

5 Hindered Diffusion Concepts

The nature of the solution for the potential and the concentrations or mole fractions for the PNP system has been discussed in the literature.[2,3,16] As an ion or biomolecule approaches the entry to the small channel from the large bath, there is a resistance to motion from the walls. Thus the diffusion coefficient in the bath is likely to be much larger than that in the channel due to the proximity of the walls of the channel. Specifically, as a species enters the channel the diffusion coefficient should rapidly drop as shown on Figure 5. The diffusion coefficient should be constant in the bath and in the channel. The diffusion coefficient in the channel can be over an order of magnitude smaller in the channel than in the upstream and downstream reservoirs.

For dilute and moderately dense gases, excellent theories exist by which diffusion coefficients can be calculated from information about intermolecular forces.[18] However, no such theories exist for ordinary diffusion in dense gases and liquids, which results in numerous approximations and empirical relations.

An estimate of the diffusion coefficient is provided by the Nernst-Einstein equation. According to the Nernst-Einstein equation, the diffusion coefficient of a single particle or solute molecule A through a medium B may be described by[18]

$$D_{AB} = k_b T \left(\frac{m_A}{F_A} \right) \tag{18}$$

where $u_A = m_A/F_A$ is the mobility of the component A, and F_A is the drag between the solute and solvent molecules, $k_b = R/N_A$ is Boltzmann's constant. The relation between force and velocity may be obtained for a rigid sphere moving in the creeping flow limit(*Re* << 1). If slip at the surface of the sphere is taken into account, then[19]

$$F_A = 6\pi\mu_B m_A a \left[\frac{2\mu_B + a\beta_{AB}}{3\mu_B + a\beta_{AB}}\right] \tag{19}$$

in which μ_B is the viscosity of the pure solvent, a is the radius of the diffusing particle, and β_{AB} is the coefficient of sliding friction. The coefficient of sliding friction, β_{AB}, can be exploited in two limiting cases. In the case where there is no tendency for the fluid to stick at the surface of the diffusing particle(i.e. a hydrophobic particle in the case of a water solvent), then β_{AB} = 0, and equation (3.5) becomes $F_A = 4\pi\mu_B m_A a$. This slip limit is approached when a molecule diffuses through a medium consisting of molecules of comparable size[19] The other limiting case is for the no-slip condition of $\beta_{AB} = \infty$, which results in equation (19) reducing to $F_A = 6\pi\mu_B u_A a$; this may be the case of a hydrophobic particle and in both these cases the result is known as Stokes' Drag Law. This would be the case for a sphere in a continuum or for a large spherical particle in a solvent of low relative molecular mass.[19]

According to Peters,[21] human serum albumin has a hydrophilic surface and is very soluble in water. Glucose molecules have polar hydroxyl groups (OH groups) that attract water molecules, which form a hydration shell[1]; hence, glucose is also hydrophilic. Therefore, both molecules should be described by the no-slip case of equation (19).

Substitution of equation (19) into equation (18) results in the following equation for the diffusion coefficient for the no-slip case:

$$D_A = \frac{k_b T}{6\pi\mu_B a} = \frac{RT}{6\pi N_A \mu_B a} \tag{20}$$

which is recognized as the Stokes-Einstein equation. Here N_A is Avogadro's number. The Stokes-Einstein equation has been shown to be fairly good for describing the diffusion of large spherical particles or molecules in cases where the solvent appears to the diffusing species as a continuum.[18] The hydrodynamic theory further suggests that the shape of the diffusing species is very important. Tyrell and Harris[19] note that the validity of equation (20) is also restricted by the fact that the motion of only one diffusing particle is considered, and so the relationship can strictly only apply in the limit of infinite dilution.

The Stokes-Einstein equation assumes that the diffusing particles are isolated. That is, it does not take interactions with other particles or with boundaries such as walls into account. When a particle is diffusing near a wall, the Stokes drag will increase due to wall effects and the diffusion coefficient will be smaller than when the particle is far from the wall. In the small channels of interest in this work, the walls of the channel may affect transport. One value that can be used to quantify wall effects is the ratio of the diffusing particle radius a to its distance from the wall y. The expectation is that for finite a/y_p, wall effects will become important and the diffusion coefficient will decrease according to

$$D_H = CD_A \tag{21}$$

where D_H is the so-called hindered diffusion coefficient and C<1 is some function of $\frac{a}{y_p}$. As the particle radius decreases compared with y_p, $i.e.$ in the limit as $\frac{a}{y_p}$ becomes very small, the D_H should

[1]http://staff.jccc.net/pdecell/chemistry/hydrophilic.html (04, 2004)

Ion	D_A (x$10^{-5} cm^2/sec$)	Ionic Diameter(nm)
Li^+	1.03^*	0.133
Na^+	1.33^*	0.200
K^+	1.96^*	0.276
Cs^+	2.06^*	0.340
Mg^{2+}	0.71^*	0.178
Ca^{2+}	0.79^*	0.214
Cl^-	2.032^*	0.362
H_2O	—	0.280
Albumin	0.061^{**}	7
Glucose	0.94^{***}	1
IgG	0.04^{**}	10

Table 1: Diffusion coefficient and ionic diameters.

approach D_A as given in equation (20). Some representative ionic radii and diffusion coefficients are depicted on Table 1.

Several models have been presented in the literature that attempt to correct the diffusion coefficient for wall interactions. Lin, Yu, and Rice[22] examine hindered diffusion of an isolated uncharged sphere in a density-matched fluid confined between two parallel flat walls. The measured diffusion coefficients are used to test the predictions of the wall drag effect predicted by several approximate theories. The text by Happel and Brenner[23] examines the motion of a sphere moving relative to plane walls using results established by Faxen, which are valid in the context of low Reynolds number hydrodynamics. Levitt[25,26] uses the pioneering work of Haberman and Sayre[28] in order to apply continuum fluid mechanics to the nonelectrolyte and volume flux across a membrane. The work of Haberman and Sayre[28] provides the important result of a series solution for the hindered diffusion coefficients for several special cases using the method of images; this is the solution on which the Levitt model[25,26] is based. Unlike the previously discussed models,[22,23] the Levitt model is based on analysis of a biological system. Bevan and Prieve[27] have used experimental method of called total internal reflection microscopy (TIRM) to deduce an average diffusion coefficient of a charged sphere in the presence of a wall experimentally.

The hindered diffusion models are of the form

$$D_H = C(a, y_p) D_A$$

where $C < 1$ and a is the molecular size, and y_p is the distance of the particle from the wall. In this work we assume that $y_p = h/2$. Here we discuss in detail the models of Levitt[25,26] and Bevan and Prieve[27] because they seem to give the best results in comparison with experimental data as shown below. In the Levitt[25,26] model the constant C for the hindered diffusion coefficient is given by

$$C = \frac{D_H}{D_{AB}} = \frac{1 - 2.1050\frac{a}{y_p} + 2.0865\left(\frac{a}{y_p}\right)^3 - 1.7068\left(\frac{a}{y_p}\right)^5 + 0.72603\left(\frac{a}{y_p}\right)^6}{S\left(\frac{a}{y_p}\right)} \qquad (22)$$

where

$$S\left(\frac{a}{y_p}\right) = 1 - 0.75857\left(\frac{a}{y_p}\right)^5$$

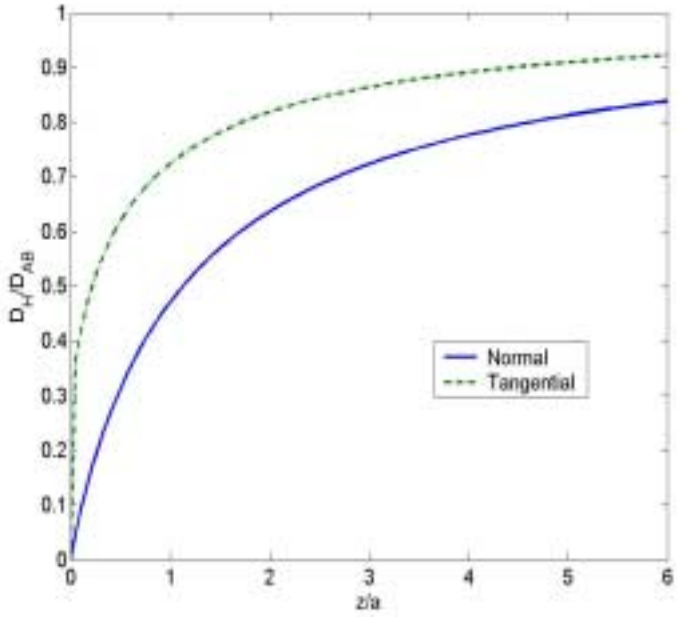

Figure 6: Hindered diffusion coefficient of Bevan and Prieve.[27]

The Bevan and Prieve model[27] based on their experimental measurements is depicted on Figure 6. A curve is given for the diffusion coefficient and a best-fit curve was developed after taking several points from the graph. The result is

$$C = \frac{D_H}{D_A} = \frac{4.2 + 3\left(\frac{a}{y_p}\right)}{6 + 9\left(\frac{a}{y_p}\right) + 2\left(\frac{a}{y_p}\right)^2} + 0.3 \tag{23}$$

Note that as $a/y_p \rightarrow 0$, the value of C approaches unity because the value of the hindered diffusion coefficient in this case will approach the Stokes-Einstein value of the diffusion coefficient.

The transport properties of the channels are determined by the diffusion coefficient and the potential within the channel. Thus as a first approximation the boundary layers at the entrance and exit of the channel can be neglected and the flux of solute may be determined from the values of the hindered diffusion coefficients in the interior of the channel along with the potential. We discuss the calculation of the potential next.

6 Calculating the Electrical Potential

Gillespie[2] presents detailed results for a $(-1, 2, 1)$ electrolyte system. We may consider a PBS solution along with a protein, say albumin or glucose. In PBS, Na and Cl are the two most populous species and if we consider this case we have for the potential

$$\epsilon_1^2 \phi'' + X_A - X_B + z_C X_C = -2\epsilon^2 \sigma_0, \tag{24}$$

where $\phi'' = \frac{d^2\phi}{dx^2}$, X_A is the sodium, X_B is the chloride and X_C is the biomolecule. For simplicity, the average bars are removed from equation (24) and all of the following equations, but the variables are all still averages over y. A single prime denotes a first derivtive with respect to x, while a double prime denotes a second derivative with respect to x. Applying the same scaling factor and simplification to equation (15) and the other ions yields

$$X_A{}' + X_A\phi' = -\frac{n_A}{D_A} \tag{25}$$

$$X_B{}' - X_B\phi' = \frac{n_B}{D_B} \tag{26}$$

$$X_C' + z_C X_C \phi' = \frac{n_C}{D_C}. \tag{27}$$

where n_i is the flux of species i and is constant. Note that here the diffusion coefficients can be a function of x.

The diffusion coefficients are often used as fit parameters in numerical simulations.[14] In fact usually $D_A = D_A(x)$ with the diffusion coefficient in the bath being the normal bulk value and in the channel a "hindered" value which is much less than in the bulk.

We can obtain solutions for the mole fractions easily. After multiplying equation (25) by an integrating factor e^{ϕ} we find the solution for the mole fraction is given by

$$X_A = -n_A e^{-\phi} \int_0^x e^{\phi} \frac{dx}{D_A} + X_L e^{\phi(0)-\phi(x)} \tag{28}$$

where to satisfy the boundary condi6ions

$$n_A = \frac{X_L e^{\phi(0)} - X_R e^{\phi(1)}}{\int_0^1 e^{\phi} \frac{dx}{D_A}} \tag{29}$$

and we have written $n_A = n_{Ax}$. The problem now reduces to obtaining the electric potential. Note that in the case where there is no potential drop and the diffusion coefficient is constant then the flux n_A is determined solely by the values of the mole fractions in the two baths.

In the case where $\epsilon_1 << 1$ there will be boundary layers near the entrance and exits due to the rapid change diffusion coefficient. Away from these boundary layers in the channel where the diffusion coefficient is constant and for small ϵ_1 the core of the channel is electrically neutral leading to the result

$$X_A - X_B + z_C X_C = -2\epsilon^2 \sigma_0 \tag{30}$$

for a $(1, -1, z_C)$ system. If the perturbation from the ζ-potential at the wall is computed, then the Debye-Huckel approximation may be employed to compute an analytical solution for the surface charge density in terms of the wall mole fractions.[29]

To calculate the surface charge density, we can assume that the Debye-Huckel approximation, valid for potential below $26mV$, holds as described earlier. If we compute the perturbation from the ζ-potential at the wall, then we can use the Debye-Huckel approximation to compute an analytical solution for the surface charge density in terms of the wall mole fractions.[29] It is easily shown that the dimensionless surface charge density is[29]

$$\sigma_0 = -\frac{1}{\epsilon^2} \frac{\sum_{i=1}^N z_i X_i^0}{\sum_{i=1}^N z_i^2 X_i^0} tanh(\frac{1}{\epsilon}) \tag{31}$$

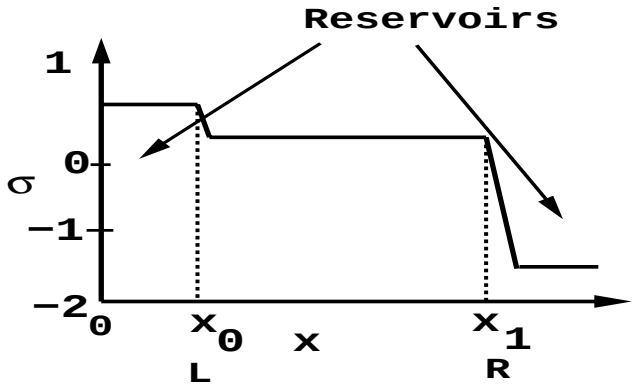

Figure 7: Sketch of the fixed charge on the side wall as depicted in Chen *et al*.[31] The units of the charge are in Molar.

where the X_i are the concentrations scaled by ionic strength and N is the number of species. Thus the correction term is O(1). As seen in equation (11) the presence of the fixed charge term leads to a parabolic correction. In practice, however as noted by Chen *et al*.[31] the surface charge distribution is not constant but varies along the channel. It turns out that for many channels, the surface charge density is piecewise constant as shown on Figure 7.[31] The scale shown is from Chen[31] for a synthetic protein channel called the LS channel. From this distribution it is seen that the correction term results in boundary layers near the entrance and exit of the channel. For the purposes of this paper we consider only the case where the fixed charge distribution is constant, effectively for $x_0 \leq x \leq x_1$.

We first present results for uncharged side walls; to gain an appreciation of the basic behavior, in all of these results the potential and mole fractions are computed numerically and the diffusion coefficients are assumed equal. Figure 8(a) shows the result for an additional species of valence -1; in these results we assume the correction is zero. The dash dot line in the potential curve is the asymptotic result in the interior. The channel length is $L = 20nm$ and the EDL thickness is based on the ionic strength at $x = 0$. Note that the core of the channel is electrically neutral as noted by the net volume charge density curve.

Figure 9 shows results for the same parameters as on Figure 8 except now there is a potential drop of $V = 2$ across the channel. On Figure 10 are results for the parameters of Figure 8 except that the valence of the third species is $z_{n2} = -3$. On Figure 11 are results for the parameters of Figure 8 except the length of the channel is $L = 5nm$. Note now that the core of the channel is not electrically neutral.

It is useful to note that if the upstream and downstream concentrations are chosen to satisfy electroneutrality at $x = 0, 1$ there are no boundary layers and all of the quantities are linear with x.

We now look at the case where the surface charge density correction is not zero. On Figure 12 are results for the case of Figure 8 with the correction added in. Here we note that the sidewall mole fractions are not that different yet there is a large difference in the potential profile.

On the other hand, when there is significant difference in the mole fractions there is both a significant difference in the potential and the mole fractions as noted in Figure 13. These results show that the potential is extremely sensitive to the fixed charge distribution.[12]

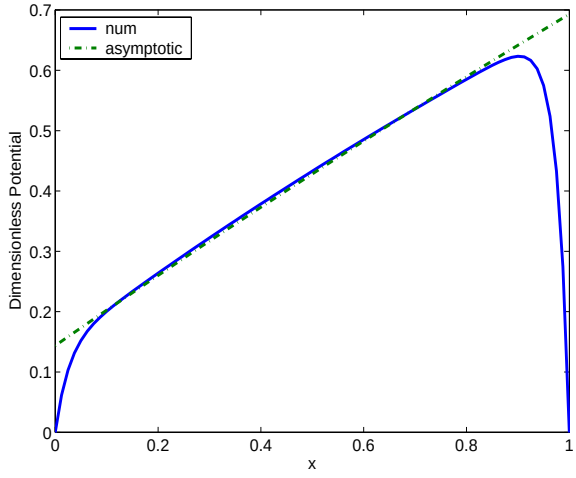

(a)

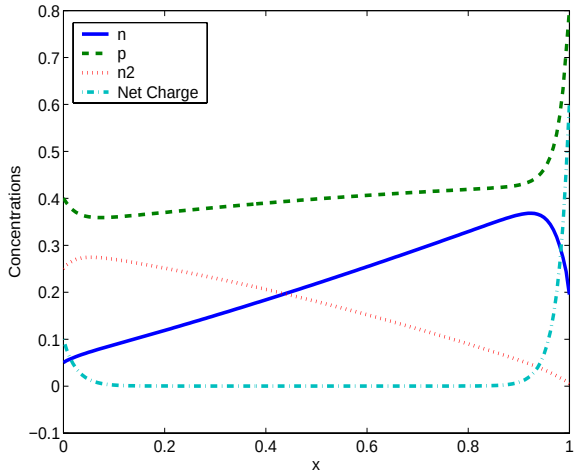

(b)

Figure 8: Concentration and potential results for the three component solution for constant surface charge density for the length of the channel $L = 20$ nm. Boundary conditions: $X_{AL} = 0.4(p), X_{BL} = 0.05(n), X_{CL} = 0.25(n2), X_{AR} = 0.8, X_{BR} = 0.195, X_{CR} = 0.005, V = 0$. (a) Potential (b) Concentrations.

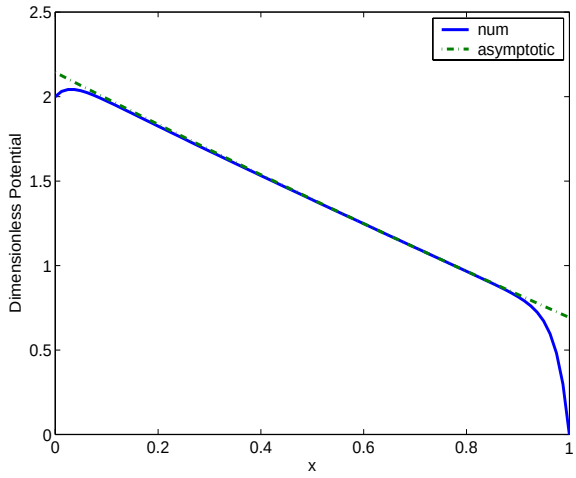

(a)

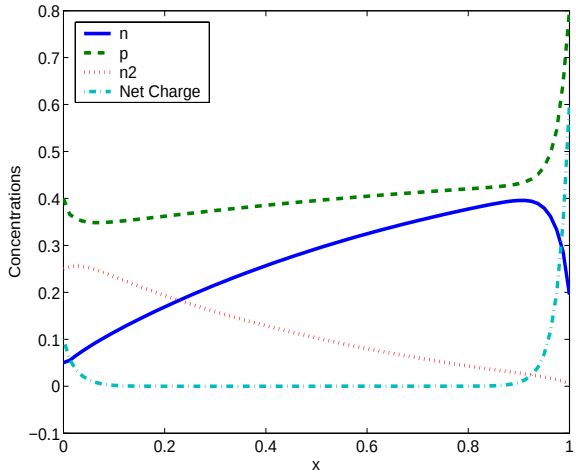

(b)

Figure 9: Concentration and potential results for the parameters of Figure 8, except $V = 2$. (a) Potential (b) Concentrations.

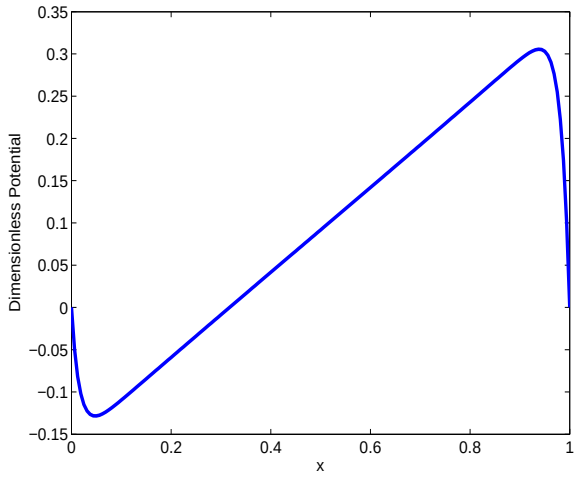

(a)

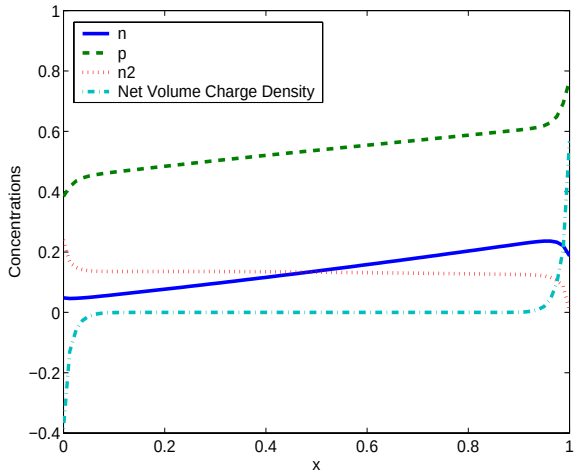

(b)

Figure 10: Concentration and potential results for the paremeters of Figure 8 except the valence $z_C = -3$(n2). (a) Potential (b) Concentrations.

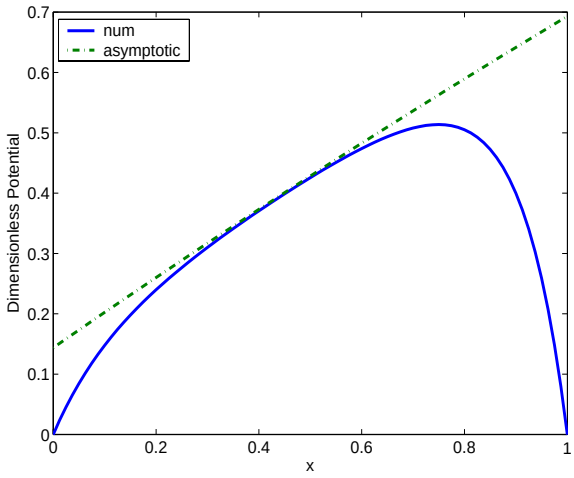

(a)

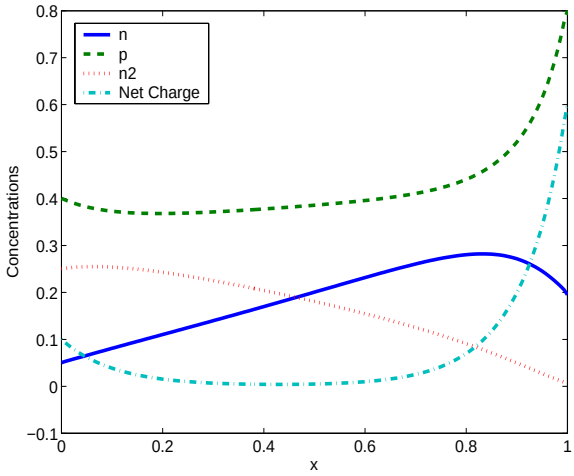

(b)

Figure 11: Concentration and potential results for the paremeters of Figure 8 except the length of the channel $L = 5nm$. (a) Potential (b) Concentrations.

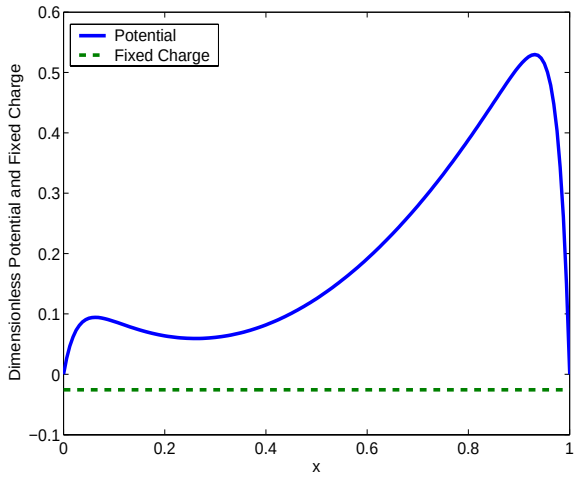

(a)

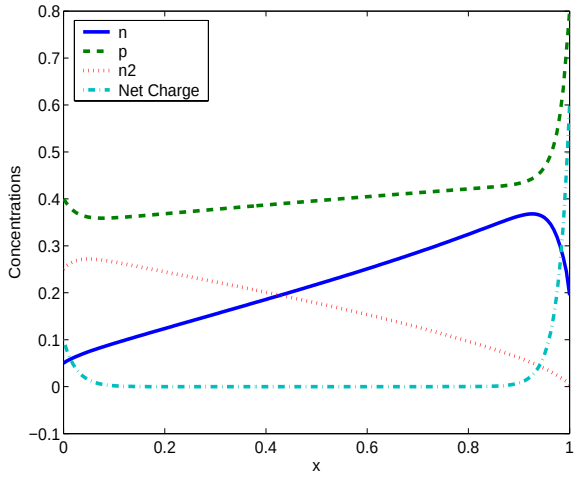

(b)

Figure 12: Concentration and potential results for the paremeters of Figure 8 including the effect of permanent or fixed charge. Here the wall concentrations scaled by ionic strength at $x = 0, p^0 = 2.0$, $n^0 = 1.9$. The length $L = 20nm$. (a) Potential (b) Concentrations.

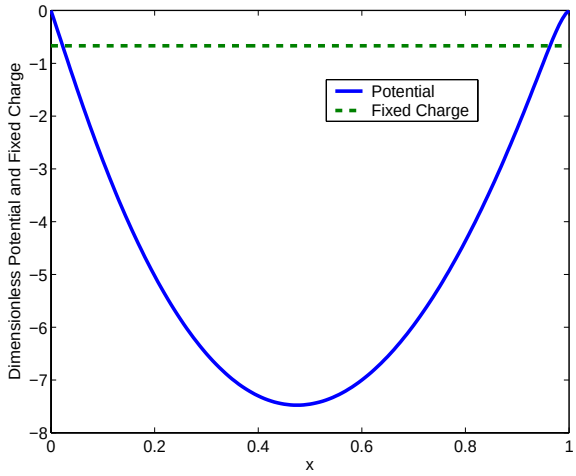

(a)

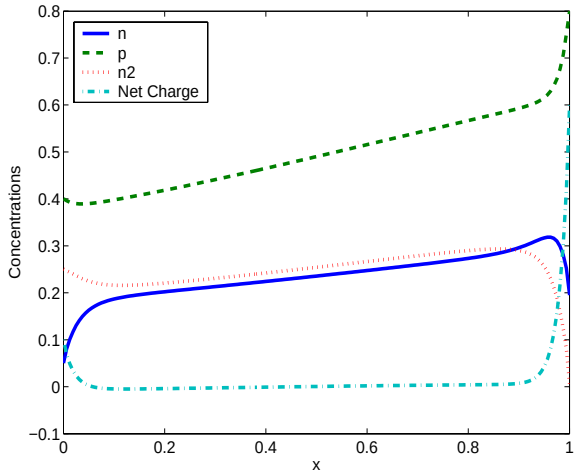

(b)

Figure 13: Concentration and potential results for the paremeters of Figure 8. including the effect of permanent or fixed charge. Here the wall concentrations scaled by ionic strength at $x = 0$, $p^0 = 2.0$, $n^0 = 0.4$. The length $L = 20nm$. (a) Potential (b) Concentrations.

7 PNP Model Comparison with Experiment

Current voltage relationships can be predicted for a number of natural ion channels and ionic transport is well predicted by one-dimensional PNP theory.[13] Here we investigate a simpler case of the transport of glucose and albumin in a synthetic ion channel.

The experimental data to which our results are compared is from a series of experiments using Costar Transwell 6-well plates. Each well consists of a small donor region separated by a nanochannel membrane from a large receiver region as depicted on Figure 2. The volume of the donor region is 0.22 mL, while the volume of the receiver region is 11 mL. The nanoscale pores in the membranes are assumed to be of uniform length L and width W, but have different values for channel height h. Specifically, all of the nanopores have L = 5 μm and W = 45 μm. The values of h are 7, 13, 20 and 27 nanometers.

In this section the models for the hindered diffusion coefficients will be used to calculate the flux of albumin and glucose and the results will be compared with experimental data from iMEDD, Inc. The nanopore membranes are made from silicon and are therefore biologically, thermochemically, and mechanically stable[2]. The experiments using Costar Transwell 6-well plates. Each well consists of a small donor region separated by a nanochannel membrane from a large receiver region as depicted on Figure 2; essentially the same device was used for these experiments for which there is no transmembrane potential as for the electroosmotic pumping problem.[30] The volume of the donor region is 0.22 mL, while the volume of the receiver region is 11 mL. The nanoscale pores in the membranes are assumed to be of uniform length L and width W, but have different values for channel height h. Specifically, all of the nanopores have L = 5 μm and W = 45 μm. The values of h are 7, 13, 20 and 27 nanometers. The nanopore membranes have about 10^6 pores/cm^2, so for the purpose of modeling, the entire membrane is treated as a single channel with a length of 5 μm and an effective cross-sectional area A_{eff} given by

$$A_{eff} = \frac{A_m P}{10^4}$$

where A_m is the physical area of the membrane (taken as 2 mm^2), and P is the membrane porosity. The porosity is given by

$$P = \frac{42.5\,(h)}{10^4}$$

Both the Levitt and the Bevan and Prieve hindered diffusion models were used to predict the flux. The Since there is no potential drop across the membrane and the transport is by diffusion only, through uncharged channels the dimensional flux of species i is given by Fick's Law as

$$n_i = \frac{D_i}{L}(C_{iL} - C_{iR}) \tag{32}$$

where D_i is the hindered diffusion coefficient. and L and R denote the values of the concentration in the left and right reservoirs. The molecular length scale a used to calculate the hindered diffusion coefficient is also presented. The numerical predictions of the flux are listed under the "model" column, while the experimental results are given in the "iMEDD" column.

The experimental data is calculated from a correlation developed by iMEDD. In principal the experimental results represent a time-averaged flux. Both the Levitt and the Bevan and Prieve

[2] http://www.imeddinc.com/

models were tested. For all of the glucose results $C_L = 300\frac{gm}{liter}$ and $C_R = 0$. The results for Glucose are shown in Figure 14. Notice that when the molecular length scale a is given by the nominal radius of glucose (a = 0.373 nm), both the Levitt and the Bevan and Prieve models predict a much larger flux than the experimental results. If the length scale is increased by a factor of four (a = 1.49 nm), then both models predict a much closer flux to that of the experimental value. One could argue that increasing the molecular length scale corresponds to the hydration of the glucose molecules. It is surprising how close this simple model is to the experimental data.

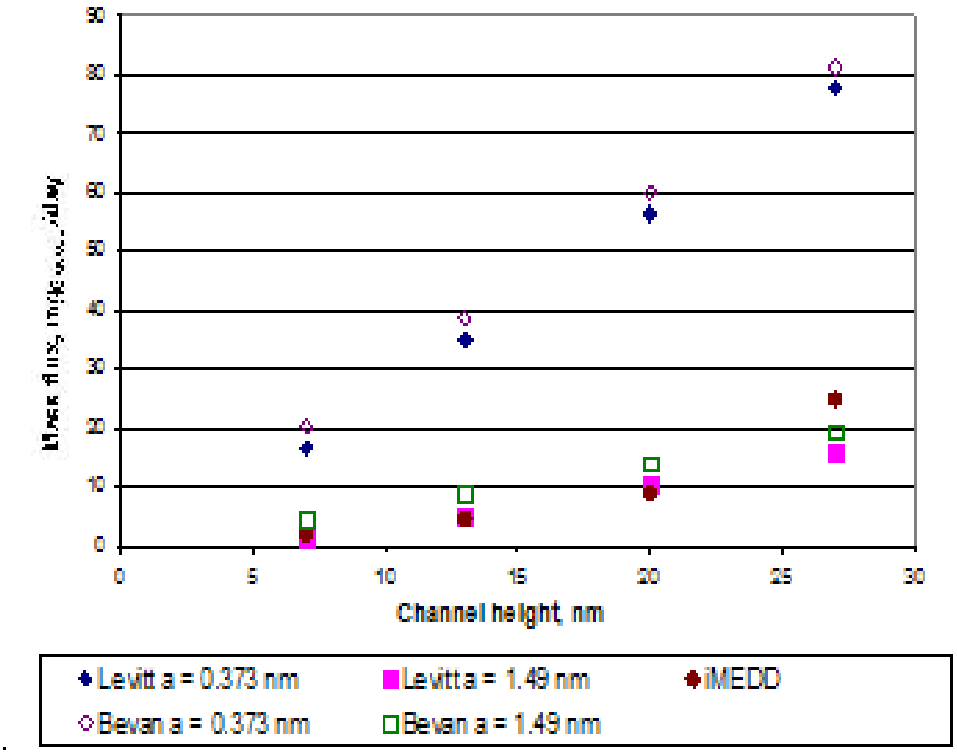

Figure 14: Results for the mass flow of glucose through the iMEDD membrane.

The results for Albumin are shown in Figure 15. As in the case of glucose, the experimental data represents a time-averaged flux. Here $C_L = 80\frac{gm}{liter}$ for $h = 7nm$ and $C_L = 5\frac{gm}{liter}$ for all other channel heights; $C_R = 0$ for all channel heights. Note that when the molecular length scale a is taken as the nominal molecular radius (a= 3.55 nm) both hindered diffusion models yield poor predictions of the flux at the h = 7 nm channel height. In the case of the Levitt model, a negative flux is predicted, which comes from the fact that the hindered diffusion coefficient is negative. A negative flux could be interpreted as the inability of of a molecule to enter the channel, but this interpretation is tenuous at best.

In the case of the channel heights of h= 13, 20, and 27 nm, the Bevan and Prieve model clearly yields a closer prediction than the Levitt model when the nominal molecular radius (a= 3.55 nm) is used for the molecular length scale. In order for the Levitt model to better predict the experimental data, the molecular length scale must be decreased to a= 2.80 nm. Davidson and Dean[24] suggests that large proteins are subject to random changes in configuration and flow-induced deformation

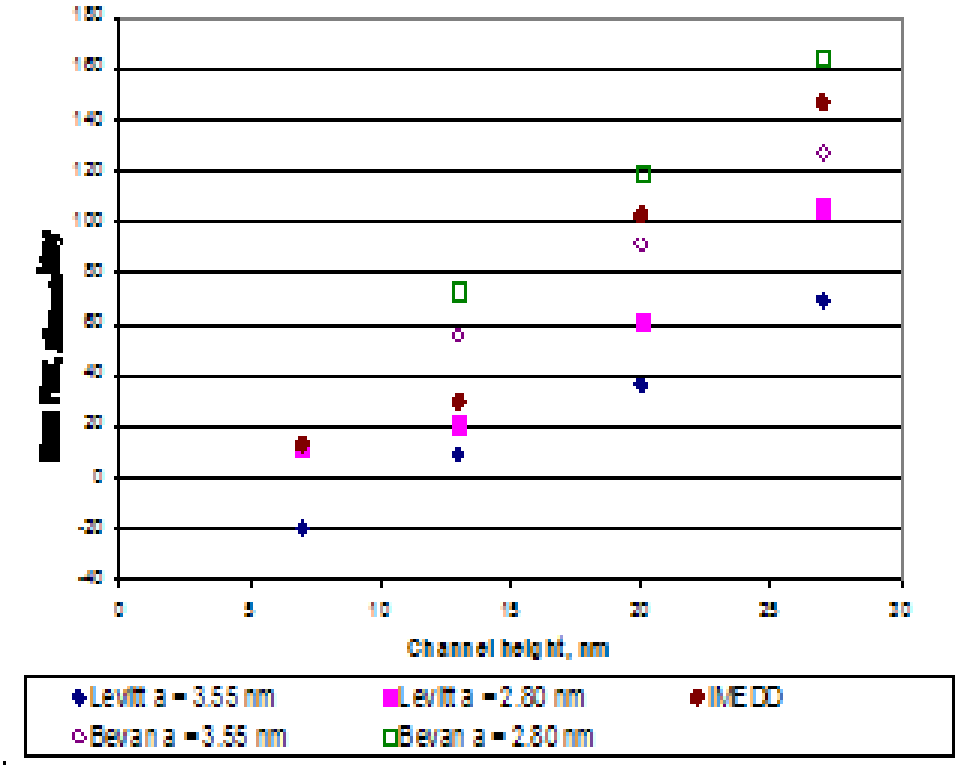

Figure 15: Results for the mass flow of albumin through the iMEDD membrane.

Thus, the albumin molecules may be deformed, and their nominal molecular radii are decreased. This eliminates the problem of a negative hindered diffusion coefficient at h= 7 nm. For comparison the Bevan and Prieve model was also used for a = 2.80 nm, but the results do not improve from the a = 3.55 nm case.

8 Brownian Dynamics

Brownian Dynamics is the next step toward a full molecular simulation; in this procedure the solvent is treated as a continuum. The solute whether it be an ionic species or long chain polymer is treated on an individual molecule basis.

In modeling natural ion channels the equation governing the motion of an ion in solution is of the Langevin type and is given by

$$m_i \frac{d^2 \vec{r_i}}{dt^2} = -F_D \frac{d\vec{r_i}}{dt} + z_i \vec{E}_i + \vec{F}_R + \vec{F}_S \tag{33}$$

where F_D is the viscous drag coefficient(not dimensionless!) on the ion,$\vec{E}_i$ is the electric field on the ion and $\vec{F}_R$ is a random thermal force representing the interaction of the ion with the solvent and the walls.[32] The random force and the viscous force are related by the fluctuation-dissipation theorem as noted by Li *et al*.[33] This is a second order ordinary differential equation in time which may be integrated using any number of methods subject to specification of an initial distribution of ions. The key step in the calculation is the specification of the three-dimensional electric field and its variation in space. The one-dimensional equations are obtained by taking averages over space of each of the forces. As is the case for the use of PNP, Brownian Dynamics methods reproduce current-voltage curves for the Gramicidin ion channel[34] although some reservations remain for very small channels.[34] In particular, Corry *et al*[35] show that the chloride current in a model channel essentially vanishes in the BD calculations whereas in the PNP computation the chloride current is approximately linear ranging from -20 pA to about 5pA when the voltage varies from -125 mV to 125 mV.

The modeling of a long chain biopolymer is considered in a similar way. Theoretical modeling of polymer chains began with the work of Kuhn[36] and several others[37,38] and many other models of polymer chains have been developed over the years. The polymer, say a biomolecule is assumed to consist of a number of nodes connected by a structure such as a rigid rod(bead-rod model) or a flexible srping(bead-spring chain) or a combination of structures. Different methods of connecting the beads is described by Hur *et al*[39] and Larson *et al*.[40]

We will describe in detail the bead-spring chain discussed in the work of Panwar and Kumar[41] and depicted on Figure 16. While acknowledging that the field of polymer modeling is vast, this analysis is typical of how such models are developed. Each pair of beads simulating a node of the polymer is separated by a spring to simulate the flexible nature of the polymer. The motion of the molecule is described by following the motion of the beads whose positions evolve in time according the force balance

$$\vec{F}_i^{drag} + \vec{F}_i^{brown} + \vec{F}_i^{spring,tot} + \vec{F}_i^{ext} = 0 \tag{34}$$

where the subscript i denotes a node on the polymer. The right side of the force balance, the acceleration term is zero since the inertia time scale is much smaller than the polymer relaxation

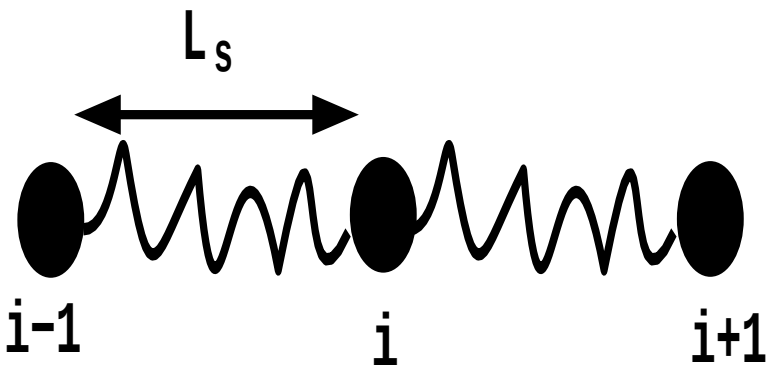

Figure 16: Sketch of a bead-spring chain model of a long chain polymer.

time. The drag force is defined by the Stokes Drag Law defined above; we write the drag law as

$$\vec{F}_i^{drag} = F_D \left(\vec{u} - \frac{d\vec{r}_i}{dt} \right)$$

where F_D is a drag coefficient(not dimensionless!) and $\vec{u}$ is the bulk fluid velocity. In this formulation the disturbance to the bulk velocity due to the polymer has been neglected.

The Brownian motion force is given by the formula

$$\vec{F}_i^{brown} = \left(\frac{6 c_D k_B T}{\Delta t} \right)^{1/2} \vec{n}_i$$

where k_B is Boltzmann's constant, T is the temperature, Δt is the time step in the simulation and $\vec{n}_i$ is a random vector distribution such that $\mid \vec{n}_i \mid \leq 1$.

The springs connecting the beads are assumed to be finitely extensible. The force that the spring exerts on the beads is proportional to the spring displacement so that

$$\vec{F}_i^{spring,tot} = k_s \vec{R}_i = k_s \left(\vec{r}_{i+1} - \vec{r}_i \right)$$

where k_s is the spring constant. Actually k_s can depend on the displacement and Panwar and Kumar[41] take

$$k_s = \frac{k_B T}{b_k} \lambda_i \frac{3 - \lambda_i^2}{1 - \lambda_i^2}$$

which is cohen's approximation to the inverse langevin function. The function

$$\lambda_i = \frac{R_i}{N_{K,s} b_K}$$

where b_K is the Kuhn length and $N_{K,s}$ is the number of Kuhn steps per spring. The total length of the spring is $L_s = N_{K,s} b_K$.

The relevant time scale for the motion of the biomolecule is given by

$$\tau = \frac{F_D b^2}{k_b T}$$

Using b as the relevant length scale then we can nondimensionalize the equation governing the motion of the polymer and the result is

$$\frac{d\vec{b}}{dt} = \frac{F_D b U_0}{k_b T}\vec{u} + \left(\frac{6}{\Delta t}\right)^{1/2}\vec{n}_i + \lambda_i \frac{3-\lambda_i^2}{1-\lambda_i^2}\left(\vec{b}_{i+1} - \vec{b}_i\right) - \lambda_{i-1}\frac{3-\lambda_{i-1}^2}{1-\lambda_{i-1}^2}\left(\vec{b}_i - \vec{b}_{i-1}\right) + \vec{F}^{ext} \quad (35)$$

where $\vec{F}^{ext}$ has been made dimensionless on $\frac{k_b T}{b}$. This is a first order nonlinear initial value problem for all of the beads which may be solved using a standard numerical technique such as Euler, modified Euler or the more accurate Adams-Moulton and Runge-Kutta methods.

9 Molecular Dynamics Simulations

Non-equilibrium Molecular Dynamics(NEMD) simulation is a deterministic calculation most often used to compute particle trajectories in liquids. The actual procedure is no more than solving conservation of linear momentum for N-bodies. The use of NEMD simulations to describe the trajectories of molecules in multicomponent mixtures characteristic of problems in biology and chemistry in a bulk fluid flow is in its relative infancy because of the relatively large computation time required. In this section we will describe the basic computational methodology for the Lennard-Jones potential, while recognizing that there are many other potentials describing intermolecular potentials in the literature.[42–44]

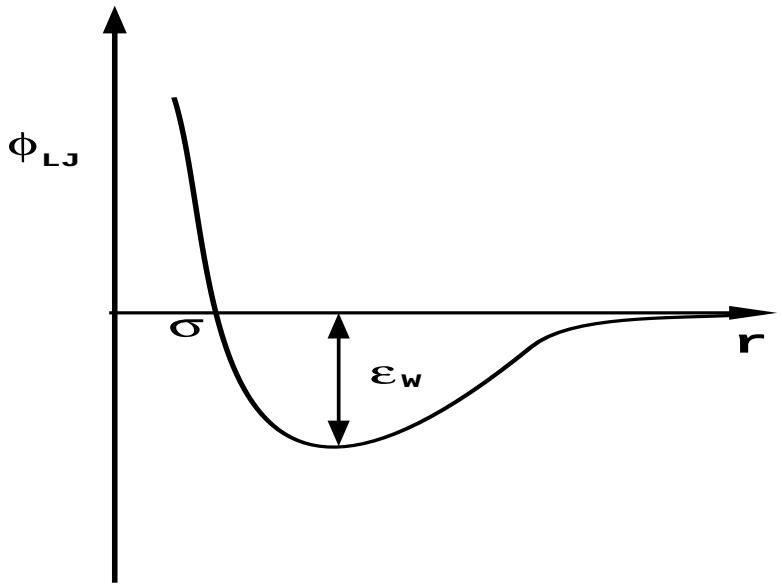

Figure 17: Sketch of the Lennard-Jones potential.

The Lennard-Jones(LJ) potential is perhaps the most popular description of the intermolecular force field between two particles and is given by

$$\phi_{LJ} = 4\epsilon_W \left[\left(\frac{\sigma}{r}\right)^{12} - \left(\frac{\sigma}{r}\right)^{6}\right] \quad r < r_c$$

$$= 0 \;\; r \geq r_c \tag{36}$$

where ϵ_W is the well depth at $\frac{d\phi_{LJ}}{dr} = 0$ and σ is the particle diameter. A sketch of this potential is given on Figure 17. The first term in the potential is the repulsive term and the second term represents the attractive part of the force field. An LJ fluid is a collection of colliding balls that are smooth. Note here that the "balls" are not polar and so strictly speaking the LJ potential cannot describe water; nevertheless an LJ calculation often gives useful results for aequous solutions.

Now the force corresponding to the potential is given by

$$\vec{F} = -\nabla \phi_{LJ}$$

and performing the integration we find that

$$\vec{F}_{ij} = \left(\frac{48\epsilon_W}{\sigma^2}\right)\left[\left(\frac{\sigma}{r_{ij}}\right)^{14} - \frac{1}{2}\left(\frac{\sigma}{r_{ij}}\right)^{6}\right]\vec{r}_{ij} \tag{37}$$

for $r < r_c$ and zero otherwise. Note that the potential is continuous at $r = r_c$ but higher order derivatives are discontinuous there; however experience has shown that the discontinuity does not adversly affect the computation. Then Newton's Law is given by

$$m_i \frac{d^2\vec{r}_i}{dt^2} = \vec{F}_i + \vec{F}_{exti} = \sum_{j=1}^{N} \vec{F}_{ij} + \vec{F}_{exti} \tag{38}$$

where $\vec{F}_{exti}$ is an external force field, perhaps an electric field(EOF), N is the number of atoms or molecules and m is the mass of each molecule. The sum in equation (38) excludes the value $i = j$.

The problem can also be formulated in terms of the Hamiltonian which is defined as

$$H = \sum_{i=1}^{N} \frac{p_i^2}{2m} + \sum_{i<j} \phi_{LJij} \tag{39}$$

and the force associated with the Hamiltonian is given by

$$\vec{F} = -\nabla H + \vec{F}_{ext} = m\vec{a} \tag{40}$$

Note that the we have described the interaction potential between the atoms or molecules in the fluid; however the interaction potential between the the walls and fluid also need to be specified. If the walls are taken to be smooth round spheres then the interaction potential can also be of the LJ type but with possibly different different values of the LJ parameters although they are taken to be the same in some cases.[45]

Equation (38) is usually put in dimensionless form to reduce the number of parameters required to vary to describe the system; chemists often refer to these dimensionless variables as reduced units. We define dimensionless variables by chosing σ, m and ϵ_W to be the units of length mass and energy respectively. Thus, for example the dimensionless length is

$$r^* = \frac{r}{\sigma}$$

Pair	σ(Å)	ϵ_W(KJ/mol)	Pair	σ(Å)	ϵ_W(KJ/mol)
$O-O$	3.151	0.6366	$Na^+ - Na^+$	2.73	0.3576
$Na^+ - O$	2.876	0.5216	$Cl^- - Cl^-$	4.86	0.1679
$Cl^- - O$	3.785	0.5216	$Na^+ - Cl^-$	3.87	0.1706

Table 2: Lennard-Jones parameters for a sodium–chloride aqueous solution.[47]

The unit of time is $\sqrt{\frac{m\sigma^2}{\epsilon_W}}$ and substituting into equation (38) we have

$$\frac{d^2\vec{r_i}}{dt^2} = 48\sum_{j=1}^{N}\left[r_{ij}^{-14} - \frac{1}{2}r_{ij}^{-6}\right]\vec{r_{ij}} + \vec{F}_{exti} \tag{41}$$

where again the sum excludes the value $i = j$.

Because of the computational intensity of the MD simulations, boundary conditions are important. In simulations in nanochannels, the nanoconstrained dimension can exhibit realistic boundary conditions; typically in a 6 nm channel, there will be about 20 water molecules and so this is a reasonable number.[45] On the other hand, periodic boundary conditions must be used in the other two directions to reduce the computation time to a reasonable amount.

Ionic species are charged and so a potential must be specified between the individual ionic species. Consider a pair of ions, then the Coulombic interaction is of the form[45]

$$\phi_C = \zeta\frac{z_i z_j}{r_i - r_j} \tag{42}$$

where the variables are in dimensionless form and

$$\zeta = \frac{e^2}{\epsilon_r\epsilon_W\sigma}$$

is the dimensionless interaction energy, e is the electron charge and ϵ_r is the dielectric constant of the medium. Typical Lennard-Jones parameters fo a sodium-chloride aqueous solution are shown on Table 9.

It is important to note that when an external force is applied to a system, a simulation cell will rapidly heat up if heat is not removed. The term "thermostat is given to the procedure used to remove the excess energy to keep the temperature of the cell constant. Various means have been used to do this and Berendson, Nose-Hoover and Isokinetic thermostats[43,44] have been employed.

Once the problem is set up the equations, since they are nonlinear, need to be solved numerically. This can be done by any standard numerical method such as the lower order Euler and Modified Euler methods, or the more accurate single step Runge-Kutta methods and multistep Adams-Moulton mwthod. A particularly useful method for MD simulations is to replace the second derivative by a discrete central difference approximation; this approximation may be derived simply from Taylor series approximations and the approximation at time level k for any position x is defined by

$$\frac{d^2x_i}{dt^2} = \frac{x_i^{k+1} - 2x_i^k + x_i^{k-1}}{\Delta t^2} + O(\Delta t) \tag{43}$$

Such an approximation in the context of MD simulations is called the Verlet algorithm.[46] This method is multi-step because it involves evaluation of the right side of equation (41) at two time levels. The Verlet algorithm is particularly attractive because it conserves energy much better than it accuracy would suggest.

Zhu *et al*[45] have performed molecular synamics study of electroosmotic flow in a nanochannel and compare their results with the classical Poisson-Boltzmann theory. This work is discussed elsewhere in this volume and we summarize the results briefly as follows. The MD solutions show that ions are excluded from the wall and so the bulk velocity is much higher than that from Poisson-Boltzmann theory which allows ions reght up to the wall. The PB theory can be fixed up by redefining the boundary of the channel.

Cui[47] has studied the transport of ssDNA in 2.4 and 3.0 nm hydrophilic silica channels. He found that the water and ion density profiles are unaffected by the ssDNA and thus depend only on the pore diameter. Four types of ssDNA are modeled (G10,A10,C10,T10) where the "10" denotes that ten nucleotides are included. In each case the end-to-end distance or length of the ssDNA oscillates about a mean value just over $3nm$ as shown on Figure 18. Additional computations for a $2.4nm$ pore show increased fluctuation amplitude. The calsulations are carried out over approximately $10 - 12ns$. Reduced adorption of ions onto the ssDNA is also observed. These results show that the ssDNA remains extended in the nanopore as expected because it is negatively charged as is the walls of the channel.

10 Summary

We have reviewed the state-of-the-art of modeling biomolecular transport in micro and nanochannels. We have focussed on those methods which can be used to predict both transport of a polymeric species and the structure of the background bulk flow. Thus only deterministic models have been discussed while recognizing that there is a large literature on stochastic techniques. The techniques discussed here are appropriate for the design of devices for which fluid transport is a crucial part of the process. Thus these methods do not, in general, resolve the complex substructure of the biomolecule.

We have compared and contrasted natural ion channels with what we have called synthetic ion channels which can be used to pump ions and bioploymers into and out of nanochannels for rapid molecular analysis, separations, sensing and other applications. The primary difference between the two is the size and cross-section of the channels; due to fabrication limitations, and often the application, synthetic ion channels are rectangular and bigger, while natural ion channels have roughly circular cross-section and are smaller. In many other respects, the basic physics of natural and synthetic ion channels are similar.

We have discussed three types of modeling techniques beginning with a continuum approach using the Poisson-Nernst-Planck system. In this method, ionic species and a simulated biomolecule are treated as point charges and the deformation of the biomolecule is therefore not modeled. This method seems to work well for cases where the biomolecule is not too large and this simple diffusion model compares well with a set of experimental data for the transport of glucose and albumin.

Of course, strictly continuum approaches do not incorporate the size of the biomolecule explicitly and thus do not account for shape changes. The next level of approximation is the Brownian

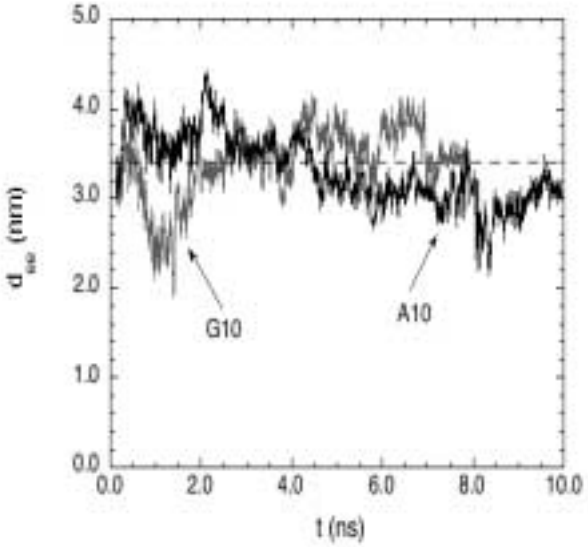

(a)

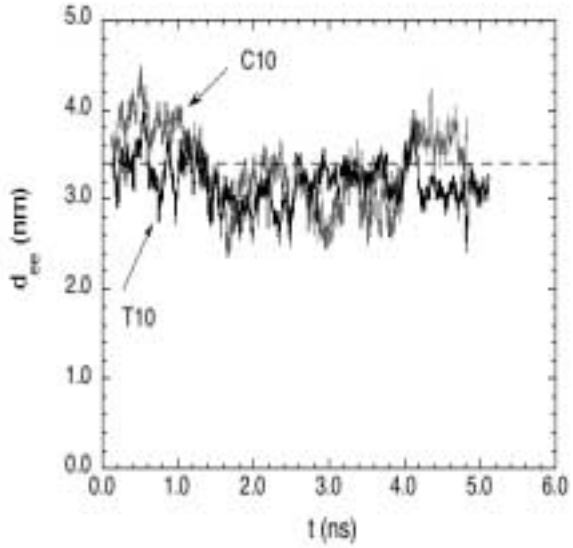

(b)

Figure 18: End to end distance of a ssDNA molecule. Dashed line indicates the length of a single pitch double helix B-form DNA. (a) poly(G_{10}) and poly(A_{10}). (b) poly(T_{10}) and poly(C_{10}).

Dynamics approach in which the solvent is treated as a continuum. This procedure leads to a first or second order order differential equation in time for the position of the solute molecules. If the solute is a large polymer, the polymer is then discretized using a ball and spring approach, or a ball-rod approach which defines how the polymer moves within the flow. The solvent and the other ionic species, if present are treated as a continuum. Treating the background fluid mixture as a continuum is necessary if the flow is in a microchannel since the domain is too large to treat the other constituents of the fluid on the molecular level.

The final level of approximation is to treat all of the constituents as individual molecules; this is the Molecular Dynamics approach and this method may be used as the domain of flow approaches nanoscale. However, it must be pointed out that the actual computation of the transport of a biopolymer in an imposed mean flow is in its infancy and much more work needs to be done in this area.

All devices no matter what their objective must involve system level modeling; the MD simulation technique is difficult to apply to the system design because of the computationally intensive nature of the solution. Thus it is desireable to perform system design studies with a continuum model of a given component; this can only be done if a lower order continuum model can be developed from the results of an MD simulation.

Acknowledgements: Portions of this work is supported by DARPA, Defense Sciences Office. The authors are grateful to the contract monitors Dr. Anantha Krishnan(DARPA), Mr Clare Thiem and Duane Gilmour of the Air Force Research Lab(IFTC) for their support. ATC is grateful to students Kelly Evers, Jennifer McFerran and Drew Kebbel some of whose work appears in this review. Thanks also to Sherwin Singer and Shengting Cui who read a preliminary draft of this paper. Thanks also to Prof. Derek Hansfod and Dr. Mauro Ferarri both of whom got me started in this field.

References

[1] Hille, B., *Ionic Channels of Excitable Membranes*, 2^{nd} Edition, Sinauer Associates, Sunderland, MA, 1992.

[2] Gillespie, Dirk, 1999 “A Singular Perturbation analysis of the Poisson-Nernst-Planck System: Applications to Ionic Channels”, PhD Thesis, Rush Medical School, Chicago.

[3] Gillespie, Dirk and Eisenberg, Robert S., 2001, “Modified Donnan Potentials for Ion Transport Through Biological Ion Channels”, *Physical Review E*, v. 63, pp. 061902-1-06192-8 .

[4] Braha, Orit, Gu, Li-Qun, Zhou, Li Lu, Xiaofeng, Cheley, Stephen, and Bayley, Hagan, “Simultaneous Sensing of Divalent Metal Ions”, *Nature Biotechnology*, v. 18, pp. 1005-1007 (2000).

[5] Levitt, D.G., 1999 “Modeling of Ion Channels,” *J. Gen. Physiol.*, v. 113, p. 789-794.

[6] Cardenas, Alfredo E., Coalson, Rob D., and Kurnikova, Maria G.,2000, “Three-Dimensional Poisson-Nernst-Planck Theory Studies: Influence of Membrane Electrostatics on Gramicidin A Channel Conductance”, *Biophysical Journal*, v. 79, no. 1, pp. 80-93.

[7] Alberts, Bruce *et al. Essential Cell Biology*, Garland Publishing, New York, 1998.

[8] Eisenberg, Bob, 1998 “Ion Channels in Biological Membranes-Electrostatic Ananysis of a Natural Nanotube”, *Contemporary Physics*, v. 39, no. 6, pp. 447-466.

[9] Barcilon, Victor, Chen, D. P., Eisenberg, R. S., and Jerome, J. W., 1997, “Qualitative Properties of Steady-State Poisson-Nernst-Planck Systems: Perturbation and Simulation Study,” *SIAM J. Appl. Math.*, v. 57, No. 3, pp. 631-648.

[10] Chen, D. P., W. Nonner, and R. S. Eisenberg, 1995, “PNP theory fits current-voltage (IV) relations of a neuronal anion channel in 13 solutions,” *Biophys. J.*, v. 68, A370.

[11] Roux, Benoit, 2002 “Theoretical and Computational Models of IonChannels,” *Current Opinion in Structural Biology*, v. 12, pp. 182-189.

[12] Nonner, Wolfgang and Eisenberg, Bob, 1998, “Ion Permeation and Glutamate Residues Linked by Poisson-Nernst-Planck Theory in L-Type Calcium Channels”, *Biophysical Journal*, v. 75, pp. 1287-1305.

[13] Nonner, Wolfgang, Gillespie, Dirk, Henderson, Douglas, and Eisenberg, Bob, 2001 “Ion Accumulation in a Biological Calcium Channel: Effects of Solvent and Confining Pressure,” *J. Phys. Chem. B*, v. 105, pp. 6427-6436.

[14] Hollerbach, Uwe, Chen, Duan P., and Eisenberg, Robert, 2001 “Two- and Three-Dimensional Poisson-Nernst-Planck Simulations of Current Flow Through Gramicidin A,” *Journal of Scientific Computing*, v. 16, No. 4, pp. 373-409.

[15] Schuss, Z., Nadler, B., and Eisenberg, R. S., 2001 “Derivation of Poisson and Nernst-Planck equation in a bath and channel from a molecular model,” *Physical Review E*, v. 64, pp. 036116-1-036116-14.

[16] Gillespie, Dirk, Nonner, Wolfgang and Eisenberg, Robert S., 2002 “Coupling Poisson-Nernst-Planck and Density Functional Theory to Calculate Ion Flux”, *J. Condensed Matter*, v. 14, pp. 12129-12145.

[17] Conlisk, A. T., McFerran, J., Zheng, Z., Hansford, D., 2002 “Mass Transfer and Flow in Electrically Charged Micro- and Nanochannels,” *Analytical Chemistry*, v. 74, n. 9), pp. 2139-2150.

[18] Bird, R.B.; Drew, T.B. and Hoopes, J.W. *ed*. “Theory of Diffusion,” *Advances in Chemical Engineering*, v. 1, Academic Press, New York (1956), p. 156-239.

[19] Tyrell, H.J.V., Harris, K.R. *Diffusion in Liquids: A Theoretical and Experimental Study*, Butterworth & Co. Ltd., 1984.

[20] Peters, T. Jr. *All About Albumin: Biochemistry, Genetics and Medical Applications*, 3^d Ed., Academic Press, San Diego, 1996.

[21] Peters, T. Jr. *All About Albumin: Biochemistry, Genetics and Medical Applications*, 3^d Ed., Academic Press, San Diego, 1996.

[22] Lin, B. Yu, J. Rice, S.A. “Direct Measurements of Constrained Brownian Motion of an Isolated Sphere Between Two Walls,” *Physical Review E.*, v. 62, n. 3 (2000), p. 3909.

[23] Happel, John and Brenner, Howard, *Low Reynolds Number Hydrodynamics: with Special Applications to Particulate Media*, Kluwer, Boston, 1983.

[24] Davidson, M. G., Deen, W. M., 1988 "Hydrodynamic Theory for the Hindered Transport of Flexible Macromolecules in Porous Membranes," *Journal of Membrane Science*, v. 35, p. 167-192.

[25] Levitt, D. G., 1975 "General Continuum Analysis of Transport through Pores, I. Proof of Onsager's Reciprocity Postulate for Uniform Pore," *Biophysical Journal*, v. 15, p. 533-551.

[26] Levitt, D. G., 1975 "General Continuum Analysis of Transport Through Pores, II. Nonuniform Pores," *Biophysical Journal*, v. 15, p. 553-563.

[27] Bevan, M.A., Prieve, D.C. "Hindered Diffusion of Colloidal Particles Very Near to a Wall: Revisited," *J. Chem. Phys*., v. 113, n.3 (2000), p. 1228.

[28] Haberman, W.L., Sayre, R.M. "Motion of Rigid and Fluid Spheres in Stationary and Moving Liquids Inside Cylindrical Tubes," David Taylor Model Basin (Dept. of the Navy), Report 1143, U.S. Department of Defense, Navy Department, Washington, D.C., 1958.

[29] Conlisk, A. T. 2002 "On the Debye-Huckel Approximation in Electroosmotic Flow in Micro and Nanochannels", AIAA paper 2003-2869, AIAA 3^{rd} Theoretical Fluid Mechanics Meeting, St. Louis, June 2002.

[30] Zheng, Zhi, Hansford, Derek J., Conlisk, A. T., 2003 "Effect of Multivalent Ions on Electroosmotic Flow in Micro and Nanochannels", *Electrophoresis*, v. 24, no. 17 pp. 3006-3017, August.

[31] Chen, Duan P., Lear, James and Eisenberg, Robert, 1997 "Permeation through an Open Channel: Poisson-Nernst-Planck Theory of a Synthetic Ion Channel", *Biophysical J.*, v. 72, pp. 97-116.

[32] Chung, S. H., Hoyles, M., Allen, T. and Kuyucak, S. " "Study of Ionic Currents across a Model Membrane Channel Using Brownian Dynamics", *Biophysical Journal*, vol. 75, pp. 893-809, 1998.

[33] Li, SW. C., Hoyles, M., Kuyucak, S. snd Chung, S. H., Brownian Dynamics Study of Ion Transport in the Vestibule of Membrane Channels, *Biophysical Journal*, vol. 74, pp. 37-47, 1998.

[34] Edwards, Scott, Corry, Ben, Kuyucak, S snd Chung, S. H., "Continuum Electrostatics Fails to Describe Ion Permeation in the Gramicidin Channel, *Biophysical Journal*, vol. 83, pp. 1348-1360, 2002.

[35] Corry, Ben, Kuyucak, S. snd Chung, S. H., "Tests of Continuum Theories as Models of Ion Channels,II. Poisson-Nernst-Planck Theory versus Brownian Dynamics", *Biophysical Journal*, vol. 78, pp. 2364-2381, 2000.

[36] Kuhn, W. and Grun, F., "Relationships Between Elastic Constants and Stretching Double Refraction of Highly Elastic Substances", *Kolloid-Z*, v. 101, pp. 248-253, 1942.

[37] Yamakawa, Hiromi, *Modern Theory of Polymer Solutions*, Harper and Row, New York, 1971.

[38] Bird, R. B., Curtiss, R. C., Armstrong, R. C., and Hassager, O. , *Dynamics of Polymeric Liquids*, 2nd Ed., Wiley, New York, 1987, Vol. II.

[39] Hur, Joe S., Shaqfeh, Eric S. G., and Ronald G. Larson, "Brownian Dynamics Simulations of Single DNA molecules in Shear Flow", *J. Rheology*, v. 44, no.4, pp. 713-742, 2000.

[40] Larson, R. G., Hu, Hua, Smith, D. E. and Chu, S., "Brownian Dynamics Simulations of a DNA Molecule in an Extensional Flow Field", *J. Rheology*, vol. 43, no. 2, pp. 267-304, 1999.

[41] Panwar, Ajay S. and Kumar, Satish "Brownian Dynamics Simulations of Polymer Stretching and Transport in a Complex Electroosmotic Flow", *J. Chemical Physics*, v. 118, no. 2, pp. 925-936, 2003.

[42] Sadus, Richard J. *Molecular Simulation of Fluids: Theory, Algorithms and Object-Orientation*, Elsevier, Amsterdam, 1999.

[43] Rapaport, D. C. *The Art of Molecular Simulation* , 2nd Edition, Cambridge, 2004.

[44] Heyes, David M., *The Liquid State: Applications of Molecular Simulations*, Wiley, Chichester, 1998.

[45] Zhu, Wei, Singer, Sherwin, Zheng, Zhi, and Conlisk, A. T., " Electroosmotic Flow of a Model Electrolyte", to appear *Phys Rev. E*.

[46] Verlet, L. "Computer Experiments on Classical Fluids I. Thermodynamical Properties of Lennard-Jones Molecules", *Phys. Rev.* , vol 159, p. 98, 1967.

[47] Cui, Shengting, "Molecular Duynamics Study of Single-Stranded DNA is Aqueous Solution Confined in a Nanopore", *Molecular Physics*, vol. 102, no. 2, pp. 139-146, 2004.

Appendix I:

Nano-Particle Image Velocimetry: A Near-Wall Velocimetry Technique with Submicron Spatial Resolution*

Minami Yoda†

Abstract

Although fluid flows at the micro- and nanoscale have recently become an important area of fluid mechanics, there are few experimental techniques at present with a spatial resolution small enough measure velocity fields in such flows. This chapter describes a novel technique, nano-particle image velocimetry (nPIV), which exploits the properties of evanescent waves generated by the total internal reflection of light at a refractive index interface to obtain velocity field measurements within the first *O*(100 nm) next to the wall. The technique is compared with current "state of the art" microfluidics diagnostic techniques such as micro-particle image velocimetry and molecular tagging velocimetry. After some background on evanescent waves and a brief description of a simple model of the image intensity for a fluorescent spherical particle illuminated by evanescent waves, the effects of hindered Brownian diffusion on the accuracy of nPIV results are evaluated using artificial images. Representative nPIV results from electroosmotic flow through rectangular microchannels are presented and validated using both analytical and experimental results.

1 Introduction

Over the last decade, characterizing and understanding fluid flow and transport at spatial scales of 100 μm or less has become a major area of research in fluid mechanics because of the rapid development of microscale devices based upon microelectromechanical systems (MEMS) fabrication techniques. Examples of such microfluidic devices include Labs-on-a-Chip for biochemical separation and analysis, inkjet printer heads, various types of microelectronic cooling devices, microscale fuel cells, microthrusters, and genomic and proteomic "chips" capable of sequencing and identifying various proteins including RNA and DNA. More recently, nanotechnology and the promise of engineering new devices at the molecular scale has sparked interest in understanding flow at spatial scales below 1 μm. Optimizing and controlling the flow of liquids and gases in

micro- and nanoscale devices requires both well-validated models of transport down to the molecular scale and diagnostic techniques with spatial resolution well below 1 μm.

A major "bottleneck" in developing such flow models is our limited fundamental understanding of microscale flows and limitations in our ability to measure flow parameters such as velocity, pressure, concentration and temperature at these spatial scales. At the microscale, surface (*vs.* bulk) effects become significant; the new physical phenomena that may therefore be significant in micro- and nanoscale flows include apparent slip[3] (*i.e.*, nonzero flow velocity at the wall due possibly to a "soft" dissociated fluid or gas layer[4,5]); the effects of surface properties such as chemistry (*e.g.* hydrophobic *vs.* hydrophilic[6,7]), molecular-scale roughness[8], and charge; and discrepancies in fluid properties (*e.g.* viscosity) between the interfacial and bulk flow regions. Diagnostic techniques capable of interrogating the near-wall region to measure flow parameters within the first 100 nm of the wall are therefore important in understanding how surface effects impact micro- and nanoscale transport, and validating our current models of transport at these spatial scales.

This chapter first briefly reviews current experimental techniques in microfluidics, with an emphasis on velocimetry techniques and their spatial resolution and near-wall capabilities. The chapter then describes a new technique, nano-particle image velocimetry (nPIV), based upon evanescent-wave illumination generated by the total internal reflection of light at a refractive index interface. The applications of nPIV are illustrated by velocity and mobility results obtained in steady, fully-developed two-dimensional electroosmotic flow (EOF) of liquids.

2 Diagnostic Techniques in Microfluidics

The majority of diagnostic techniques in fluid mechanics were originally developed for turbulent flows, where flow parameters such as velocity and pressure have strong stochastic fluctuations. "Classical" flow measurement diagnostic techniques such as hot-wire anemometry and laser-Doppler velocimetry (LDV) therefore emphasized

measurements at a single spatial location with high temporal resolution or sampling rate. Over the last twenty years, advances in lasers and imaging technology have led to the development of a variety of nonintrusive optical diagnostic techniques for obtaining spatially and temporally resolved measurements of velocity and such as particle-image velocimetry (PIV) and molecular-tagging velocimetry (MTV).

Given that a microchannel typically has a cross-section dimension of $O(100\ \mu m)$ and speeds of $O(1$ mm/s) or less, nearly all microchannel flows are laminar, and, in most applications, steady. Spatial (*vs.* temporal) resolution is therefore the major limiting issue in microfluidic measurements. Given the limited amount of available space and access in most microdevices, diagnostic techniques must also be nonintrusive methods. Yet most of the nonintrusive optical diagnostic techniques have minimum spatial resolutions that are comparable to or exceed the entire dimension of the microchannel—perhaps 50 μm for LDV and 500 μm for PIV.

Nevertheless, both PIV and MTV have been extended to microscale flows. The most common microfluidic diagnostic technique, micro-particle image velocimetry (μPIV), has been used extensively over the last five years to obtain velocity fields in steady flows in microchannels with dimensions of $O(1–100\ \mu m)$.[9] In μPIV, water is seeded with 200–500 nm diameter colloidal fluorescently dyed polystyrene spheres (density $\rho \approx 1.05$ g/cm^3) at volume fractions of $O(10^{-4}–10^{-3})$. The region of interest in the flow is then volumetrically illuminated by light of the wavelength required to excite the fluorescent dye (*e.g.* from an argon-ion or frequency-doubled Nd:YAG), and the longer-wavelength fluorescence from the particle tracers is imaged through a high-magnification microscope objective and epi-fluorescent filter cube onto a CCD camera. The small depth of field of the microscope objective ensures that only tracer particles in a "slice" of the flow centered about the focal plane of the imaging optics are in focus, and hence have relatively high grayscale values and small particle diameters, on the CCD.

Assuming that the flow component along the optical axis is negligible, the depth of field of the imaging system therefore determines the "out-of-plane" spatial resolution (*i.e.*, the

spatial resolution along the optical axis). Santiago *et al.*[9] cited a depth of field of 1.5 μm for a 100×1.4 oil immersion objective based upon a criterion that particle images more than 25% larger than "in-focus" particle images were considered out of focus. More recently, Tretheway and Meinhart[6] reported a depth of field of 1.8 μm for a 60×1.4 oil immersion objective. The minimum out-of-plane spatial resolution of μPIV therefore exceeds 1 μm at present.

In most μPIV measurements, "interrogation windows", or portions of two images (the "image pair") separated by a given time interval Δt are cross-correlated. The location of the cross-correlation peak then gives the average displacement for the tracer particles in both interrogation windows, and this displacement divided by Δt gives the average velocity of the group of tracers, and presumably the flow velocity. The minimum "in-plane" spatial resolution (*i.e.*, the spatial resolution in the plane normal to the optical axis) of μPIV is then determined by the largest of the following factors:

- the dimensions of the interrogation window;
- the displacement over the time interval;
- the minimum spatial resolution of the image;
- the size of the tracer particle.

For most μPIV applications, the minimum in-plane spatial resolution is determined by the interrogation window. Santiago *et al.*[9] used 32 × 32 pixel interrogation windows, corresponding to an in-plane spatial resolution of 6.9 μm; Tretheway and Meinhart[6] used 128 × 8 pixel rectangular interrogation regions, corresponding to an in-plane spatial resolution of 14.7 × 0.9 μm.

MTV using both caged fluorophores and phosphorescent supramolecules has also been used to measure velocity fields in microchannels. In molecular tagging velocimetry, molecular tracers (*e.g.* phosphorescent supramolecules and caged fluorophores) are excited or uncaged by light at UV wavelengths and emit light (after excitation by a visible laser for caged fluorophores) at visible wavelengths.[10,11] The velocity field can then be obtained by exciting or "tagging" a material line or grid of material lines in the

flow of a liquid seeded with molecular tracers and measuring the convection of the tagged lines over a known time interval. Paul *et al.*[12] used a relatively high molecular weight caged fluorophore, caged fluorescein dextran, to visualize Poiseuille and electroosmotic flows through 100 μm open capillaries. Sinton and Li[13] used 5-carboxymethoxy-2-nitrobenzyl (CMNB)-caged fluorescein to obtain electroosmotic flow velocity profiles through 20–200 μm square and circular microchannels. Lum and Koochesfahani[14] recently reported MTV measurements in Poiseuille flow through a 300 μm channel using the phosphorescent supramolecule based upon the lumophore 1-Bromonaphthalene (1-BrNp).

Assuming negligible flow along the optical axis, the minimum out-of-plane spatial resolution of MTV data is usually determined by the dimensions of the tagged line normal to the object plane. The minimum in-plane spatial resolution for MTV is determined by the largest of the following three factors: 1) the dimension of the tagged line; 2) the displacement over the time interval; and 3) the spatial resolution of the image. It is therefore usually determined by the dimension of the tagged line. To date, the smallest dimension reported for a tagged line is about 25 μm,[14] but the diffraction-limited spot size at UV wavelengths for high magnification and numerical aperture optics can be as small as a few micrometers, suggesting that the minimum spatial resolution for MTV should be comparable to the values reported for μPIV.

Nevertheless, both μPIV and MTV have minimum spatial resolutions exceeding 1 μm, suggesting that neither technique is capable of spatially resolving velocity fields for geometries with dimensions below 10 μm. Moreover, the near-wall capabilities of both techniques are limited. The best μPIV measurements to date were obtained within 450 nm of the wall, and are actually the velocity averaged over the first 900 nm (based upon interrogation window size) next to the wall.[6] The near-wall capabilities of MTV are yet largely unexplored. Nevertheless, assuming that velocity data can be obtained within a few pixels of the wall for MTV, the current minimum pixel dimension for intensified CCD cameras is just below 10 μm. For a magnification of 100, MTV may ultimately be able to obtain velocity data averaged over the first 300–400 nm next to the wall.

Current microfluidics diagnostic techniques therefore appear to be limited to measuring velocities averaged over about the first 400 nm next to the wall. This near-wall capability is inadequate to investigate many interfacial phenomena of interest such slip length, with reported values ranging from about 8 nm to 1 μm. [7,15] Over the last three years, we have therefore developed an extension of μPIV based upon evanescent-wave illumination generated by total internal reflection (TIR) of a laser beam at the fluid-solid interface between the flow and the wall.[16] This nano-particle image velocimetry (nPIV) technique is inherently limited to interrogating the near-wall region, and as such, complements bulk flow velocimetry techniques such as μPIV and MTV.

3 Nano-Particle Image Velocimetry Background

Nano-PIV, like μPIV, obtains measurements of two components of the flow velocity field by tracking the motion of groups of fluorescent colloidal tracer particles over time as they are convected by the flow. Nano-PIV differs from μPIV, however, in its use of evanescent-wave (*vs.* volumetric) illumination.

3.1 Theory of Evanescent Waves

Consider a beam of light propagating through a dense transparent medium of refractive index n_2 incident upon a interface with a less dense transparent medium of refractive index $n_1 < n_2$. If the angle of incidence θ_i measured with respect to the y-axis, or the normal to the interface, is greater than the critical angle $\theta_c = \sin^{-1}(n_{12})$, where the relative index of refraction $n_{12} = n_1 / n_2$, then the light will undergo total internal reflection (TIR) at the interface (Figure 1). Snell's Law gives:

$$n_2 \sin\theta_i = n_1 \sin\theta_t \quad \Rightarrow \quad \begin{cases} \sin\theta_t = \sin\theta_i / n_{12} > 1 \\ \cos\theta_t = \sqrt{1-\sin^2\theta_t} = \dfrac{\sqrt{n_{12}^2 - \sin^2\theta_i}}{n_{12}} = \pm i\beta \end{cases} \tag{3.1}$$

where the angle of transmission θ_t has a complex cosine. The wavefunction of the transmitted electric field is therefore:[17]

$$\begin{aligned}\mathbf{E}_t &= \mathbf{E}_{0t}\exp\{i\,k_t[\sin\theta_t x + \cos\theta_t y - \omega t]\} \\ &= \mathbf{E}_{0t}\exp\{\mp k_t \beta y\}\exp\left\{-i\left[\omega t - \frac{k_t}{n_{12}}(\sin\theta_i)\,x\right]\right\}\end{aligned} \tag{3.2}$$

where k_t is the wavenumber. The solution with the positive exponential is physically impossible. The resultant wave therefore has an amplitude that decays exponentially with distance normal to the interface y and propagates along the direction parallel to the interface x. The intensity of the evanescent wave is proportional to the square of the transmitted electric field magnitude, and it can then be shown that this intensity

$$I(y) = I_o \exp\left\{-\frac{y}{y_p}\right\} \quad \text{where} \quad y_p = \frac{1}{2k_t\beta} = \frac{\lambda_o}{4\pi n_2}\frac{1}{\sqrt{\sin^2\theta_i - n_{12}^2}} \tag{3.3}$$

Here, I_o is the intensity at the interface (*i.e.*, $y = 0$), y_p is the penetration depth of the evanescent wave, and λ_o is the wavelength of the light in vacuum.

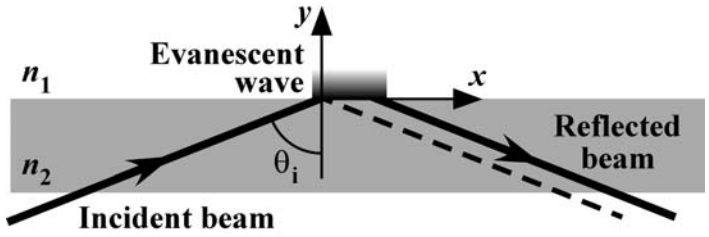

Figure 1 TIR of an incident beam of light at a refractive index interface and the generation of an evanescent wave in the less dense medium of index n_1. Note that the actual reflected beam is slightly offset from the geometrically reflected light ray due to the Goos-Hänchen effect.[18]

The components of the electric field tangential to the interface must be continuous across the interface. For light polarized perpendicular to the plane of incidence (*i.e.*, the *x*-*y* plane) with an electric field magnitude incident upon the interface of $E_i^{\perp}$, the Fresnel Equations for the amplitude transmission coefficient gives the *y*-component of the electric field of the evanescent-wave at the interface as:[17, 19]

$$E_z^{\mathrm{o}} = E_{\mathrm{i}}^{\perp} \frac{2\cos\theta_{\mathrm{i}}}{\cos\theta_{\mathrm{i}} + n_{12}\cos\theta_{\mathrm{t}}}$$
$$= E_{\mathrm{i}}^{\perp} \frac{2\cos\theta_{\mathrm{i}}}{\sqrt{1-n_{12}^2}} \exp\{-i\delta_{\perp}\} \quad \text{where} \quad \delta_{\perp} = \tan^{-1}\left\{\frac{\sqrt{\sin^2\theta_{\mathrm{i}} - n_{12}^2}}{\cos\theta_{\mathrm{i}}}\right\} \tag{3.4}$$

For parallel polarized light with an electric field magnitude incident upon the interface of $E_{\mathrm{i}}^{\parallel}$, the Fresnel Equations give the *x*- and *y*-components of the evanescent-wave electric field at the interface as:

$$E_x^{\mathrm{o}} = E_{\mathrm{i}}^{\parallel} \frac{2\cos\theta_{\mathrm{i}}\cos\theta_{\mathrm{t}}}{\cos\theta_{\mathrm{t}} + n_{12}\cos\theta_{\mathrm{i}}} = E_{\mathrm{i}}^{\parallel} \frac{2\cos\theta_{\mathrm{i}}\sqrt{\sin^2\theta_{\mathrm{i}} - n_{12}^2}}{\sqrt{n_{12}^4\cos^2\theta_{\mathrm{i}} + \sin^2\theta_{\mathrm{i}} - n_{12}^2}} \exp\left\{-i\left(\delta_{\parallel} + \frac{\pi}{2}\right)\right\}$$

$$E_y^{\mathrm{o}} = E_{\mathrm{i}}^{\parallel} \frac{2\cos\theta_{\mathrm{i}}\sin\theta_{\mathrm{t}}}{\cos\theta_{\mathrm{t}} + n_{12}\cos\theta_{\mathrm{i}}} = E_{\mathrm{i}}^{\parallel} \frac{2\cos\theta_{\mathrm{i}}\sin\theta_{\mathrm{i}}}{\sqrt{n_{12}^4\cos^2\theta_{\mathrm{i}} + \sin^2\theta_{\mathrm{i}} - n_{12}^2}} \exp\{-i\delta_{\parallel}\}$$

where
$$\delta_{\parallel} = \tan^{-1}\left\{\frac{\sqrt{\sin^2\theta_{\mathrm{i}} - n_{12}^2}}{n_{12}^2\cos\theta_{\mathrm{i}}}\right\} \tag{3.5}$$

Note that these two components are exactly 90° out of phase with each other.

The evanescent-wave intensity at the interface I_{o} depends on θ_{i} and the polarization of the incident beam, with I_{o} proportional to square of the magnitude of the electric field **E** at the refractive-index interface. The evanescent-wave intensities for parallel and perpendicular polarized light, or $I_{\mathrm{o}}^{\parallel}$ and $I_{\mathrm{o}}^{\perp}$, respectively, are then:

$$\frac{I_{\mathrm{o}}^{\parallel}}{\mathcal{I}^{\parallel}} = \frac{4\cos^2\theta_{\mathrm{i}}}{1-n_{12}^2} \frac{2\sin^2\theta_{\mathrm{i}} - n_{12}^2}{(1+n_{12}^2)\sin^2\theta_{\mathrm{i}} - n_{12}^2}$$
$$\frac{I_{\mathrm{o}}^{\perp}}{\mathcal{I}^{\perp}} = \frac{4\cos^2\theta_{\mathrm{i}}}{1-n_{12}^2} \tag{3.6}$$

where $\mathcal{I}^{\parallel}$ and $\mathcal{I}^{\perp}$ are the intensities of light incident upon the interface with polarizations parallel and perpendicular to the plane of incidence, respectively. Surprisingly, the evanescent-wave intensity at the interface often exceeds that of the incident light. For $\theta_{\mathrm{i}} = \theta_{\mathrm{c}}$, Eq. (3.6) reduces to $I_{\mathrm{o}}^{\parallel} / \mathcal{I}^{\parallel} = 4 / n_{12}^2$ and $I_{\mathrm{o}}^{\perp} / \mathcal{I}^{\perp} = 4$; note that higher evanescent-wave intensities can be achieved with parallel polarized light since $n_{12} < 1$. Even for TIR at a glass-water interface with $n_2 = 1.5$ and $n_1 = 1.33$, and an angle of

incidence slightly above the critical angle $\theta_i = 63°$, for example, the evanescent-wave intensity is several times that of the incident light, with $I_o^{\parallel} / \mathcal{I}^{\parallel} = 4.89$ and $I_o^{\perp} / \mathcal{I}^{\perp} = 3.86$.

Since $y_p < \lambda_o$ for most cases and the intensity of the evanescent wave decays exponentially with y, this illumination is confined to a narrow region immediately adjacent to the interface. For TIR of blue light with $\lambda_o = 488$ nm at a glass-water interface, $y_p < 120$ nm. Evanescent waves are hence the basis of the total internal reflection fluorescence (TIRF) microscopy used to visualize cell-substrate contact and measure binding kinetics of proteins to cell surface receptors (for example) in biophysics[20] and the total internal reflection microscopy (TIRM) technique used to measure colloidal forces in surface science.[21] Based upon the properties of evanescent-wave illumination, nPIV should therefore be able to obtain velocity data averaged over the first O(100 nm) thick layer next to the wall with an out-of-plane spatial resolution based upon the penetration depth of O(100 nm).

Nano-PIV tracks the displacement of fluorescent particle tracers illuminated by evanescent waves. To model the resultant particle image intensity, consider a fluorescent sphere of radius a illuminated by an evanescent wave with penetration depth y_p where $a \sim y_p$ whose center and edge are at distances z' and h from the interface, respectively (Figure 2). Under the assumptions that:

a) disturbances due to the presence of the sphere have a negligible effect on the exponential decay of the evanescent wave-intensity in the vicinity of the sphere (note that essentially a single "layer" of spheres are illuminated by the evanescent wave since $y_p \sim 2a$ at these low tracer seeding densities),
b) only the fluorophores on the surface of the sphere are excited by the evanescent wave, and
c) the intensity at the interface I_o is constant,

the net power emitted by this sphere when illuminated by the evanescent wave is directly proportional to the product of $I(y)$ and the surface area of the sphere. Moreover, since

this fluorescence is typically detected by a microscope objective placed below the sphere through the dense medium, only light emitted by the bottom half of the sphere facing the interface will be detected by the imaging system, the amount of light imaged, or the"brightness" $\mathcal{B}$ of the particle, will be proportional to the net power emitted by the bottom half of the sphere. It can then be shown that the image brightness of a spherical particle illuminated by an evanescent wave also decays exponentially, albeit in h, or the distance from its nearest edge to the interface, as follows:

$$\mathcal{B} \propto \mathcal{B}_o \exp\left\{-\frac{h}{y_p}\right\} \tag{3.7}$$

where $\mathcal{B}_o$ is the brightness of the particle when it is in contact with the wall.[22]

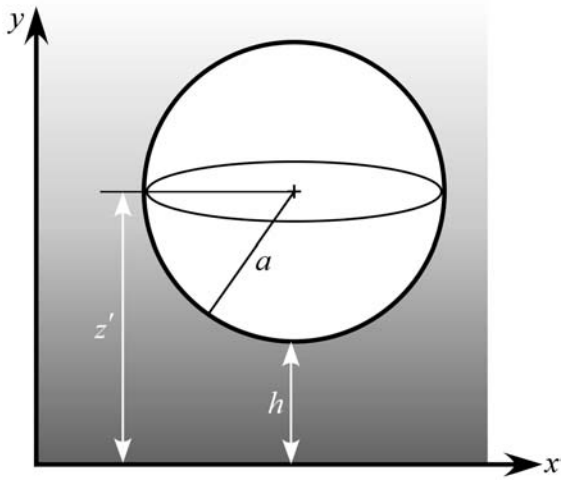

Figure 2 Sphere illuminated by an evanescent wave.

The size of such a particle imaged through a microscope objective and recorded on a CCD camera is essentially the convolution of the geometric and diffraction-limited images since $a < \lambda_o$ in nPIV. If both these images can be approximated as Gaussian functions, this convolution is then also a Gaussian function for a spherical particle with its center at the focal plane with an effective diameter[23,24]

$$d_e = \sqrt{4M^2a^2 + d_{s\infty}} \quad \text{where} \quad d_{s\infty} = 1.22M\lambda\sqrt{\left(\frac{n_o}{\mathrm{NA}}\right)^2 - 1} \tag{3.8}$$

Here, M and NA are the magnification and numerical aperture, respectively, of the microscope objective and n_o is the refractive index of the immersion medium (*e.g.*, oil) between the objective and the object.

3.2 Generation of Evanescent Waves

Most TIRM experiments use one of two methods to generate evanescent-wave illumination, namely the prism method based upon a prism optically coupled to the sample, or the "prismless" method, where the evanescent wave is introduced through a high numerical aperture (NA) objective (Figure 3).[19] In general, the prism method gives more flexibility in terms of optical setup, since the optics for generating the evanescent wave can be aligned independently of the imaging system. Two more advantages of the prism method are that it usually gives cleaner illumination, with better control over autofluorescence and/or autoluminescence, and, given the high cost of high NA microscope objectives, the prism method is usually more economical. Note that neither the prism nor the optical coupling fluid between the prism and the microchannel wall are required to have the same refractive index as the wall.

The prismless method requires a high NA immersion objective. For such an objective, Snell's Law gives:

$$\mathrm{NA} = n_2 \sin\theta_i > n_1 \tag{3.9}$$

For water, n_1 = 1.33, suggesting that NA must be well above this value; the few microscope objectives with magnifications of 60 or greater with numerical apertures of 1.45 or 1.65 are quite expensive. The major advantages of the prismless method are that this method is generally easier to implement in most microscopes, with commercial microscope vendors offering "off-the-shelf" TIRF configurations, and that arc-lamp illumination (*vs.* a laser) can be used to generate the evanescent wave.

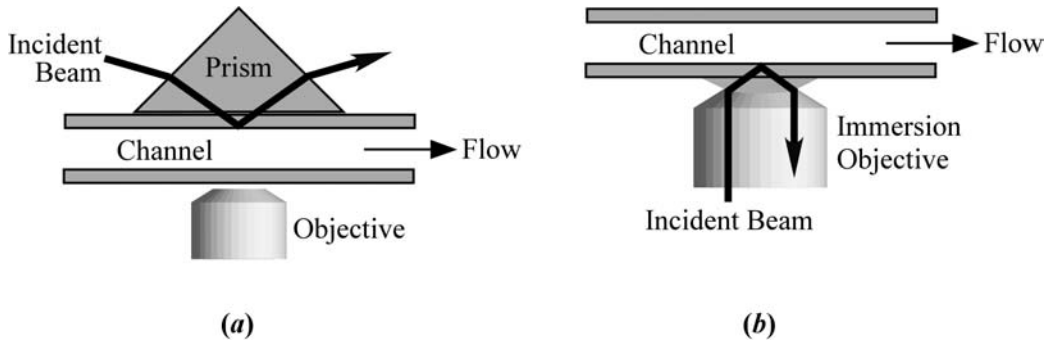

Figure 3 Examples of TIRM configurations where the evanescent wave is generated using the (*a*) prism or (*b*) "prismless" methods.

3.3 Brownian Diffusion Effects in nPIV

Brownian diffusion of the 100–500 nm diameter colloidal particle tracers used in micro- and nano-PIV can be a major source of error in both techniques. For a convective timescale $\tau_c = 1$ s (based upon a velocity scale of 100 μm/s and a length scale of 100 μm), the Peclet number, which compares the time required for a particle to diffuse its own radius to the convective timescale, is

$$Pe \equiv \frac{6\pi\mu a^3}{kT\tau_c} \sim 10^{-3}$$

for a particle of radius $a = 50$ nm suspended in water at absolute temperature $T = 300$K. In this expression, μ is the fluid viscosity and k is the Boltzmann constant. Early μPIV studies noted that the error due to Brownian diffusion imposes a practical lower limit on both the time interval between images within an image pair and the tracer particle size for a given accuracy.[9] Olsen and Adrian[25] showed that Brownian motion reduces the signal-to-noise ratio (SNR) of the cross-correlation. In steady flows, the effects of "in-plane" Brownian diffusion can be greatly reduced by temporal averaging, with the best results achieved by averaging the cross-correlation (*vs.* the actual displacement).[26] "Out-of-plane" Brownian diffusion is usually not an issue, given the out-of-plane spatial resolution of μPIV of at least 1.5 μm.

In contrast with μPIV, Brownian diffusion of nPIV tracers is hindered by the presence of the wall since particles experience increased hydrodynamic drag as they approach the

wall. One of the consequences of hindered Brownian diffusion is that the diffusion coefficients are now functions of the particle distance from the wall; the hindered diffusion coefficients normal and parallel to the wall $D_\perp$ and $D_\parallel$ are: [27,28]

$$D_\perp \approx \frac{6h^2 + 2ah}{6h^2 + 9ah + 2a^2} D_\infty$$
$$D_\parallel = \left[1 - \frac{9}{16}\left(\frac{a}{z'}\right) + \frac{1}{8}\left(\frac{a}{z'}\right)^2 - \frac{45}{256}\left(\frac{a}{z'}\right)^4 - \frac{1}{16}\left(\frac{a}{z'}\right)^5 \right] D_\infty \tag{3.10}$$

where h and z' are the distances of the particle edge and center from the wall, respectively, and $D_\infty = kT/(6\pi\mu a)$ is the Brownian diffusion coefficient for unconfined flow.[29] Note that the expression for $D_\perp$ is an approximation of the infinite series solution given by Goldman *et al.*[30]

If the tracers sample all values of h with equal probability within the y-extent illuminated by the evanescent wave, in-plane hindered Brownian diffusion can be greatly reduced for steady flows by time-averaging the nPIV data. Out-of-plane Brownian diffusion is, however, a major issue for nPIV (unlike μPIV) due to its much smaller out-of-plane spatial resolution. Diffusion normal to the wall leads to "particle mismatch, where the tracers leave ("drop out") or enter ("drop in") the region illuminated by the evanescent wave within the image pair, affecting the SNR of the cross-correlation.

To quantify the error due to this Brownian diffusion-induced particle mismatch, simulations were carried out of colloidal particles with initial locations generated using a Monte Carlo approach.[22] The particles were then convected over a given time interval Δt by a uniform velocity along x of magnitude U subject to hindered Brownian diffusion using the Langevin Equation. If the particles interact with the wall through some type of collision (instead of sticking to the wall), it was assumed that the particles interacted with the wall via perfectly elastic collisions as $z'/a \rightarrow 1$. This "wall interaction model" has a marked effect on the hindered diffusion normal to the wall, biasing the displacements due to diffusion towards lower values. Table 1 compares $D_\perp$, the diffusion coefficients predicted by Eq. (3.6) from the y-position of each particle, with $\mathcal{D}_\perp$, the diffusion

coefficient calculated directly from the actual particle displacement based upon the wall interaction model used here, averaged over the motion of 10^5 particles over 6 ms with an initial position z'/a = [1:Π]. For all values of Π, $\mathcal{D}_\perp < D_\perp$, and, as expected, the discrepancy between the two values decreases as Π increases. This result demonstrates that experimental measurements of hindered Brownian diffusion normal to the wall where the particle interacts with the wall via some type of elastic collision will underestimate the Brownian diffusion coefficient and that any such measurement will be very sensitive to particle-wall interaction effects due, for example, to surface charge or roughness.

Π	$D_\perp / D_\infty$	$\mathcal{D}_\perp / D_\infty$
3	0.582	0.261
5	0.637	0.353
7	0.683	0.440
9	0.720	0.516
11	0.750	0.578

Table 1 Comparison of hindered Brownian diffusion coefficients for motion normal to the wall.

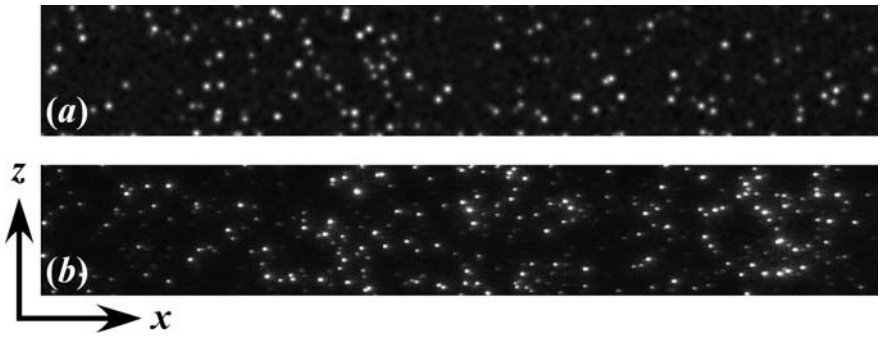

Figure 4 Representative (*a*) artificial and (*b*) experimental particle tracer images.

An artificial image pair is then generated based upon the initial locations of these particle tracers and their locations after a time interval Δt. The particle images are modeled as a Gaussian intensity distribution with an effective diameter given by Equation (3.7) and a peak grayscale value calculated using Equation (3.8). The particle number density, image shape and image background noise characteristics are adjusted so that they match

those for a typical experimental nPIV image following the guidelines suggested by Westerweel.[31] Figure 4 shows representative artificial and experimental images.

Datasets consisting of 5000 such artificial image pairs were processed using FFT–based cross-correlation (*cf.* Sec. 4.1) and a Gaussian (correlation) peak-finding algorithm using a Gaussian surface fit over at least 11 neighboring points for 118×98 pixel interrogation windows with 50% overlap. These relatively large interrogation windows were chosen to match experimental data (*cf.* Section 4); in all cases, at least 30 particle images were present in each window. Figure 5 shows the fraction of mismatched particles (as a percentage of the total number of particles) within an image pair ξ as a function of the time interval within the image pair normalized by the time required for a particle to diffuse its radius due to Brownian motion $\tau = \Delta t / (a^2 / D_\infty)$. The results averaged over 5000 image pairs for both unconfined (□) and hindered (■) Brownian diffusion show that the percentage of mismatched particles increases logarithmically with τ for $\tau > 5$, and that mismatch is reduced by about 5% for hindered diffusion.

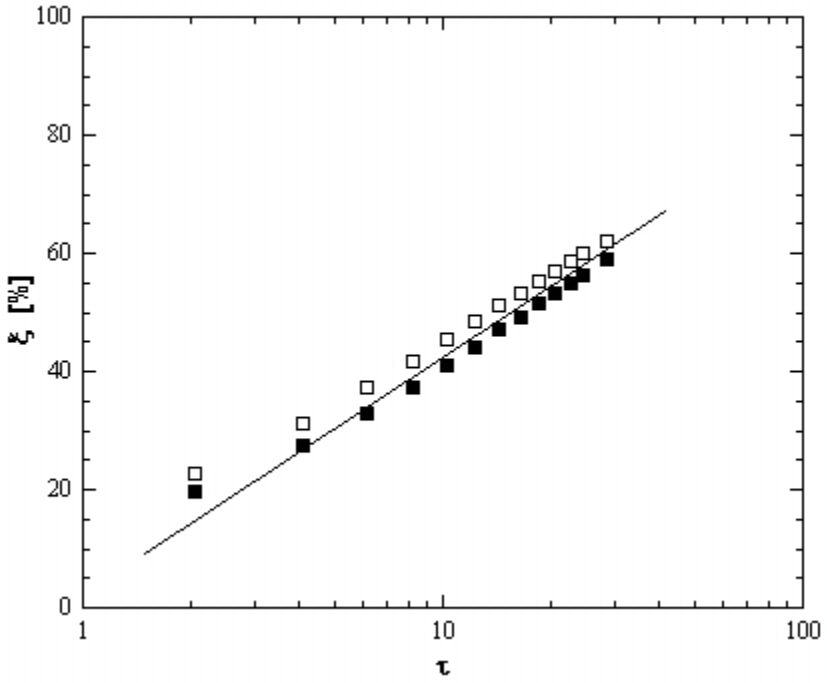

Figure 5 Plot of particle mismatch as a function of normalized time interval within the image pair

Figure 6 shows the displacement error ε between the results obtained by processing an artificial image pair with the actual displacement of $U(\Delta t)$ as a function of particle mismatch averaged over 5000 image pairs. This error is well below the typical minimum accuracy of cross-correlation-based PIV results of about 0.05 pixels[32] and essentially constant for $\xi < 45\%$. Results for both unconfined (□) and hindered (■) Brownian diffusion show a sharp increase in the displacement error once ξ exceeds 55%. This rapid increase in ε for larger values of ξ is due to a decrease in SNR of the cross-correlation peak from both a decrease in the height and an increase in the width of the peak.[22] Note that for a minimum of 30 particles per interrogation window, $\xi = 55\%$ implies that there are at least 13 "matched" particles in each image pair, more than twice the minimum value of 5 matched particles recommended for cross-correlation-based PIV based upon Monte Carlo simulations.[33] The consequences of Brownian diffusion-induced particle mismatch on the accuracy of nPIV data are illustrated in the next Section, which describes the use of nPIV to measure velocity fields in steady, fully-developed electroosmotic flow.

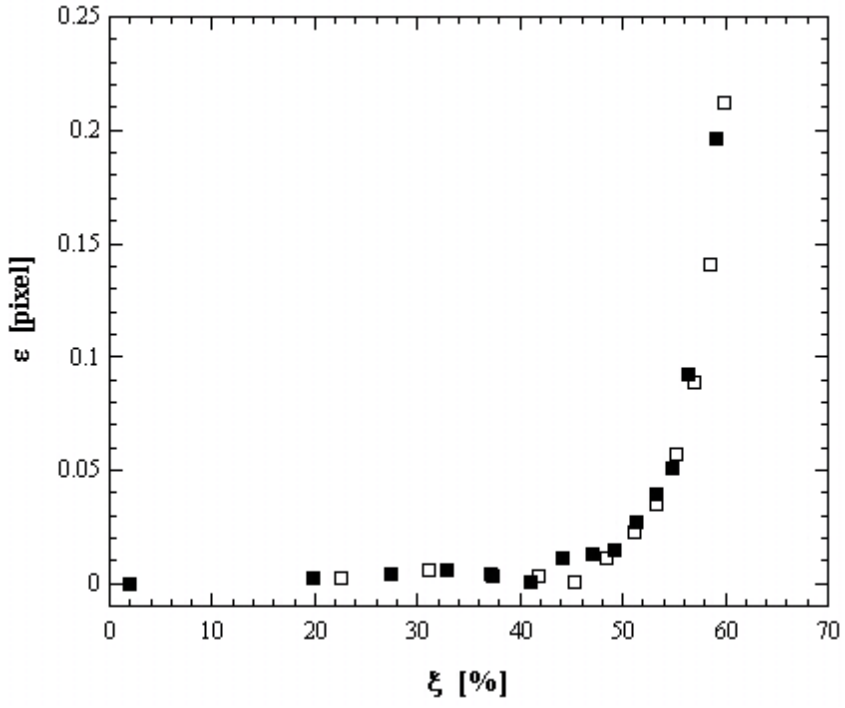

Figure 6 Plot of displacement error in pixels as a function of particle mismatch

4 Nano-PIV Results in Electroosmotic Flow

4.1 Experimental Details

Electroosmotic flow (EOF) of dilute aqueous solutions of the weak base sodium tetraborate ($Na_2B_4O_7$), or borax, at molar concentrations C = 0.19–36 mM was studied in rectangular fused silica microchannels with cross-sectional dimensions $h \times W$ (Figure 7).[34] At these concentrations, the salt dissociates in aqueous solution to give anion and cation species with a valence of unity:

$$Na_2B_4O_7 + 7\ H_2O \rightleftharpoons 2\ Na^+ + 2\ B(OH)_3 + 2\ B(OH)_4^-$$

The ionic strength of the solution $I = 2C$ ($I \equiv \sum_{i=1}^{N} z_i^2 c_i$, where z_i and c_i are the valence and molar concentration of the ith ionic species, respectively).

The microchannels were fabricated using chemical wet etching to produce an open trapezoidal channel, which was then sealed with a cover slip. The region of the microchannel imaged in these experiments was at least 360h downstream of any bends or intersections to ensure fully-developed flow, next to the cover slip at the bottom of the channel to minimize surface roughness and in the center of the channel to ensure uniform flow along the z-direction.

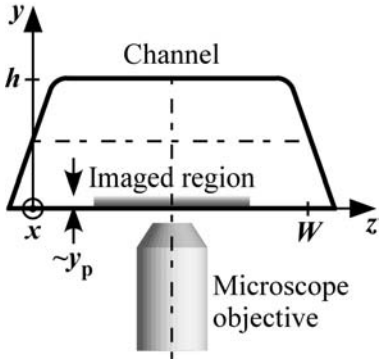

C [mM]	(h, W) [μm]
0.19	(4.9, 17.3)
1.9	(10.2, 26.1)
3.6	(24.7, 51.2)
18.4	(4.8, 17.9)
36	(24.7, 51.2)

Figure 7 Definition sketch of channel cross-section and summary of channel dimensions. Here, x is the flow direction, y is the direction normal to the wall (*i.e.*, along the optical axis) and z is along the wall normal to x.

The working fluid was seeded with 100 nm diameter fluorescent polystyrene spheres (Estapor XC, Bangs Laboratories, Inc.) at volume fractions of 0.07–0.1%. The spheres have excitation and emission maxima at 480 nm and 520 nm, respectively, and a density $\rho = 1.05$ g/cm^3. The microchannel was allowed to sit for several minutes after filling the reservoirs at both ends of the channel with the working fluid to ensure that any Poiseuille flow was eliminated before imposing an electric field using platinum electrodes in the reservoirs.

The evanescent-wave illumination was generated using the prism method (*cf.* Section 3.2) from a continuous argon-ion laser (Coherent Innova 90) beam at 488 nm with an output power of approximately 0.1 W. The beam is refracted through an isosceles right-angle triangle prism and undergoes TIR with an angle of incidence $\theta \approx 70°$ at the interface between the fused silica cover slip with a refractive index $n_2 = 1.46$ and the water with refractive index $n_1 = 1.33$. The penetration depth of the evanescent wave y_p, which determines the out-of-plane spatial resolution of these measurements, is 90–110 nm.

The fluorescent particle tracers are imaged with an inverted epi-fluorescent microscope (Leica DMIRE2) equipped with a 63×0.5 objective (Leica PL Fluotar L) and a dichroic beamsplitter cube (Leica I3) to ensure that only the longer-wavelength fluorescence from the particles is imaged as 100 row × 653 column images (nominal dimensions) on a CCD camera with on-chip gain (Photometrics Cascade 650) at typical framing rates of 160 Hz with 1 ms exposure.

In-house software, implemented in MATLAB version 6.5, was used to calculate flow velocities from the particle images. This processing software uses a combined correlation-based interrogation and tracking algorithm[35] to analyze an interrogation window from the first (*i.e.*, earlier) image within the pair with dimensions (X, Z) and a larger interrogation window from the second image with dimensions of $(X + 2\Delta,\ Z + 2\Delta)$. The interrogation windows are cross-correlated using an FFT-based algorithm that can be applied to windows of arbitrary dimensions. The overlap between

adjacent windows was 50%, and no window shift was used since the displacement in all cases was 5 pixels or less. In processing these data, the window dimensions varied with dataset, with X = 120–200 pixels, Z = 58–88 pixels and Δ = 10–16 pixels. Note that typical window dimension of 120 × 80 pixels ($x \times z$) corresponding to an in-plane spatial resolution of 18 × 13 μm, with 50% overlap, gives 18 particle displacement vectors for each image. The range of window sizes were chosen to ensure that the number of particle images in each window is at least 20 to ensure a cross-correlation peak with a good signal to noise ratio, even with significant particle mismatch between two successive exposures due to Brownian diffusion normal to the wall. Cross-correlation averaging[26] or "single-pixel interrogation"[36], originally used to improve the spatial resolution of μPIV data, can also be used to improve the spatial resolution of nPIV data. Although not shown here, cross-correlation averaging of a subset of these images with windows as small as 16 × 10 pixels ($x \times z$), corresponding to an in-plane spatial resolution of 2.5 × 1.5 μm, give average velocity results within 2% of those reported here.

4.2 Results and Discussion

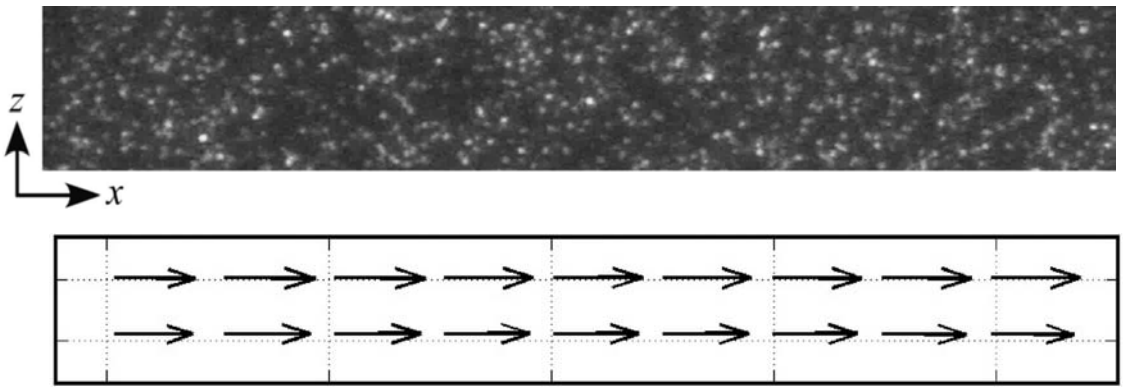

Figure 8 Representative image of particle tracers over a 110 × 16 μm ($x \times z$) field of view [top] and corresponding nPIV result [bottom] averaged over 999 image pairs. The velocity vectors represent an average velocity U = 17.6 μm/s.

The EOF studied here is essentially uniform normal to the wall, since the electric double layer is very thin compared with y_p, with a Debye length λ < 9 nm. Figure 8 shows a

typical raw particle image and the nPIV result obtained by averaging velocity data obtained over 1000 such consecutive images (= 999 image pairs) for C = 3.6 mM and E = 1.0 kV/m. The measured velocity field verifies that the flow is essentially uniform over this x-z plane.

The nPIV results were therefore spatially and temporally averaged to obtain the bulk flow velocity U. Figure 9 shows U as a function of the external electric field E for various $Na_2B_4O_7$ concentrations C. The average velocity is a linear function of the driving electric field, corresponding to constant mobility. The error bars represent conservative 95% confidence intervals; these error estimates include both the uncertainty in determining particle displacement in each set of images and other experimental uncertainties associated with converting this displacement into actual velocities, such as the estimated physical dimension of one pixel in each image and the CCD camera framing rate.

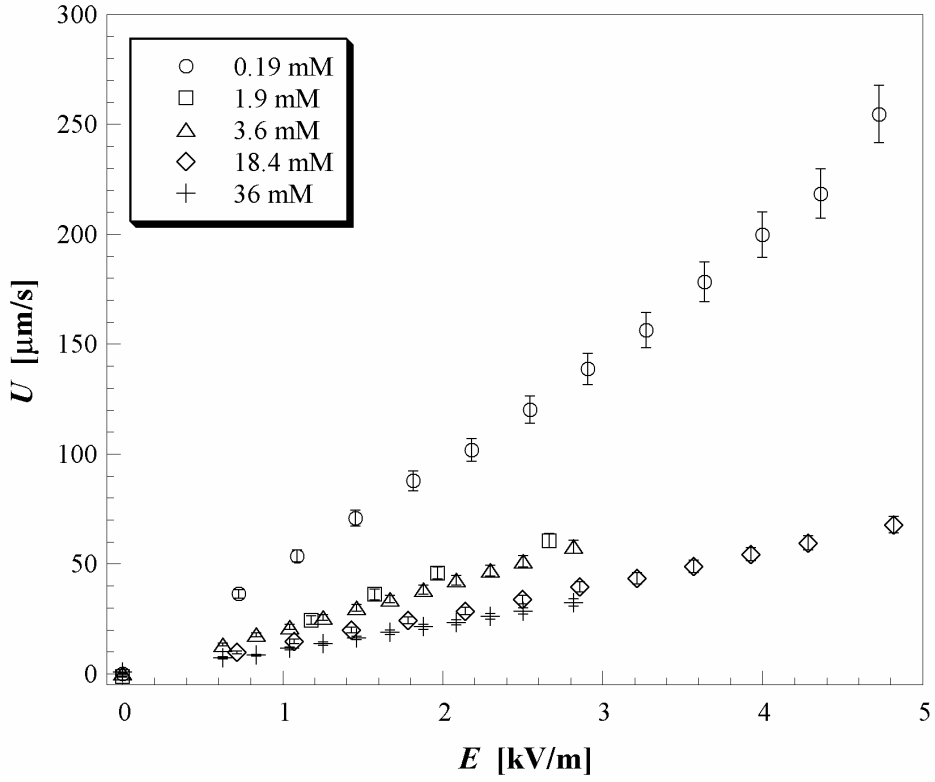

Figure 9 Graph of average velocity U as a function of external electric field E for C = 0.19–36 mM sodium tetraborate buffer.

As discussed in the previous Section, Brownian diffusion of the 100 nm tracers can be a significant issue in nPIV data. Errors due to out-of-plane Brownian diffusion can be estimated using the results from the previous Section. For a time interval between images within the image pair Δt = 6.5 ms, τ = 13.3, corresponding in Figure 5 to a fraction of mismatched particles ξ = 45%. The results shown in Figure 6 suggest that the displacement error due to hindered Brownian diffusion for this level of particle mismatch is negligible.

In-plane Brownian diffusion can be estimated using calculations similar to those used to generate Table 1.[22] A tracer with an initial position $z'/a \leq 3$ has a mean diffusion coefficient for motion parallel to the wall $D_{\|} / D_{\infty} = 0.774$ averaged over 10^5 particles; the rms Brownian displacement parallel to the wall for a particle using this value is then $\Delta x_{\|} \approx 220$ nm, corresponding to a displacement of about one pixel, *vs.* the maximum displacement due to the flow of three pixels, in these experiments. Errors due to in-plane Brownian diffusion can be greatly reduced by averaging the flowfield for this steady flow over time. A typical value for the standard deviation for a single velocity vector at a given spatial location over 999 realizations—which should give an estimate of the in-plane Brownian diffusion averaged over all the tracer particles within the interrogation window—is 6%. After temporal averaging, this standard deviation in turn accounts for about 2% of the 95% confidence intervals given in Figure 9. Errors associated with the imaging system (due, for example, to errors in determining the magnification of the images and the limiting spatial resolution of the CCD camera) are therefore much more significant sources of error in these experimental results.

To validate the nPIV data, the mobility μ_{ex} was calculated using linear regression from the results of Figure 9 and compared with the electroosmotic mobility μ_{eo} predicted by the asymptotic model of Conlisk *et al.*[37]

$$\mu_{eo} = \frac{\varepsilon_e \phi_o}{2\mu} \ln\left\{\frac{g^0}{f^0}\right\} \tag{4.1}$$

In this equation, ε_e and μ are the electrical permittivity and absolute viscosity, respectively, of the fluid, $\phi_o \equiv RT/F$ is the characteristic scale for the potential formed from R the universal ideal gas constant, T the fluid absolute temperature and F Faraday's constant, and (g^0, f^0) are the wall mole fractions of the cationic and anionic species, respectively. As shown in Figure 10, the experimental and model values for mobility agree within 4.5% over a 200-fold change in molar concentration, suggesting that the particle tracers follow the flow with good fidelity over this range of electric fields. The mobility values are also compared with a single independent measurement using neutral fluorescent molecular tracers for C = 0.2 mM.[38] These independently obtained analytical and experimental results suggest that particle slip with respect to the fluid due to electrophoresis has a negligible effect on mobility for the EOF cases studied here. Furthermore, the mobility obtained from the nPIV data appears to be unaffected by tracer particle properties such as size and charge.

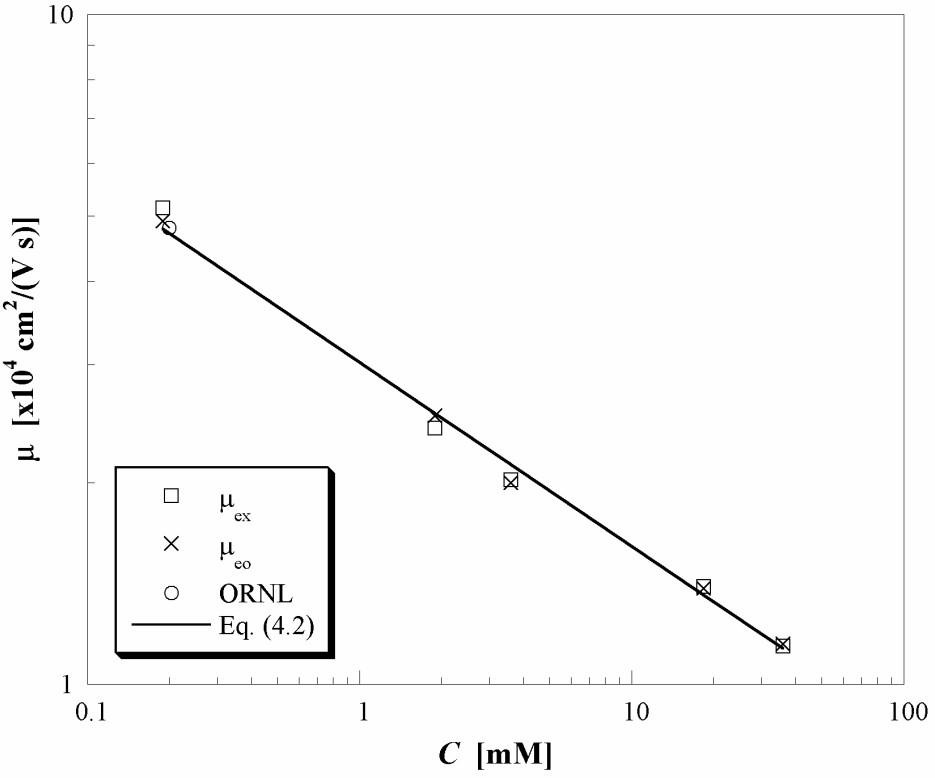

Figure 10 Log-log plot of electroosmotic mobility values as a function of *C*.

Finally, these results suggest that the mobility μ has a novel power-law scaling with concentration:

$$\frac{\mu}{3.03\times10^{-4}\ \mathrm{cm}^2/(\mathrm{V}\cdot\mathrm{s})} = \left(\frac{C}{1\ \mathrm{mM}}\right)^{-0.275} \tag{4.2}$$

Note that this scaling cannot be directly derived from the analysis because of the iterative method used to derive (g^0, f^0).

5 Summary

Over the last three years, nano-particle image velocimetry—based upon tracking the motion of colloidal fluorescent particles illuminated by evanescent waves—has been developed as a new method for measuring near-wall velocity fields with submicron spatial resolution. Initial results from this novel technique have been validated for steady fully-developed electroosmotic flows in microchannels, and suggest a novel scaling of electroosmotic mobility with electrolyte concentration.

Nano-PIV can measure velocities averaged over the first 100 nm based upon penetration depth next to the wall with an out-of-plane spatial resolution of 100 nm based upon tracer particle diameter. In comparison, the near-wall capability of μPIV is about 900 nm based upon interrogation window size and its out-of-plane spatial resolution based upon depth of field is at least 1.5 μm. The method therefore represents about an order of magnitude improvement in near-wall access and out-of-plane spatial resolution over current microfluidic diagnostic techniques. The in-plane spatial resolution of these nPIV data of 18 μm × 13 μm obtained here without cross-correlation averaging is significantly larger than that of the best reported μPIV measurements using cross-correlation averaging. Nevertheless, initial results using cross-correlation averaging of nPIV data show that the minimum in-plane spatial resolution of nPIV should be comparable to that for μPIV, namely 1–2 μm.

Brownian diffusion is potentially a significant source of error in nPIV, given typical Peclet numbers for the tracers used in this technique of $O(10^{-3})$. Results from artificial and experimental images suggest, however, that hindered Brownian diffusion—and more specifically, particle mismatch within the image pair due to Brownian diffusion—has relatively little impact on the accuracy of nPIV data for the steady uniform flows studied here provided that the interrogation window size is chosen to ensure enough (here, at least 11) matched tracers within an image pair.

These initial results demonstrate the potential of this technique. In terms of extending nPIV, the exponential decay of particle image intensity with distance from the wall given by Equation (3.4) suggests that it may be possible, for tracer images with sufficient contrast and tracers with consistent fluorescence intensity, to obtain not just the x- and z-positions of the particles, but also their y-position. If so, it should be possible to measure all three velocity components using nPIV without any additional imaging equipment. Particle tracking studies are already underway to measure hindered Brownian diffusion normal to the wall using this concept.[39]

Finally, issues associated with particle tracers such as Brownian diffusion and, for EOF, electrophoresis, may be avoided altogether by using molecular tracers illuminated by evanescent waves to obtain near-wall velocimetry measurements. Current intensified CCD technology may not yet be sufficient for nanoscale MTV, given that the quantum efficiency of molecular tracers such as phosphorescent supramolecules is 3.5%,[11] more than an order of magnitude lower than that of the fluorophores used in nPIV tracers of at least 90%. Nevertheless, Pit *et al.*[8] have already used a related technique, fluorescence recovery after photobleaching, with evanescent waves at a single point to show evidence of slip in hexadecane. The rapid development of single-photon and molecule imaging technology suggests that molecular tracers illuminated by evanescent waves will ultimately be the most accurate method for measuring near-wall velocity fields and studying interfacial phenomena such as apparent slip at the submicron scale.

Acknowledgements

This work would not have been possible without the contributions of Dr. Reza Sadr, Haifeng Li and Claudia M. Zettner in my group at Georgia Tech. We also wish to thank Dr. Terry Conlisk and Zhi Zheng at Ohio State University and Dr. Mike Ramsey and J.-P. Alarie at Oak Ridge National Laboratories for sharing their results and numerous suggestions.

* Supported by DARPA DSO (F30602-00-2-0613) and NSF (CMS-9977314)
† G. Woodruff School of Mechanical Engineering; Georgia Institute of Technology; Atlanta, GA 30332–0405 USA E-mail: minami.yoda@me.gatech.edu

[3] S. Granick, Y. Zhu, and H. Lee, *Nature Materials* **2**, 221 (2003).
[4] P.G. De Gennes, *Langmuir* **18**, 3413 (2002).
[5] P. Attard, *Advances in Colloid and Interface Science* **104**, 75 (2003).
[6] O.I. Vinogradova, *International Journal Mineral Processing* **56**, 31 (1999).
[7] D.C. Tretheway and C.D. Meinhart, *Physics of Fluids* **14**, L9 (2002).
[8] R. Pit, H. Hervet, and L. Léger, *Physical Review Letters* **85**, 980 (2000).
[9] J.G. Santiago, S.T. Wereley, C.D. Meinhart, D.J. Beebe, and R.J. Adrian, *Experiments in Fluids* **25**, 316 (1998).
[10] W.R. Lempert, K. Magee, P. Ronney, K.R. Gee, and R.P. Haughland, *Experiments in Fluids* **18**, 249 (1995).
[11] C.P. Gendrich, M.M. Koochesfahani, and D.G. Nocera, *Experiments in Fluids* **23**, 361 (1997).
[12] P.H. Paul, M.G. Garguilo, and D.J. Rakestraw, *Analytical Chemistry* **70**, 2459 (1998).
[13] D. Sinton and D. Li, *Colloids and Surfaces A: Physicochemical Engineering Aspects* **222**, 273 (2003).
[14] C. Lum and M. Koochesfahani, *Bulletin of the American Physical Society* **48**(10), 58 (2003).
[15] E. Bonaccurso, M. Kappl, and H.-J. Butt, *Physical Review Letters* **88**, 076103 (2002).
[16] C. M. Zettner and M. Yoda, *Experiments in Fluids* **34**, 115 (2003).
[17] E. Hecht, *Optics*, 3rd ed. (Addison-Wesley, Reading, 1998), p. 124.
[18] H.K.V. Lotsch, *Optik* **32**, 189 (1970).
[19] D. Axelrod, E. H. Hellen, and R. M. Fulbright, *Topics in Fluorescence Spectroscopy, Vol. 3: Biochemical Applications*, edited by J. R. Lakowicz (Plenum Press, New York, 1992), p. 289.
[20] D. Axelrod, T.P. Burghardt, and N.L. Thompson, *Annual Review of Biophysics and Bioengineering* **13**, 247 (1984).
[21] D.C. Prieve and N.A. Frej, *Langmuir* **6**, 396 (1990).
[22] R. Sadr, H. Li, and M. Yoda, to appear in *Experiments in Fluids* (2004).
[23] R.J. Adrian, *Annual Review of Fluid Mechanics* **23**, 261 (1991).
[24] C.D. Meinhart and S.T. Wereley, *Measurement Science and Technology* **14**, 1047 (2003).
[25] M.G. Olsen and R.J. Adrian, *Optics and Laser Technology* **32**, 621 (2000).
[26] C.D. Meinhart, S.T. Wereley, and J.G. Santiago, *Journal of Fluids Engineering* **122**, 285 (2000).
[27] M.A. Bevan and D.C. Prieve, *Journal of Chemical Physics* **113**, 1228 (2000).
[28] H. Faxén, *Annalen der Physik* **4**(68), 89 (1922).
[29] A. Einstein, *Annalen der Physik* **17**, 549 (1905).
[30] A.J. Goldman, R.G. Cox and H. Brenner, *Chemical Engineering Sciences* **22**, 637 (1967).
[31] J. Westerweel, *Experirments in Fluids* **29**, S3 (2000).
[32] M. Raffel, C. Willert, and J. Kompenhans, *Particle Image Velocimetry: A Practical Guide* (Springer, Berlin, 1998), p. 129.
[33] R.D. Keane and R.J. Adrian, *Applied Scientific Research* **49**, 191 (1992).
[34] R. Sadr, M. Yoda, Z. Zheng, and A.T. Conlisk, *Journal of Fluid Mechanics* **506**, 357 (2004).
[35] D. F. Liang, C. B. Jiang and Y. L. Li, *Experiments in Fluids* **33**, 684 (2002).
[36] J. Westerweel, P.F. Gelhoed and R. Lindken, *Experiments in Fluids* **37**, 375 (2004).
[37] A.T. Conlisk, J. McFerran, Z.Zheng, and D.J. Hansford, *Analytical Chemistry* **74**, 2139 (2002).
[38] J.M. Ramsey, J.P. Alarie, S.C. Jacobson, and N.J. Peterson, in *Micro Total Analysis Systems 2002*, edited by Y. Baba, S. Shoji and A. J. van den Berg (Kluwer Academic Publishers, Dordrecht, 2002), p. 314.
[39] K. D. Kihm, A. Banerjee, C. K. Choi, and T. Takagi, to appear in *Experiments in Fluids* (2004).

Appendix J:

Modeling Electroosmotic Flow in Nanochannels

A. T. Conlisk
Department of Mechanical Engineering
The Ohio State University
Columbus, Ohio 43202
conlisk.1@osu.edu
and
Sherwin Singer
The Department of Chemistry
The Ohio State University
Columbus, Ohio 43210-1107
singer@chemistry.ohio-state.edu

Abstract

In this chapter we discuss the fundamentals and modeling of electroosmotic flow in micro- and nano-channels. It is well known that the volume flow rate varies linearly with channel height for electrically driven flow in contrast to pressure driven flow which varies as height cubed. This means that very large pressure drops are required to drive flows in small channels thus making electroosmotic flow the method of choice for flows in very small channels, of the order of $1\mu m$ or less. We discuss the structure of the electric double layer and its role in the transport of ions and solvent in channels. The flow is driven by the difference in cation/anion concentrations at the walls of the channel. At small cation, anion concentration differences the Debye-Huckel approximation is appropriate; at larger concentration differences, the Gouy-Chapman picture of the electric double emerges naturally. We show how analytical solutions for the velocity and concentrations or mole fractions may be derived for electric double layer thicknesses small compared with the channel height. Analytical results are compared with several sets of experimental data and the model compares well. In addition, the comparisons with experiment suggest that the continuum approximation may break down for channel hieghts on the order of $5nm$ and so the mechanics and results of molecular dynamics simulations are also described. It is shown that MD simulations allow preferential solvation near the wall in contrast to the continuum Poisson-Boltzmann approach, resulting in significant differences in the magnitude of bulk solution and ionic transport.

1 Introduction

The determination of the nature of fluid flow at small scales is becoming increasingly important because of the emergence of new technologies. These techologies include Micro-Electro Mechanical Systems(MEMS) comprising micro-scale heat engines, micro-aerial vehicles and micro pumps and compressors and many other systems. Moreover, new ideas in the area of drug delivery and its control, in DNA and biomolecular sensing, manipulation and transport and the desire to manufacture laboratories on a microchip(lab-on-a-chip) require the analysis and computation of flows on a

length scale approaching molecular dimensions. On these small scales, new flow features appear which are not seen in macro-scale flows. In this chapter we review the state-of-th-art in modeling liquid flows at nanoscale with particular attention paid to liquid mixture flows applicable to rapid molecular analysis and drug delivery and other applications in biology.

The governing equations of fluid flow on length scale orders of magnitude greater than a molecular diameter are well known to be the Navier-Stokes equations which are a statement of Newton's Law for a fluid. Along with conservation of mass and appropriate boundary and initial conditions in the case of unsteady flow, these equations form a well-posed problem from which, for an incompressible flow(constant density) the velocity field and the pressure may be obtained.

However, as the typical length scale of the flow approaches the micron level and below, several new phenomena not important at the larger scales appear. A perusal of the literature suggests that these changes may be classified into three rather general groupings:

- Fluid properties, especially transport properties(e.g. viscosity and diffusion coefficient) may deviate from their bulk values.
- Fluid, especially gases may slip at a solid surface.
- Channel/tube surface properties such as roughness, hydrophobicity/hydrophilicity and surface charge become very important.

Evidence already exists that there may be slip at hydrophobic surfaces in liquids; no slip still appears to hold at a hydrophilic surface. In liquids, slip or no-slip at the wall is a function of surface chemistry and roughness whereas in gases, slip is entirely controlled by the magnitude of the Knudesn number, the ratio of the mean free path to the characteristic length scale.

Transport at the nanoscale especially in biological applications is dominated by electrochemistry. There are a number of textbooks on this subject typified by[1–7] among many others. The term electrokinetic phenomena in general refers to three phenomena: (1) electrophoresis, which is the motion of ionic or biomolecular transport in the absence of bulk fluid motion; (2) electroosmosis, the bulk fluid motion due to an external electric field, (3) streaming potential, the potential difference which exists at the zero total current condition. In this chapter we focus primarily on electroosmosis and in the spirit of addressing biological applications we consider aqueous solutions only.

We shall see that it is impossible to pump fluid through very small channels mechanically via a pressure drop; one alternative is to pump the fluid by the imposition of an external electric field. *Electroosmosis* requires that the walls of the channel or duct be charged. Biofluids such as Phosphate Buffered Saline(PBS) in aqueous solution contain a number of ionic species. Because the mixture contains charged species an electric field oriented in the desired direction of motion can be employed to induce bulk fluid motion. In addition, at the same time, because of the different diffusion coefficients of the different species, the ionic species will move at different velocities relative to the mass or molar averaged velocity of the mixture. This process is called *electrophoresis*.

In dissociated electrolyte mixtures, even in the absence of an imposed electric field, an electric double layer(EDL) will be present near the (charged) surfaces of a channel or tube. The nominal thickness of the EDL is given by

$$\lambda = \frac{\sqrt{\epsilon_e RT}}{F(\sum_i z_i^2 c_i)^{1/2}} \tag{1}$$

where F is Faraday's constant, ϵ_e is the electrical permittivity of the medium, c_i the concentrations of the electrolyte constituents, R is the gas constant, z_i is the valence of species i and T is the

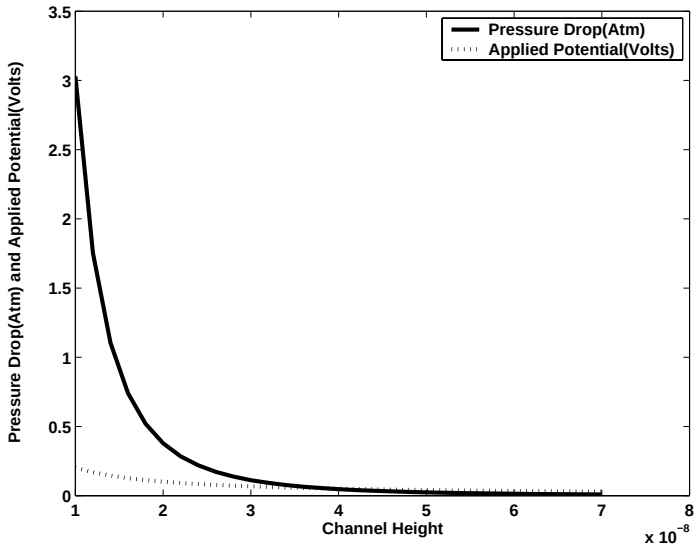

Figure 1: Pressure drop and applied voltage as a function of channel height to achieve a flowrate of $Q = 10^{-6} L/min$ in the system of Figure 2.

temperature. Here the ionic strength $I = \sum_i z_i^2 c_i$. The actual thickness of the electrical double layer is actually an asymptotic property much like the boundary layer thickness in classical external fluid mechanics. If we define the dimensionless parameter

$$\epsilon = \frac{\lambda}{h}$$

where h is the channel height, then for $\epsilon << 1$ the thickness of the EDL is normally $\sim 4 - 6\epsilon$. For $\epsilon \sim 1$ we say that the electrical double layers overlap.

Typically, the width of the electric double layer is on the order of $1 \ \ nm$ for a moderately dilute mixture; for extremely dilute mixtures, width of the electric double layer may reach several hundred nanometers. In the case where $\epsilon << 1$ the problem for the electric potential and the mole fraction of the ions is a singular perturbation problem and the fluid away from the electric double layers is electrically neutral. In the case where $\frac{\lambda}{h} = O(1)$ the channel height is of the order of the EDL thickness. In this case, electroneutrality need not be preserved in the core of the channel; however, the surface charge density will balance this excess of charge to keep the channel(or tube) electrically neutral. We assume that the temperature is constant and that the ionic components of the mixture are dilute.

There is a clear advantage to electroosmotic pumping versus pressure pumping in very small channels. When the EDLs are thin the flow rate is given to leading order by

$$Q_e \sim U_0 h W \tag{2}$$

where U_0 is independent of h(as we will see) and W is the width. Thus the flow rate is proportional to h and not h^3 as for pressure-driven flow for which the volume flow rate in a parallel plate channel is

$$Q_p = \frac{W h^3}{12 \mu L} \Delta p \tag{3}$$

where Δp is the pressure drop. This means that driving the flow by a pressure gradient is not feasible as depicted on Figure 1; note that at a channel height of $10nm$ three atmospheres of pressure drop are required to drive a flow of $Q = 10^{-6} L/min$ which is a characteristic flow rate in many applications. This is a large pressure drop in a liquid and clearly, a relatively awkward pump would be required to provide this pressure drop.

The plan of this chapter is as follows. We consider electroosmotic flow for the transport of ionic species; we focus on internal flow since the vast majority of the biomedical applications involve internal flow. In the next section various aspects of electrokinetic phenomena are outlined and then the governing equations are derived; the flow field, the electric field and the mass transfer problems are coupled. We then present results for several different parameters including channel height. The channels considered here are nano-constrained in one dimension. Next we discuss comparisons with experiment and conclude with a discussion of molecular dynamics simulations for probing the limits of continuum theory.

2 Background

2.1 Micro/nanochannel Systems

Because it is not feasible to transport fluids in nanochannels using an imposed pressure drop, electroosmosis and electrophoresis are often used. Application areas include rapid bio-molecular analysis; these devices are called lab-on-a-chip. Small drug delivery devices may employ electrokinetic flow to control the rate of flow of drug to the patient. These devices may also be used as biomolecular separators because different ionic species travel at different speeds in these channels. Natural nanochannels exist in cells for the purpose of providing nutrients and discarding waste. In general, these devices act as electroosmotic and/or diffusion pumps(Figure 2). The diffusion pump for drug delivery depicted on Figure 2(a) has been tested on rats; the human version is expected to be orders of magnitude smaller. On Figure 2(b) is a sketch of an electroosmotic nanopump whose operation has been documented by iMEDD, Inc. of Columbus, Ohio.[8]

Nanochannel systems applicable to biomolecular analysis require interfacing microchannel arrays with nanochannel arrays. An example is depicted on Figure 3. These nanochannels are fabricated by a sacrificial layer lithography method which can produce channels with different surface properties.[9] On Figure 3, note that fluid enters from a bath on one side and is forced through several microchannels. The fluid is then forced to turn into a number of much smaller nanochannels which have the ability to sense and interrogate single molecules. Many biomolecules have a characteristic size on the order of 1-5 nm. On the other hand, in the iMEDD device(Figure 2(b)), fluid is forced directly into the nanochannels. In most systems of this type, the flow must pass through a micro scale channel into a nanochannel and then into a micro channel again.

One difficulty with modeling these systems is that the voltage drop in the nanochannels is not easily determined. This is because in systems of this type, the electrodes are placed in the baths upstream and downstream of the channels. The electric field must be determined in a complex geometry and in general must be calculated numerically. Moreover, the iMEDD device has over 47,000 nanochannels each of which may operate independently. Clearly each channel cannot be modeled independently in a single numerical simulation.

(a)

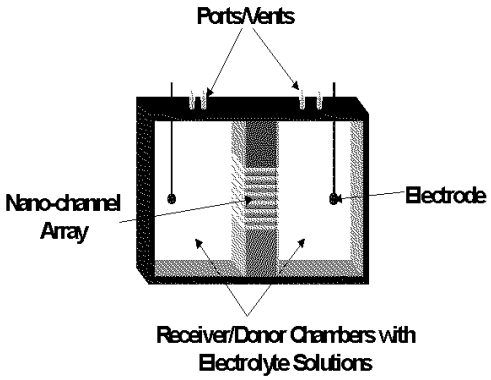

(b)

Figure 2: (a) Diffusion pump fabricated by iMEDD, Inc. of Columbus, Ohio. (b) Nanochannels fabricated by iMEDD, Inc. of Columbus, Ohio.[8]

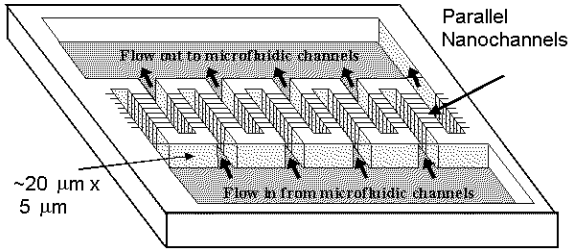

Figure 3: A micro/nanochannel system fabricated by Hansford.[9]

2.2 Previous Work on Electroosmotic Flow

Compared to the amount of work done on flow in micro-channels, there has been relatively little modeling work done on flow in channels whose smallest dimension is on the order of the electric double layer. In all of this work fully-developed flow is assumed. The problem for channel heights on the order of the electric double layer, that is for overlapped double layers has been investigated by Verwey.[10] There the solution for the potential is based on a Boltzmann distribution for the number concentration of the ions; the potential is calculated based on a symmetry condition at the centerline. Note that the electric double layer will always be present near charged walls whether or not an external potential is used to drive a bulk motion of the liquid. Qu and Li[11] have recently produced solutions which do not require the Boltzmann distribution, but they also assume symmetry at the centerline; the results show significant differences from the results of Verwey and Overbeek.[10] The results of Qu and Li[11] are valid for low voltages since the Debye-Huckel approximation is invoked.

The first work on the electroosmotic flow problem discussed here appears to have been done by Burgeen and Nakache[12] who also considered the case of overlapped double layers. They produced results for the velocity field and potential for two equally charged ions of valence z; a Boltzmann distribution is assumed for the number of ions in solution. The convective terms in the velocity momentum equation are assumed to be negligible and the solution for the velocity and potential is assumed to be symmetric about the centerline of the channel.

Levine et al.[13] solved the same problem as Burgeen and Nakache[12] and produced results for both thin and overlapping double layers for a single pair of monovalent ions. Again symmetry of the flow with respect to the direction normal to the channel walls is assumed. The current flow is also calculated.

Rice and Whitehead[14] seem to be the first to calculate the electrokinetic flow in a circular tube; they assume a weak electrolyte and so assume the Debye-Huckel approximation holds. Levine et al.[15] also consider flow in a tube under the Debye-Huckel approximation; an analytical solution is found in this case. Stronger electrolyte solutions valid for higher potentials are also condidered using a simplified ad hoc model for the charge density.

Conlisk et al.[16] solve the problem for the ionic mole fractions and the velocity and potential for strong electrolyte solutions and consider the case where there is a potential difference in the direction normal to the channel walls corresponding in some cases to oppositely charged walls. They find that under certain conditions reversed flow may occur in the channel and this situation can significantly reduce the flow rate.

All of the work discussed so far assumes a pair of monovalent ions. However, many bio-fluids contain a number of other ionic species. As noted above, an example of one of these fluids is the common Phosphate Buffered Saline(PBS) solution. This solution contains five ionic species, with some being divalent. Zheng et al.[17] have solved the entire system of equations numerically; they show that the presence of divalent ions has a significant effect on the flow rate through the channel.

2.3 Structure of the Electric Double Layer

Consider the case of an electrolyte mixture which is bounded by a charged wall. If the wall is negatively charged then a surplus of positively charged ions, or cations can be expected to be drawm to the wall. On the other hand, if the wall is positively charged, then it would be expected that there would be a surplus of anions near the wall. The question then becomes, what is the concentration of the cations and anions near a charged surface? This question has vexed chemists for years and the

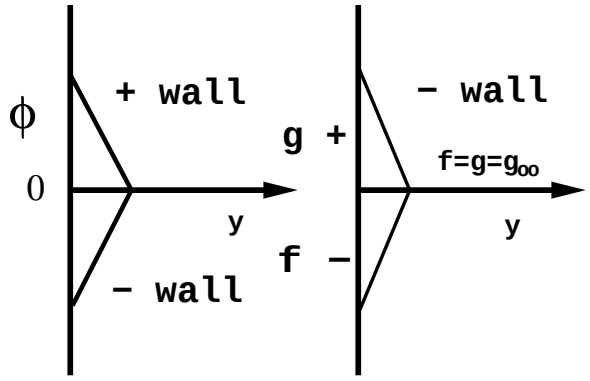

Figure 4: Potential and mole fractions near a negatively charged wall according to the ideas of Helmholtz.[18] Here g denotes the cation mole fraction and f denotes the anion mole fraction.

concepts described below are based on qualitative, descriptive models of the region near a charged surface.

The electric double layer has been viewed as consisting of a single layer of counterions pined to the wall outside of which is a layer of mobile coions and counterions. The simplest model for the EDL was originally given by Helmholtz[18] long ago and he assumed that electrical neutrality was achieved in a layer of fixed length. For a negatively charged wall he assumed the distributions of the anions and the cations are linear with distance from the wall as depicted on Figure 4.

In the Debye-Huckel picture of the electric double layer,[19] the influence of the ionic species are equal and opposite so that the wall mole fractions of the coion(anion for a negatively charged wall), f^0 and counterion g^0 are symmetric about their asymptotic value far from the wall and the picture is as on Figure 5. The Gouy-Chapman[20,21] model of the electric double layer allows for more counterions to bind to the wall charges so that the counter ions accumulate near the wall. This means that for a negatively charged wall g^0 can be much larger than its asymptotic value, whereas f^0, is not much lower than the asymptotic value in the core. This situation is depicted on Figure 6. Whether the Debye-Huckel picture or the Gouy-Chapman model of the EDL obtains depends on the surface charge density with the Debye-Huckel picture occuring at low surface charge densities and the Gouy-Chapman model occuring for higher surface charge densities.

Stern[22] recognized that there are a number of other assumptions embedded in these qualitative and simple models. In the models discussed so far the ions have been assumed to be point charges and the solvent is not modified by the presence of the charges. He proposed that the finite size of the ions affects the value of the potential at the surface. Finite-size ion effects in stagnant solutions are discussed by Bockris and Reddy.[6] Figure 7 shows the Stern layer consisting of a single layer of counterions at a negatively charged wall. Stern suggested that the surface potential be evaluated at the surface of shear as shown on Figure 7. The potential there is called the ζ potential and is a measured quantity.

3 Governing Equations For Electrokinetic Flow

We consider now the case of flow of an electrolyte mixture in a slit channel for which the width and length of the channel are much bigger than its height as depicted on Figure 8. We have in mind

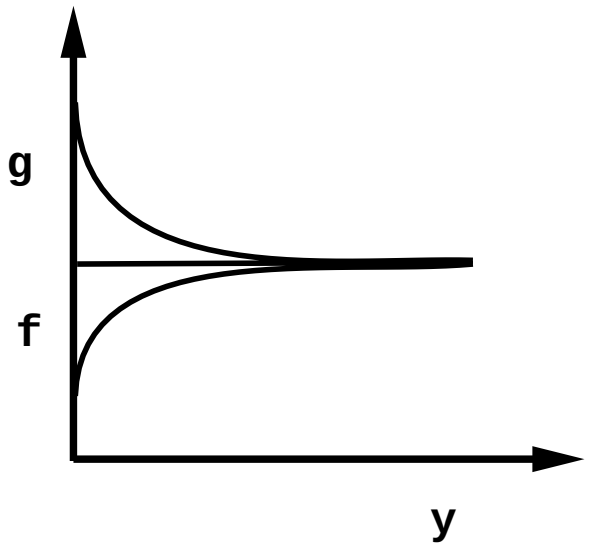

Figure 5: Debye-Huckel[19] picture of the electric double layer. Here g denotes the cation mole fraction and f denotes the anion mole fraction.

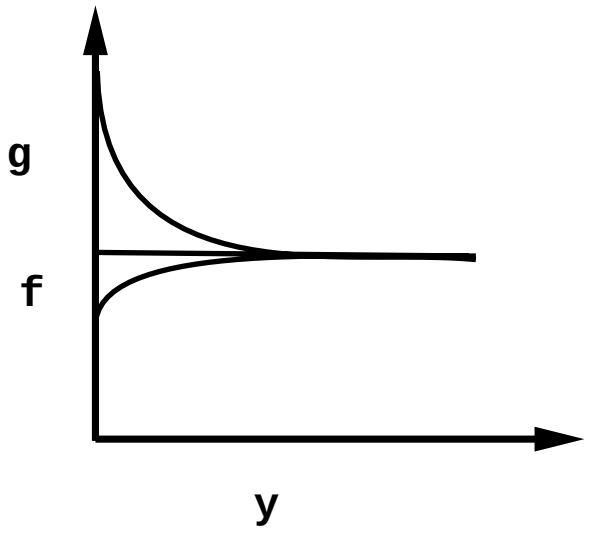

Figure 6: Gouy-Chapman model[20,21] of the EDL.

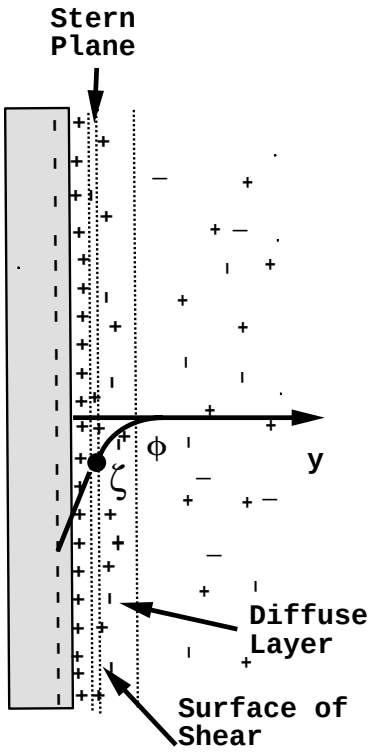

Figure 7: The Stern Layer. The potential at the edge of the plane of shear is called the ζ potential and the potential inside the Stern layer is linearly varying with distance from the wall.

the mixture consisting of water and a salt such as sodium chloride, but it is easy to see how to add additional, perhaps multivalent components. We consider the case where the salt is dissociated so that mixture consists of positively and negatively charged ions, say Na^+ and Cl^-.

In dimensional form, the molar flux of species A for a dilute mixture is a vector and given by[2]

$$\vec{n}_A = -cD_{AB}\nabla X_A + u_A z_A F X_A \vec{E}^* + cX_A \vec{u}^* \tag{4}$$

Here D_{AB} is the diffusion coefficient, c the total concentration, X_A is the mole fraction of species A, which can be either the anion or the cation, p is the pressure, M_A is the molecular weight, R is the gas constant, T is the temperature, u_A is the mobility, z_A is the valence, F is Faraday's constant, $\vec{E}^*$ is the total electric field and $\vec{u}^*$ is the mass average velocity of the fluid. The mobility u_A is defined by $u_A = \frac{D_{AB}}{RT}$. The mass transport equation for steady state is then

$$\nabla \bullet \vec{n}_A = 0 \tag{5}$$

In non-dimensional form the equation for the mole fraction of species A is given by

$$\frac{\partial^2 X_A}{\partial y^2} + \epsilon_1^2 \frac{\partial^2 X_A}{\partial x^2} + \epsilon_2^2 \frac{\partial^2 X_A}{\partial z^2} = ReSc\left(\epsilon_1 u \frac{\partial X_A}{\partial x} + v\frac{\partial X_A}{\partial y} + \epsilon_2 w \frac{\partial X_A}{\partial z}\right)$$
$$+ z_A\left(\epsilon_1 \frac{\partial X_A E_x}{\partial x} + \frac{\partial X_A E_y}{\partial y} + \epsilon_2 \frac{\partial X_A E_z}{\partial z}\right) \tag{6}$$

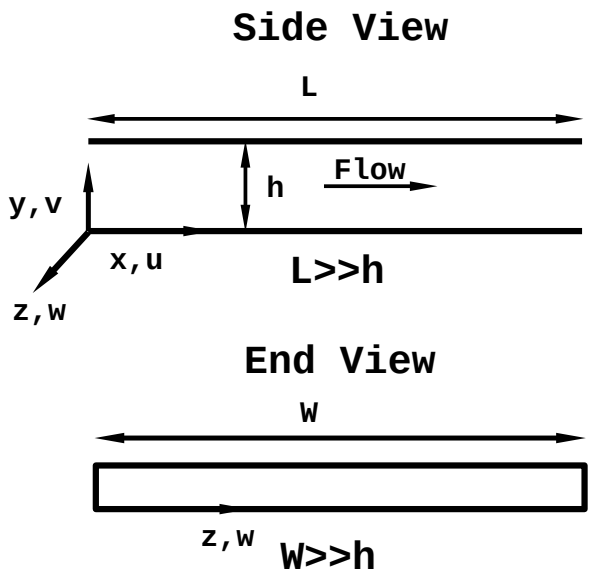

Figure 8: Geometry of the channel. Here it is only required that $h << W, L$ where W is the width of the channel and L its length in the primary flow direction. u, v, w are the fluid velocities in the x, y, z directions.

and we have assumed that the fluid and transport properties are constants. The externally imposed electric field, E_0, is constant in the x direction, whereas variations in the potential in y and z directions are permitted. The coordinates (x,y,z) are nondimensional; for example, $x = \frac{x^*}{L}$ and the scaling lengths in the three directions are (L, h, W) as depicted on Figure 8. Also (u, v, w) are the dimensionless velocities in each of the coordinate directions (x, y, z); for example $u = u^*/U_0$ where u^* is dimensional. Here $\epsilon_1 = \frac{h}{L}$ and $\epsilon_2 = \frac{h}{W}$. We assume $h << W, L$ so that both ϵ_1 and ϵ_2 are small. $Re = \frac{U_0 h}{\nu}$ is the Reynolds number and $Sc = \frac{\nu}{D_{AB}}$ is the Schmidt number, where ν is the kinematic viscosity. The valence $z_A = 1$ for the positive ion and $z_B = -1$ for the negative ion, although generalization to arbitrary valence is obvious. The determination of the velocity scale U_0 will be discussed below.

The mass transfer equation is subject to boundary conditions at a solid surface. Consider the wall at $y = 0$. Then if A refers to either of the ion distributions, it follows that we can specify the ion concentration or the flux at the surface. For the case of specified mole fraction,

$$X_A = X^0 \;\; y = 0$$

and

$$X_A = X^1 \;\; y = 1$$

where X^0 is the mole fraction at $y = 0$ and X^1 is the mole fraction at $y = 1$. Similar boundary conditions will hold at $z = 0$ and $z = 1$.

The mass transfer equation must be supplemented by an equation for the electric field. Most often in these problems, the channel is connected to large baths upstream and downstream. In this case the electric field in both baths and the channel should be calculated. To simplify the problem we have assumed that the x-component of the electric field is constant. This means that the dimensional

potential is of the form

$$\phi^* = -\gamma x^* + \phi_1^*(y^*, z^*)$$

where it is seen that ϕ_1^* is the perturbation potential and γ is a constant. This form of the potential is consistent with the situation within the channel for a liquid, assuming a uniform dielectric constant across the channel. Note that a variable dielectric constant could be easily incorporated into our analysis as a function of y to accommodate changes in concentration and temperature.

Now, the potential scale is defined by taking $\phi_0 = \frac{RT}{F}$ and the equation for the electric potential is

$$\epsilon^2 \left(\frac{\partial^2 \phi}{\partial y^2} + \epsilon_1^2 \frac{\partial^2 \phi}{\partial x^2} + \epsilon_2^2 \frac{\partial^2 \phi}{\partial z^2} \right) = -\beta(X_+ - X_-) \tag{7}$$

where

$$\beta = 1 + \frac{c_3}{I}$$

where c_3 is the concentration of the solvent and $\epsilon = \frac{\lambda}{h}$ and I is the ionic strength. For very wide channels $\epsilon >> \epsilon_1, \epsilon_2$; in addition, it is important to note that there will be boundary layers near the entrance and the exit of the channel and near the side walls where all of the independent variables vary rapidly. However, these regions are small, and in particular for very wide channels the influence of the side wall boundary layers will be negligible.

Since only differences in potential are important in this analysis we can specify the potential boundary conditions as

$$\phi = 0 \;\; y = 0$$

and

$$\phi = \phi^1 \;\; y = 1$$

The velocity field is coupled to the mass transfer equations and the equation for the potential. The governing equations of fluid flow express conservation of linear momentum along with the continuity equation which expresses conservation of mass. Conservation of mass requires

$$\epsilon_1 \frac{\partial u}{\partial x} + \frac{\partial v}{\partial y} + \epsilon_2 \frac{\partial w}{\partial z} = 0 \tag{8}$$

The $x-$direction is the primary direction of flow. Here it is noted that the velocity v is small and of $O(max(\epsilon_1, \epsilon_2))$.

We assume that the flow may be driven by an electrical body force oriented in the $x-$direction. The three momentum equations for an incompressible, steady flow are, in dimensionless form,

$$\epsilon^2 Re \left(\epsilon_1 u \frac{\partial u}{\partial x} + v \frac{\partial u}{\partial y} + \epsilon_2 w \frac{\partial u}{\partial z} \right) = -\epsilon_1 \epsilon^2 \frac{\partial p}{\partial x} + \beta(X_+ - X_-) + \epsilon^2 \nabla^2 u \tag{9}$$

$$\epsilon^2 Re \left(u\epsilon_1 \frac{\partial v}{\partial x} + v \frac{\partial v}{\partial y} + \epsilon_2 w \frac{\partial v}{\partial z} \right) = -\epsilon^2 \frac{\partial p}{\partial y} + \beta\Lambda \frac{\partial \phi}{\partial y}(X_+ - X_-) + \epsilon^2 \nabla^2 v \tag{10}$$

$$\epsilon^2 Re \left(\epsilon_1 u \frac{\partial w}{\partial x} + v \frac{\partial w}{\partial y} + \epsilon_2 w \frac{\partial w}{\partial z} \right) = -\epsilon_2 \epsilon^2 \frac{\partial p}{\partial z} + \epsilon_2 \Lambda \beta \frac{\partial \phi}{\partial z}(X_+ - X_-) + \epsilon^2 \nabla^2 w \tag{11}$$

where Re is the Reynolds number,

$$Re = \frac{\rho U_0 h}{\mu}$$

and U_0 is the velocity scale. These equations are the classical Navier-Stokes equations for constant density and viscosity which govern fluid flow of Newtonian liquids in a continuum. Here $p = \frac{p^*}{\mu U_0/h}$ is the dimensionless pressure and

$$\nabla^2 = \frac{\partial^2}{\partial y^2} + \epsilon_1^2 \frac{\partial^2}{\partial x^2} + \epsilon_2^2 \frac{\partial^2}{\partial z^2}$$

Also $\Lambda = \frac{\phi_0}{E_0 h}$ and the velocity scale is

$$U_0 = \frac{\epsilon_e E_0 \phi_0}{\mu}$$

The momentum equations are subject to boundary conditions for which

$$u = v = w = 0 \, on \;\; all \;\; solid \;\; surfaces$$

The governing equations form a set of seven equations in seven unknowns for the three velocity components, the two mole fractions of the electrolytes, the electric potential and the pressure. In electrochemistry these equations are usually not solved in their full form and several approximations may be made. First, the nonlinear terms can be neglected for small Reynolds numbers which usually is the case in biological problems. This makes the solution of the equations a lot easier. Second, if the channel is such that $h << W, L$ then essentially the entire problem may be said to be fully developed, that is all of the flow variables only in the y-direction. In this case the equations reduce to

$$\frac{\partial}{\partial y}\left(\frac{\partial X_+}{\partial y} + X_+ \frac{\partial \phi}{\partial y}\right) = 0 \tag{12}$$

$$\frac{\partial}{\partial y}\left(\frac{\partial X_-}{\partial y} - X_- \frac{\partial \phi}{\partial y}\right) = 0 \tag{13}$$

$$\epsilon^2 \frac{\partial^2 \phi}{\partial y^2} = -\beta(X_+ - X_-) \tag{14}$$

and

$$\epsilon^2 \frac{\partial^2 u}{\partial y^2} = -\beta(X_+ - X_-) \tag{15}$$

These are now four equations in four unknowns. Further it is easy to see how to generalize these equations to more ionic species of arbitrary valence.

For clarity and completeness we repeat the boundary conditions for the simplified problem (with $X_+ = g$ and $X_- = f$) as

$$\phi = 0 \, at \, y = 0 \tag{16}$$

$$\phi = \phi^1 \, at \, y = 1 \tag{17}$$

$$f = f^0 \, at \, y = 0 \tag{18}$$

$$f = f^1 \, at \, y = 1 \tag{19}$$

$$g = g^0 \, at \, y = 0 \tag{20}$$

$$g = g^1 \, at \, y = 1 \tag{21}$$

$$u = 0 \ at \ y = 0, \ and \ y = 1 \tag{22}$$

The last equation is the no-slip condition for the velocity.

The governing equations indicate that the flow, in the symmetric case has a four-parameter family of solutions: $\epsilon, \beta, g^0, f^0$. However, we can define

$$\delta^2 = \frac{\epsilon^2}{\beta g^0}$$

and rescale the mole fractions g, f on the quantity g^0. In this case, for symmetry the boundary conditions become

$$f = \gamma \, at \, y = 0, 1 \tag{23}$$

$$g = 1 \, at \, y = 0, 1 \tag{24}$$

where $\gamma = \frac{f^0}{g^0}$ and we now have only a two-parameter family of solutions δ, γ. The only thing that needs to be done is to specify δ, γ and then to calculate the effective channel height from the definition of ϵ given a concentration. Note that β is a large number and g^0 is a small number so that in general $\delta = O(\epsilon)$.

The theory is easily extended to mixtures having an arbitrary number of species. In this case there will be N parameters corresponding to $\gamma_k, k = 1, ..., N-1$, in addition to δ. In the asymmetric case where there may be walls of opposite charge, for two electrolyte species, there will be two additional parameters associated with the boundary conditions at $y = 1$. Thus for N species all of which have boundary values at $y = 1$ that are different from those at $y = 0$, we will have $2N$ parameters to specify plus the value of the potential at $y = 1$, so that the total number of parameters is $2N + 1$.

The classical Poisson-Boltzmann distribution is obtained by integrating equations (12) and (13) resulting in

$$f = f^0 e^{\phi} \tag{25}$$

$$g = g^0 e^{-\phi} \tag{26}$$

where we have taken $\phi^1 = 0$. Note that the functional form of equations (25) and (26) are valid both inside and outside the electric double layer. This is termed the Poisson-Boltzmann distribution for the ionic species and is valid even in more than one dimension.

4 Fully Developed Electroosmotic Channel Flow

4.1 Asymptotic and Numerical Solutions for Arbitrary Electric Double Layer Thickness

Most often the fully developed assumption in slit pores is invoked because channels with more than one nano-constrained dimension have not been fabricated. As mentioned above we will consider only the case of two ionic species although the extension to an arbitrary number of species is easy to formulate; thus we consider a three component mixture containing the ionic species plus the solvent water; however it is easy to extend the theory to mixtures such as PBS[17] . Because the mole fractions sum to one, it is sufficient to consider only the equations governing the ionic species.

Equations (14) and (15) suggest clearly the nature of the solution as a function of ϵ. For $\epsilon << 1$, the electric double layers are thin and equations (14) and (15) reduce to

$$g - f = 0$$

and so the core region away from the walls the fluid is electrically neutral. Near the walls, the velocity and potential vary rapidly and so we define the new variable appropriate in the region near $y = 0$, $\hat{y} = \frac{y}{\epsilon}$ and, for example equation, (15) becomes

$$\frac{\partial^2 u}{\partial \hat{y}^2} = -\beta(g - f)$$

This is expected to be the situation in the case of a micro-channel. On the other hand when $\epsilon = O(1)$ the fluid is not electrically neutral and the whole problem must be solved in the entire domain $0 \leq y \leq 1$. This is the case for a nano-channel.

The case of $\epsilon << 1$ has been considered in detail by Conlisk *et al*[16] and we now outline the solution. Electroneutrality requires

$$f_o = g_o \tag{27}$$

where the subscript o denotes the outer solution outside of the double layers.

Now since the outer solutions for f and g are equal, we can subtract the equations for g and f to find

$$\phi_o = C \int_y^1 \frac{dy}{g_o} + D \tag{28}$$

Now the dimensionless velocity in the outer region satisfies

$$u_o = \phi_o + Ey + F \tag{29}$$

and in the inner region near $y = 1$ for example,

$$u_i = \phi_i + G \tag{30}$$

Near $y = 0$ we have

$$u_i = \phi_i + K \tag{31}$$

The unknown constants are obtained by matching and the solution in the core of the channel is

$$u_o = \phi_o = \frac{1}{2} ln \left(\frac{g^0}{f^0} \right) \tag{32}$$

$$f_o = \sqrt{g^0 f^0} = g_o \tag{33}$$

Note that both positive and negative velocities may occur based on the relative values of the mole fractions f^0 and g^0. If the two electrolytes have valences z_g and z_f, the solution is

$$u_o = \phi_o = \frac{1}{z_g - z_f} ln \frac{-z_g g^0}{z_f f^0} \tag{34}$$

$$f_o = \sqrt{-\frac{z_g}{z_f} g^0 f^0 e^{-(z_g + z_f)\phi_o}} = g_o \tag{35}$$

Now consider the inner solution within the electric double layer. Substituting expressions (25) and (26) in the potential equation (14) we can integrate once to obtain

$$-\frac{1}{2}(\phi_i')^2 = -f^0(e^{\phi_i} - 1) - g^0(e^{-\phi_i} - 1) \tag{36}$$

leading to the solution for ϕ in integral form as

$$\phi_i(y) = \sqrt{2(g^0 + f^0)} \int_0^{\phi} \sqrt{ae^{-\phi} + be^{\phi} - 1}d\phi \tag{37}$$

where

$$a = \frac{g^0}{g^0 + f^0}$$

$$b = \frac{f^0}{g^0 + f^0}$$

The integral is over the domain $(0, \phi_o)$ which is given above.

Much information about the solution in the inner region may be obtained without performing the integration explicitly. The uniformly valid solution for the velocity is given by[23]

$$u_{uv} = u_i^0 + -\phi^1 y + u_i^1 \tag{38}$$

where u_i^0 is the inner solution near $y = 0$ for example. Note that near $y = 0$, $u_{uv} = \phi_i^0$, and $u_{uv} = \phi_i^1 - \phi^1$ near $y = 1$ where ϕ_i^0 is the inner solution for the potential near $y = 0$.

Once the solution for the potential and velocity is computed, the flow rate can be calculated in the asymptotic case as

$$Q == U_0 A \int_0^1 u dy = U_0 A(\frac{g^0 - f^0}{g^0 + f^0} - 2\epsilon)$$

where $A = Wh$ is the cross-sectional area of the channel. The corresponding surface charge density is given by

$$\sigma_0 = \frac{\epsilon_e RT}{\epsilon hF} \int_0^{\infty} \frac{\partial^2 \phi}{\partial \hat{y}^2} d\hat{y} = -\frac{\epsilon_e RT}{\epsilon hF} \frac{\partial \phi}{\partial \hat{y}} \mid_0 \tag{39}$$

In classical electrochemistry it is argued that for the case of thin, non-overlapping double layers, the appropriate reference concentration or mole fraction to use is the value in the bulk. Thus $\phi = \frac{\partial \phi^*}{\partial y^*} = 0$ in the bulk and[10]

$$\phi^*(y^*) = \frac{2RT}{zF\epsilon_e} ln \left(\frac{1 + \gamma e^{-\kappa y^*}}{1 - \gamma e^{-\kappa y^*}} \right) \tag{40}$$

where

$$\gamma = \frac{e^{\frac{zF\phi_0^*}{2RT}} - 1}{e^{\frac{zF\phi_0^*}{2RT}} + 1}$$

and all variables are dimensional. The quantity $\phi_0^* = \zeta^*$ the ζ-potential and $\kappa = \frac{1}{\lambda}$. This approach may be useful for non-overlapping bouble layers but is not appropriate for overlapping EDLs.

We will present results for an aqueous solution at a temperature $T = 300^{\circ}K$, imposed electric potential is six volts applied over a length of $3.5\mu m$ with a dielectric constant of water, 78.54. We

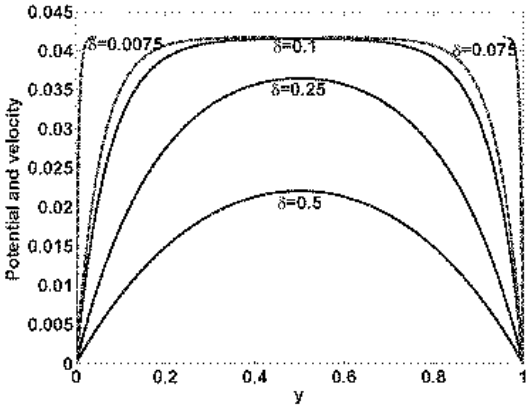

(a)

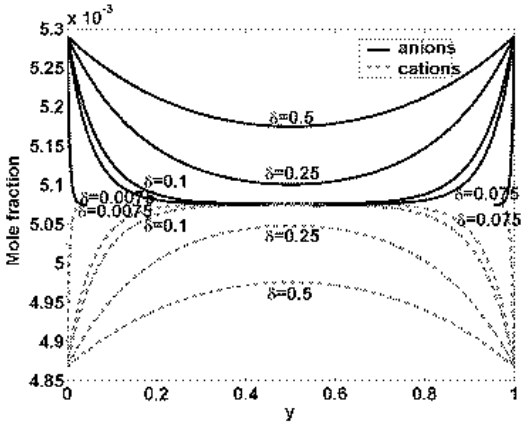

(b)

Figure 9: Results for the dimensionless velocity and potential along with mole fractions for the symmetric case of a pair of monovalent ionic species for an electric field of 6 volts over a channel of length $L = 3.5\mu m$; the channel height varies and the value of δ is shown; here $\gamma = 0.92$. (a) Velocity and potential. (b) Mole fractions for $f^0 = f^1 = 0.00252$ and $g^0 = g^1 = .00276$.

assume two monovalent ions, say Na+ and Cl- ; the baseline mixture wall mole fractions correspond to a concentration of Na equal to .154 M, Cl .141 M and water 55.6 M for which $\beta \sim 190$. Results are also produced for other concentrations as noted.

On Figure 9 are the results for a number of values of δ corresponding to different channel heights from overlapping double layers to vary thin double layers. In the overlapped case, a numerical solution using classical finite-difference techniques[16] is computed for the potential. Note the plug flow nature of the velocity for small δ; this is the classical electroosmotic velocity as depicted in textbooks. Note that we compute the potential as a perturbation from the ζ potential at the side walls and thus the velocity is equal to the potential. Moreover, the ζ potential is not needed in the simulation.

Figure 10 demonstrates the concentration, velocity, and potential profiles across channels of different heights and oppositely charged surfaces. That is, $y = 0$ corresponds to a negatively charged surface and $y = 1$ corresponds to a positively charged surface. Accordingly, the ionic wall mole concentrations show an increase in the counterion for each surface, leading to increased concentrations of opposing ions at the opposite walls. For this simulation, the same mole fractions were used at $y = 0$ as in Figure 9 with the cation concentration at $y = 1$ equal to 0.5 that of the concentration at $y = 0$. The anion concentration at $y = 1$ is dictated by the condition of equal electrochemical potential at each wall. Note that within the channel there is flow in opposing directions due to competing electroosmotic effects at the two surfaces. This gives the considerably lower flowrate of $Q = 6.5 \times 10^{-13} \frac{L}{min}$ when compared with the symmetric case for which the velocity is always positive.

4.2 Equilibrium Considerations

The results of the previous section are for arbitrarily specified wall boundary conditions and they do not take into account the prescence of upstream and downstream reservoirs present in actual systems; the situation has been decpicted on Figure 2(b). In experiments, the molarities in the reservoirs are known and the mixture is electrically neutral there. In this situation, incorporation of the reservoirs without calculating the solutions there can be achieved by calculating the wall mole fractions using the requirement that the electrochemical potential in the reservoirs far upstream be the same as the average value at any channel cross section as described by Zheng, Hansford and Conlisk.[17] This requirement leads to the Nernst equation[3] which is given by

$$\Delta \Psi = \frac{RT}{z_i F} ln \frac{c_{iR}}{\bar{c}_{iC}} \;\; i = 1, ..., N \tag{41}$$

where c_{iR} and $\bar{c}_{iC}$ are the average values of the concentration of species i in the reservoir and the fully developed region within the channel respectively.

The channel must be electrically neutral as well so that

$$z_f c_f + \sum_i z_i \bar{c}_{iC} = 0 \tag{42}$$

where z_f and c_f are the valence and the concentration of the fixed charges on the wall. Electroneutrality in the reservoir requires

$$\sum_i z_i c_{iR} = 0 \tag{43}$$

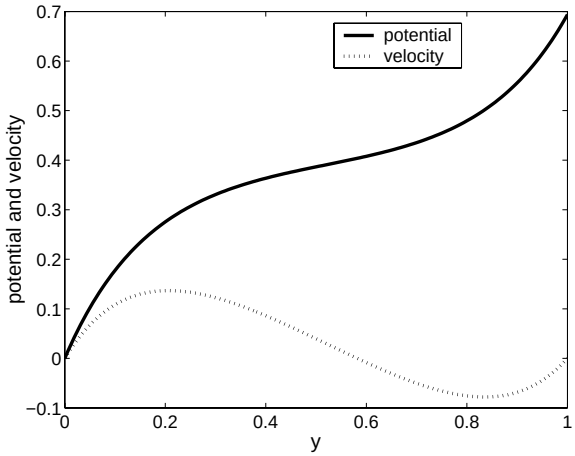

(a)

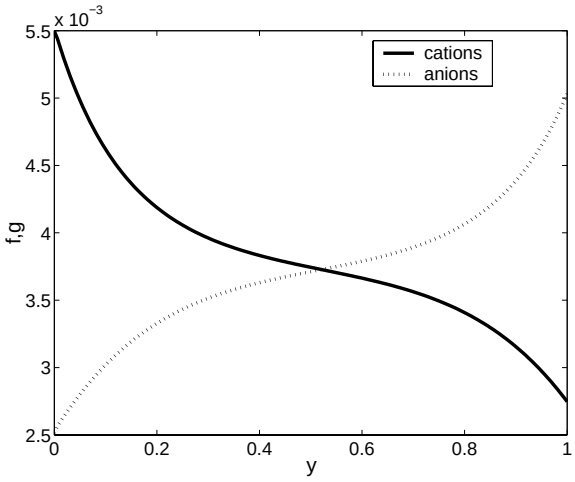

(b)

Figure 10: Results for the dimensionless velocity and potential along with mole fractions for the asymmetric case of an NaCl-water mixture. Here the electric field corresponds to 6 volts over a channel of length $L = 3.5\mu m$; the channel height $h = 4\ nm$. (a) Velocity and potential. (b) Mole fractions for $f^0 = 0.00252, f^1 = 0.00503$ and $g^0 = .00550, g^1 = 0.00275$.

Equations (41) and (42) are N+1 equations in N+1 unknowns for the average concentrations in the channel and the Nernst Potential $\Delta\Psi$.

If the volume of the reservoir is much larger than the volume of the channels as is the case in practice, then the concentration in the reservoir will be fixed at the value of the concentration prior to the initiation of flow into the channel. To obtain each of the average concentrations in the channel, we equate the Nernst potential for each of the species and substituting into equation (42) we have

$$z_f c_f + z_1 \bar{c}_{1C} + \sum_{i=2}^{N} \frac{z_i c_{iR}}{(c_{1R})^{\frac{z_i}{z_1}}} (\bar{c}_{1C})^{\frac{z_i}{z_1}} = 0 \tag{44}$$

where 1 is the most populous species, for example. This is a single equation for the average concentration of species 1 in the chaannel $\bar{c}_{1C}$, assuming the surface charge density is known.

To be dimensionally consistent in equation (44) the surface charge density should be converted to Moles/liter(M) and

$$c_f = \frac{A\sigma}{1000 V_0 F} \tag{45}$$

where A is the surface area and V_0 is the volume. The factor 1000 converts m^3 to liter.

The average concentration in the channel is defined in dimensional form as

$$\bar{c}_i = \frac{1}{h} \int_0^h c_i dy^* \tag{46}$$

and in nondimensional form, dividing by the total concentration of the mixture we have

$$\bar{X}_i = \int_0^1 X_i dy \tag{47}$$

where X_i is the mole fraction. Using equations (44) and (47) we can iterate until the wall mole fractions are consistent with the reservoir concentrations for given surface charge density defined by

$$\sigma = -\frac{\epsilon_e RT}{\epsilon h F} \int_0^1 (g - f) dy \tag{48}$$

The precise procedure is described by Zheng et al.[17] It is useful to point out that for small surface charge densities($\sim 0.01 \frac{C}{m^2}$) the Debye-Huckel picture of the EDL is recovered, whereas for $\sigma \sim 0.1 \frac{C}{m^2}$ the Gouy-Chapman picture of the EDL is recovered.

5 Comparison of Continuum Models with Experiment

In this section we compare the continuum model of EOF with several sets of experimental data. The first set of data is for channels fabricated by a group at Oak Ridge National Laboratory[1] as depicted on the left side of Figure 11. The mixture is 50% sodium tetraborate, 50% methanol solution. The wall mole fractions are calculated by the procedure described in the previous section and the geometry of the channels is described on Table 1.[24] These channels are essentially slit pores as we

[1]The authors appreciate the use of the data received from Dr. J. Michael Ramsey and his group at Oak Ridge National Laboratoriy. This group included at the time of receipt of the data Dr. Steve Jacobson and Dr. J. P. Alarie.

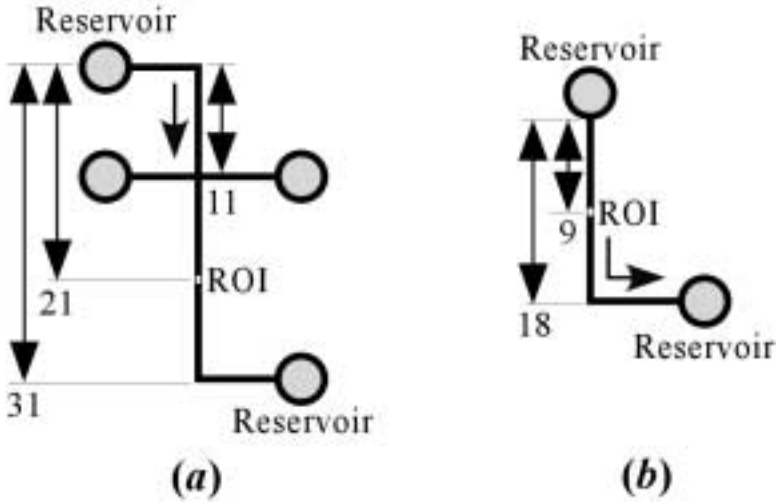

Figure 11: Oak Ridge(left) and Georgia Tech(right) configurations for the experimental measurement of the mobility.

Channel height(nm)	Channel widthμm
83	20.3
98	18.4
290	18.3
300	20.2
1080	20.1

Table 1: ORNL channel dimensions.

mM	$\mu_e \times 10^4$	$\mu \times 10^4$	$\mu_a \times 10^4$	σ	ζ_e	ζ	ζ_a
0.2	3.23	3.52	7.53	-0.0154	-0.138	-0.141	-0.185
2	2.85	2.97	3.28	-0.0154	-0.098	-0.114	-0.125
20	1.89	1.44	1.21	-0.0154	-0.054	-0.049	-0.050
150	0.80	0.58	0.59	-0.0154	-0.017	-0.019	-0.019

Table 2: Results for the mobility and dimensional ζ potential for the indicated molarities in the $83nm$ channels of ORNL. Both numerical and asymptotic values of the mobility and ζ potential are shown. The subscript e stands for experimental, a for asymptotic and the units of the mobility μ are $\frac{cm^2}{Vsec}$. The units of surface charge density are $\frac{C}{m^2}$ and ζ is in volts.

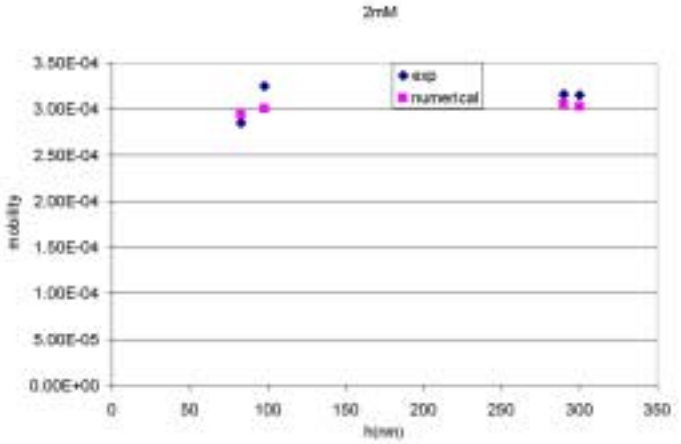

(a)

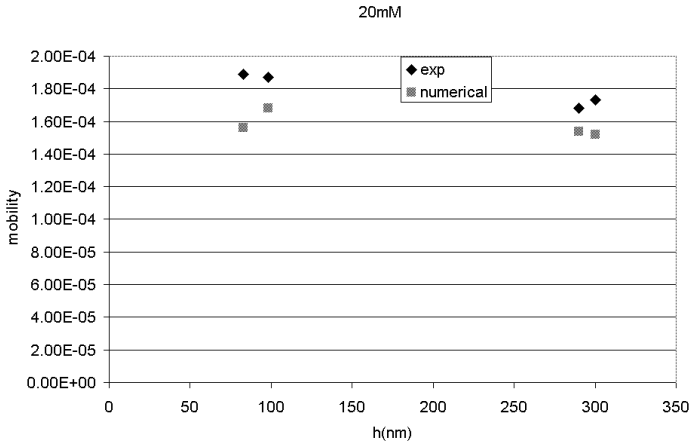

(b)

Figure 12: Comparison of the experimental data with the theoretical model for the mobility. The converged surface charge density is held fixed at $-0.0154 C/m^2$. (a) Ionic strength $2mM$; (b) $20mM$.

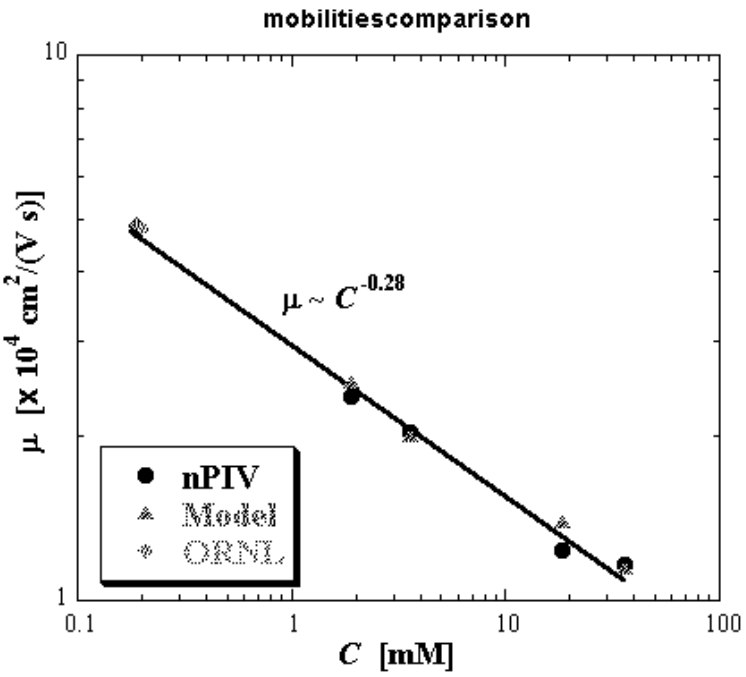

Figure 13: Graph of mobility values μ_{ex} () and μ_{eo} ($\times$) as a function of molar concentration for EOF of sodium tetraborate buffer. The solid line shows Equation 50 with $\mu_b = 3.00 \times 10^{-4}$ cm^2/(V·sec) and $N = 0.277$

have considered in the analysis. We have compared the model with data for over fifteen operating conditions and a small portion of those data comparisons are shown here. Figure 12 shows the results for the case of $2mM$ and $20mM$ in the upstream reservoir. Here the results are very good; clearly the basic electrochemical effects are present in the model. Note that the model yields a true prediction; there are no adjustable parameters with which to match the data.

It is useful to point out that the ζ potential can be defined by setting the potential

$$\psi = \phi + \zeta$$

equal to zero in the core. This yields in dimensionless form

$$\zeta = -\frac{1}{2} ln \frac{g^0}{f^0}$$

and note that this implies a theoretical relationship between the ζ potential and the surface charge density. On Table 2 are the results at various molarities for the $83nm$ channel. Note the good agreement between the experimental data and the model. Clearly the prediction of the ζ potential by the model is extremely good. The differences in the numerically computed ζ potential(ζ) and the asymptotic value(ζ_a) valid for $\epsilon << 1$ on Table 2 indicates that the double layers on the channel walls may be overlapping.

A similar set of results have been produced by Yoda's group at Georgia Institute of Technology.[25] Figure 13 compares the experimentally measured mobility μ_{ex} with the electroosmotic mo-

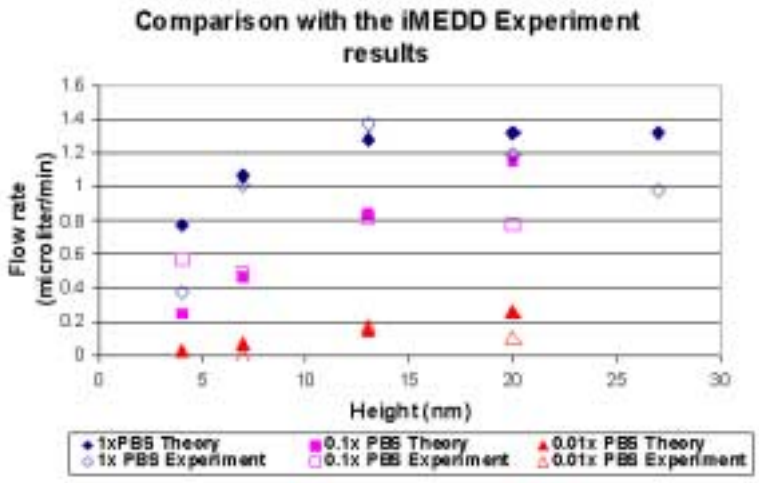

Figure 14: Comparison of the experimental data with the theoretical model for the flow rate through the iMEDD membrane.

bility $\mu_{\rm eo}$ predicted by an asymptotic model described in Section 4.

$$\mu_{\rm eo} = \frac{\varepsilon_{\rm e}\phi_{\rm o}}{2\mu} \ln\left\{\frac{g^0}{f^0}\right\}. \tag{49}$$

Here, $\varepsilon_{\rm e}$ and μ are the electrical permittivity and absolute viscosity, respectively, of the fluid and $\phi \equiv RT/F$ (R is the universal ideal gas constant, T the absolute temperature of the fluid and F is Faraday's constant) is the characteristic scale for the potential, and (g^0, f^0) are the wall mole fractions of the cationic and anionic species, respectively. The wall mole fractions are predicted by the method described in the previous section. The experimental and model values for mobility agree within 10% over a 200-fold change in molar concentration, suggesting that the particle tracers follow the flow with good fidelity over the range of E studied.

The linear result on Figure 13 suggests that the mobility scales as a power of the concentration:

$$\mu = \mu_o \left(\frac{C}{1mM}\right)^{-N} \tag{50}$$

A curve-fit of the experimental data points gives $\mu_o = 2.94 \times 10^{-4}$ cm^2/(V·sec) and $N = 0.278$. These are the first results suggesting this correlation which cannot be directly derived from the analysis because of the iterative method used to derive f^0 and g^0.

We have compared the model with another data set taken by iMEDD, Inc. of Columbus, Ohio. Using techniques developed by Hansford. et. al. [21], they fabricate a variety of silicon membranes consisting of a series of nanochannels and measure electroosmotic flow rate across those membranes. The membranes are 3.5mm long, 1.5mm wide, and 3.5(m thick. In their configuration, there are 47,500 nanochannels on each of these membranes. The nanochannels themselves are 3.5 (m in length and 44 (m in width. iMEDD inc. fabricate and made tests to channels with different heights: 4nm, 7nm, 13nm, 20nm, 27nm and 49nm in particular. The geometry of the iMEDD nanochannel membrane and the testing apparatus are shown in Figure 2(b).

The two reservoirs are filled with buffer solution. The buffer used in iMEDD's experiments are PBS, ten times diluted PBS, and 100 times diluted PBS. 17 Volts DC is applied on the two electrodes at the far ends of the two reservoirs. It should be noted that the voltage drop across the membrane is much less than 17 Volts, because most of the 17 Volts is dissipated outside the nanopore membrane, due to the resistance of the buffer in the reservoir. In addition to those experimental parameters mentioned in the ORNL comparison section, the voltage drop across the membrane is required and this value is calculated from a resistance model for each channel height.

Using membrane resistance data determined by iMEDD, we can calculate the volume flow rates based on the calculated voltage drops. The comparison of the calculated flow rates with iMEDD's experimental results is shown in Figure 14. They agree very well except at 4nm. It is possible that at this channel height, some non-continuum effects are present which cannot be captured by the purely continuum theory described here. Also there is some disagreement at larger heights; we believe these discrepancies are due to the estimate of the voltage drop.

Note the interesting result that there appears to be a maximum in the flowrate at the 13 nm location. In the iMEDD experimental configuration, as the channel height increases, the total cross-sectional area of the channels increases, and the resistance of the nanopore membrane decreases. Therefore the percentage of the cross membrane voltage to the total voltage decreases, so the cross membrane voltage decreases. The rapid drop in the cross membrane voltage leads to a maximum in the volume flow rate curve. This phenomenon is unusual and does not occur in pressure-driven flow.

From these results it is clear that continuum models compare well with the experimental data. There may be a lower limit down around channel heights of $4 - 5nm$ where continuum theory may begin to fail, but this can only be confirmed by comparisons with a molecular dynamics simulation. This is considered next.

6 Molecular Dynamics Simulations

6.1 Introduction

Non-equilibrium molecular dynamics (NEMD) offers a completely molecular description of electroosmotic flow (EOF) in nanochannels, and some studies have recently appeared.[26–28] Implementation of NEMD requires specification of an interaction model for the fluid and channel walls. To date, the chemical composition and roughness of the channel walls has not been characterized well experimentally. Therefore, currently MD studies of EOF have used, to varying extent, schematic models, particularly with respect to the channel walls. A further consideration is the model used to describe how frictional heating is dissipated. Despite the simplifying assumptions that, at this stage of our understanding, have to be made, simulation studies have helped determine the extent to which continuum theories will apply at the nanoscale and have identified important issues that need further study.

The issues involved in comparing with continuum theory can be divided into two groups. First, the driving force for EOF is determined by the charge distribution within the fluid. In the linear response regime, the charge distribution governing EOF is the equilibrium ionic distribution within the electrolyte. Therefore, one important issue concerning EOF is essentially static in nature: how well continuum methods like Poisson-Boltzmann theory predict the equilibrium ion distribution. Secondly, there is a group of issues in setting up continuum equations for fluid flow. The type o

boundary conditions, i.e. no-slip or partial slip, and where to place the boundary surface are crucial issues. There is also a question of whether a linear constitutive relation between shear stress and strain exists, and whether this relation can be taken as fixed throughout the channel.

6.2 Statics: the Charge Distribution in a Nanochannel

In nanochannels, the width of the channel is typically between 10 and 100 solvent molecular diameters. Under many experimental conditions this is less than a Debye length. Since Poisson-Boltzmann theory (PBT) neglects the molecular nature of solvent and ions, it is not surprising that simulation studies of nanochannel flow indicate that PBT is a poor starting point for description of the charge distribution in very small channels.[26–28] Here we identify and discuss several shortcomings of Poisson-Boltzmann theory – neglect of specific ion-wall interactions, molecular nature of the solvent, ion correlations, and finite-size corrections to the solvent dielectric response.

PBT theory is a mean field theory in which the instantaneous, fluctuating interactions of ions with other fluid particles and the walls are replaced by an average potential. PBT has been solved analytically for ions between uniform charged surfaces.[29,30] Classical PBT neglects any specific interactions between ions and the wall, other than incorporating very strong binding of some ions in the Stern layer through a modified wall charge. Simulations show that specific ion-wall interactions significantly affect the ion density and need to be incorporated to predict EOF flow characteristics.

Liquids tend to order near walls, an effect which arises form the molecular nature of the solvent. The effect has been elegantly confirmed by the oscillatory dependence of the force on distance as solvent is squeezed out between mica sheets. To illustrate this effect, the density profile of a fluid of spherical particles interacting via a Lennard-Jones interaction is shown in Fig. 15, where layering is clearly visible in the snapshot and density profile. The ion distribution is consequently modified by the structured environment near the channel walls in a complex fashion. Spherical ions in a solvent of spherical particles of the same size tend to lie within the solvent layers.[28] However, in simulations of ions in water using the SPC[31] or SPC/E[32] water models, the ions tend to fit between solvent layers.[26,27]

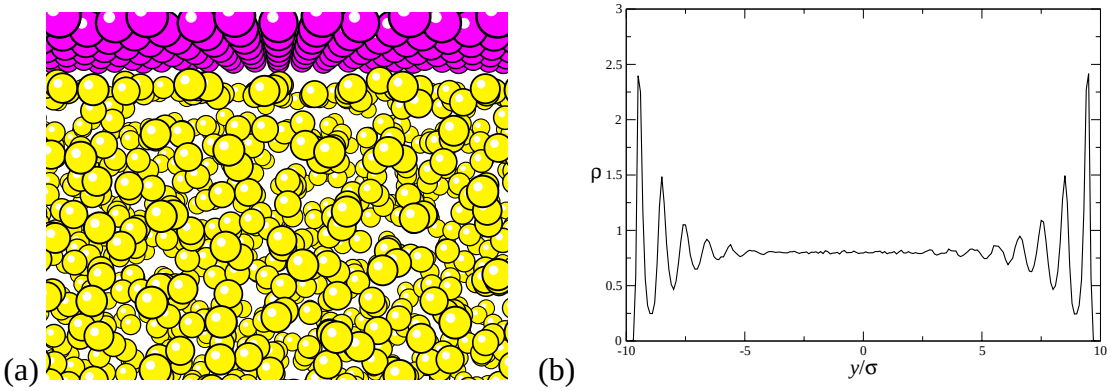

Figure 15: An illustration of fluid layering near a wall. Panel (a) is a snapshot of the region near the wall from a simulation of particles interacting via pairwise Lennard-Jones potentials, $4\epsilon\left[\left(\frac{\sigma}{r}\right)^{12}-\left(\frac{\sigma}{r}\right)^{6}\right]$. The overall density of the fluid is $\rho\sigma^3 = 0.8$. Fluid layers are visible next to the wall, near the top of the figure. Panel (b) is the equilibrium density profile across the channel.

Since PBT is a mean field theory, it neglects correlations between ions. Recently, the problem of ion correlation has received much attention. While PBT predicts that the effective interaction between like-charged walls, rods or spheres will always be repulsion, correcting for ion correlations predicts an effective attraction at high ionic strength. It remains to be seen whether correlation effects are significant under typical EOF conditions.

Finally, in classical PBT the solvent dielectric response is captured by modifying Coulomb interactions with a dielectric constant. This procedure is only correct for a dielectric medium of infinite size. The well-known correction when ions approach an interface with a medium of differing dielectric constant takes the form of image charges. For example, Onsager and Samaras showed that ions in a medium with a high dielectric constant, such as water, will be repelled from an interface with a medium of low dielectric constant.[33] What the fictitious image charge repulsion describes is the actual lessened dielectric solvation when the ion is near the interface. This is the likely situation for aqueous electrolyte flow in nanochannel fabricated in low silicon or polymeric materials. Image charge effects are included in molecular dynamics simulations. In simulations of a model electrolyte, decreased solvation near the wall results in complete exclusion of ions from the solvent layer adjacent to the wall.[28]

6.3 Fluid Dynamics in Nanochannels

As discussed in the previous section, we know that classical PBT does not give sufficient accuracy to understand EOF in nanochannels.[26–28] Now we consider whether, with an accurate ion distribution, linear hydrodynamics can predict EOF in nanochannels. There are two studies of this issue, one by Qiao and Aluru[27] (QA) and the other by Zhu, Singer, Zheng and Conlisk[28] (ZSZC). In both studies simulations are compared with continuum fluid mechanics using an ion density that agreed with simulations (and not from PBT). The conclusions reached concerning the applicability of linear hydrodynamics are somewhat different.

QA compared continuum theory with simulations in simulations of aqueous chloride ions confined by walls of Lennard-Jones particles. The width of their nanochannel is $3.49nm$. They enforce no-slip boundary conditions at the positions of the outermost wall particles, and find that continuum theory predicts a velocity profile more than double that of simulations. They attribute this disagreement to a steep rise of solvent viscosity near the channel walls, and advocate incorporation of position-dependent viscosity into the Navier-Stokes equations.

ZSZC simulate EOF in a model fluid composed of spherical Lennard-Jones solvent and ions, as pictured in Fig. 16. Reflecting the exclusion of ions from the wall layer because of solvation forces discussed in the previous region, ZSZC find that solving the PBT equations within a region excluding the fluid near the walls gives a qualitatively accurate description of the charge density, and also yields analytic expressions for the velocity profile. In their comparison with continuum theory, ZSZC enforce no-slip boundary conditions at a surface that represents the furthest penetration of solvent against the walls. This surface is closer to the channel center than that of QA. In contrast to QA, ZSZC find that continuum hydrodynamics gives a good account of the velocity profile.

Differing points of view about the placement of the no-slip surface led QA and ZSZC to different conclusion about the applicability of standard hydrodynamics with a constant viscosity throughout the channel. By placing their continuum fluid up to the position of wall particles, QA neglect excluded volume interactions which keep solvent and walls atoms separated by the sum of their radii. To correct this picture, they invoke position dependent viscosity. ZSZC estimates a surface

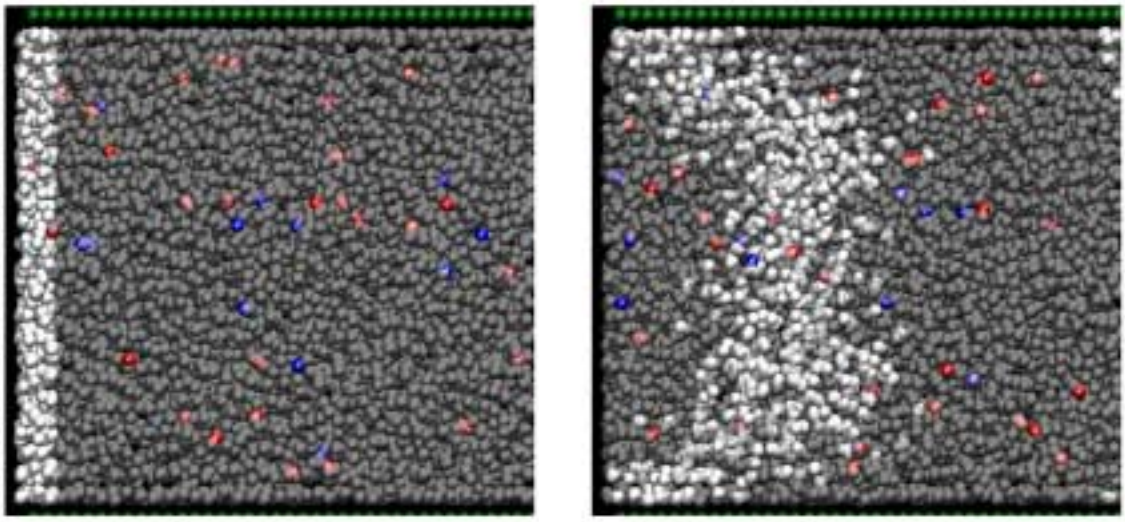

Figure 16: Snapshots from a simulation of EOF by Zhu, Singer, Zheng and Conlisk.[28] Cations are red, anions are blue, wall particles are green. In the left-hand frame the solvent particles within a slab are colored white, and the other solvent particles are left as gray. The right-hand frame, from a later time, shows the evolution of the slab of white-colored particles.

of closest penetration of solvent against the wall, which can be done in several ways. One method ZSZC uses is to fit the velocity profile from Poiseuille flow to the well-known analytical formula and set the no-slip surface at the point where the Poiseuille flow profile went to zero. They find that this procedure set the no-slip surface very close to the simple estimate of Travis and Gubbins,[34] which is half a Lennard-Jones particle diameter from the centers of the wall particles. Using a better estimate of the no-slip surface for the system simulated by QA, ZSZC recalculate the velocity profile and found much better agreement between continuum theory and MD simulation without having to invoke position-dependent viscosity.

To obtain a completely analytical expression that matches simulation results, ZSZC solve PBT and corresponding hydrodynamic equations for fluid flow with adjustable volume available to the ions. The original intent is to describe the exclusion of ions from the wall region found in their simulations. However, the theory also brings to light a qualitative relationship between ion distribution and velocity profile: When ions are excluded from the wall region, the flow increases. Conversely, attraction of the ions to the walls decreases the flow rate. This trend exists because the greatest flow response occurs when the driving force is in the center of the channel, away from the no-slip boundaries.

7 Summary

In this chapter we have described modeling of electroosmotic flow in micro- and nano-channels. We have reviewed the structure of the electric double layer and its role in the transport of ions and solvent in channels. The flow is driven by the difference in cation/anion concentrations at the walls of the channel. At small cation, anion concentration differences the Debye-Huckel picture

of the electric double layer is appropriate; at larger concentration differences, the Gouy-Chapman picture of the electric double emerges naturally. We show how analytical solutions for the velocity and concentrations or mole fractions may be derived for electric double layer thicknesses small compared with the channel height.

Analytical results are compared with several sets of experimental data and the model compares well. In addition, the comparisons with experiments suggest that the continuum approximation may break down for channel hieghts on the order of $5nm$ and so the mechanics and results of molecular dynamics simulations are also described. It is shown that MD simulations allow preferential solvation near the wall in contrast to the continuum Poisson-Boltzmann approach, resulting in significant differences in the magnitude of bulk solution and ionic transport.

The persistence of the validity of continuum theory down to under about $5nm$ in height, at first glance seems surprising. However, on further reflection, since liquid molecules are so close together an effective Knudsen number defined as the ratio of a molecular diameter to the smallest dimension of the channel remains small down to under $10nm$. For water, the molecular diameter is about $0.3nm$ and so using the well-developed gas phase theory, an effective knudsen number of 0.1 corresponds to a channel height of $3nm$. Indeed it has often been mentioned that continuum theory in liquids persists to about 10 molecular diameters.

Most of the devices being fabricated today have channels greater than 2 or 3 nanometers. Thus continuum or near continuum behavior should obtain down to these scales. Thus despite the well-known lack of a well-defined theory of liquids, modeling of liquid flows at nanoscale seems to be relatively straightforward when compared to gases, even though there is a well-developed kinetic theory for gases. Indeed, for air a Knudsen number of around 1 corresponds to a channel height of about $60nm$; in the transition regime where continuum theory breaks down and expensive and time consuming molecular simulations are required.

Acknowledgements: Much of the work described in this chapter was begun under funding from DARPA under agreement number F30602-00-2-0613. ATC is grateful to the contract monitors Dr. Anantha Krishnan (DARPA), Mr. Clare Thiem and Mr. Duane Gilmour of Air Force Research Lab (IFTC) for their support. ATC is also grateful to Dr. Mauro Ferrari and Professor Derek Hansford for getting him involved in this work.

References

[1] R. A. Robinson and R. H. Stokes. *Electrolyte Solutions*, Academic Press: New York, pp. 284-335, 1959.

[2] J. S. Newman, *Electrochemical Systems*, Prentiss-Hall : Englewood Cliffs, NJ, pp. 138-240, 1973.

[3] R. J. Hunter, *Zeta Potential in Colloid Science*, Academic Press: London, pp. 59-124, 1981.

[4] R. F. Probstein, *Physicochemical Hydrodynamics*, Butterworths: Boston, pp. 161-200, 1989.

[5] Paul Delahay, *Double Layer and Electrode Kinetics*, Wiley Interscience, New York, 1965.

[6] John O'M. Bockris and Amulya K. N. Reddy, *Modern Electrochemistry, Volume 1 Ionics*, Second Edition. Plenum Press, New York and London, pp. 273f, 1998.

[7] Jacob Israelachvili, *Intermolecular and Surface Forces*, 2nd Edition, Academic Press, London, 1991.

[8] Private communication by Tony Boiarski, 2002.

[9] Derek Hansford, T. Desai, M. Ferrari, "Nanoscale Size-based Biomoleculart Separation Technology", *Biochip Technology*, eds. J. Cheng, L. J. Kricka, Harwood Academic Publishers, 341(2001).

[10] E.J.W. Verwey and J.Th. G. Overbeek, *Theory of Stability of Lyophobic Colloids*, Elsevier: Amsterdam, 1948.

[11] W. Qu and D. Li, "A Model for Overlapped EDL Fields", *J. Colloid and Interface Science* **224**, 397(2000).

[12] D. Burgeen and F. R. Nakache, "Electrokinetic Flow in Ultrafine Capillary Slits", *The Journal of Physical Chemistry* **68**, 1084(1964).

[13] S. Levine, John R. Marriott, and Kenneth Robinson, "Theory of Electrokinetic Flow in a Narrow Parallel-plate Channel", *Faraday Transactions II* **71**, 1(1975).

[14] C. L. Rice and R. Whitehead, "Electrokinetic Flow in a Narrow Capillary", *Journal of Physical Chemistry* **69**, no. 11, 4017(1965).

[15] S. Levine, J. R. Marriott, G. Neale, and N. Epstein, N., "Theory of Electrokinetic Flow in Fine Cylindrical Capillaries at High Zeta Potentials", *Journal of Colloid and Interface Science* **52**, no. 1, 136(1975).

[16] A. T. Conlisk, Jennifer McFerran, Zhi Zheng, and Derek Hansford, "Mass Transfer and Flow in Electrically Charged Micro- and Nano-channels", *Analytical Chemistry* **74**, Issue 9, 2139(2002).

[17] Zhi Zheng, Derek J, Hansford, and **A. T. Conlisk**, "Effect of Multivalent Ions on Electroosmotic Flow in Micro and Nanochannels", *Electrophoresis*,**24**, pp. 3006-3017, August 2003.

[18] Helmholtz, H. L. F., *Ann. Physik.*, (3), Vol. 7, p. 337, 1879.

[19] Debye, P. and Huckel, E., "The Interionic Attraction Theory of Deviations from Ideal Behavior in Solution", *Z. Phys.* , Vol. 24, p. 185, 1923.

[20] Gouy, G., "About the Electric Charge on the Surface of an Electrolyte", *J. Physics A*, Vol. 9, pp. 457-468, 1910.

[21] Chapman, D. L., *Phil. Mag.* , "A Contribution to the Theory of Electrocapillarity", Vol. 25, p. 475-481, 1913.

[22] Stern, O., *Z. Elektrochem.*, "The Theory of the Electrolytic Double Layer", Vol. 30, p. 508-516, 1924.

[23] Kevorkian, J. and Cole, J. D. *Perturbation Methods in Applied Mathematics*, Springer-Verlag, New York, 1981

[24] Jacobson, S. C., Ermakov, S. V., and Ramsey, J. M., "Minimizing the Number of Voltage Sources and Fluid Reservoirs for Electrokinetic Valving in Microfluidic Devices", *Anal. Chem.*, **71**, pp. 3273-3276(1999).

[25] Sadr, R., Yoda, M., Zheng, Z. and Conlisk, A. T., "An Experimental Study of Electroosmotic Flow in Rectangular Microchannels," *Journal of Fluid Mechanics*, **506**, 357-367 (2004)

[26] J. B. Freund, i"Electro-osmosis in a nanometer-scale channel studied by atomistic simulation", *J. Chem. Phys.*, **116**(5), 2194 (2002).

[27] R. Qiao and N. R. Aluru, " Ion concentrations and velocity profiles in nanochannel electroosmotic flows", *J. Chem. Phys.*, **118**(10), 4692 (2003).

[28] W. Zhu, S. J. Singer, Z. Zheng, and A. T. Conlisk, "Electroosmotic flow of a model electrolyte", *J. Chem. Phys.* (2004), (submitted, 2004).

[29] A. J. Corkhill and L. Rosenhead, "Distribution of charge and potential in an electrolyte bounded by two infinite parallel plates", *Proc. Royal Soc.*, **172**(950), 410 (1939).

[30] S. Levine and A. Suddaby, "Simplified forms for free energy of the double layers of two plates in a symmetrical electrolyte", *Proc. Phys. Soc.*, **A 64**(3), 287 (1951).

[31] H. J. C. Berendsen, J. P. M. Postma, W. F. von Gunsteren, and J. Hermans, "Interaction models for water in relation to protein hydration", in *Intermolecular Forces*, edited by B. Pullman, page 331, (Reidel, Dordrecht, Holland, 1981).

[32] H. J. C. Berendsen, J. R. Grigera, and T. P. Straatsma, "The missing term in effective pair potentials", *J. Phys. Chem.*, **91**(24), 6269 (1987).

[33] L. Onsager and N. N. T. Samaras, "The surface tension of Debye-Hückel electrolytes", *J. Chem. Phys.*, **2**(8) (1934).

[34] K. P. Travis and K. E. Gubbins, "Poiseuille flow of Lennard-Jones fluids in narrow slit pores", *J. Chem. Phys.*, **112**(4), 1984 (2000).

43rd AIAA Aerospace Sciences Meeting
Reno, Nevada
AIAA 2005-xxxx
January 10-13, 2005

Appendix K:

Transient Electroosmotic Flow in Nano-Channels *

Pradeep Gnanaprakasam
Ankan Kumar
A.T.Conlisk †
Department of Mechanical Engineering
The Ohio State University
Columbus, Ohio 43202-4500

ABSTRACT

One dimensional transient Electroosmotic flow in a rectangular nano-channel under the presence of an oscillating and an impulsive electric field is studied numerically. We consider aqueous electrolyte of three species, consisting of Na^+, Cl^- and a third species being a bio-molecule with a net negative charge. The parameters of interest are the mole fractions, velocity, potential, flow rate and current in the channel. The problem is a multiple time scale problem in the sense that the velocity field responds on a very short time scale while the electrolyte species respond to the long time scale. The results have application to bio-molecular sensing processes.

INTRODUCTION

There has been growing interest in the study of electroosmotic transport in recent years owing to its use in the areas of MEMS and NEMS. Electroosmotic transport is easy to use in miniature systems and compares favorably with pressure driven flow.[1] Modeling, simulation and control of electroosmotic transport has been a key factor in the development of Micro Total Analysis Systems in recent years. There is now a growing interest in modeling and simulating nanoscale fluidic devices which shall be capable of manipulation at molecular levels. These systems can have the potential for use in molecular separation and analyte detection with very small level of sample volumes.[2] In this light and understanding of flow phenomenon in nano-constrained channels under the action of externally applied electrical forces is important for the design of nanofluidic systems. Therefore, it is important to do modeling and simulation studies for such systems.

There have been numerous studies on electroosmotic flow, particularly in last few years. Most of these studies have been limited to steady state solution of the problem in micron sized channels.[3–5] Although time dependent electroosmotic flow has potential in biotechnology and separation science, it has been addressed in only a relatively few publications.[6–8] These studies give an analytical solution to the problems for special cases such as an alternating A/C field and have been performed at much higher channel heights of the order of microns. For example, Sodermann and Jonsson[9] reported analytical solutions for impulsively started electroosmotic flow in different channel geometries and Green *et al.*[10] investigated A/C electroosmosis on planar microelectrodes using steady and unsteady electric fields.

There have been many modeling and simulation studies on electroosmotic transport in microchannels. In majority of cases, a continuum models have been used for modeling the fluid flow parameters and a Poisson-Boltzmann distribution is used to find concentration profiles in the solution as outlined by Probstein.[11] In electroosmotic flow, electrical double layer (EDL) thickness is an important parameter that

* Supported by DARPA.
† Corresponding author E.Mail: conlisk.1@osu.edu.

governs the nature of solutions.[12] If the EDL thickness is of the order of the channel height, or in other words the EDLs overlap, the velocity profile is not same as the classical flat electrosoomotic profile that we are familiar with.[1] Also, the distribution of ions in such cases cannot be described appropriately by the Poisson Boltzmann distribution and hence the concentration distributions of different species have to be found by solving the actual equations of mole fractions.[13]

In this paper we consider the flow, the electric filed and mass transfer problems in a rectangular channel in which the mass transfer is due to diffusion and to the presence of an imposed square wave electric field. Numerical solutions have been found to transient electroosmotic flow problem. We have also presented in this paper the results for three component ion mixtures. This study will have important implications in the time domain control of electroosmotic flow which is of importance in drug delivery, Lab-on-a-chip devices and micromixing applications.

The present work has application to biosensors detecting single molecules. These sensors rely on the detection of small but sudden changes in the current density; these sudden changes will occur when a sufficiently large molecule enters a sufficiently small channel.

We do not explicitly consider this problem in this paper; however we will calculate the current density due to sharp changes in the magnitude of the imposed electric field, . In particular, the total current density in the channel is shown to arise from two reasons, the classical electrostatic current due to the movement of ionsunder the applied electric field and the flow current which is due to the bulk velocity of the fluid.

GOVERNING EQUATIONS

We consider a rectangular channel, whose height is nano-constrained. The length and width of the channel are very large compared to the height of the channel, so that the variations along the length and the width of the channel are negligible. The channel is shown in Figure 1.

The aqueous electrolyte in the channel is a dilute solution of three ionic species in water. The species considered are sodium, chloride and a bio-molecule with a net negative charge. The driving forces for mass transfer in such a problem are Fickian diffusion, pressure diffusion, migration due to the presence of an electric field and migration to the bulk flow. The molar flux for a species A in a dilute mixture is given by

$$\vec{n}_A = -cD_{AB}\nabla X_A + cu_A z_A F X_A \vec{E}^{+} cX_A\vec{u} \quad (1)$$

Here c is the total concentraion, D_{AB} is the diffusion coefficient, X_A is the mole fraction of species A, u_A is the mobility, z_A is the valence of the ion, in the case of a bio-molecule this is the net charge on the bio-molecule, F is the Faraday's constant, $\vec{E}$ is the total electric field and $\vec{u}$ is the mass average velocity of the fluid. The mobility u_A is defined by the Nernst-Planck equation as

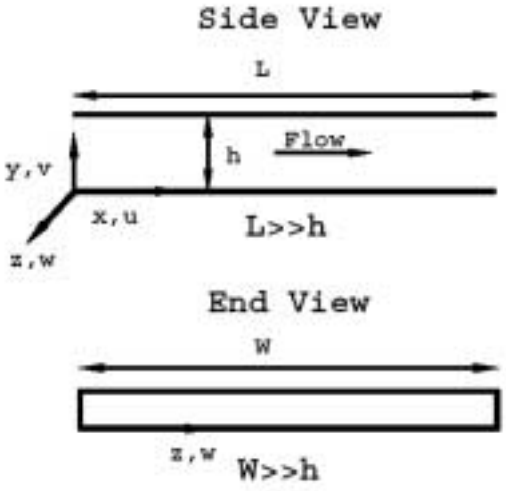

Figure 1: Geometry of the channel. Here h is very small compared to W and L, where W is the width of the channel and L its length in theprimary flow direction. u, v, and w are the fluid velocities in the x, y and z directions, respectively.

$$u_A = \frac{D_{AB}}{RT} \quad (2)$$

Then the mass transport equation for the transient EOF is,

$$c\frac{\partial X_A}{\partial t} + \nabla \bullet \vec{n}_A = 0 \quad (3)$$

In the current work we study the mass transport in the channel due to the applied electric field and in the 1D case the mass transport equation becomes,

$$\frac{\partial X_A}{\partial t} - D_{AB}\frac{\partial^2 X_A}{\partial y^2} + \frac{D_{AB}}{RT} z_A F \frac{\partial}{\partial y}(X_A E_y) = 0 \quad (4)$$

In the above equation , E_y is the electric field in the y direction and is due to the distribution on ions alone. Substituting for the The mass transfer equation is substituted by an equation for the electric field. The electric field E must satisfy the Maxwell's equation in the form,

$$\nabla \times \vec{E} = 0 \quad (5)$$

which along with the Poison equation is given by

$$\nabla \bullet (\epsilon_e \vec{E}) = -\nabla \bullet \nabla \phi = \rho_e \tag{6}$$

determines the potential. Here ρ_e is the charge density per unit volume. The charge density is defined by,

$$\rho_e = F \sum_{i=1}^{n} z_i c_i = Fc \sum_{i=1}^{n} z_i X_i \tag{7}$$

where n is the number of species, c_i is the molar concentration of species i, and c is the total molar concentration and is assumed a constant.

$$\vec{E} = -\frac{\partial \phi}{\partial y} \tag{8}$$

and,

$$\frac{\partial^2 \phi}{\partial y^2} = -\frac{Fc}{\epsilon_e} \sum_{i=1}^{n} z_i X_i \tag{9}$$

which is the dimensional form of the equation and for the potential. Using equations (8) and (9) we simplify the mole fraction governing equation. The final mole fraction equation in the dimensional form is,

$$\frac{\partial X_A}{\partial t} - D_{AB} \frac{\partial^2 X_A}{\partial y^2} -$$

$$\frac{D_{AB}}{RT} z_A F \left(\frac{-Fc}{\epsilon_e} X_A \sum_{i=1}^{n} z_i X_i + \frac{\partial \phi}{\partial y} \frac{\partial X_A}{\partial y}\right) = 0 \tag{10}$$

The velocity is given by the Navier Stokes equation as,

$$\rho \left(\frac{\partial u}{\partial t} + (u \bullet \nabla) u\right) = -\nabla p + \mu \nabla^2 u + \rho_e \vec{E} \tag{11}$$

where, ρ is the density of the electrolyte, and μ is the dynamic viscosity. For 1D the equation the dimensional form of the velocity equation becomes,

$$\rho \frac{\partial u}{\partial t} = \mu \frac{\partial^2 u}{\partial y^2} + \rho F c E_x(t) \sum_{i=1}^{n} z_i X_i \tag{12}$$

Now we rewrite the mole fraction, potential and velocity equation in non-dimensional form as follows,

$$\frac{\partial X_A}{\partial t} - \frac{\partial^2 X_A}{\partial y^2} + \frac{\beta}{\epsilon^2} z_A X_A \sum_{i=1}^{n} z_i Xi - z_A \frac{\partial \phi}{\partial y} \frac{\partial X_A}{\partial y} = 0 \tag{13}$$

The time scale for the mole fraction is $t_X = h^2/D_{AB}$, length scale is h the potential scale is $\phi_0 = \frac{RT}{F}$ given by 26mV, R is the universal gas constant, T is the temperature and , $\epsilon = \frac{\lambda}{h}$, λ is the EDL thickness given by,

$$\lambda = \frac{1}{F} \sqrt{\frac{\epsilon_e RT}{I}} \tag{14}$$

where I is the ionic concentration given by

$$I = \sum_{i=1}^{n} z_i^2 c_i \tag{15}$$

and

$$\beta = \frac{c}{I} \tag{16}$$

The potential equation in the non-dimensional form is given by

$$\frac{\partial^2 \phi}{\partial y^2} = -\frac{\beta}{\epsilon^2} \sum_{i=1}^{n} z_i X_i \tag{17}$$

and the non-dimensional velocity equation is ,

$$\frac{\partial u}{\partial t} = \frac{\partial^2 u}{\partial y^2} + \beta E_x(t) \sum_{i=1}^{n} z_i X_i \tag{18}$$

the time scale for the velocity equation is $t_u = \frac{h^2}{\nu}$, comparing the time scales of mole fraction and velocity equation we get,

$$\frac{t_u}{t_X} = \frac{h^2/\nu}{h^2/D_{AB}} = \frac{D_{AB}}{\nu} = O(10^{-3})$$

for a typical $D_{AB} = 10^{-9}$, thus the velocity equation follows a very short time scale compared to the mole fraction equation and the transient term in the velocity equation is neglected and we get,

$$\frac{\partial^2 u}{\partial y^2} + \beta E_x(t) \sum_{i=1}^{n} z_i X_i = 0 \tag{19}$$

as the final non-dimensional velocity equation. Equations (13), (17) and (19) are the final non-dimensional equations for the mole fractions, potential and velocity.

Boundary condition

The wall mole fraction g^0,f^0 and e^0 at y = 0, are assumed as g^0 = 0.154, f^0 = 0.0141 and e^0 = 0.01. The potential ϕ^0 = 0 ans for velocity no slip condition is assumed. A symmetric case is considered so that we have the same values are assumed at y = 1. ie $g^0 = g^1$, $f^0 = f^1$, $e^0 = e^1$, $\phi^0 = \phi^1$ and $u^0 = u^1$.

Initial condition

The initial condition for g,f,e,ϕ and u are taken from the solution to the steady state problem.

CURRENT DENSITY

The total current in the channel is contributed by two parts: the electrostatic current (current in the absence of flow) due to the migration of ions under the applied electric field and the flow current due to ions flowing in the channel because of the bulk velocity. The non-dimensional current density in the channel is given by the following equation.

$$I_{total} = Ielectrostatic(I_{es}) + Idueto flow(I_{fl})$$

$$I_{total} = \frac{E_x E(t)}{\phi_0 u_0} \sum_{i=1}^{n} z_0^2 D_i \int_0^1 X_i dy + \int_0^1 \sum_{i=1}^{n} z_i X_i u dy \tag{20}$$

where I_{total} is the total current density, I_{es} is the Electrostatic current,I_{fl} - Current due to flows,D_i is the Diffusion coefficient of i^{th} species, X_i - mole fraction of i^{th} species.The current in the channel is an important parameter, in the bio-sensing point of view.

Periodic forcing (square pulse electric fields) will naturally occur in synthetic ion channels due to two factors:

1. the opening and closing, or gating, of the ion channel will create (essentially) square pulses in the flow rate;

2.sensing binding and unbinding events at the channel surface will lead to sudden step-like decreases and increases, respectively, in wall concentration and electric potential.

Binding events in synthetic ion channels are detected at present by a drop in current density. Biosensors rely on the ability of a receptor to bind with a target biomolecule on the surface. This binding is usually detected by the associated decrease in the current density (Braha, et al, Gu et al).

Another application where the measurement of current will help is in determining Ischemia. The ability of the N-terminal region of human albumin to bind cobalt is diminished by myocardial ischemia, and it is called Ischemia modified albumin (IMA). The fact that the binding affinity reduces to cobalt, means that the unbound cobalt can be measured in terms of current, while analyzing the IMA in a nano-channel.

RESULTS

Numerical Method: The governing equations are solved using a crank Nichlolson scheme. The equations are non-linear and coulpled so the equations are solved simultaneously with a iterative process, with a convergence based on mole fraction of one species. 41 points are used across the channel for the 5nm channel and 81 points are used for the 20nm channel, as the EDL thickness is very small compared to the height of the channel. In both the cases the program was run with double the number of points and the results were validated for an accuracy of four decimal places.

Analytical Solution: The analytical solution assumes a Poison Boltzman distribution for the mole fractions, given by

$$X_A = X_A^0 e^{-z_A \phi} \tag{21}$$

Here X_A^0 is the wall mole fraction of species A. The potential values are taken from the numerical result and the above equation is used to calulate the mole fraction evolution in the channel, and compared with the numerical result which uses the mass transfer equation for mole fractions.

For the sake of convenience the following notations are used. Mole fraction of Na^+ and Cl^- is denoted by g,f. The mole fraction of the third species whose charge is -3 is denoted by e.

Figure 2 shows the applied square wave across the channel, with an amplitude of 1 and a period of 0.5. After $t = 2$ the electric field sets at +1. Figure 3, 4 and 5 show the evolution of mole fraction of Na^+, Cl^- and the bio-molecule with a charge of -3, denoted by g, f and e respectively for the 5nm channel. The evolution is shown at y = 0.5, y = 0.25 and y = 0.125. The flow is symmetric so the evolution is similar for the other half of the channel. The solid lines show the numerical result and the dotted line shows the analytical result. It has to be noted that the analytical solution (which assumes a Poison-Boltzman distribution of ions) does not match with the numerical results (which use the mass transfer equation for the ions) during the transient period. The wall concentrations assumed are g^0 = 0.0028, f^0 = 0.00052 and e^0 = 0.000179. The analytical solution is valid only when the difference between the wall mole fractions of the species are small. In the present case we have assumed wall mole fraction so that the difference in the wall concentration of positive and negative species as large.This is the reason why the numerical result is more accurate. It can also be seen that the applied electric field does not have any influence on the mole fractions.

Figure 6 shows the distribution of mole fractions across the 5nm channel. As the EDLs over lap in this case the profile is curved and the core of the channel is not neutral.

It is also to benoted that the mole fraction of the positive species g is more near the negatively charged wall and less at the core and vice versa for the negatively charged species.

Figure 7 shows the evolution of potential at different regions in the 5nm channel. Note that the core of the channel has higher potential than the wall of the channel. In other words the wall is negatively charged compared to the core of the channel. The applied electric field does not have an influence on the potential also. The potential solely depends on the distribution of the mole fraction of ions Figure 8 shows the evolution of potenital across the channel with time. The parabolic profile of the potential implies that the EDLs are overlapped.

Figure 9 shows the evolution of velocity at different positions in the channel. The velocity is maximum at the core as expected and it follows the applied electric field. The velocity responds instantaneoulsy to the applied electric field as the inertial terms are neglible. Figure 10 shows the current in the channel in pico Amps. Note that the electrostatic current dominates and overlaps with the total current shown by the dotted line. The solid line shows the flow current which is very small as the velocities involved in nano-channels are small.

Figures 11, 12, 13 show the evolution of mole fractions for the 20nm channel under same conditions. It takes a little longer time to reach the steadt state. Figure 14 shows the mole fraction profiles across the channel at steady state. It matches exactly with the numerical solution. In a 20nm channel the EDLs are relatively thin, so we obtain a flat profile and the core in electrically neutral.Figure 15 shows the evolution of potential in the 20nm channel. Figure 16 shows the velocity and Figure 17 shows the current in the channel. Note that the current in the 20nm channel is roughly four times that of the current in the 5nm channel.

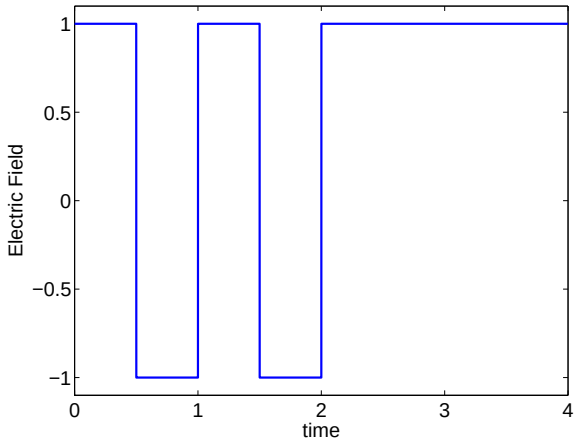

Figure 2: Applied square wave electric field with period = 0.5.

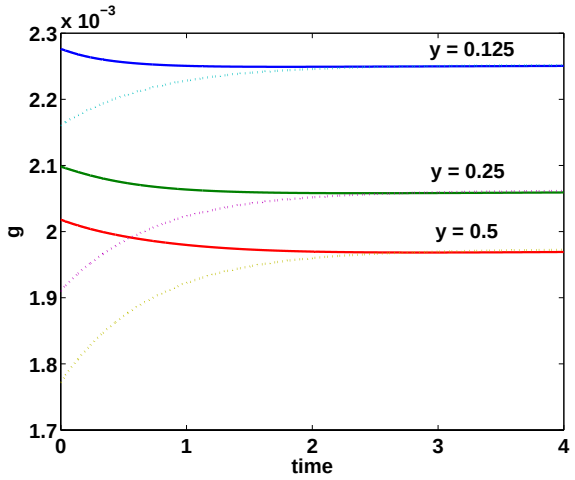

Figure 3: Evolution of mole fraction g with time for h=5nm, g^0=0.0028, f^0 = 0.000252, e^0 = 0.000179 under the applied square pulse. Solid line is numerical result and dottedline is analytical result. Note that during the transient period numerical and analytical result does not match.

SUMMARY

Transient electroosmotic flow was studied in a rectangular channel numerically and the results were compared with analytical solution for the mole fractions. It is seen that at the transient state the evolution of mole fractions is different that that given by the analytical solution. The mole fractions and potential are independent of the applied electric field. The velocity, flow rate and current in the channel are directly dependent on the applied electric field. The currrent in the channel is mainly due to the electrostatic component. The current due to flow is much less compared to the elecrostatic current as the velocities involved are very low.

In the full paper the impulsively started problem will be solved as well as the case where E(t) drops suddenly to zero.

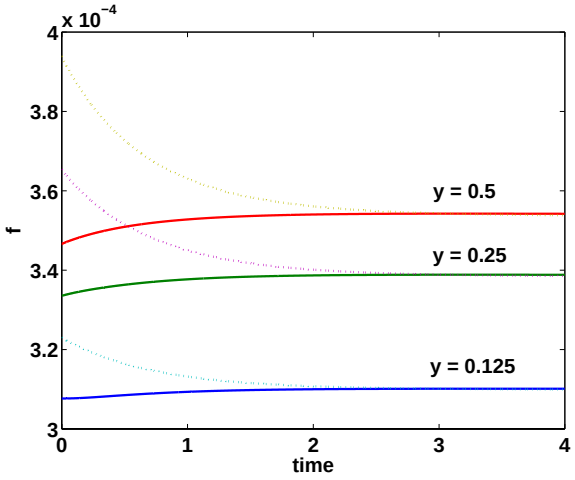

Figure 4: Evolution of mole fraction f with time for h=5nm, g^0=0.0028, f^0 = 0.000252, e^0 = 0.000179 under the applied square pulse. Solid line is numerical result and dottedline is analytical result. Note that during the transient period numerical and analytical result does not match.

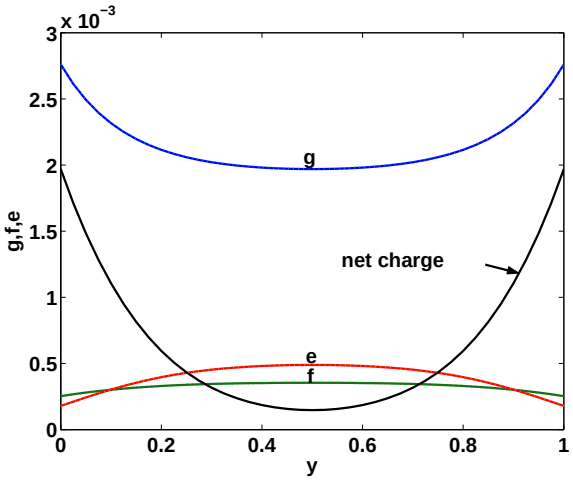

Figure 6: Distribution of mole fraction g,f,e across the channel at steady state for h=5nm, g^0=0.0028, f^0 = 0.000252, e^0 = 0.000179 under the applied square pulse. Solid line is the numerical result and the dotted line is the analytical result.The numerical and the analytical result match exactly at the steady state. Note that the net charge at the core of the channel is not zero.

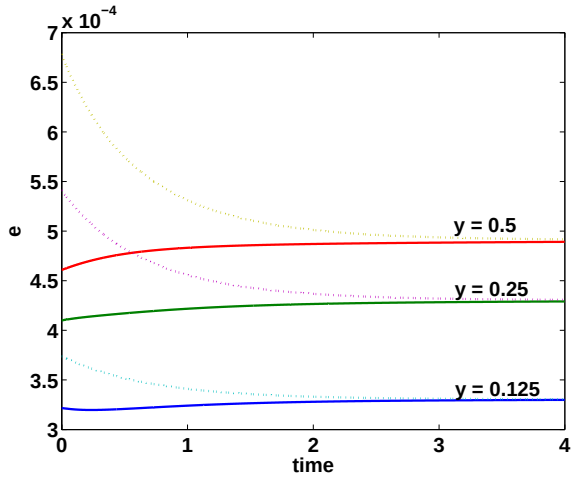

Figure 5: Evolution of mole fraction e with time for h=5nm, g^0=0.0028, f^0 = 0.000252, e^0 = 0.000179 under the applied square pulse. Solid line is numerical result and dottedline is analytical result. Note that during the transient period numerical and analytical result does not match.

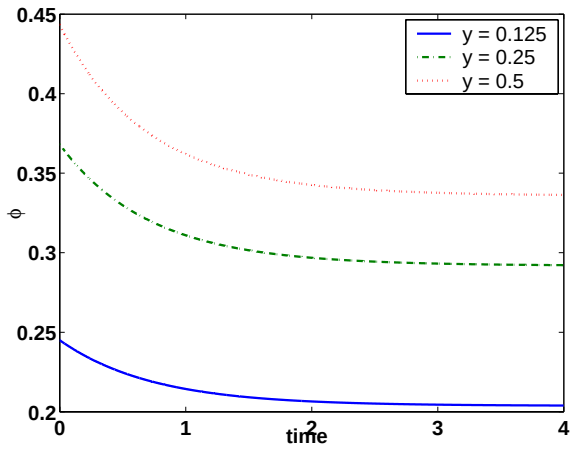

Figure 7: Evolution of potential with time at differnt heights of the channel, for h=5nm, g^0=0.0028, f^0 = 0.000252, e^0 = 0.000179 under the applied square pulse.

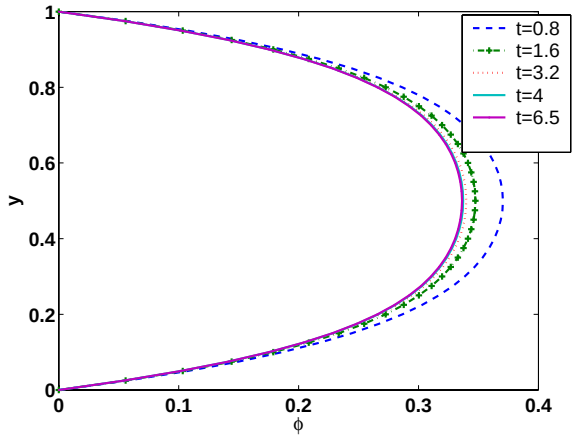

Figure 8: Evolution of potential across the channel for h=5nm, g^0=0.0028, f^0 = 0.000252, e^0 = 0.000179 under the applied square pulse. Note that the potential is not affected by the applied electric field.

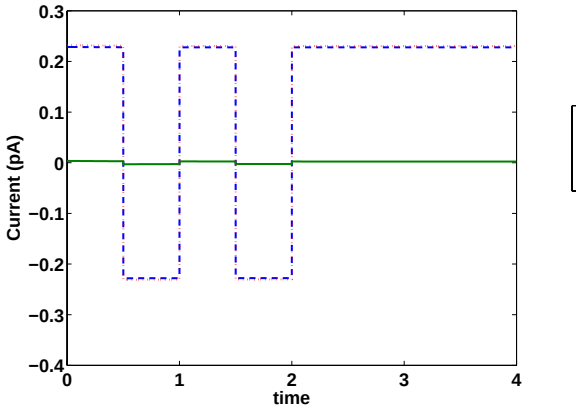

Figure 10: Evolution of current in the channel due to EOF for h = 5nm , g^0=0.0028, f^0 = 0.000252, e^0 = 0.000179 under the applied square pulse.Note that the flow current is very low compared to the electrostatic current.

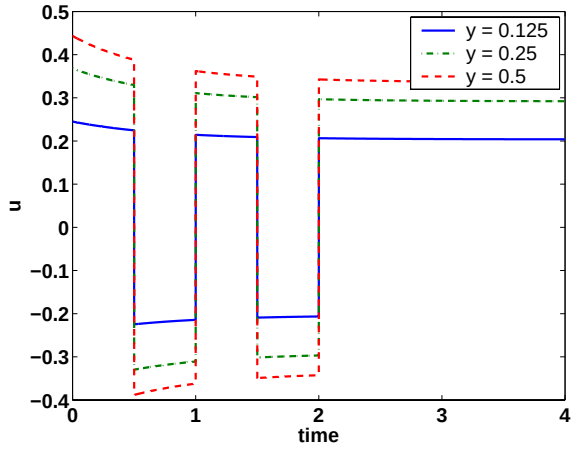

Figure 9: Evolution of velocity with time at different heights of the channel for h=5nm, g^0=0.0028, f^0 = 0.000252, e^0 = 0.000179 under the applied square pulse. Note that the velocity follows the applied electric field.

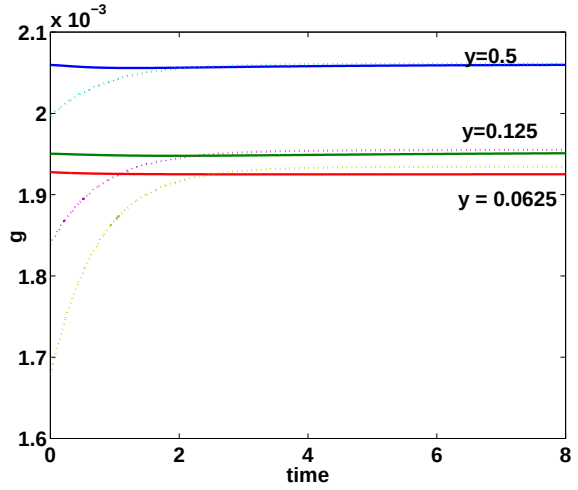

Figure 11: Evolution of mole fraction g with time for h=20nm, g^0=0.0028, f^0 = 0.000252, e^0 = 0.000179 under the applied square pulse. Solid line is numerical result and dottedline is analytical result. Note that during the transient period numerical and analytical result does not match.

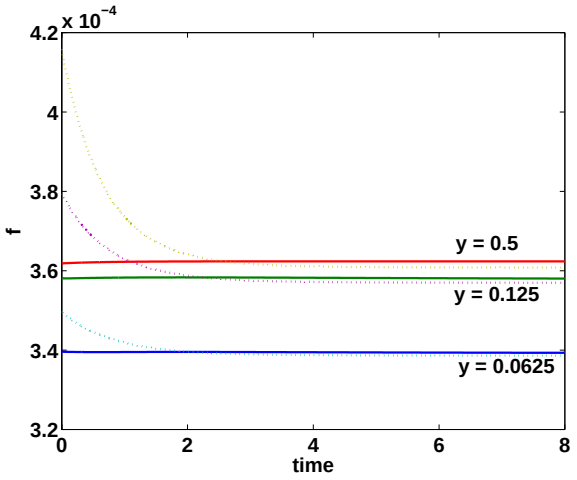

Figure 12: Evolution of mole fraction f with time for h=20nm, g^0=0.0028, f^0 = 0.000252, e^0 = 0.000179 under the applied square pulse. Solid line is numerical result and dottedline is analytical result. Note that during the transient period numerical and analytical result does not match.

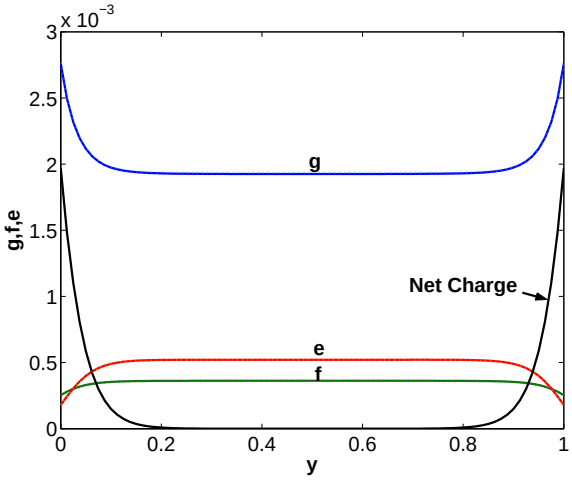

Figure 14: Distribution of mole fraction g,f,e across the channel at steady state for h=20nm, g^0=0.0028, f^0 = 0.000252, e^0 = 0.000179 under the applied square pulse. Solid line is the numerical result and the dotted line is the analytical result.The numerical and the analytical result match exactly at the steady state.

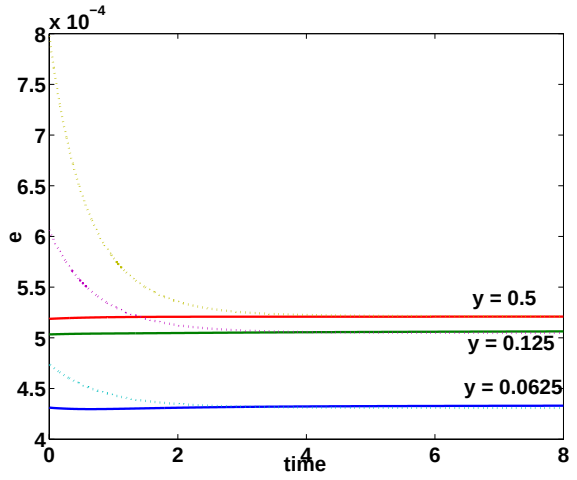

Figure 13: Evolution of mole fraction e with time for h=20nm, g^0=0.0028, f^0 = 0.000252, e^0 = 0.000179 under the applied square pulse. Solid line is numerical result and dottedline is analytical result. Note that during the transient period numerical and analytical result does not match.

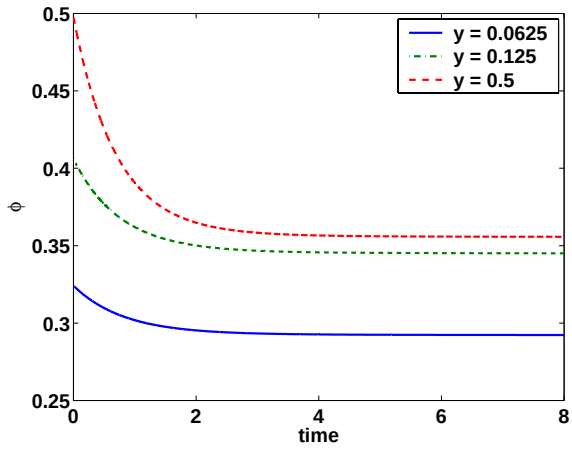

Figure 15: Evolution of potential with time at differnt heights of the channel, for h=20nm, g^0=0.0028, f^0 = 0.000252, e^0 = 0.000179 under the applied square pulse.

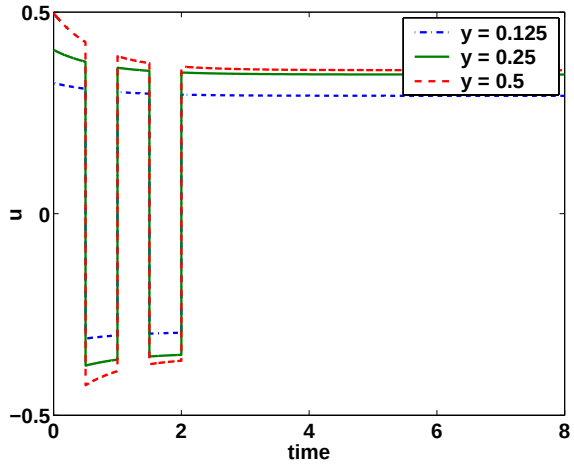

Figure 16: Evolution of velocity with time at different heights of the channel for h=20nm, g^0=0.0028, f^0 = 0.000252, e^0 = 0.000179 under the applied square pulse. Note that the velocity follows the applied electric field.

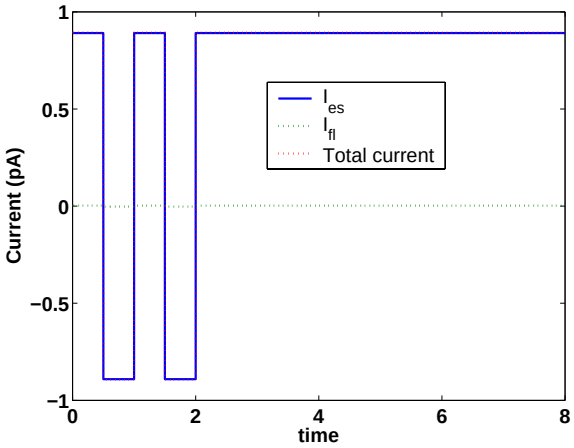

Figure 17: Evolution of current in the channel due to EOF for h = 20nm , g^0=0.0028, f^0 = 0.000252, e^0 = 0.000179 under the applied square pulse.Note that the flow current is very low compared to the electrostatic current.

ACKNOWLEDGEMENTS

This work is funded by DARPA and the authors are grateful to the contract monitors Dr. Anantha Krishnan(DARPA), Mr. Clare Thiem and Mr. Duane Gilmour of the Air Force Research Lab(IFTC) for their support.

References

[1] Conlisk A.T., McFerran J., Zheng Z., Hansford D. (2002) "Mass Transfer and Flow in Electrically Charged Micro- and Nanochannels" Anal. Chem., 74,pp2139-2150.

[2] Qiao R., Aluru N.R.,(2003) "Ion Concentrations and Velocity Profiles in nanochannel electroosmotic flows" J. Chem. Phys. 118, pp 4692-4701.

[3] Theemsche A. V., Deconinck J., Bossche B. V., Bortels L.,(2002) "Numerical Solution of a Multi-ion One-Potential Model for Electroosmotic Flow in Two-Dimensional Rectangular Microchannels" Anal. Chem., 74, pp 4919-4926.

[4] Hu H. H., Patankar N.A. (1998) "Numerical Simulation of Electroosmotic Flow" Anal. Chem., 70, pp 1870-1881.

[5] Sadr R., Yoda M., Zheng Z., Conlisk A. T. (2004) "An experimental study of electroosmotic flow in rectangular microchannels" J. Fluid Mech., 506, pp 357-367.

[6] Dutta, P., Beskaok A. (2001) "Analytical Solutions to Time Periodic Electroosmotic Flows: Analogies to Stoke's Second Problem" Anal. Chem., 73, pp 5097-5102.

[7] Qiao R., Aluru N.R., (2003) "Transient Analysis of electro-osmotic transport by a reduced order modeling approach" Int. J. Numer. Meth. Engg. 56, pp 1023-1050.

[8] Hanna W.T., Osterle J.F. (1968) "Transient Electroosmotic Flow in Capillary Tubes" J Chem Phys., 49(9), pp 4062-4068.

[9] Soderman O., Jonsson, B(1996) "Elecroosmosis: Velocity Profiles in different geometries with both temporal ans spatial resolutions " J. Chem. Phys. 105.pp 10300-10311.

[10] Green, N.G., Ramos. A., Gonzalez. A/ Morgan H. Castellanos , A. (2000) "Flow induced by non-uniform AC fields in electrolytes on microelectrodes" Phys Rev. E,61(4), pp 4011-4018.

[11] Probstien R. F., (1999) "Physiochemical Hydrodynamics" Butterworth Publishers, Boston.

[12] Hunter R.J., (2001) "Foundation of Zeta Potential in Colloid Science" Oxford Univ. Press., New York.

[13] Zheng Z., Conlisk A.T., Hansford D. (2003), "Effect of multivalent ions on electroosmotic flow in micro- and Nanochannels" Electrophoresis, 17, pp. 3006 - 3017.